Stellar Populations in the SAMI Galaxy Survey



Peter Jonathan Watson

Christ Church

University of Oxford

A thesis submitted for the degree of

Doctor of Philosophy

Trinity 2023

For Vera.

"Everything starts somewhere,
although many physicists disagree."
– Terry Pratchett

Abstract

We present a set of line index-based measurements of the relative α-element abundance, [α/Fe], for up to 2097 galaxies in the Sydney-Australian-Astronomical-Observatory Multi-object Integral-field Spectrograph (SAMI) Galaxy Survey using aperture spectra normalised to the effective radius $R_{\rm e}$. We derive a best-fit linear relation between [α/Fe] and the galaxy effective velocity dispersion $\sigma_{\rm e}$ for early-type galaxies (ETGs), $[\alpha/{\rm Fe}] = (0.307 \pm 0.015)\log_{10}\left(\sigma_{\rm e}/{\rm km\,s^{-1}}\right) - (0.41 \pm 0.03)$, observing a strong correlation betwen the residuals and the local environmental surface density. We find evidence for galaxies in high-density environments (HDEs) being α-enhanced over their counterparts in low-density environments (LDEs), and that this offset varies with morphological type, with ellipticals α-enhanced by $\gtrsim 0.06$ dex and spirals by ≈ 0.02 dex. We use the offset in ellipticals to estimate that star formation in HDEs was truncated ≈ 1 Gyr earlier than in LDEs, at a fixed velocity dispersion of $\sigma_{\rm e} = 100\,{\rm km\,s^{-1}}$. We also find support for a parabolic relationship between [α/Fe] and $\sigma_{\rm e}$ in ellipticals, indicating contributions from both environment and mass-based quenching mechanisms, although there is no evidence for this behaviour in later-type galaxies.

We then refit a global [α/Fe]-$\sigma_{\rm e}$ relation, using a subset of 1317 galaxies with measurements of the inclination-corrected spin proxy $\lambda^{\rm eo}_{R_{\rm e}}$. We derive an anti-correlation between the residuals $\Delta\,[\alpha/{\rm Fe}]$ and the spin proxy, $\Delta\,[\alpha/{\rm Fe}] = (-0.060 \pm 0.009)\lambda^{\rm eo}_{R_{\rm e}} + (0.027 \pm 0.004)$, which appears to be driven by star-forming galaxies, with a gradient $\Delta\,[\alpha/{\rm Fe}] \propto (-0.14 \pm 0.02)\lambda^{\rm eo}_{R_{\rm e}}$. This indicates that disc-dominated galaxies have an extended duration of star-formation, with an estimated increase in the half-mass formation time of ≈ 0.8 Gyr between our low- and high-$\lambda^{\rm eo}_{R_{\rm e}}$ samples. We also observe that slow rotators do not have significantly different stellar populations than other low-$\lambda^{\rm eo}_{R_{\rm e}}$ galaxies, concluding that galaxies with $\lambda^{\rm eo}_{R_{\rm e}} \lesssim 0.4$ experience a similar range of star formation histories, despite their differing structural parameters.

Next, we introduce a novel application of the contour binning method. We compare this method against the use of Voronoi tessellation and fixed-width annuli, demonstrating that it maximises the available radial information in low signal/noise

observations. We apply this method to galaxies drawn from the SAMI Galaxy Survey, deriving seeing-corrected radial stellar population gradients for 1453 galaxies. On average, galaxies in our sample have flat age and [α/Fe] gradients, but negative metallicity gradients. We show the variations of these gradients and radial profiles in the size-mass plane, simultaneously separating galaxies by morphological type and environment. Our results reinforce the earlier analysis using global measurements, in that at all galactocentric radii, ETGs in HDEs are older by $\gtrsim 2\,\mathrm{Gyr}$, and have higher metallicities and α-abundance by $\approx 0.05\,\mathrm{dex}$ compared to their counterparts in LDEs. These offsets are not present in late-type galaxies (LTGs).

Finally, we demonstrate that radial population gradients do not have any significant dependence on environment, for fixed morphological type. The exception to this is [α/Fe] gradients in high-mass LTGs, which we show is consistent with existing models of star formation in disc galaxies. We discuss the physical implications of our results, including the support for inside-out quenching mechanisms and comparisons with existing literature, and explore potential avenues for further study.

Statement of Originality

The work presented in this thesis was undertaken at the Department of Astrophysics at the University of Oxford between October 2019 and May 2023 under the supervision of Prof. Roger Davies, and was funded by a Hintze Family Charitable Foundation Scholarship. This included time spent at the Research School of Astronomy and Astrophysics (RSAA) at the Australian National University (ANU) between August 2022 and January 2023 under the supervision of Prof. Matthew Colless, which was funded by the Oxford-ANU Exchange Travel Grant. I hereby declare that no part of this thesis has been submitted in support of another degree, diploma, certificate, or other qualification at the University of Oxford or elsewhere. Except where otherwise stated, or where reference is made to the work of others, the work in this thesis is entirely my own.

The work presented in Chapters 2, 3, and 4 is based on the peer-reviewed, published papers Watson et al., 2022a and Watson et al., 2022b, of which I am the first author.

The work presented in Chapters 5 and 6 was carried out in collaboration with Prof. Roger Davies and Prof. Matthew Colless. These chapters form the basis of a paper that is in preparation for submission to Monthly Notices of the Royal Astronomical Society (MNRAS), for which I am the first author.

In Chapters 4 and 6, the measurements of the inclination-corrected spin proxy were kindly provided by Dr. Jesse van de Sande (private communication).

The work throughout this thesis makes extensive use of data from the SAMI Galaxy Survey (Croom et al., 2012; Bryant et al., 2015). The SAMI Galaxy Survey is based on observations made at the Anglo-Australian Telescope, and was developed jointly by the University of Sydney and the Australian Astronomical Observatory. The SAMI input catalogue is based on data taken from the Sloan Digital Sky Survey (SDSS), the Galaxy and Mass Assembly (GAMA) Survey, and the Very Large Telescope Survey Telescope (VST) ATLAS Survey. The SAMI Galaxy Survey is supported by the Australian Research Council Centre of Excellence for All Sky Astrophysics in 3 Dimensions (ASTRO 3D), through project number CE170100013, the

Australian Research Council Centre of Excellence for All-sky Astrophysics (CAASTRO), through project number CE110001020, and other participating institutions. The SAMI Galaxy Survey website is https://sami-survey.org/.

The copyright of this thesis rests with the author. No quotation or figure from it, or information derived from it, may be published without the prior consent and acknowledgement of its author.

Peter J. Watson
(*May 2023*)

Acknowledgements

First and foremost, I have to thank my supervisor, Prof. Roger Davies, for all his support and encouragement over the last few years. From keeping me grounded by occasionally asking *why* I'd decided to reinvent the wheel, to his incredibly useful insights into seemingly every area of astrophysics, I couldn't have asked for a better supervisor. A massive thank you also has to go to Prof. Matthew Colless, for both stepping into those shoes, and hosting me at the RSAA – I'll never forget my time in Australia.

Many thanks to those in the department who've helped in any way over the last few years. To Tanya, Ashling, and Leanne, for keeping everything running so smoothly behind the scenes. Chiara, thanks for many enlightening discussions on stellar populations, and for humouring me in debates over the differences between [Mg/Fe] and [α/Fe]. To everyone who's had the (mis)fortune to share an office (or even house!) with me – Sarah, Tobias, Jamie, Susanna, Joe, Amy, Annabella, and not least Jakob, whose bizarre remarks I'll surely come to miss dearly.

I'd also like to thank everyone in the SAMI team, without whom this thesis would have looked very different. Nic Scott, for paving the way on stellar population studies in SAMI; Scott Croom and Julia Bryant for all the work put in to organising absolutely everything; and many, many others who contributed to making the survey run so well. Special thanks of course, to Jesse van de Sande, for some fantastic discussions on stellar populations, kinematic fits, and peculiar ring galaxies. To Stefania, Sree, Henry, Philip, and everyone else in the RSAA and ASTRO 3D, thank you for making me feel so welcome on the other side of the planet, and I hope our paths will cross again soon enough.

It would be impossible to thank everyone else who's helped me through the last few years individually, and this thesis is quite long enough already. From those in Oxford who've been there from the start - Evan, Eimear, Marin, Anna, Connor - to those who've joined along the way (Marion, Ben, Arthur, and many others), it's been quite the journey to reach this point.

Last, but most definitely not least, I'd like to thank my family. To Mum and Dad, thank you for your love and support – I'm not sure if this is quite what you expected

when you gave me those physics books all those years ago, but I definitely wouldn't be here without you. To Helena and Susannah, I couldn't be prouder seeing how far you've both come, and congratulations on avoiding careers in physics (for now). And finally, special thanks to Poppy. Whilst your suggestions for me to get more sleep might have often fallen on deaf ears these last few weeks, I couldn't imagine doing this without you. Thank you for always being there.

Peter
(*May 2023*)

Contents

1 Introduction **1**

1.1 Background . . . 1

1.1.1 A Brief History of Observational Astronomy . . . 1

1.1.2 The History of Galaxy Observations . . . 4

1.1.3 The State of Cosmology . . . 6

1.1.4 Measuring Stellar Populations . . . 8

1.2 Previous Research . . . 14

1.2.1 Scaling Relations . . . 14

1.2.2 The Influence of the Environment . . . 16

1.2.3 Kinematics . . . 17

1.2.4 Radial Gradients . . . 20

1.3 The SAMI Galaxy Survey . . . 21

1.3.1 The Instrument and Survey Design . . . 22

1.3.2 Ancillary Data . . . 24

1.3.3 Photometry and Stellar Masses . . . 24

1.3.3.1 MGE Fits . . . 25

1.3.3.2 Environmental Metrics . . . 25

1.3.3.3 Classifications of Morphological Type . . . 28

1.3.3.4 Star-formation Rate . . . 28

1.3.3.5 Kinematic Measurements . . . 29

1.4 Thesis Outline . . . 30

2 Measuring Stellar Populations **32**

2.1 Spectral Fitting . . . 32

2.1.1 Combining the Blue and Red Arms . . . 33

2.1.2 pPXF . . . 34

2.1.3 Template Spectra . . . 35

2.1.4 Iterative Fitting . . . 35

2.1.4.1 Initial Fit . . . 36
2.1.4.2 Subsequent Fits . . . 38
2.2 Line Indices . . . 39
2.2.1 The Lick/IDS Index System . . . 39
2.2.2 Measuring Line Indices . . . 41
2.2.3 Index Dispersion Corrections . . . 44
2.3 Stellar Population Parameters . . . 45
2.3.1 Parameter Space Limitations . . . 47
2.3.2 Sky Line Contamination . . . 50
2.3.3 Nomenclature . . . 52

3 Global Stellar Populations as a Function of Morphology and Environment 53
3.1 Sample Selection . . . 53
3.1.1 Quality cuts . . . 54
3.1.2 Completeness . . . 54
3.1.3 DR3 Consistency Checks . . . 57
3.1.4 Line Fitting . . . 58
3.2 Environmental Dependence . . . 59
3.2.1 Separation by Colour . . . 59
3.2.2 Early-type Galaxies . . . 63
3.2.3 Morphology Dependence . . . 65
3.2.4 Separation by Velocity Dispersion . . . 68
3.2.4.1 Non-linear Behaviour . . . 70
3.3 Discussion . . . 72
3.3.1 Comparisons to Previous Studies . . . 72
3.3.2 Physical Implications . . . 73
3.4 Conclusions . . . 77

4 The Dependence of Global Stellar Populations on Kinematic Morphology 79
4.1 Sample Selection . . . 79
4.1.1 Quality Cuts . . . 80
4.1.2 Completeness . . . 80
4.1.3 Kinematic Classification . . . 82
4.2 Results . . . 84
4.2.1 Global Relations . . . 84

4.2.2 Slow Rotators . . . 86
4.2.3 Relations for the Quenched Sample . . . 88
4.3 Discussion . . . 92
4.3.1 Comparisons to Previous Studies . . . 92
4.3.2 Physical Implications . . . 94
4.3.2.1 Similarities Between Slowly-spinning Systems . . . 97
4.4 Conclusions . . . 102

5 Measuring Radial Gradients 104
5.1 Binning Methods . . . 104
5.1.1 Fixed Annuli . . . 105
5.1.2 Voronoi Tessellation . . . 107
5.1.3 Flux Contours . . . 110
5.1.3.1 Source Images . . . 111
5.1.3.2 PSF Matching . . . 112
5.1.3.3 Binning Procedure . . . 117
5.1.4 A Comparison of Methods . . . 121
5.2 Seeing Corrections . . . 127
5.3 Conclusions . . . 132

6 Radial Gradients of Stellar Populations 135
6.1 Sample Selection . . . 135
6.1.1 Gradient Quality Cuts . . . 138
6.1.2 Bayesian Line Fitting . . . 141
6.2 Correlations With Velocity Dispersion . . . 143
6.3 The Stellar Mass-size Plane . . . 146
6.3.1 Optical Morphology . . . 150
6.3.2 Environmental Density . . . 151
6.4 Radial Profiles . . . 154
6.5 Discussion . . . 162
6.5.1 Comparison with Previous Studies . . . 162
6.5.1.1 Global Properties . . . 162
6.5.1.2 Gradients . . . 166
6.5.1.3 Radial Profiles and Kinematic Morphology . . . 168
6.5.2 Physical Implications . . . 171
6.6 Conclusions . . . 177

7 Conclusions **179**
7.1 Future Work 185

A Comparing Integrated and Radial SSP Measurements **189**

B The Virial Theorem **191**

Bibliography **194**

List of Figures

1.1 The distribution of local surface densities against group halo masses. 27

2.1 A SAMI spectrum, showing how the variance depends on wavelength. 34
2.2 The three-stage spectral template fit using PPXF. 37
2.3 The distribution of the noise scaling factor. 38
2.4 The locations of the Lick indices on a spectrum. 40
2.5 An equivalent width measurement. 42
2.6 The index correction factors for high σ galaxies. 46
2.7 The χ^2 distribution of the SSP parameters. 48
2.8 The distribution of the $\pm 1\sigma$ uncertainties on each SSP parameter. . . 49
2.9 The redshift dependence of $\Delta\,[\alpha/\mathrm{Fe}]$. 50
2.10 The σ_e distribution of galaxies with $z > 0.0732$. 51

3.1 Quality cuts in the σ_e-S/N plane. 55
3.2 Sample selection shown in the σ_e-M_r plane. 57
3.3 A comparison of $[\alpha/\mathrm{Fe}]$ measurements to SAMI DR3. 58
3.4 The selection of "red sequence" and "blue cloud" galaxies. 60
3.5 The $\log_{10}\left(\Sigma_5/\mathrm{Mpc}^{-2}\right)$ distribution of red and blue galaxies. 61
3.6 The $[\alpha/\mathrm{Fe}]$-σ_e and $\Delta\,[\alpha/\mathrm{Fe}]$-$\log_{10}\left(\Sigma_5/\mathrm{Mpc}^{-2}\right)$ relations for red and blue galaxies. 62
3.7 The distribution of $\Delta\,[\alpha/\mathrm{Fe}]$ for ETGs, separated by environment. . . 64
3.8 Unconstrained fits between $[\alpha/\mathrm{Fe}]$ and σ_e, separated by environment and morphological type. 66
3.9 Fits between $[\alpha/\mathrm{Fe}]$ and σ_e, separated by environment and morphological type, constrained to a single gradient. 69
3.10 A parabolic $[\alpha/\mathrm{Fe}]$-σ_e relation, fit to ETGs. 71
3.11 The distribution of galaxies in σ_e-Σ_5 space. 75

4.1 Sample selection as a function of σ_e and M_r. 81
4.2 The selection of slow rotators, and division of fast rotators. 83

4.3 The residuals $\Delta\,[\alpha/\mathrm{Fe}]$ as a function of $\lambda^{\mathrm{eo}}_{R_\mathrm{e}}$. 85
4.4 A comparison of structural and SSP parameters for low-$\lambda^{\mathrm{eo}}_{R_\mathrm{e}}$ galaxies. 87
4.5 The distribution of SAMI galaxies in the SFR-M_* plane. 89
4.6 Correlations between $\Delta\,[\alpha/\mathrm{Fe}]$ and $\lambda^{\mathrm{eo}}_{R_\mathrm{e}}$, separated by SFR. 91
4.7 Galaxies in the $\lambda^{\mathrm{eo}}_{R_\mathrm{e}}$-$\epsilon_\mathrm{e}$ plane, separated by morphological type. 93
4.8 Galaxies in the $\lambda^{\mathrm{eo}}_{R_\mathrm{e}}$-$\epsilon_\mathrm{e}$ plane, coloured by $\Delta\,[\alpha/\mathrm{Fe}]$. 98
4.9 The morphological distribution of quenched low-$\lambda^{\mathrm{eo}}_{R_\mathrm{e}}$ galaxies. 100

5.1 SAMI galaxies in the $R_{\mathrm{e,circ}}$-HWHM plane. 106
5.2 A comparison of $R_{\mathrm{e,circ}}$ and R_e, with linearly- and logarithmically-scaled annuli. 107
5.3 Examples of Voronoi tessellation for low- and high-S/N galaxies. . . . 109
5.4 The relative transmission of g-band filters for different instruments. . 113
5.5 A colour *gri* image against the SExtractor-derived segmentation map. 114
5.6 Convolving an image to match the resolution of the SAMI datacube, with examples of the PSF. 116
5.7 The structure in the photometric residuals of SAMI datacubes. 120
5.8 A comparison of logarithmic and linear sampling for isophotal contours. 121
5.9 The distributions of S/N and R/R_e, using linearly-sampled annuli. . . 123
5.10 As Fig. 5.9, using logarithmically-sampled annuli. 124
5.11 As Fig. 5.9, using Voronoi tessellation. 125
5.12 As Fig. 5.9, using contour binning. 126
5.13 The distribution of $R_\mathrm{last}/R_\mathrm{e}$ for each binning method. 127
5.14 The ratio of the radius R_last to HWHM and R_e against R_e and M_*. . 128
5.15 A graphical representation of the seeing-correction method. 129
5.16 The distribution of MCMC samples for seeing corrections, with the derived gradients. 132

6.1 Sample selection shown in the R_e-M_* plane. 136
6.2 The selection criteria for reliable radial gradient measurements. . . . 138
6.3 An example of a two-phase radial profile. 139
6.4 Gradients and intercepts at $R = R_\mathrm{e}$, plotted against σ_e. 144
6.5 R_e intercepts in the size-mass plane, before and after smoothing via LOESS. 148
6.6 Gradients in the size-mass plane, before and after smoothing via LOESS. 149

6.7 Locally-smoothed R_e intercepts in the size-mass plane, separated by local environment and morphological type. 152
6.8 Locally-smoothed gradients in the size-mass plane, separated by local environment and morphological type. 153
6.9 Galaxies in the size-mass plane, separated by both environment and morphological type. 155
6.10 The radial age profiles of galaxies in regions of the size-mass plane, separated by both environment and morphological type. 158
6.11 As Fig. 6.10, but for [Z/H]. 159
6.12 As Fig. 6.10, but for [α/Fe]. 160
6.13 As Fig. 6.5, but separated into slow and fast rotators. 170
6.14 The distribution of ∇[α/Fe] against M_* for LTGs, separated by environment. 176

7.1 The characteristics of an internal ring galaxy. 187

A.1 A comparison of SSP parameters, measured from the intercept of radial gradients at R_e, with measurements of the integrated flux within R_e. 190

List of Tables

3.1 The number of galaxies used for each stage of the analysis in this chapter, separated by morphological type. 56
3.2 The gradients and intercepts for best-fit relationships between [α/Fe] and σ_e, separated by environment and morphological type. 67
3.3 As Table 3.2, but the gradient is fixed by fitting to galaxies for which $\log_{10}\left(\sigma_e/\mathrm{km\,s^{-1}}\right) > 2$. 70

4.1 The number of galaxies used for each stage of the analysis in this chapter, separated by both morphological type and kinematic classification. 82
4.2 The median values of structural parameters, [α/Fe], and Δ[α/Fe] for each kinematic classification. 88

5.1 The sources for the imaging used in the contour binning method. . . 112

6.1 The sample sizes and median gradients for each SSP parameter, before and after the gradient quality cuts. 140
6.2 The best fitting linear relations, for all measurements as a function of σ_e. 143
6.3 The Spearman rank correlation coefficients (ρ), for correlations between the SSP R_e intercepts, and M_*, M_*/R_e, and $M_*/{R_e}^2$, for each morphological type and environment. 165
6.4 The sample sizes and median SSP intercepts at R_e, for a subsample of low-$\lambda^{eo}_{R_e}$ ETGs. 171
6.5 For each sample in morphology and environment: the median SSP gradients and R_e intercepts, and the slopes of the correlations with M_* and σ_e. 173

Acronyms

AGN active galactic nuclei.

ANU Australian National University.

ASTRO 3D Australian Research Council Centre of Excellence for All Sky Astrophysics in 3 Dimensions.

CAASTRO Australian Research Council Centre of Excellence for All-sky Astrophysics.

CALIFA Calar Alto Legacy Integral Field Area.

CB classical bulge.

CCD charge-coupled device.

CDM cold dark matter.

CGM circumgalactic medium.

DECam Dark Energy Camera.

EAGLE Evolution and Assembly of GaLaxies and their Environments.

ELT Extremely Large Telescope.

ETG early-type galaxy.

FJ Faber-Jackson.

FR fast rotator.

FWHM full-width at half-maximum.

GAMA Galaxy and Mass Assembly.

GMT Giant Magellan Telescope.

HDE high-density environment.

HST Hubble Space Telescope.

HWHM half-width at half-maximum.

IDS image dissector scanner.

IFU integral-field unit.

IMF initial mass function.

ISM interstellar medium.

KiDS Kilo-Degree Survey.

LDE low-density environment.

LOSVD line-of-sight velocity distribution.

LTG late-type galaxy.

MaNGA Mapping Nearby Galaxies at Apache Point Observatory.

MGE multi-Gaussian expansion.

MICADO Multi-Adaptive Optics Imaging Camera for Deep Observations.

MILES medium-resolution Isaac Newton Telescope library of empirical spectra.

MNRAS Monthly Notices of the Royal Astronomical Society.

MUSE Multi-Unit Spectroscopic Explorer.

NGC New General Catalogue.

NIR near-infrared.

NSW New South Wales.

PA position angle.

PB pseudo-bulge.

PSF point-spread function.

RSAA Research School of Astronomy and Astrophysics.

S/N signal/noise ratio.

SAMI Sydney-Australian-Astronomical-Observatory Multi-object Integral-field Spectrograph.

SAURON Spectroscopic Areal Unit for Research on Optical Nebulae.

SDSS Sloan Digital Sky Survey.

SED spectral energy distribution.

SFMS star-forming main sequence.

SFR star-formation rate.

SNe supernovae.

SPHERE Spectro-Polarimetric High-contrast Exoplanets REsearch.

SR slow rotator.

SSP simple stellar population.

TF Tully-Fisher.

TMT Thirty Meter Telescope.

UBV ultraviolet-blue-visual.

VST Very Large Telescope Survey Telescope.

WiFeS Wide-Field Spectrograph.

Chapter 1

Introduction

The evolution of the field of observational astronomy is a tale almost as interesting as the evolution of galaxies themselves, albeit occurring over a slightly shorter timescale. In this chapter, we begin with an overview of the history of astronomy, leading into spectroscopy, and galaxy surveys. We then delve into the existing literature relevant to this thesis, and finish with a description of the instruments and ancillary measurements used in later chapters.

1.1 Background

1.1.1 A Brief History of Observational Astronomy

A full description of the emergence of astronomy is all but impossible, with the archaeological record incomplete in many areas, and scant few cultures surviving into the modern era. Whilst the oldest known stone tools date to over 3.3 million years ago, made by the early hominin *Australopithecus* (Harmand et al., 2015), the first confirmed astronomical artefact is a mere 32,000 years old – a carved ivory mammoth tusk, with a drawing of the constellation of Orion (Rappenglück, 2003). Contemporaneous with this, it is highly likely that the ancestors of modern Aboriginal

Australians, who settled across the continent up to ≈ 60,000 years ago (Crabtree et al., 2021), began using observations of the night sky. Whilst there is no written record, the strong oral traditions display the importance of astronomy to the Aboriginal peoples, with Norris, 2016 presenting a thorough review. A Wiradjuri Dreaming of the emu chase can be related to the annual movement of the constellations across the night sky (Leaman et al., 2019), whilst the Meriam people of the Torres Strait studied the scintillation of stars to predict changes in temperature and weather (Hamacher, 2018). The Wadawurrung people carefully marked the positions of the solstices at the stone arrangement of Wurdi Youang, predating European Neolithic monuments such as Stonehenge by up to 8,000 years (Norris et al., 2013).

It is not until the second millennium BC that astronomy began to develop into what would now be recognised as a scientific discipline. Whilst the detailed star maps decorating ancient Egyptian tombs enabled a precise calibration of the date on which they were observed, sometimes down to the month (Von Spaeth, 2000), Babylonian astronomers were the first to apply a mathematical approach to their observations. The extant text MUL.APIN, dating to ≈ 1370 BC (Schaefer, 2007), included schemes to predict the heliacal rising of certain bright stars such as Sirius and Arcturus (Hunger et al., 2019). Thus began the predictive era of astronomy, in which astronomers attempted to describe the motions of stars and planets through increasingly complex mathematical models. Eudoxus introduced the concentric sphere model, which would be iterated upon by Callippus and Aristotle, until the development and formalisation of the epicycle respectively by Hipparchus and Ptolemy (Dreyer, 2014). This geocentric model would not be seriously challenged until the time of Nicolaus Copernicus, and a concise mathematical description of the planetary orbits remained elusive until the seminal works of Johannes Kepler and Isaac Newton (Copernicus, 1543; Kepler, 1609; Newton, 1687).

Concurrently, this era heralded one of the most significant advances in astronom-

ical instrumentation, potentially of all time – the telescope, which enabled far more precise observations of fainter objects than possible with the naked eye. Following a failed patent application from Hans Lipperhey for the design of a simple refracting telescope, Thomas Harriot used such a telescope to make the first recorded telescopic observations (Pumfrey, 2009). This design would be rapidly improved upon by Galileo Galilei, who went on to publish the first astronomical results from his observations in the treatise *Sidereus Nuncius* (Galilei, 1610). However, telescopes using a refractor design suffered strongly from physical limitations – the requisite large-diameter lenses for increased magnification were (and still remain) correspondingly expensive, and even more difficult to manufacture. In 1668, Isaac Newton constructed the first successful reflecting telescope, presenting it to the Royal Society in 1672 at the same time as Laurent Cassegrain independently developed a compact design that folded the light path back on itself (Watson, 2004). These early reflectors used speculum (an alloy of tin and copper) for the optical surfaces, which tarnished quickly, thus requiring constant re-polishing and re-figuring. This in turn fuelled competition between the advancement of refractor and reflector telescopes in observatories during the mid to late 19^{th} century, with the Yerkes Observatory's 1.02 m aperture refractor becoming the largest operational refracting telescope (Hale, 1896). Around the beginning of the 20^{th} century, the refinement of the ability to deposit a layer of metal on the surface of glass mirrors led to the development of the first modern research telescopes, such as the $60''$ telescope at Mount Wilson Observatory (Ritchey, 1909).

Whilst the majority of astronomical research up to this point focussed on the movement and appearance of objects, in 1802 William Wollaston published the first spectroscopic results, identifying seven absorption lines in the solar spectrum quite incidentally (Hearnshaw, 2014). This was followed by the seminal discovery of Joseph Fraunhofer, who in 1814 observed numerous dark solar absorption lines, inventing in the process the modern spectroscope (Fraunhofer, 1817). Some years later Christian

Doppler, building on the (incorrect) hypothesis that the colours of binary stars are due to orbital motion, correctly established that the frequency of a wave depends on the relative speed of the source to the observer, a phenomenon now termed the Doppler effect (Doppler, 1843). Other crucial advancements in the field of spectroscopy came throughout the 20$^{\text{th}}$ century, as astronomers progressed from visual estimation of the relative line brightness, through the use of dry photographic plates pioneered by Henry Draper and William Huggins, and to the charge-coupled devices (CCDs) used to the current day (see Hearnshaw, 2014 for a comprehensive review).

In the modern era, one of the more significant advancements in astronomical research is the ability to counteract the atmospheric seeing (the degradation of an image due to atmospheric turbulence). The first method to be put into practice was simply to put a telescope in low-earth orbit, outside the atmosphere, demonstrated aptly by the Hubble Space Telescope (HST) in 1990. The HST also demonstrated the importance of the old adage "measure twice, cut once", and it was not until the installation of corrective optics in 1993 that the expected benefits in image resolution were realised. Simultaneously, the development of adaptive optics (an idea first proposed by Babcock, 1953), was finally accomplished in Rousset et al., 1990 to produce real-time diffraction-limited imaging. Adaptive optics are now commonplace in current and next-generation large-aperture telescopes, and are essential to realise the full benefits of larger primary mirrors (Rousset et al., 2003; Bacon et al., 2010; Davies et al., 2010).

1.1.2 The History of Galaxy Observations

The earliest recorded observation of a galaxy outside our own comes from the Persian astronomer ʿAbd al-Rahman al-Ṣūfī in 964 AD, who noted the Andromeda Galaxy and the Large Magellanic Cloud in his seminal text *Kitāb suwar al-kawākib* (translated: *The Book of Fixed Stars*, Hafez, 2010). However, it was not until 1750 that

Thomas Wright proposed that these "nebulae", as all diffuse sources were termed at the time, may in fact be regions of stars distinct from the Milky Way, but so distant as to be unresolved (Wright, 1750). This heavily influenced the philosopher Immanuel Kant, who just five years later proposed that the Milky Way was a rotating disk held together by gravity, and similarly for the nebulae, which he termed "island universes" (Kant, 1755). Charles Messier, searching for comets using a 100-mm refracting telescope, published a catalogue of 103 diffuse objects, 34 of which are now known to be galaxies (Messier, 1781). William Herschel later drew upon this list when compiling his own catalogue of deep-sky objects, using the increased resolving power of his 47-cm telescope to discern that some of the Messier objects were star clusters, and catalogued the remaining objects based on their approximate morphology (Herschel, 1786; Herschel, 1789; Herschel, 1802). This catalogue was later supplemented by his sister, Caroline, and son, John, and compiled by John Dreyer into the *New General Catalogue* (NGC), a label still in use to this day (Dreyer, 1888). In the meantime Lord Rosse, having constructed the "Leviathan" (a 1.8-m reflecting telescope), used his telescope to reveal the spiral structure of a galaxy for the first time (Hoskin, 1982).

The next significant advancements came in the early 20$^{\text{th}}$ century, when Slipher used spectroscopy to observe the shift of spectral lines in the Andromeda Galaxy, indicating a recession velocity (Slipher, 1913). In 1917, Heber Curtis noticed that novae in Andromeda were approximately 10 magnitudes fainter than those observed in the Milky Way, supporting the claim that the "island universes" are distinct from our own galaxy (Curtis, 1917). This "Great Debate" was finally settled by Edwin Hubble with the discovery of Cepheid variables in Andromeda, and by utilising the period-luminosity relation of Shapley, 1918 he was able to prove that the stars were too distant to belong in the Milky Way. He later collated the Doppler shifts of spectral lines in a number of galaxies, including his own observations, and provided the first evidence of the expansion of the universe (Hubble, 1929). Hubble, seemingly

not content with two major contributions to the field of galaxy observations, then established a classification scheme termed the "Hubble Tuning Fork" (Hubble, 1936), which after refinement by Sandage et al., 1975 is still in use today.

1.1.3 The State of Cosmology

Following Hubble's discovery that the Milky Way was merely one amongst many varied galaxies, an entirely new avenue of astronomical research opened up – cosmology. At present, the most widely accepted cosmological theory is the Λ-CDM model. This can be broken down as containing dark energy Λ driving the expansion of the universe, now known to be accelerating (Riess et al., 1998; Perlmutter et al., 1999), and cold dark matter (CDM), which interacts only gravitationally. Baryonic "normal" matter constitutes only a small fraction in this paradigm, but is the only portion which we can currently observe directly. This relies on the assumption of the Copernican Principle, that humans are not privileged observers of the universe – in other words, there is no reason to assume that observations from Earth are any different to observations at the average position throughout the universe. If then, from Earth we observe that the universe appears to be the same in all directions (isotropic), we can infer more generally that the universe must also be the same everywhere (homogeneous). These two conditions that the universe is both homogeneous and isotropic on large scales (*i.e.* hundreds of megaparsecs) form the Cosmological Principle, a prerequisite for Λ-CDM. Throughout this thesis, we assume a geometrically flat and infinite universe, parameterised by

$$\begin{aligned} \Omega_\Lambda &= 0.7, \\ \Omega_\mathrm{m} &= 0.3, \\ H_0 &= 70\,\mathrm{km\,s^{-1}}, \end{aligned} \tag{1.1}$$

where Ω is the fraction of the energy density contributed by either dark energy Λ or matter m (the combined contribution from both baryonic and dark matter), relative

to the critical density of the universe (*i.e.* the density required for a flat universe). H_0 is the Hubble constant at the present time, indicating the current expansion rate of the universe (see Freedman, 2021 for a thorough review).

In this cosmological model, the creation of the universe happened approximately 13.8 billion years (Gyr) ago, forming out of a singularity in an event termed the "Big Bang". This was followed by a period of exponential expansion called "inflation" (Starobinskiĭ, 1979; Guth, 1981; Linde, 1982; Albrecht et al., 1982). Quantum fluctuations in the pre-inflationary era were magnified, forming large scale variations in the matter density of the universe (Mukhanov et al., 1981; Guth et al., 1982; Starobinsky, 1982; Hawking, 1982). This naturally leads to the hierarchical formation of structure, as regions with slight over-densities collapse under their own gravity, forming dark matter halos and the filamentary large-scale structure visible in the universe today (Press et al., 1974; White et al., 1978; Gott et al., 1975; Peebles, 1982; Blumenthal et al., 1984; Davis et al., 1985; see Frenk et al., 2012 for a review). These dark matter halos attract baryonic matter, which undergoes radiative cooling, condensing in the centres of the potential wells. If enough matter accretes, typically in the form of clouds of hydrogen and helium gas, then stars begin to form through gravitational collapse, creating the familiar objects we know as galaxies. Tidal torques present in the dark matter halos can also impart angular momentum to the baryonic matter, creating rotating disk galaxies in the initial stages of their lives (Fall et al., 1980; Barnes et al., 1987; Mo et al., 1998).

More recently, observations and cosmic hydrodynamical simulations have shown that this picture of solely merger-driven growth is incomplete. Whilst a model considering only dark matter can reproduce well the overall sizes, masses, and abundances of galactic halos, it cannot account for the observed internal structures of galaxies. It is now known that continual gas accretion is a necessary component of galaxy formation, without which galaxies would exhaust their gas reservoirs in $\approx 2\,\mathrm{Gyr}$ (Bigiel

et al., 2008; Leroy et al., 2008; Bigiel et al., 2011; Leroy et al., 2013; Rahman et al., 2012). This accretion can take several forms, whether by gas accumulation along dark matter filaments (Dekel et al., 2009; Kleiner et al., 2017), or through gas-rich (so-called "wet") mergers, which can contribute to gas reservoirs in the circumgalactic medium (CGM) as well as trigger bursts of star formation (Kereš et al., 2005). However, these are not the only processes regulating star formation, with feedback from stars and active galactic nuclei (AGN) also playing a role. AGN feedback can take the form of ionised winds (Veilleux et al., 2005; Westmoquette et al., 2012) and neutral gas outflows (Sturm et al., 2011; Rupke et al., 2011; Cicone et al., 2014; Fiore et al., 2017), which transport enriched material out of star-forming galaxies into the CGM (Rubin et al., 2014). AGN jets, seen directly at radio wavelengths, also work to heat the surrounding gas, preventing it from cooling and forming stars (Best et al., 2012; McNamara et al., 2012). On much smaller scales, stellar feedback (including winds, photoionisation, and radiation pressure) acts in a similar manner, heating the surrounding interstellar medium (ISM) and prolonging star formation in galaxies (Kim et al., 2018; Haid et al., 2019; Bending et al., 2020; Rathjen et al., 2021; Fichtner et al., 2022).

1.1.4 Measuring Stellar Populations

Understanding the formation history of individual galaxies requires both observations and modelling of their physical properties in multiple dimensions. Even in the current era of large spectroscopic surveys, and with the wealth of data this yields, we are intrinsically limited by only being able to observe galaxies at a single point in their evolution. One vital tool is that of stellar population analysis, which provides an insight into the timescales and assembly history of the stellar components of galaxies, although this is not an insignificant task. For the overwhelming majority of galaxy observations so far, it is not possible to resolve individual stars, limiting any analysis

to the integrated light over the observable areas.

Within any given galaxy, the contributions to the integrated spectral energy distribution (SED, the total observed light as a function of wavelength) come from many varied sources. These range from hot accretion disks around black holes to individual cool stars, with emitted photons spanning the entire electromagnetic spectrum from radio waves all the way through to gamma rays. In the majority of galaxies, the optical portion of the SED is dominated by stellar emission, with some contributions from ionised gas, and AGN on rare occasions. The light emitted from stars depends on their surface temperatures, and thus the shape of an individual stellar SED is approximately described by thermal black body emission. The consequence of this is that hotter stars show a peak in their emission towards bluer wavelengths, whilst colder stars are redder. However, this is a significant simplification. The outer atmospheres of stars can contain many heavy elements, leading to absorption lines, that can significantly affect the shape of the stellar SED. These heavy elements can be described in aggregate by the metallicity Z, the mass fraction of elements heavier than helium,

$$\mathrm{Z} \equiv \sum_{e>\mathrm{He}} \frac{m_e}{M} \tag{1.2}$$

for elements e and total mass M. Whilst this quantity is often used for modelling the evolution of individual stars, spectral features depend instead on the number density, quoted as the logarithm relative to the solar abundance $\mathrm{Z}_\odot$,

$$[\mathrm{Z/H}] \equiv \log_{10}\left(\frac{N_\mathrm{Z}}{N_\mathrm{H}}\right)_* - \log_{10}\left(\frac{N_\mathrm{Z}}{N_\mathrm{H}}\right)_\odot \tag{1.3}$$

for N_Z and N_H, the number of metallic and hydrogen atoms respectively, per unit volume.

The total metallicity is not the only useful grouping of elements in stellar population analysis. One of the more common abundance patterns to be measured is

the α-element abundance, [α/Fe]. These so-called α-elements are those whose most abundant isotope comprises an integer number of α particles, such as C, O, Mg, Ca, and Ti, leading to the definition

$$\begin{aligned}[\alpha/\mathrm{Fe}] &\equiv \langle [X/\mathrm{Fe}] \rangle \\ &\equiv \langle \log_{10}\left(\frac{N_X}{N_\mathrm{H}}\right)_* - \log_{10}\left(\frac{N_X}{N_\mathrm{H}}\right)_\odot \rangle, \\ \text{where } X &\in [\mathrm{C},\ \mathrm{O},\ \mathrm{Ne},\ \mathrm{Mg},\ \mathrm{Si},\ \mathrm{S},\ \mathrm{Ar},\ \mathrm{Ca},\ \mathrm{Ti}]\ .\end{aligned} \tag{1.4}$$

These elements are predominantly formed in massive stars ($M \geq 8\,\mathrm{M}_\odot$) during the O and Si burning processes, the two penultimate stages before the stellar core collapses, giving rise to a Type II supernova. This contrasts with Type Ia supernovae (SNe) from white-dwarf binaries, which mainly form Fe-peak elements such as Mn, and Co, with progenitor lifetimes of $\approx 1\,\mathrm{Gyr}$. Thus, [α/Fe] for a given star measures the relative contributions of Type Ia and Type II supernovae to the ISM, at the point in time when that star formed. If star formation continues over long timescales, the relative contribution from SNe Ia becomes more significant, and so [α/Fe] for any newly formed star trends towards the solar value (Greggio et al., 1983). Over a larger stellar population, many factors can affect the integrated [α/Fe], such as the delay-time distribution of SNe Ia and discrete bursts of star formation. Considering that current studies have found a consistent SNe Ia delay-time distribution across models and observations via multiple techniques (Maoz et al., 2012; Walcher et al., 2016), the general consensus is that [α/Fe] is a good indication of the integrated star-formation timescale (Peletier, 1989; Worthey et al., 1992; de La Rosa et al., 2011; Barbosa et al., 2021).

Historically, analyses of stellar populations were rather limited. Following the seminal paper of Baade, 1944, which established the existence of distinct populations, the majority of research was performed with the well-defined colour indices of

Whipple, 1935. By observing resolved stars in specific filters, such as those in the now ubiquitous ultraviolet-blue-visual (UBV) photometric system of Johnson et al., 1953, galaxies could be compared against these measurements, and hence classified according to their colour.

These early attempts at classification provided a basis for the core component of galaxy evolution analysis – stellar population synthesis. By combining various properties of resolved stars with stellar evolutionary tracks and an initial distribution of stellar mass (initial mass function, IMF), it was possible to synthesise the UBV colours of a model galaxy. Spectrophotometric models such as those of Searle et al., 1973 provided a straightforward reference for the age, star-formation rate, and mass distribution of extragalactic stellar populations (see also: Tinsley, 1968; Tinsley, 1972; Larson et al., 1978; Guiderdoni et al., 1987). However, the intrinsic lack of a unique stellar population solution severely limited the use of colour for population analysis, with a strong degeneracy between stellar age and metallicity in the model colours (Williams, 1976; Faber, 1977).

Far stronger constraints could be placed on the composition of galaxies through the use of spectroscopy. Within the restframe optical and near-infrared (NIR) region, there are a multitude of strong spectral features. Whilst emission lines can be used to derive star-formation rates and gas kinematics, absorption lines reveal a wealth of information on the stellar content. The absorption lines in the wavelength region 4000-6000 Å are largely insensitive to dust attenuation (MacArthur, 2005), and can be measured easily and calibrated to a common system, with one of the most widely used being the the Lick/image dissector scanner (IDS) system (Worthey et al., 1997).

The Lick/IDS Index System is a set of 25 absorption-line features at optical wavelengths, including five Balmer absorption-line features, defined by the Lick group over a series of papers, using observations made with the IDS on the 3-m Shane Telescope at Lick Observatory (Burstein et al., 1984; Faber et al., 1985; Gorgas et al., 1993;

Worthey et al., 1994; Worthey et al., 1997; Trager et al., 1998). By combining features that are separately sensitive to age and metallicity, the degeneracy between these two variables can be significantly reduced, a marked improvement over the use of UBV colours. This allowed the creation of simple stellar population models (SSP, sometimes *single* stellar population), which model the evolution in time of the SED from a single coeval population of stars, with a single metallicity and abundance pattern (Bruzual et al., 1993; Bressan et al., 1993; Leitherer et al., 1999; Bruzual et al., 2003).

Although non-trivial, the variation of some of these absorption-line indices with individual elemental abundances can also be calculated. Thomas et al., 2003 were among the first to produce model predictions of Lick indices with variable elemental abundances, based on synthesised stellar populations. By comparison with index measurements from galaxy spectra, these models and others like them, such as Schiavon, 2007 and Thomas et al., 2011, allow a straightforward determination of the luminosity-weighted constituent SSP parameters. In most cases, these models predict index measurements as a function of age, metallicity, and the α-element abundance.

Alongside the Lick Index System, there are many alternative methods for extracting the integrated star-formation history from spectra. One attractive concept is that of full-spectrum fitting, where models of the SED are compared against the observed galaxy spectrum, allowing a more direct determination of properties such as the IMF. Various implementations exist, such as BAGPIPES from Carnall et al., 2018, based on the models of Bruzual et al., 2003, or PYSTAFF from Vaughan et al., 2018, which utilises the models of Conroy et al., 2018, and techniques first implemented in PPXF (Cappellari, 2017), which itself is often used for stellar population analysis.

The significant advantage of full-spectrum fitting over using only indices is the ability to fit for individual elemental abundances simultaneously, without limiting the analysis to pre-selected regions of interest, although this comes with a correspondingly

steep computational cost, and very stringent requirements for the wavelength and flux calibration. The choice of techniques used to create the underlying SED models can also strongly influence the results, with models such as Conroy et al., 2018 "correcting" an empirical spectrum to some arbitrary elemental abundance via individual elemental response functions, whereas the self-consistent models of Walcher et al., 2009 and Vazdekis et al., 2015 include the additional constraint of matching the elemental abundances of the isochrones.

Some studies, among them Sánchez-Blázquez et al., 2011; Conroy et al., 2014; Carlsten et al., 2017 have directly compared the output from models relying on full-spectrum fitting and that using line indices. Whilst Conroy et al., 2014 found quantitative differences between various models, the qualitative trends were consistent. Similarly, Carlsten et al., 2017 found that although the index-derived measurements much more closely resembled the light-weighted measurements from full-spectrum fitting (when using the same models) rather than the mass-weighted measurements, the resulting scaling relations and radial gradients were in very good agreement between the methods, consistent with Sánchez-Blázquez et al., 2011. However, a common theme amongst all full-spectrum fitting methods is that it is not so straightforward to derive an estimate of the uncertainty on the stellar population parameters, which can rapidly become extremely time-consuming (Cid Fernandes et al., 2014; Barbosa et al., 2021). Thus, Lick indices still represent arguably the best compromise between the wealth of data that can be extracted from an individual spectrum, and the computational cost of doing so. This makes them ideal for larger galaxy surveys, where the cost of full-spectrum fitting becomes prohibitively expensive.

1.2 Previous Research

1.2.1 Scaling Relations

In the field of extragalactic astrophysics, the term "scaling relation" refers to an observed correlation between two or more properties of the galaxies in a sample, and can frequently span several orders of magnitude. As with any observational science, the observed correlations can be used as a benchmark for simulations, which must also attempt to explain the existence of the relation itself.

Early studies on galaxy scaling relations typically focussed on correlations with the luminosity L. Fish, 1963 introduced a log-log correlation between luminosity and the effective radius $R_{\rm e}$, the radius enclosing half of the total luminosity $L_{\rm tot}$ (de Vaucouleurs, 1948). The discovery of a link between L and the galaxy colour led to the development of the optical colour-magnitude diagram, which later revealed two distinct populations – the so-called "blue cloud" and "red sequence", separated by the "green valley" (Chester et al., 1964; Sandage, 1972; Bower et al., 1992; Bell et al., 2004; Driver et al., 2006).

Other examples include the Tully-Fisher (TF, Tully et al., 1977) and Faber-Jackson (FJ, Faber et al., 1976) relations, which both looked at linking the luminosity of a galaxy to its dynamics. Whilst the TF relation originally linked the distance-independent measurement of the neutral HI line profile width to the absolute physical diameter (or as is more commonly quoted, the absolute magnitude), it is now used to correlate the total baryonic mass to the maximum circular velocity $v_{\rm c}$ (McGaugh et al., 2000; Bell et al., 2001). Similarly, the FJ relation, originally linking the stellar velocity dispersion σ in a $2''$ slit to the absolute magnitude, was later found to be a projection of the "fundamental plane" of elliptical galaxies (Djorgovski et al., 1987; Dressler et al., 1987; Faber et al., 1987). This plane is a remarkably tight correlation between the central stellar velocity dispersion σ_0, the effective radius $R_{\rm e}$, and mean

surface brightness within the effective radius $\langle I_e \rangle$[1].

Of particular relevance to this thesis are the scaling relations of elemental abundance patterns. Early studies into the strengths of individual line indices such as Mg_2 focussed on correlations with the absolute magnitude or luminosity (Faber, 1973; Burstein, 1979; Terlevich et al., 1981), and only later were the absorption features related to the central stellar velocity dispersion σ_0 (Burstein et al., 1988; Bender et al., 1993; Colless et al., 1999). This was then followed by transforming the line strength indices into a measure of the relative elemental abundance, described by Eq. 1.4. Tantalo et al., 1998 first measured [Mg/Fe], plotting the linear regression against the absolute V-band magnitude, although their measurements suffered from systematic errors (Trager et al., 2000a). Kuntschner, 1998 instead fitted a relationship between [Mg/Fe] and σ_0, finding a clear correlation, followed swiftly by Colless et al., 1999 with a similar analysis. Trager et al., 2000b generalised this relation to encompass multiple elements, denoted by [E/Fe][2], deriving the relationship

$$[\mathrm{E/Fe}] = (0.33 \pm 0.01) \log_{10} \left(\sigma_e / \mathrm{km\,s^{-1}} \right) - (0.058 \pm 0.01) \ . \tag{1.5}$$

This empirical relation is an ideal test for cosmological simulations and semi-analytic models of galaxy formation. Using the Evolution and Assembly of GaLaxies and their Environments (EAGLE) project, Segers et al., 2016 have shown that the correlation can be reproduced for simulated galaxies with stellar masses of $\log_{10}(M_*/\mathrm{M}_\odot) > 10.5$. They attribute this to quenching from AGN feedback, which suppresses star formation in more massive galaxies at earlier times, and show that the observations are inconsistent with simulations in the absence of this feedback. Calura et al., 2011 posit that "fly-by" harrassments may be a significant factor in causing brief bursts of

[1]The exact parameterisation can vary depending on the study and observational context. However, since the absolute luminosity L, effective radius R_e, and mean surface brightness $\langle I_e \rangle$ are not all independent, these formulations are all equivalent.

[2]This differs from our formalisation of [α/Fe] by the inclusion of Na, and the absence of Ar, Ca, and Ti.

star formation.

1.2.2 The Influence of the Environment

Whilst the [α/Fe]-σ_e relation has been the focus of many previous studies, the high signal/noise ratio (S/N) required to make an accurate measurement of [α/Fe] (Gallazzi et al., 2005) means that this is still under-researched relative to SSP-equivalent ages and metallicities. In particular, there remains considerable uncertainty over the behaviour of galaxies at low masses, and in different environments. Having a clear understanding of star-formation timescales as a function of these variables can highlight the relative importance of different quenching mechanisms (the processes by which star formation in a galaxy ceases). For example, in high-density environments, ram-pressure stripping (Gunn et al., 1972; Abadi et al., 1999) and strangulation (Larson et al., 1980; Peng et al., 2015) can remove the gas from galaxies, preventing any further star formation. In addition, weaker processes such as harassment (Moore et al., 1998), gravitational interactions (Moore et al., 1999), and tidal forces (Dekel et al., 2003) may play a role, some of which are also suggested as contributing to the low fraction of spirals in such dense environments (Dressler, 1980).

Looking at morphologically selected early-type galaxies (ETGs, see Section 1.3.3.3), Thomas et al., 2010 found scaling relations with [α/Fe] were not sensitive to the environmental densities, although $\approx 10\%$ of galaxies displayed signs of ongoing star formation, and were correspondingly less α-enhanced by approximately 0.1 dex. Annibali et al., 2011 instead found that dwarf galaxies, selected by $1.6 < \log_{10}\left(\sigma_e/\mathrm{km\,s^{-1}}\right) < 2$, in high-density environments (HDEs) were enhanced in [α/Fe] by 0.22 dex compared to galaxies in low-density environments (LDEs). La Barbera et al., 2014 looked at the variation of SSP parameters in both central and satellite ETGs in high- and low-density environments. They found no environmental dependence for [α/Fe] in satellite galaxies, but a consistent α-enhancement of ≈ 0.025 dex for central galaxies

in LDEs over their counterparts in HDEs.

Scott et al., 2017, looking at a volume-limited sample separated by local environmental density, found an increase $\Delta\,[\alpha/\mathrm{Fe}] = 0.14 \pm 0.02$ from LDEs to HDEs, in galaxies with stellar masses $M_* > 10^{10.5}\,\mathrm{M}_\odot$. Scott et al., 2017 also investigated correlations with morphology, and found ETGs were α-enhanced by 0.07 ± 0.03 dex over spirals with the same stellar mass. They also found that this dependence was primarily driven by galaxy size, which was anti-correlated with environmental density. McDermid et al., 2015 fitted their own sample, consisting of ETGs, to a common $[\alpha/\mathrm{Fe}]$-σ relationship. Separating these galaxies into Virgo cluster members and non-members, they were able to show that the residuals for each sample were unlikely to be drawn from the same parent distribution.

Whilst some previous studies have investigated the $[\alpha/\mathrm{Fe}]$-σ_e correlation in low-mass galaxies, finding a similar behaviour as in high-mass galaxies (Smith et al., 2009; Liu et al., 2016; Sybilska et al., 2017), this remains an under-explored area, particularly across environments and morphological types. The primary limitation of many of these studies has been the small sample size, especially when comparing galaxies with low velocity dispersions.

1.2.3 Kinematics

Whilst we have already established the utility of measuring galaxy kinematics, in order to derive scaling relations, this is far from the only use for these measurements. The build-up of mass and angular momentum is vital to our understanding of galaxy assembly, and can be determined from dynamical studies of the stellar component (de Zeeuw et al., 1991; Bender et al., 1994; Cappellari, 2016). Although this particular field has a long and detailed history, dating back to the first discovery of "nebular rotation" (Slipher, 1913), the introduction of integral-field units (IFUs; see Section 1.3.1) such as the Spectroscopic Areal Unit for Research on Optical Nebulae

(SAURON; Bacon et al., 2001) marked a major advancement. For the first time, it was possible to measure the kinematics of a galaxy in two dimensions, enabling new techniques for the measurement and classification of galaxy dynamics.

One of these classifications sought to separate galaxies based on a proxy for the spin parameter, denoted by λ_{R_e} and defined as

$$\begin{aligned} \lambda_{R_\mathrm{e}} &\equiv \frac{\langle R|V|\rangle}{\langle R\sqrt{V^2+\sigma^2}\rangle} \\ &\equiv \frac{\sum_{i=0}^{N_\mathrm{spaxels}} F_i R_i |V_i|}{\sum_{i=0}^{N_\mathrm{spaxels}} F_i R_i \sqrt{V_i^2+\sigma_i^2}}\,, \end{aligned} \tag{1.6}$$

where for a given spatial pixel (spaxel) i, R_i is the radius, V_i the mean line-of-sight stellar velocity, σ_i the stellar velocity dispersion, and F_i the flux. We sum over the N_spaxels within the effective radius R_e, which can be either the circular radius $R_\mathrm{e,circ}$, or the ellipse with semimajor axis R_e covering the same area. This spin proxy enabled a quantitative classification of galaxies based on their kinematics. Using the SAURON survey, galaxies were separated into fast rotators (λ_{R_e}>0.1), with ordered rotation and disks, and slow rotators (λ_{R_e}<0.1), with more complex velocity fields (de Zeeuw et al., 2002; Emsellem et al., 2004). This selection criterion was later refined, first by ATLAS$^{3\mathrm{D}}$ (Cappellari et al., 2011; Krajnović et al., 2011; Emsellem et al., 2011), and later by Cappellari, 2016. Despite small modifications by individual IFU surveys (van de Sande et al., 2021a), the presence of a distinct bimodality in the kinematic distribution of galaxies has remained (Graham et al., 2018), suggesting multiple formation scenarios.

There are many studies whose motivation has been to investigate the build-up of mass and angular momentum, in order to better understand the origin of present-day morphologies (Naab et al., 2014, contains a thorough review). There are, however, fewer studies linking galaxy kinematics and elemental abundance ratios. Historically, Eggen et al., 1962 investigated the motion of stars within the Milky Way, finding an

anti-correlation between the ellipticity of an orbit and the inferred stellar metallicity. They utilised this result in a model galaxy to estimate the formation timescale, providing one of the first links between stellar dynamics and stellar properties. Franx et al., 1990 made the assumption that colour differences within and between galaxies were due only to changes in the stellar metallicity, and found a correlation between this inferred metallicity, and the local escape velocity. This was confirmed by Davies et al., 1993, using a spectroscopic measurement of metallicity, alongside the observation that the line indices Mg_2 and $\langle Fe \rangle$ coupled differently to the galaxy kinematics. This eventually led to Trager et al., 2000b formalising the relationship between $[\alpha/Fe]$ and σ_e, as discussed in Section 1.2.1. More recently, studies such as McDermid et al., 2015 have focussed on the internal kinematics of early-type galaxies, and have shown that non-regularly rotating galaxies are offset to lower metallicities compared to the global mass-metallicity relation.

Here, we focus again on the $[\alpha/Fe]$-σ_e scaling relation, with a few examples. In McDermid et al., 2015, the authors also looked at offsets from a global $[\alpha/Fe]$-σ relation, using the regular/non-regular rotator classification from Krajnović et al., 2011. Using a sample of 260 ETGs, they found no measurable difference between the two kinematic classes. Bernardi et al., 2019, after stacking spectra from elliptical galaxies in the Sloan Digital Sky Survey (SDSS) IV Mapping Nearby Galaxies at Apache Point Observatory (MaNGA) survey (Bundy et al., 2015), instead found slow rotators were α-enhanced by 0.04 dex. However, they also used different selection criteria to Cappellari, 2016, in order to prevent contamination of their fast rotator sample, which may have the unintended effect of obscuring or altering any underlying trends. Krajnović et al., 2020 briefly touched on the $[\alpha/Fe]$-σ relation, but showed no obvious difference in the residuals $\Delta\,[\alpha/Fe]$ between fast and slow rotators. There are relatively few studies which directly link elemental abundance patterns to kinematic classifications.

1.2.4 Radial Gradients

The study of radial population gradients is an incredibly useful tool for understanding the formation of galaxies, constraining accretion, mergers (Di Matteo et al., 2009; Hopkins et al., 2009), and radial migration (Roediger et al., 2012; Zheng et al., 2015). Since the seminal paper of Aller, 1942, there has been continual interest in measuring the spatially-varying composition of galaxies other than our own, limited only by the quality of the instruments of the time. For several decades, research in this area focussed on the differences between the emission of galactic nuclei and spiral arms (Seyfert, 1943; Burbidge et al., 1965; Peimbert, 1968; Weedman, 1969). In the 1970s, interest was piqued by Searle, 1971, whose measurements of the differences between HII regions along spiral arms led to a new era of studying colour and metallicity gradients in extragalactic sources (Searle, 1971; Shields, 1974; Strom et al., 1976; see also Pagel et al., 1981 for a review).

Whilst these early studies typically focussed on emission line diagnostics, or colour indices, large scale surveys of the stellar metallicity gradients have become commonplace using IFUs such as Calar Alto Legacy Integral Field Area (CALIFA; Sánchez et al., 2012), MaNGA (Bundy et al., 2015), and Sydney-Australian-Astronomical-Observatory Multi-object Integral-field Spectrograph (SAMI; Croom et al., 2012). Typically, stellar metallicity gradients are negative (Spolaor et al., 2010; La Barbera et al., 2012; Sánchez-Blázquez et al., 2014; Li et al., 2018; Ferreras et al., 2019), and show a clear dependence on mass, with a stronger correlation seen for late-type galaxies than early types (González Delgado et al., 2015; Goddard et al., 2017b). These studies also reveal that stellar age gradients are typically shallow, with some ambiguity over the sign, and show no clear correlation with environment (Tortora et al., 2011; Goddard et al., 2017a; Ferreras et al., 2019; Santucci et al., 2020). As always, the higher S/N requirements for an accurate determination of elemental abundances limit the number of studies which investigate this. Looking specifically at the relative

α-element abundance, whilst Bernardi et al., 2019, Ferreras et al., 2019, and Santucci et al., 2020 all find weakly positive [α/Fe] gradients, correlated with stellar mass, they each only cover a limited range of morphological types.

As an alternative to investigating correlations with only stellar mass, some studies also account for the varying sizes of galaxies. Following on from the fundamental plane of galaxies discussed in Section 1.2.1, one possibility is to replace the luminosity L with stellar mass M_*, or even the total mass from dynamical modelling (Cappellari et al., 2006; Bolton et al., 2007; Hyde et al., 2009). By plotting galaxies in a face-on view of the plane, or the projection in the mass-size plane, it is possible to account for the scatter visible in mass correlations. Previous studies have found that the variation of metallicity [Z/H] seems to follow closely the variation of velocity dispersion σ across the plane (making some assumptions about virialised populations, see Appendix B), which can also be seen as a proxy for the depth of the gravitational potential (Vaughan et al., 2022). However, there remains some disagreement over whether ages are more tightly correlated to σ_e or the stellar mass surface density $M_*/{R_e}^2$ (Cappellari et al., 2013; McDermid et al., 2015; Scott et al., 2017; Beverage et al., 2021; Barone et al., 2022). Whilst there have been a small number of studies that map the variation in elemental abundances across the size-mass plane (McDermid et al., 2015; Scott et al., 2017; Beverage et al., 2021), there are scant few that consider the variation in stellar population gradients across the plane (Li et al., 2018). We therefore investigate this variation ourselves, using a large sample of galaxies drawn from the SAMI Galaxy Survey.

1.3 The SAMI Galaxy Survey

The intrument and survey design for the SAMI Galaxy Survey are detailed extensively in both Croom et al., 2012 and Bryant et al., 2015, and we refer interested readers to

those papers for a full description. The SAMI survey also comprises a vast amount of reduced data products and ancillary measurements, available as part of three public data releases (Allen et al., 2015; Green et al., 2018; Scott et al., 2018; Croom et al., 2021). Here, we provide a higher-level overview of the survey, instrument, and data products utilised throughout this thesis.

1.3.1 The Instrument and Survey Design

One of the major modern advancements in astronomical spectroscopy was the development of integral-field spectroscopy (and consequently, the IFU). Spectroscopy was traditionally limited to observations using a single fibre, slit, or aperture – heavily limiting the retrieval of any associated spatial information to a single axis at most. The development of the IFU, at the time referred to as an "image dissector", allowed the observation of spectra at multiple adjacent points simultaneously, resulting in a three-dimensional "datacube". For all IFUs, the datacube has two spatial axes and one spectral, and can therefore be thought of as an image with a spectrum at every pixel (or equivalently, an image taken with a large number of narrow-band filters).

There are a number of different methods through which one can perform integral field spectroscopy. Some examples include a lenslet IFU, in which the light from an object is projected onto an array of small lenses, which in turn direct the light towards some dispersive element, feeding a spectrograph. Whilst these designs are simple, with a high throughput and spatial filling, the array design unavoidably leads to a compromise between cross-contamination of the individual spectra, and wavelength coverage. Examples include SAURON (Bacon et al., 2001) and Spectro-Polarimetric High-contrast Exoplanets REsearch (SPHERE; Beuzit et al., 2019). A second design is the image-slicer IFU. Here, the light is separated by a series of angled mirrors, each covering some small segment of the input image, such that the observation is effectively using multiple parallel slits simultaneously. As before, this design delivers

a high throughput and spatial filling, but is substantially more complicated (and therefore expensive) to manufacture. Some current examples include the Wide-Field Spectrograph (WiFeS; Dopita et al., 2007) and Multi-Unit Spectroscopic Explorer (MUSE; Bacon et al., 2010).

The third design, and also the first to be realised, is the fibre-fed spectrograph. A closely packed array of fibres in the focal plane samples the light from the object, and can be rearranged to produce a rectangular output similar to a traditional long slit. Whilst this suffers from reduced throughput, and restricted spatial filling, it also offers a more efficient use of detector space than lenslet arrays, and much greater flexibility in the location of the spectrograph than either alternative design. The first prototype IFU pioneered this design in 1980 (Vanderriest, 1980), and it is also heavily used by larger galaxy surveys today – the design inherently allows for multi-object spectroscopy, in which multiple objects are observed concurrently using different IFUs.

The SAMI Galaxy Survey is one such example, designed around the concept of multi-object integral-field spectroscopy. A crucial development was the invention of "hexabundles" (Bland-Hawthorn et al., 2011), a lightly-fused bundle of 61 circularly-packed optical fibres. Each fibre has a diameter of 105 μm or $1\farcs6$, giving an on-sky field-of-view of $15''$ for the full hexabundle, with a spatial filling factor of $> 75\%$ (Bryant et al., 2014). The SAMI instrument uses 13 of these hexabundles as IFUs, which are plugged by hand into a plate subtending a 1-degree diameter field-of-view, mounted at the prime focus of the Anglo-Australian Telescope (AAT) in New South Wales (NSW), Australia.

The fibres from the hexabundles, along with 26 additional blank sky fibres allocated for calibration purposes, are fed into the AAOmega spectrograph, a flexible dual-arm spectrograph at the AAT (Saunders et al., 2004; Smith et al., 2004; Sharp et al., 2006). This is composed of a blue arm, with spectral resolution $R = 1808$ over the wavelength range 3750-5750 Å, and a higher resolution red arm, with wave-

length coverage 6300-7400 Å and $R = 4304$ (van de Sande et al., 2017b; Scott et al., 2018). This is equivalent to a velocity dispersion $\sigma_{\rm inst} = 70.4\,{\rm km\,s^{-1}}$ for the blue, and $\sigma_{\rm inst} = 29.6\,{\rm km\,s^{-1}}$ for the red arm.

Observations for the SAMI survey took place over 250 nights from March 2013 to May 2018. Each field, containing 12 galaxy targets and one calibration star, was observed for seven 1800 s exposures, dithered in a hexagonal pattern. This dithering pattern ensured that the target was uniformly covered by the fibres, and allowed for the construction of datacubes with a $0\farcs5$ spaxel size (see Sharp et al., 2015 for details of this process). The typical full-width at half-maximum (FWHM) of the spatial point-spread function (PSF) is $\approx 2''$.

The input catalogues for SAMI were drawn from the Galaxy and Mass Assembly (GAMA) survey (Driver et al., 2011; Bryant et al., 2015), and eight cluster regions described in Owers et al., 2017. The GAMA sample is volume limited in each of four stellar mass cuts. The completed survey consists of 3426 observations of 3068 unique galaxies, available as part of the SAMI public data releases (Allen et al., 2015; Green et al., 2018; Scott et al., 2018; Croom et al., 2021). These galaxies span a redshift range $0.004 < z < 0.115$, and a stellar mass range $\log_{10}(M_*/{\rm M}_\odot) \approx 7$ to $\log_{10}(M_*/{\rm M}_\odot) \approx 12$.

1.3.2 Ancillary Data

1.3.3 Photometry and Stellar Masses

Photometric properties were taken from the third public data release for SAMI (DR3; Croom et al., 2021), and are based on the method outlined in Owers et al., 2017. The source images used are taken from the tenth data release of the SDSS (SDSS DR10; York et al., 2000; Ahn et al., 2014) and the Very Large Telescope Survey Telescope (VST) ATLAS surveys (Shanks et al., 2013; Shanks et al., 2015). The r-band images

were used for detection, and convolved to a common PSF, with a FWHM of 2″. Absolute magnitudes were calculated by K-correcting the apparent magnitudes to $z = 0$ using the code of Chilingarian et al., 2012.

Stellar masses (taken from DR3, and described in Bryant et al., 2015), were derived from the rest-frame i-band absolute magnitudes and $g-i$ colours by using the colour-mass relation following the method of Taylor et al., 2011. A Chabrier, 2003 IMF and exponentially declining star-formation history was assumed.

1.3.3.1 MGE Fits

Measurements of the ellipticity within $1\,R_{\rm e}$, $\epsilon_{\rm e}$, and the effective radius $R_{\rm e}$ were taken from DR3, with a detailed description of the method available in D'Eugenio et al., 2021. Using the r-band source imaging, the PSF was characterised by the multi-Gaussian expansion method (MGE; Emsellem et al., 1994; Cappellari, 2002). The adopted PSF is the best-fitting MGE of the star that is the best compromise between magnitude, distance to the galaxy, and goodness-of-fit. The circularised half-light radius $R_{\rm e,circ}$ was calculated from the best non-regularised MGE model, and the projected ellipticity $\epsilon_{\rm e}$ is the ellipticity of the isophote with area $\pi {R_{\rm e}}^2$.

1.3.3.2 Environmental Metrics

Throughout this thesis, we adopt fifth-nearest-neighbour number surface density estimates as a measure of the local environment. These were released as part of SAMI DR3, following the method outlined in Brough et al., 2013 and Brough et al., 2017. Using the redshift information from the GAMA survey (Driver et al., 2011; Liske et al., 2015) and the SAMI Cluster Redshift Survey (Owers et al., 2017), a volume-limited population was defined, consisting of galaxies with an absolute r-band magnitude of $M_r < 18.6$, or $M_r < 19$ for secondary targets with redshift $z > 0.1$. For each galaxy,

the number surface density was determined using

$$\Sigma_5 \equiv \frac{5}{\pi d_{\rm n}^2}\,, \tag{1.7}$$

where $d_{\rm n}$ is the projected comoving distance to the fifth nearest galaxy within the density-defining population, measured in Mpc. Galaxies are only considered as neighbours if they are within a velocity $v_{\rm lim} = \pm 1000\,{\rm km\,s^{-1}}$ of the original. The Σ_5 values are corrected to account for the effect of spectroscopic incompleteness (see Croom et al., 2021 for more details).

There are alternative measures of the local environmental density, including (but not limited to) different parameterisations of the number surface density, local mass surface density, and group halo mass. Different nearest-neighbour estimates, Σ_N, probe different length scales, and are a good measure of the underlying density field (Muldrew et al., 2012). Whilst a higher number of neighbours N more accurately recovers the large-scale structure, the resulting number surface density smooths over small-scale variations, and conversely for small N (Darvish et al., 2015). The local stellar mass surface density, as proposed by Wolf et al., 2009, better represents the strength of interactions that galaxies experience. A useful proxy to this is the stellar luminosity surface density, which is less sensitive to the magnitude limits of the samples, provided that it reaches significantly fainter than the "knee" of the galaxy luminosity function (Tempel et al., 2012). However, for our research we note that Σ_5 is the only available number surface density measured in a consistent manner across both the GAMA and cluster regions, and so we limit our investigations to this measure.

We show in Fig. 1.1 the distributions of the local number surface density and the galaxy group halo mass, $M_{\rm Halo}$. Halo masses were taken from Robotham et al., 2011 for the GAMA galaxies, and from Owers et al., 2017 for the cluster galaxies. We draw

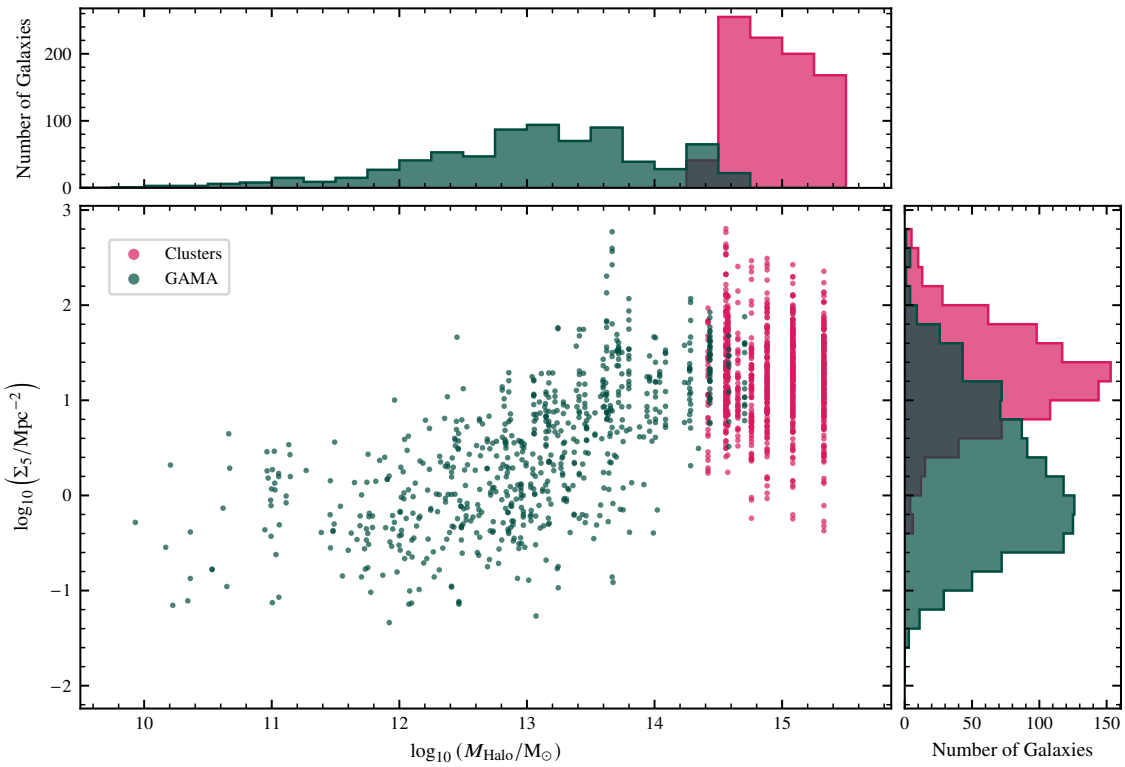


Figure 1.1: The distribution of fifth-nearest-neighbour number surface densities against group halo masses, separated into galaxies drawn from the GAMA and SAMI Cluster catalogues. We show the projected distributions on each side, drawing attention to the significant overlap in $\log_{10}\left(\Sigma_5/\mathrm{Mpc}^{-2}\right)$.

attention to the significant overlap in local number surface densities between cluster and GAMA ("field") galaxies. Approximately 10% of GAMA galaxies are found to have higher Σ_5 than the median cluster galaxy. In addition, whilst galaxies may have been observed as part of the cluster fields, this is not a guarantee that they have spent any significant time in the cluster. The uncertainties over the peculiar velocity limits lead to slightly different target selections (Owers et al., 2017). Finally, as highlighted in both Owers et al., 2017 and Croom et al., 2021, the halo mass estimates derived for each sample differ both in their methodologies and assumed cosmologies, complicating any comparisons involving the full sample. For these reasons, we use Σ_5 as our preferred measure of the local environment throughout this thesis.

1.3.3.3 Classifications of Morphological Type

Although the "Tuning Fork" classification diagram of Hubble, 1926 provides a useful tool (see also Hubble, 1936), the nomenclature can be frequently misinterpreted. Elliptical and lenticular galaxies are commonly referred to as ETGs, and spirals and irregulars as late-type galaxies (LTGs). The suggestion from some sources that this represents an evolutionary sequence (even a historical theory since disproven), is unfounded, with Hubble himself advising against drawing any temporal connotations (Hubble, 1927).

In this thesis, we rely on optical morphological classifications from SAMI DR3, following the method of Cortese et al., 2016, where galaxies were designated as one of four types (elliptical, S0, early- and late-type spiral). This was based on visual inspection of colour images by 10 SAMI team members, taken from either SDSS Data Release 9 (Ahn et al., 2012) or VST ATLAS surveys (Shanks et al., 2013; Shanks et al., 2015). Galaxies were assigned an integer between 0 (for ellipticals) and 3 (for late-type spirals and irregulars), with half-integers reserved for galaxies where the classification was split between two morphological types. For 148 galaxies, $\approx 5\%$ of the SAMI survey, the classification was deemed to be too uncertain, so we do not include these galaxies when separating by visual morphology. This integer classification scheme is referred to as MTYPE throughout this thesis, when specifying the exact morphological type.

1.3.3.4 Star-formation Rate

We obtain measurements of the integrated star-formation rate (SFR) within an elliptical R_e aperture, released as part of SAMI DR3, with the full derivation found in Medling et al., 2018. These measurements are based on the extinction-corrected Hα flux for all spaxels dominated by star formation. Through the use of the relation from Kennicutt et al., 1994, corrected to the stellar mass function of Chabrier, 2003,

the SFR can be derived through

$$\mathrm{SFR}\ [\mathrm{M}_\odot\,\mathrm{yr}^{-1}] = 5.16 \times 10^{-42}\, F_{\mathrm{H}\alpha}\ [\mathrm{erg\,s}^{-1}]\ . \tag{1.8}$$

1.3.3.5 Kinematic Measurements

Measurements of the stellar line-of-sight velocity distributions (LOSVDs) are taken from SAMI DR3, following the method laid out in van de Sande et al., 2017b. These measurements are made using PPXF (Cappellari et al., 2004; Cappellari, 2017), which calculates the best-fit template from a provided library (in this case, the medium-resolution Isaac Newton Telescope library of empirical spectra (MILES) of Falcón-Barroso et al., 2011), and derives the corresponding Gaussian LOSVD. The procedure involves a three-stage fit, first to calculate an accurate estimate of the noise, second to mask out bad pixels and emission lines, and third to derive the LOSVD and optimal template. For spatially-resolved kinematic maps, each spaxel is fitted to a restricted set of templates, which is derived from fitting up to five elliptical annuli. Additional quality cuts are applied to these spaxels, detailed in van de Sande et al., 2017b.

Measurements of λ_{R_e} are made using Eq. 1.6, with the radius R_i given by the semi-major axis of the ellipse on which each spaxel i lies. A filling factor of 95% of good spaxels is required for these measurements, within an elliptical aperture of semi-major axis R_e and axial ratio b/a, for semi-major and semi-minor axes a and b respectively. When the largest available radius is smaller than the effective radius, an aperture correction is applied, following the method detailed in van de Sande et al., 2017a. The measurements we use have also been corrected for seeing, with the procedure described in Harborne et al., 2020.

We also make considerable use of $\lambda_{R_\mathrm{e}}^{\mathrm{edge-on}}$, the λ_{R_e} measurements corrected to an edge-on projection, and hereinafter referred to as $\lambda_{R_\mathrm{e}}^{\mathrm{eo}}$. These values were kindly provided by Dr. Jesse van de Sande (private communication), and were obtained

following the method described in van de Sande et al., 2018 and van de Sande et al., 2021b. They are derived from the observed λ_{R_e} and ϵ_e measurements, assuming theoretical model predictions for galaxies as rotating, oblate spheroids with varying intrinsic shape and anisotropy. No correction is applied (*i.e.* $\lambda^{eo}_{R_e} = \lambda_{R_e}$) for galaxies that are not consistent with being simple rotating spheroids.

1.4 Thesis Outline

As highlighted throughout Section 1.2, there are several areas in which we believe there to be a gap in current astrophysical research. In this thesis, we begin by introducing the line-index method used to derive stellar populations in Chapter 2, including the index corrections applied to high-σ_e galaxies, and the effects of sky line contamination on the Mg indices. In Chapters 3 and 4, we apply this method to the integrated R_e aperture spectra from the SAMI Galaxy Survey, and investigate residual variations in the [α/Fe]-σ_e relation. Chapter 3 focusses on the behaviour of this relation across environments, and for a range of morphological types. Chapter 4 instead looks at the dependence on galaxy dynamics, using the parameterisation $\lambda^{eo}_{R_e}$, and how the residual α-element abundance varies across the slow-fast rotator boundary.

In Chapter 5, we discuss a novel application of the contour binning method, and demonstrate how this can be generalised for use on IFU datacubes, with or without corresponding photometry. We compare the contour method to other existing binning procedures, and evaluate their suitability for retrieving radial gradients in seeing or S/N-limited observations. In Chapter 6, we apply the contour binning method to SAMI IFU data to retrieve radial stellar population gradients for up to 1453 galaxies. We show the distribution of these gradients and radial profiles in the size-mass plane, and show the influence of both morphological type and environment simultaneously.

In Chapter 7 we summarise our findings, and propose ideas for future study.

Chapter 2

Measuring Stellar Populations

In this chapter, we discuss the methods used to extract the stellar populations in integral-field unit (IFU) observations of galaxies, focussing on the effective aperture spectra from the Sydney-Australian-Astronomical-Observatory Multi-object Integral-field Spectrograph (SAMI) Galaxy Survey. To summarise the procedure, we clean the spectra of any emission lines, including weak infill of absorption line features. The spectra are then broadened to the appropriate resolution for the Lick index system, and the line strengths of up to 20 absorption line features are measured. These "line indices" are then compared against model predictions of single-burst stellar population (SSP) equivalent age, metallicity [Z/H], and α-element abundance [α/Fe]. These steps are described in further detail below.

2.1 Spectral Fitting

The initial step is to remove the flux contribution from emission lines, which is performed separately for each spectrum. The method we use is based on Scott et al., 2017 (hereinafter S17), which compares spectra to a library of stellar templates unaffected by emission, replacing affected spectral pixels by the values in the best-fitting linear combination of template spectra. Particularly for weak emission, low continuum sig-

nal/noise ratio (S/N), or in the wings of emission lines, this procedure was found to provide more robust measurements of the absorption line strengths than subtracting separate emission line fits (S17; Sansom et al., 2015). A secondary consideration in favour of this method is that it is often necessary to perform a template fit regardless, in order to derive the line-of-sight velocity distribution (LOSVD) of spectra for which this is not already available (*e.g.* any galaxy binning scheme not included in the SAMI public data releases).

2.1.1 Combining the Blue and Red Arms

The design of the SAMI instrument, discussed in Section 1.3.1, results in two separate datacubes, one for each arm of the spectrograph. The full-width at half-maximum (FWHM) of the spectral instrumental line-spread function differs for each arm, with the blue arm covering the wavelength range 3750-5750 Å at a resolution of $\mathrm{FWHM_{blue}} = 2.65$ Å, and the red arm covering 6300-7400 Å at $\mathrm{FWHM_{red}} = 1.61$ Å (van de Sande et al., 2017b). For our analysis, whilst the red arm of the cube is helpful to constrain the template fits, there are minimal benefits from the increased spectral resolution. We therefore convolve the red spectra to match the instrumental resolution of the blue, using a Gaussian kernel with a FWHM given by

$$\mathrm{FWHM_{kernel}} = \sqrt{\mathrm{FWHM_{blue}^2} - \mathrm{FWHM_{blue}^2}}. \tag{2.1}$$

These convolved spectra are then interpolated onto a grid with the same wavelength scale as the blue arm, and combined with the blue spectra to form a single cube with a gap in between the two components, with an example shown in Fig. 2.1. The resulting combined spectra are shifted to rest-frame wavelengths λ_{rest} using

$$\lambda_{\mathrm{rest}} = \frac{\lambda_{\mathrm{obs}}}{1 + z_{\mathrm{spec}}}, \tag{2.2}$$

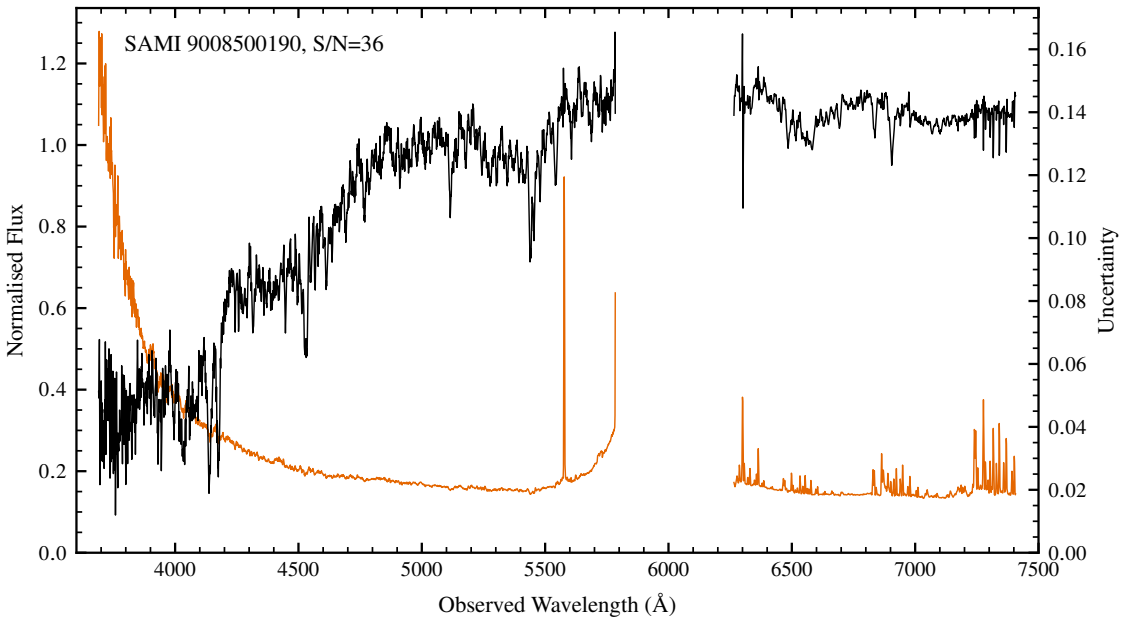


Figure 2.1: In black, the spectrum of SAMI galaxy 9008500190, summed within an elliptical R_e aperture. The blue and red arms of the spectrograph are clearly distinct, and the red spectrum has been matched to the resolution of the blue. We also show the associated uncertainties in orange, with the scale given on the right.

for observed wavelengths λ_{obs} and a spectroscopic redshift z_{spec}, taken from existing single-fibre surveys (Driver et al., 2011; Owers et al., 2017).

2.1.2 pPXF

The overall method we use for template fitting relies heavily on the penalized pixel-fitting code (PPXF; Cappellari et al., 2004; Cappellari, 2017). In brief, this method views the galaxy spectrum as a linear combination of template spectra, each convolved with a Gauss-Hermite parameterisation of the LOSVD. The best-fitting parameters and template weights are then retrieved through χ^2 minimisation by calculating the residuals between the model and observed spectra, which is a non-linear least-squares optimisation problem for the M Gauss-Hermite parameters (v, σ, h_3, ..., h_M). Additive Legendre polynomials and multiplicative polynomials can also be included in the model spectrum to account for low-frequency differences between the shape of the

galaxy and template spectra. The improvement of PPXF over earlier methods stems from the inclusion of an adjustable penalty term in the χ^2 objective function. This biases the solution towards a Gaussian shape when the higher moments cannot be adequately constrained by the available data.

2.1.3 Template Spectra

For the templates, we use the empirical stellar spectra from the medium-resolution Isaac Newton Telescope library of empirical spectra (MILES; Sánchez-Blázquez et al., 2006; Falcón-Barroso et al., 2011), which are uncontaminated by emission lines. This library consists of 985 stars, which span a large range in atmospheric parameters. These spectra are well-calibrated, with a constant spectral resolution of FWHM ≈ 2.5 Å, and cover the wavelength range 3525-7500 Å. The template spectra are convolved from their original resolution to match the de-redshifted galaxy spectra, using a Gaussian kernel with dispersion $\sigma_{\rm diff}$ characterised by

$$\sigma^2_{\rm diff} = \left(\frac{\sigma_{\rm inst}}{1+z_{\rm spec}}\right)^2 - \sigma^2_{\rm temp}, \tag{2.3}$$

where $\sigma_{\rm inst}$ and $\sigma_{\rm temp}$ are the measured spectral resolutions of the instruments used to observe the galaxy and template spectra respectively.

2.1.4 Iterative Fitting

To derive a robust estimate of the line-of-sight velocity distribution, and reliably remove faint emission from a galaxy spectrum, we perform three sequential fits with PPXF. We assume a Gaussian LOSVD, and hence only measure the stellar velocity v, and stellar velocity dispersion σ. In all cases, we include an additive $12^{\rm th}$ order Legendre polynomial to account for small errors in the flux calibration, and template mismatch effects. A detailed discussion on the impact of the additive polynomial

order on kinematic fitting in the SAMI survey can be found in Appendix A.4 of van de Sande et al., 2017b.

2.1.4.1 Initial Fit

For galaxies with a significant variation in S/N along the spectrum, as in SAMI (see Fig. 2.1), an accurate estimate of the noise is essential for PPXF to accurately measure the LOSVD. Whilst the original noise spectrum (taken as the square root of the variance spectrum) provides an accurate measure of the pixel-to-pixel variation along the wavelength axis, it is not necessarily scaled correctly for binned spectra. For the initial fit, we generate a uniform noise spectrum, such that PPXF weights all pixels equally. We do not mask out any wavelength ranges beyond those without any data, such as the gap between the two arms of the spectrograph. An example of this fit is shown in Fig. 2.2a.

If the residuals from the initial fit (δ_i) are randomly distributed as a Gaussian, and the noise spectrum (σ_i) is correctly scaled, then δ_i/σ_i should be distributed as a standard Gaussian, with a mean of zero, and unit standard deviation (denoted SD(δ_i/σ_i) to avoid ambiguity). We show the distribution of the standard deviation of this quantity for all R_e aperture spectra in the SAMI survey in Fig. 2.3. Whilst the majority of galaxies show a good agreement between the residuals and the original noise spectrum, there is a considerable tail to higher values, with a median ratio of 1.27. This implies the original noise spectrum is an underestimate of the true variance in the majority of galaxies. This is likely due to the strong covariance between spatially-adjacent pixels in the original datacube, and the difficulties in accounting for this during both the data reduction and binning processes (see Sharp et al., 2015 for a full discussion). We therefore enforce a scaling factor on the noise spectrum,

$$\sigma_{i,\mathrm{new}} = \sigma_{i,\mathrm{old}}\ \mathrm{SD}\left(\frac{\delta_i}{\sigma_{i,\mathrm{old}}}\right). \tag{2.4}$$

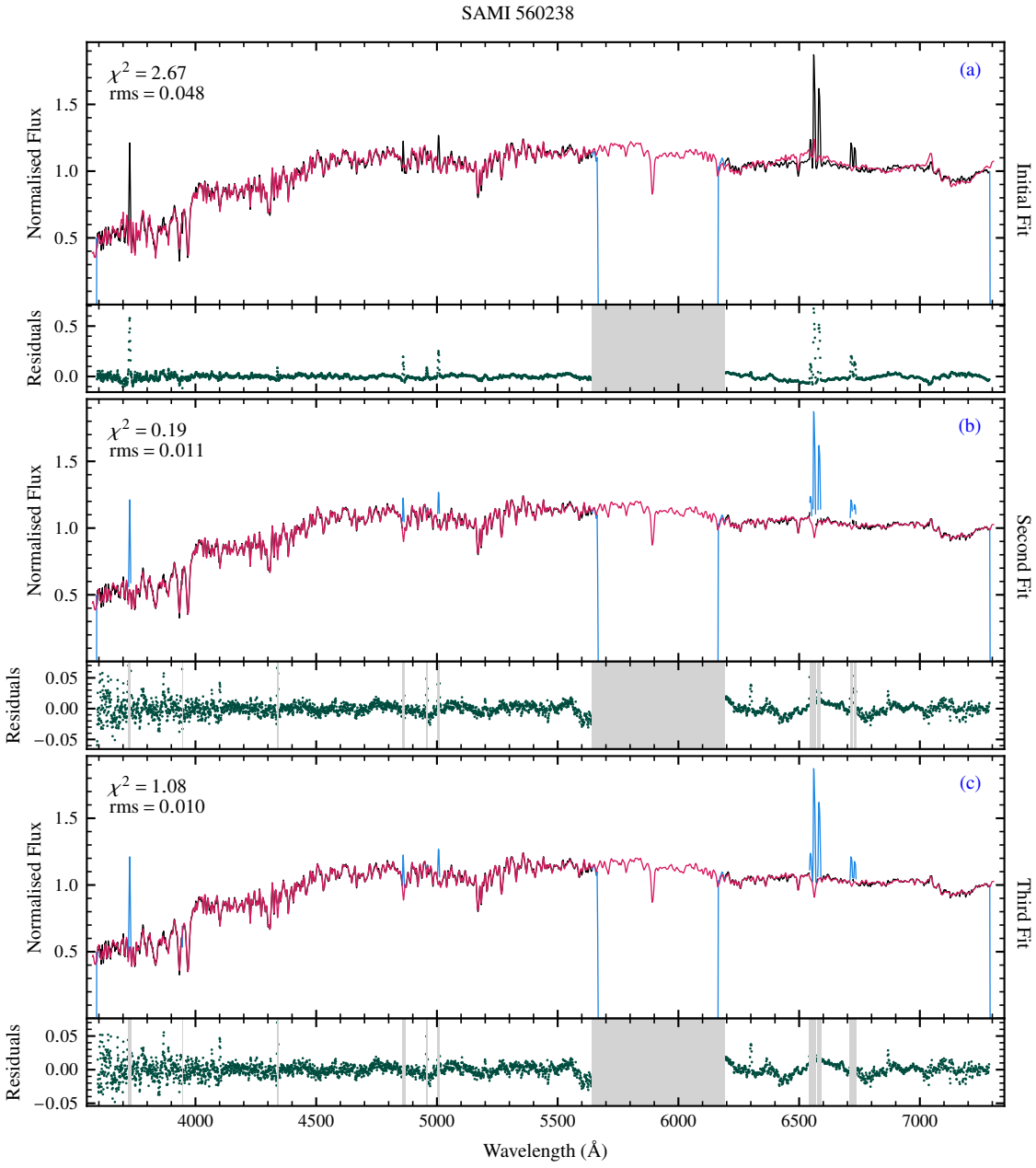


Figure 2.2: The three stages of spectral fitting, in order to obtain an emission-free galaxy spectrum. The example galaxy spectrum (SAMI 560238) is shown in black, with the best-fitting PPXF output in pink, and the residuals (data-model) underneath in green. The grey shaded regions, and corresponding blue sections of the spectra, indicate masked areas which have been excluded from the fit.

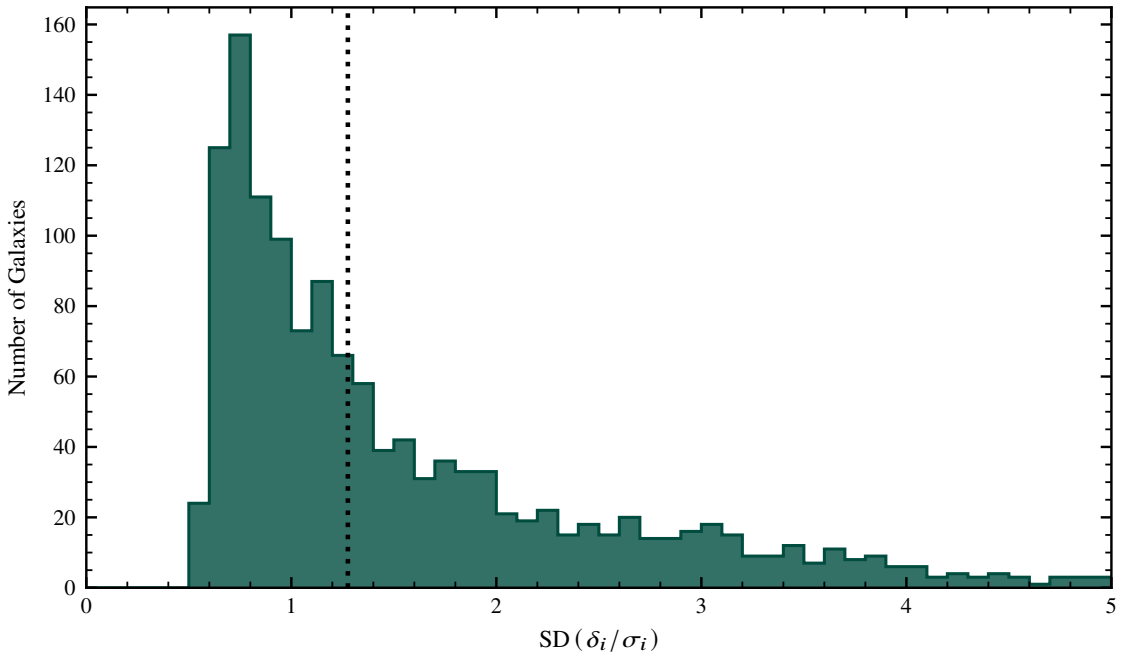


Figure 2.3: The distribution of the noise scaling factor, defined as the standard deviation of the ratio of the initial fit residuals, δ_i, to the noise spectrum, σ_i. The dashed line denotes the median of the distribution, at SD $(\delta_i/\sigma_i) = 1.27$.

2.1.4.2 Subsequent Fits

Following this, we perform a second fit to the data, using the scaled noise spectrum $\sigma_{i,new}$. We now make use of the CLEAN keyword, which employs a 3-sigma-clipping method during the fit. This rejects anomalous pixels in the spectrum, such as those contaminated by emission-line infill or bad pixels on the detector. For our example galaxy shown in Fig. 2.2b, we see that this procedure has successfully identified all visible emission lines in the spectrum, including the strong Hα and [NII] lines, as well as the much weaker Hβ absorption line infill.

For the third fit, we expand these regions of anomalous pixels by $\pm$25%, in order to account for traces of emission that may not have been picked up, and then conduct a final fit with the scaled noise spectrum, excluding the set of bad pixels we have just flagged. From this fit, we obtain the best-fitting LOSVD, with an example displayed in Fig. 2.2c. This includes our measurements for v and σ, and the PPXF best-fitting

output, which is the optimal linear combination of the template spectra and the 12^{th} order additive polynomial. Compared to the reference library of 985 stellar spectra, typically only ≈ 30 templates are given a non-zero weight in the final output.

Errors on the LOSVD are estimated following the bootstrap method of van de Sande et al., 2017b. We divide the galaxy spectrum into 10 regions, then randomly reallocate the residuals from the final fit within each region. We add these residuals to the best-fitting output, then re-measure v and σ using the original templates. After 100 realisations of this process, we take the standard deviations of the measurement distributions as the errors on v and σ.

2.2 Line Indices

2.2.1 The Lick/IDS Index System

For our analysis, we use all 20 of the standard Lick indices covered in the SAMI wavelength range, defined in Worthey et al., 1997 and Trager et al., 1998. These are as follows:

- The molecular indices: CN_1, CN_2, Mg_1, and Mg_2. These indices are measured in magnitudes, rather than Å.
- The iron-dominated indices: Fe4383, Fe4531, Fe5015, Fe5270, Fe5335, and Fe5406.
- The remaining atomic indices: Ca4227, G4300, Ca4455, $C_2$4668[1], and Mg_b.
- The Balmer absorption indices: Hδ_A, Hδ_F, Hγ_A, Hγ_F, and Hβ.

Each of these indices consists of a central bandpass, and two side bandpasses, from which we fit a 'pseudo-continuum' level. The locations of the central bandpasses are

[1]Formerly referred to as Fe4668, before it was found to be most sensitive to the carbon abundance (Tripicco et al., 1995).

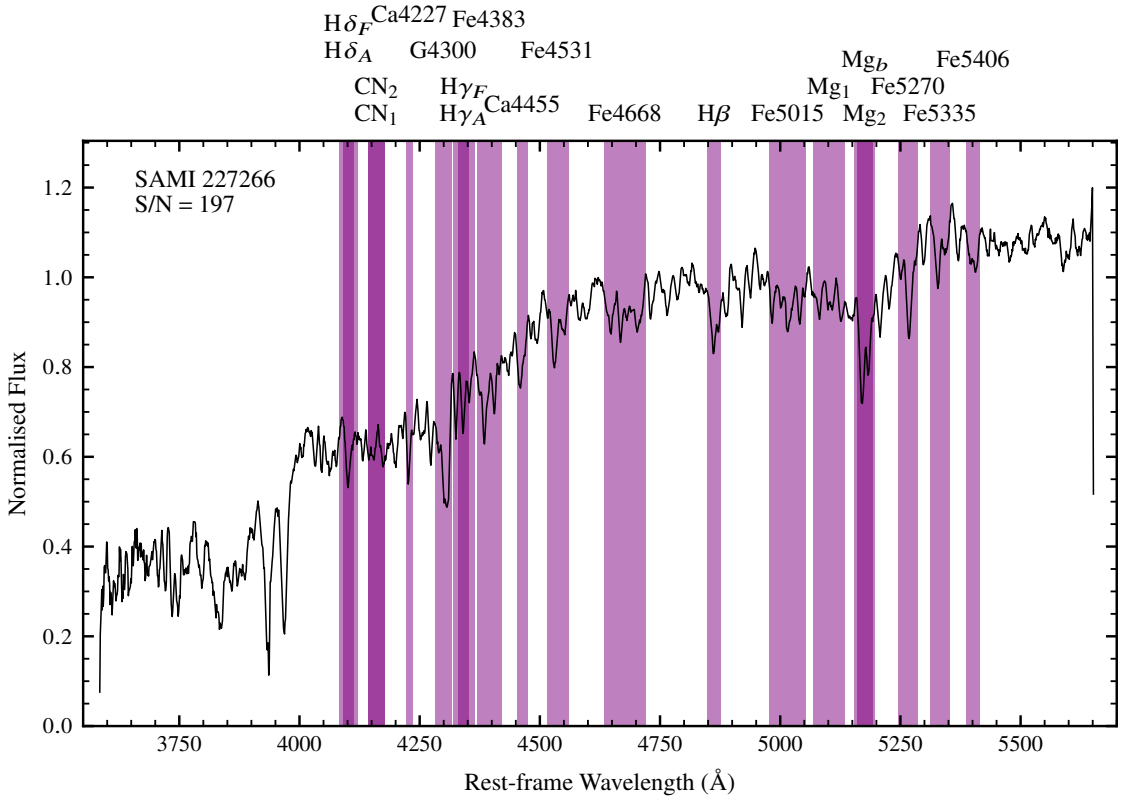


Figure 2.4: The locations of the central bandpass for each of the 20 Lick indices used in this analysis, with a redshift-corrected galaxy spectrum shown as a reference. Note that some of the central bandpasses overlap, such as the A and F Balmer indices.

displayed in Fig. 2.4.

We begin by shifting the observed spectra to the rest frame, based on the measured stellar recession velocities from PPXF. These velocities are typically very small ($< 10\,\mathrm{km\,s^{-1}}$), but ensure an accurate rest-frame wavelength calibration. The spectral resolution of the original Lick/image dissector scanner (IDS) system varied as a function of wavelength (see Appendix A1 of Worthey et al., 1997), and so we transform our spectra to match this. We utilise the method first developed by Graves et al., 2008, and previously implemented as part of their EZ_AGES package (Graves, 2014). We convolve our observed spectra with a wavelength-dependent Gaussian, where the

dispersion is characterised by

$$\sigma^2_{\rm vel} + \sigma^2_{\rm inst} + \sigma^2_{\rm app}(\lambda) = \sigma^2_{\rm IDS}(\lambda), \tag{2.5}$$

where $\sigma_{\rm vel}$ is the intrinsic broadening due to the velocity dispersion of the galaxy, $\sigma_{\rm inst}$ is the instrumental broadening, $\sigma_{\rm IDS}(\lambda)$ is the wavelength-dependent Lick/IDS system resolution, and $\sigma_{\rm app}(\lambda)$ is the additional broadening we apply to match the Lick/IDS resolution. Whilst it is also possible for the instrumental broadening to vary as a function of wavelength, this is not the case for the SAMI Galaxy Survey, which has a constant dispersion across the wavelength range (see Section 2.1.1; also van de Sande et al., 2017b). We apply this broadening individually to a cutout of the spectrum around each index, covering the side bandpasses. Since our spectra and SSP models are both flux-calibrated, we do not also transform to the IDS response curve.

2.2.2 Measuring Line Indices

We use a modified version of the method developed by Cenarro et al., 2001 (hereinafter C01) to measure the line indices, detailed thoroughly below. Each index is treated as an equivalent width, defined over three wavelength bandpasses:

- A blue bandpass, delimited by λ_{b_1} and λ_{b_2}.
- The central index feature, defined by the wavelength range λ_{c_1}-λ_{c_2}.
- A red bandpass, delimited by λ_{r_1} and λ_{r_2}.

We show an example of the layout in Fig. 2.5. From the blue and red bandpasses we derive the local pseudo-continuum, $C(\lambda)$, through an error-weighted least-squares fit.

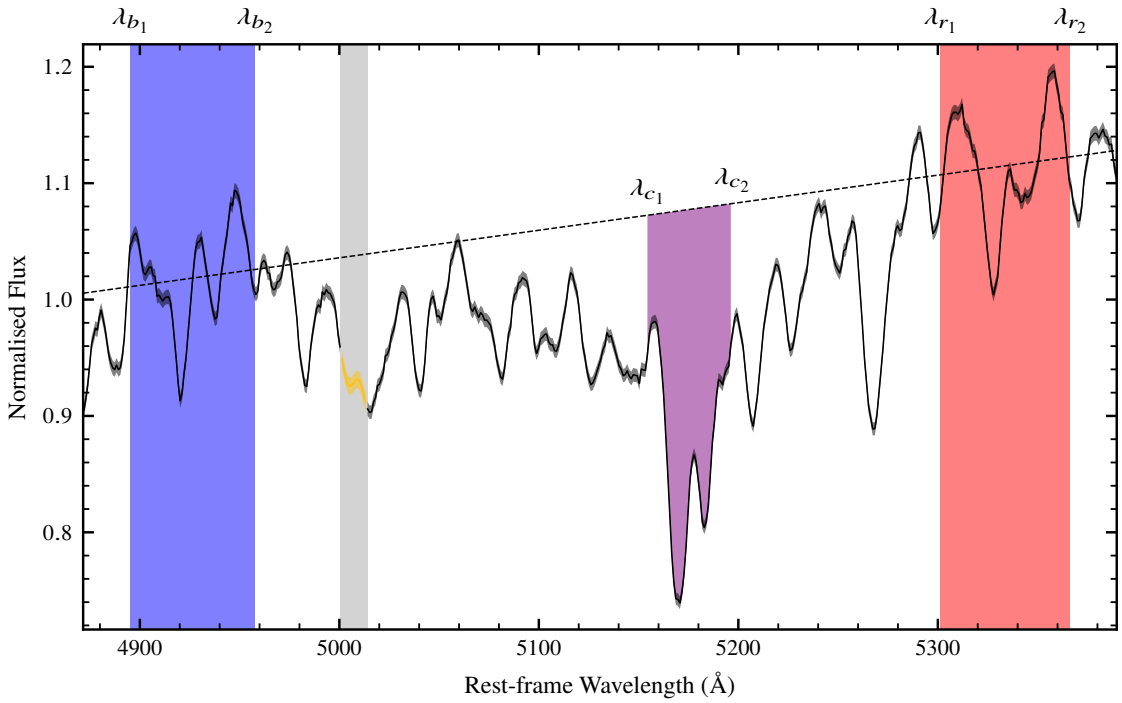


Figure 2.5: A spectral cutout around the magnesium absorption line complex. We display in black the integrated spectrum of SAMI 227266 and the associated error, previously shown in full in Fig. 2.4. The yellow region indicates pixels that have been replaced after the template fitting, which has removed weak emission from the [OIII] line at 5007 Å. The blue and red shaded areas are the side bandpasses for the Mg_1 index, from which we fit the pseudo-continuum, shown as a dashed line. The Mg_1 index is measured within the central bandpass, from the pseudo-continuum and the spectrum as shown by the shaded purple region.

We begin by writing the continuum level as

$$C(\lambda) = \alpha_1 + \alpha_2 \lambda, \tag{2.6}$$

where we use the following definitions from C01,

$$\alpha_1 = \frac{1}{\Delta} \left(\Sigma_3 \Sigma_4 - \Sigma_2 \Sigma_5 \right), \tag{2.7}$$

$$\alpha_2 = \frac{1}{\Delta} \left(\Sigma_1 \Sigma_5 - \Sigma_2 \Sigma_4 \right), \tag{2.8}$$

$$\Delta = \Sigma_1 \Sigma_3 - \Sigma_2 \Sigma_2, \tag{2.9}$$

with the parameters

$$\Sigma_1 \equiv \sum_{n=1}^{N_c} \sum_{h=1}^{M(n)} \frac{1}{\sigma^2 \left[S(\lambda_{n,h})\right]}, \tag{2.10}$$

$$\Sigma_2 \equiv \sum_{n=1}^{N_c} \sum_{h=1}^{M(n)} \frac{\lambda_{n,h}}{\sigma^2 \left[S(\lambda_{n,h})\right]}, \tag{2.11}$$

$$\Sigma_3 \equiv \sum_{n=1}^{N_c} \sum_{h=1}^{M(n)} \frac{\lambda_{n,h}^2}{\sigma^2 \left[S(\lambda_{n,h})\right]}, \tag{2.12}$$

$$\Sigma_4 \equiv \sum_{n=1}^{N_c} \sum_{h=1}^{M(n)} \frac{S(\lambda_{n,h})}{\sigma^2 \left[S(\lambda_{n,h})\right]}, \tag{2.13}$$

$$\Sigma_5 \equiv \sum_{n=1}^{N_c} \sum_{h=1}^{M(n)} \frac{\lambda_{n,h} S(\lambda_{n,h})}{\sigma^2 \left[S(\lambda_{n,h})\right]}, \tag{2.14}$$

defined following C01's notation, where we sum over the $M(n)$ pixels in $N(c)$ continuum bandpasses. We use $S(\lambda_{n,h})$ to denote the flux of the observed galaxy spectrum at the central wavelength of the h^{th} pixel in the n^{th} continuum bandpass, and $\sigma^2 \left[S(\lambda_{n,h})\right]$ its variance. In our case, we only use one red and one blue bandpass to derive the continuum level, following the definitions of the Lick indices by Worthey et al., 1997. In addition, we note that at the borders of the continuum bandpasses, the wavelength definitions will not correspond exactly to the edges of the outer pixels, and therefore contributions from fractional pixels must be included in the summations.

However, we differ from C01 for the central index bandpass, where we eschew this pixel-based summation over the central index bandpass in favour of numerical integration. This results in a slightly higher accuracy compared to the fractional pixel contributions, although it cannot easily be applied to the error-weighted method for the side bandpasses. We use the definition of a classical atomic index,

$$I_{\text{a}}(\text{Å}) \equiv \int_{\lambda_{c_1}}^{\lambda_{c_2}} \left[1 - \frac{S(\lambda)}{C(\lambda)}\right] \mathrm{d}\lambda, \tag{2.15}$$

for galaxy flux spectrum $S(\lambda)$. For the integral, we interpolate over the galaxy spec-

trum using a piecewise linear spline, and numerically integrate between the precise wavelength limits of the central bandpass. Similarly, for molecular indices, which are measured in magnitudes, we transpose Eq. 2.15 to the form

$$I_{\rm m}({\rm mag}) \equiv -2.5\log_{10}\left(1 - \frac{I_{\rm a}}{\lambda_{c_2} - \lambda_{c_1}}\right). \tag{2.16}$$

The uncertainties on the index measurements are estimated through a Monte Carlo method. We add Gaussian-distributed random noise to 100 realisations of the galaxy spectrum, where the dispersion is characterised by the scaled noise spectrum from the PPXF template fitting (see Section 2.1.4) for each pixel. We re-measure the indices for each realisation, and take the standard deviation of the resulting distribution as the uncertainty on our initial index measurement. Indices where fewer than 75% of pixels in the central feature were classified as good during the PPXF fit are not measured, and are rejected from any further analyses.

2.2.3 Index Dispersion Corrections

For some galaxies, the combined instrumental and intrinsic (velocity) broadening exceeds the defined Lick/IDS resolution for particular indices. This typically occurs at high velocity dispersions, where $\sigma_{\rm vel} \geq 190\,{\rm km\,s^{-1}}$. The higher dispersion results in flux from the absorption line feature being shifted outside the central index bandpass, and is therefore particularly problematic for narrow features such as the Balmer lines. Since a bias in the index measurements can lead to significant errors in the inferred stellar population parameters, we apply a correction to these indices following a similar method to Schiavon, 2007.

To estimate the required correction factors, we make use of the MILES SSP spectral models from Vazdekis et al., 2015, based on the MILES spectral library discussed in Section 2.1.3. These span wide ranges of ages, metallicities, and abundances, and

we assume that they are overall an accurate representation of the target galaxies. We convolve the model spectra with a Gaussian to reach the Lick/IDS resolution, creating mock galaxy spectra at the maximum permissible velocity dispersion for each index, accounting for the different instrumental resolutions using Eq. 2.5. As the Lick/IDS spectral resolution varies as a function of wavelength, the velocity dispersion above which corrections are necessary is different for each index. We measure all indices, following the method in 2.2.2, and take these values as our reference.

We then convolve each spectrum to a fixed velocity dispersion, in steps of $5\,\mathrm{km\,s^{-1}}$, up to a maximum of $400\,\mathrm{km\,s^{-1}}$, and re-measure the Lick indices. This range was chosen to encompass all galaxies in the SAMI Galaxy Survey. For indices defined as atomic (see Eq. 2.15), we derive a multiplicative correction factor from the difference between the broadened and original spectral indices, whereas we derive an additive correction for molecular indices. These factors are marginalised over the full range of metallicities spanned by the MILES SSP models, and into 4 discrete age bins of $\mathrm{Age_{SSP}} \leq 1.5\,\mathrm{Gyr}$, $1.5 < \mathrm{Age_{SSP}} \leq 3.5\,\mathrm{Gyr}$, $3.5 < \mathrm{Age_{SSP}} \leq 8\,\mathrm{Gyr}$, and $8 < \mathrm{Age_{SSP}} \leq 14\,\mathrm{Gyr}$, as shown in Fig. 2.6. We do not also bin as a function of metallicity, as scanning over both age and metallicity introduces considerable degeneracies, with limited benefit and a vastly increased computation time. Therefore, for each measured index where the combined intrinsic and instrumental broadening exceeds the IDS resolution, we can apply an iterative correction, where we check to see if the returned SSP age converges to the age range covered by the correction factor.

2.3 Stellar Population Parameters

Having measured the Lick indices, we can now derive the corresponding single-burst stellar population (SSP) parameters – age, metallicity [Z/H], and α-element abundance [α/Fe]. For this, we use the flux-calibrated SSP models of Thomas et al.,

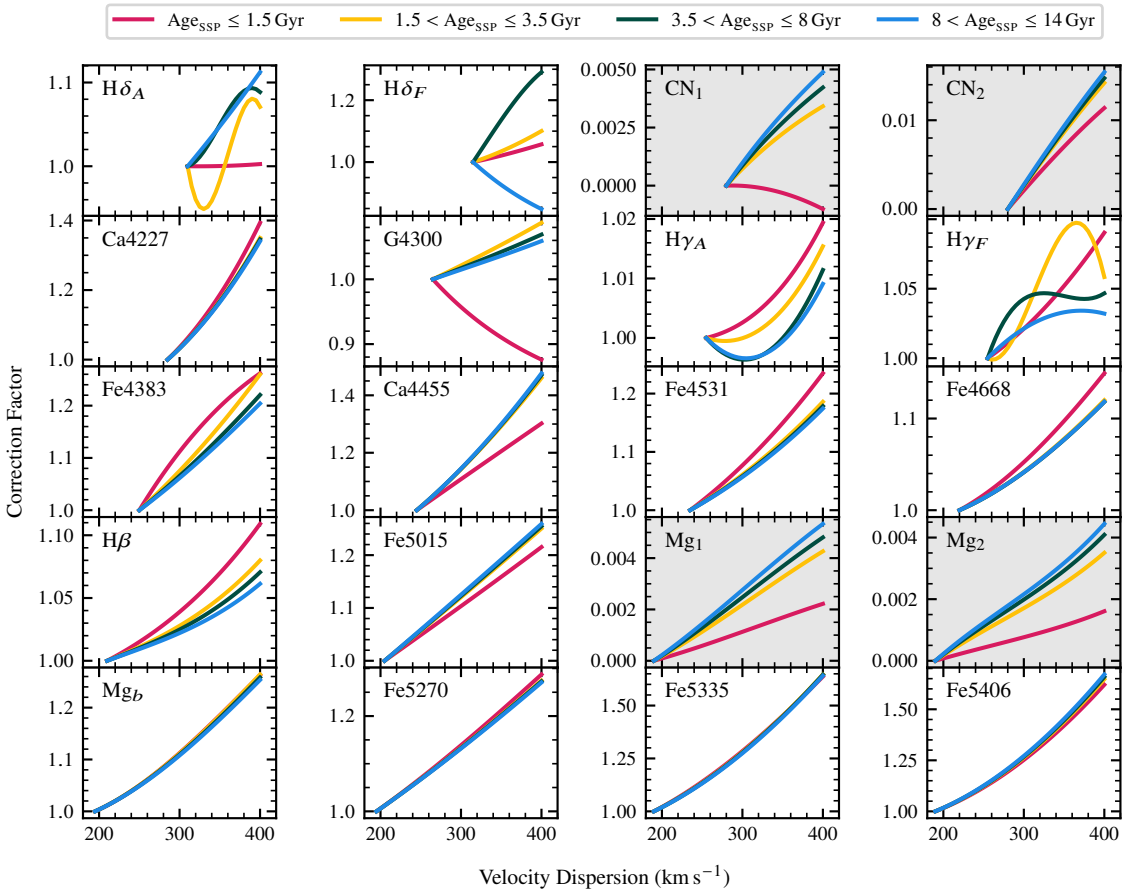


Figure 2.6: The variation of the measured Lick indices with increasing velocity dispersion, relative to their values when the combined instrumental and intrinsic broadening is equal to the Lick/IDS spectral broadening (see Eq. 2.5). The relative index response is shown for four separate bins of the model spectra ages. The grey shaded background indicates molecular indices, and hence an additive correction factor.

2011 (hereinafter TMJ11), which predict the Lick index measurements as a function of log-scaled age, [Z/H], and [α/Fe], spaced over a regular grid. For each index, we interpolate these model predictions onto a finer mesh, with a spacing of 0.02 in $\log_{10}$(age) and [Z/H], and 0.01 in [α/Fe]. The best-fitting solution is then found by following the χ^2 minimisation process of Proctor et al., 2004. For each point in the SSP parameter space, we calculate the reduced χ^2 statistic,

$$\chi^2_{\rm red} = \frac{1}{\nu}\sum_{i=1}^{n}\frac{(O_i - E_i)^2}{\sigma_i^2}, \tag{2.17}$$

where O_i is the observed index value with uncertainty σ_i, E_i is the model prediction, and we sum over n indices with ν degrees of freedom ($\nu = n - 3$, for three SSP parameters). The SSP parameters that best reproduce the measured indices are then derived by finding the minimum in $\chi^2_{\rm red}$ space, $\chi^2_{\rm min}$. The uncertainties on these parameters can be determined by finding the region of confidence bounded by

$$\chi^2_\alpha \equiv \chi^2_{\rm min} + \Delta(\nu, \alpha) \tag{2.18}$$

for some significance level α (see Avni, 1976 for more details). In our implementation, for each SSP parameter the three-dimensional $\chi^2_{\rm red}$ space is collapsed along the other two parameters, allowing us to calculate the exact extent of the $(\chi^2_{\rm min} + 3.5)$ surface, which corresponds to the $\pm 1\sigma$ uncertainties for three parameters. We display an example of this fit in Fig. 2.7. We note that [α/Fe] is more poorly constrained than either age or metallicity, despite the age-metallicity degeneracy visible in the central panel.

For each galaxy, we attempt to utilise all 20 measured indices. Indices are rejected from the fit if they lie more than 1σ beyond the extent of the TMJ11 model grids, so as not to bias the solution. No result is returned if fewer than five indices are available, or if the indices do not include at least one Balmer index, and one Fe index.

2.3.1 Parameter Space Limitations

One complication with the analysis is taking into account the finite limits of the SSP models. For each SSP parameter, we exclude from our analysis any galaxy in which the combined 1σ uncertainties cover the full extent of the parameter space ($0.1 < \text{Age} < 15\,\text{Gyr}$; $-2.25 < [\text{Z/H}] < 0.67$; $-0.3 < [\alpha/\text{Fe}] < 0.5$). In Fig. 2.8, we plot the upper 1σ uncertainties against the lower, using measurements taken from the SAMI $R_{\rm e}$ aperture spectra, with the notation $\delta \text{X} \equiv 1\sigma_{\rm X}$. It is clear that, consistent

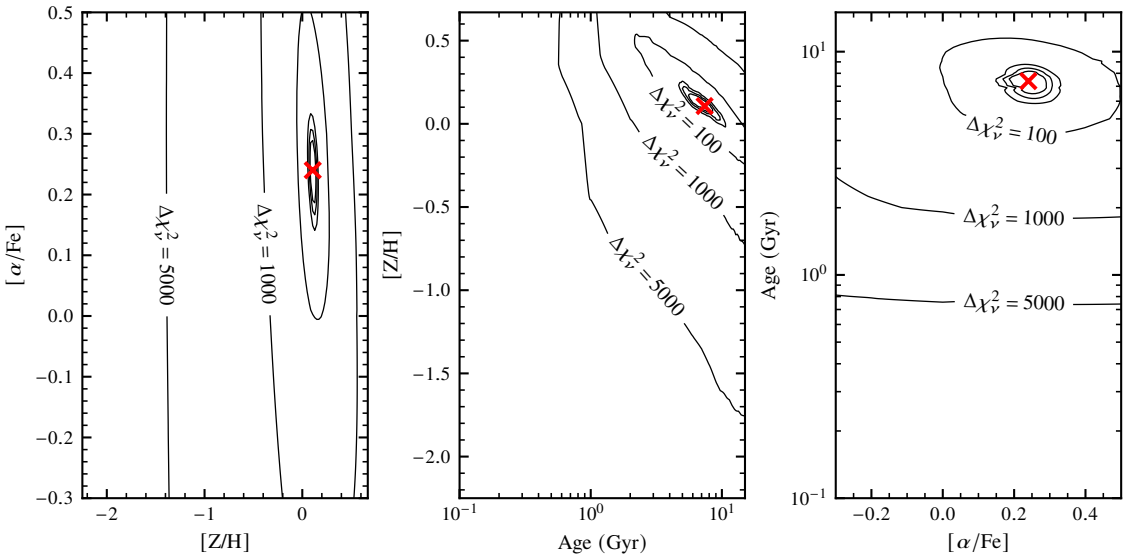


Figure 2.7: The χ^2 distribution of the SSP parameters, measured from the high-S/N R_e aperture spectrum of SAMI 227266 displayed in Fig. 2.4. The red cross denotes the point estimate, or the best-fitting combination of SSP parameters to describe the measured indices. The inner contours indicate the χ^2 level corresponding to the 1, 2, and 3σ confidence intervals, with the outer contours indicating constant offsets from ${\chi^2}_{\rm min}$.

with the example χ^2 distribution shown in Fig. 2.7, the relative uncertainties on [α/Fe] are considerably higher than on Age or [Z/H]. *A priori*, we do not expect any significant asymmetries in the uncertainties, and therefore examine any deviations from this.

δ[α/Fe] displays a noticeable offset for values of $\delta[\alpha/\mathrm{Fe}]_{\rm upper} > 0.3$, where there is no corresponding increase in the lower uncertainty bound. A brief investigation of the galaxies in this regime reveals that they are also low-mass, with low α-abundance, accounting for $\approx 10\%$ of the sample. These low values of [α/Fe], combined with a high measurement error leads to $\delta[\alpha/\mathrm{Fe}]_{\rm lower}$ being clipped by the edges of the parameter space. When performing weighted fits, these galaxies may unfairly bias the solution. For the remaining galaxies unaffected by this clipping, we calculate the asymmetry of the uncertainties, $\delta[\alpha/\mathrm{Fe}]_{\rm upper} - \delta[\alpha/\mathrm{Fe}]_{\rm lower}$. We find the mean of this distribution to be 0.017 dex, with a standard deviation of 0.052 dex. Although this would indicate

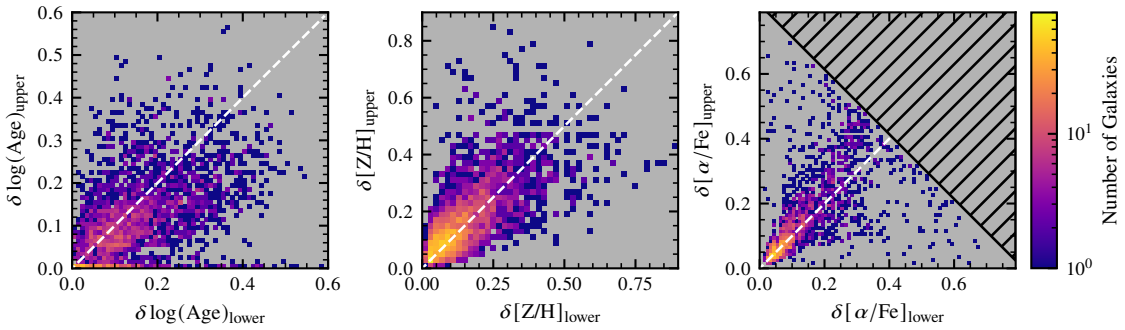


Figure 2.8: The distribution of the upper and lower 1σ uncertainties on each SSP parameter, for SAMI R_{e} aperture spectra. Points are coloured according to the number of galaxies in each bin. The dashed line indicates the ideal scenario, where the uncertainties for any given galaxy are equal, and the distribution is symmetrical. The hatched region indicates the extent of the parameter space, and galaxies lying on the edge of this region have been removed from the sample.

a slight systematic offset, once we take into account the resolution limit of 0.01 in [α/Fe], we conclude that the asymmetry is not significant.

The values of δ[Z/H] show a more uniform distribution. The scatter increases commensurate with the uncertainties, but this is symmetrical. Removing galaxies where one of $\delta[\mathrm{Z/H}]_{\mathrm{upper}}$ or $\delta[\mathrm{Z/H}]_{\mathrm{lower}}$ are clipped by the model grid, we find a median difference of 0.015 dex, and standard deviation 0.051 dex, demonstrating that the asymmetry here is minimal.

The measurement uncertainties for SSP-equivalent age show the strongest deviation from linearity. A small proportion of galaxies have $\delta \log(\mathrm{Age})_{\mathrm{upper}} = 0\,\mathrm{Gyr}$, and we see also a slight shift towards $\delta \log(\mathrm{Age})_{\mathrm{upper}} < \delta \log(\mathrm{Age})_{\mathrm{lower}}$ for increasing uncertainties. Similarly to [α/Fe], both of these effects are caused by galaxies which clip the SSP model grid. The issue of age saturation in the TMJ11 models is a known effect (Kuntschner et al., 2010), although as noted by McDermid et al., 2015, stems from measurement uncertainties on the Balmer indices such as Hβ. As the relative behaviour of the SSP-equivalent ages is robust, we are primarily concerned with ensuring an accurate weighting of the measurements. Therefore, for the galaxies where one of the 1σ intervals is bounded by the model grid, we force the uncertainties to be

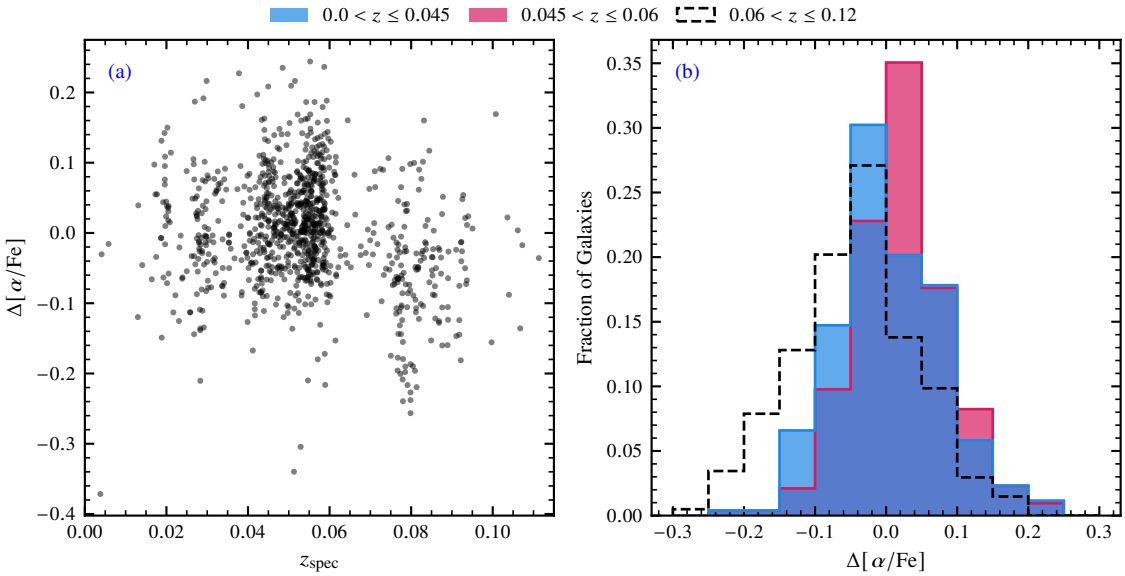


Figure 2.9: In (a), the residuals from the best-fitting linear correlation between [α/Fe] and σ_e, distributed as a function of redshift, for a sample of ETGs using the SAMI R_e aperture spectra (see Section 3.2 for more details). A shift to lower values of [α/Fe] is clearly visible for redshifts greater than ≈ 0.07. In (b), histograms of the residuals separated into three redshift bins, matching the main boundaries of the initial selection function of the SAMI survey.

symmetrical, taking the unbounded uncertainty as the guide.

2.3.2 Sky Line Contamination

Using the measurements from the SAMI R_e aperture spectra as an example, we show a further complication with the estimation of SSP parameters. At a redshift $z = 0.0732$, the centroid of the [OI] atmospheric sky line at 5577 Å is coincident with the edge of the central bandpass for Mg_2, the reddest of the three magnesium indices used in our analysis. As with all line index-based fitting methods, our SSP-equivalent measurements are very sensitive to changes in these indices, particularly in regards to an accurate determination of [α/Fe]. We show the effect of this in Fig. 2.9a, where for all early-type galaxies (ETGs), we fit [α/Fe] to a common relationship against σ, and plot the residuals Δ [α/Fe] as a function of redshift, z_{spec}. We find a clear offset

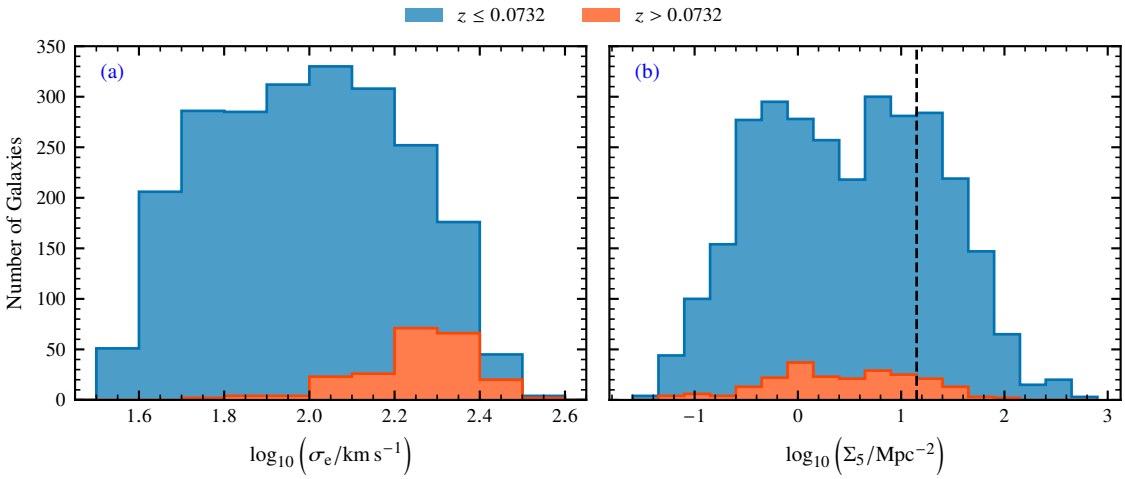


Figure 2.10: The distribution of galaxies in the SAMI survey, separated by redshift. Galaxies with $z > 0.0732$ are heavily biased towards higher velocity dispersions, shown in (a), and are predominantly found at lower local surface densities, displayed in (b). In (b), the dashed line represents the value of $\log_{10}\left(\Sigma_5/\mathrm{Mpc}^{-2}\right)$ used to separate galaxies into low- and high-density environments (see Sections 1.3.3.2 and 3.2.2 for more details).

between the low and high redshift galaxies, at $z \approx 0.07$. In Fig. 2.9b, we separate the residuals by redshift, following the boundaries for the SAMI selection function (Bryant et al., 2015), finding a difference on the order of $\Delta\,[\alpha/\mathrm{Fe}] \approx 0.05$ dex between the highest redshift sample and the others.

The effect of this sky line contamination is concerning, but we also note that these are predominantly higher-mass field and group galaxies drawn from the Galaxy and Mass Assembly (GAMA) survey (Driver et al., 2011), with the relative distributions of effective velocity dispersion σ_e and environmental number surface density Σ_5 shown in Fig. 2.10. The higher-redshift galaxies would therefore introduce a significant bias towards lower values of $[\alpha/\mathrm{Fe}]$ when separating the SAMI sample by environment. As this is one of the primary aims of our research, we elected to remove these galaxies from consideration. It is possible that this effect could be mitigated in future by the use of alternative methods for determining the stellar populations, such as different SSP models, or utilising full-spectrum fitting. Although this cut will have a measurable

influence on our analysis, we consider it necessary to avoid the possibility of a more pronounced bias, as shown in Figure 2.9.

2.3.3 Nomenclature

The line index method of determining SSP parameters is not new, and there are a considerable number of previous studies in this area (see Section 1.1.4 for an overview). However, there is some debate over the exact quantities being measured, or modelled. As noted by Barbosa et al., 2021, the line index method used in optical wavelengths traces [Mg/Fe] far better than other α-elements. This is supported by our analysis in Section 2.3.2, where contamination or removal of the magnesium indices biases [α/Fe] to lower values. Despite this, we note that is not strictly accurate to refer to the α-abundance determined in this manner as [Mg/Fe], as is sometimes the case in the literature. The TMJ11 models were calculated by varying in lockstep the abundance of all α elements, not just Mg, and therefore the response of other indices, such as $C_2$4668, depend on this variation of [α/Fe]. Hence, throughout this thesis we refer to the SSP parameter we derive as [α/Fe], whilst acknowledging that it is a simplification of the varying individual chemical abundances.

Chapter 3

Global Stellar Populations as a Function of Morphology and Environment

In this chapter, we present the measured global stellar population parameters of galaxies drawn from the Sydney-Australian-Astronomical-Observatory Multi-object Integral-field Spectrograph (SAMI) Galaxy Survey. We focus on the [α/Fe]-$\sigma_{\rm e}$ relation, showing its variation across galaxy morphological types, and environments. The results presented in this chapter were previously published in Watson et al., 2022a.

3.1 Sample Selection

Our sample is taken from the third public data release (DR3) of the SAMI Galaxy Survey (Croom et al., 2021), containing 3068 unique galaxies. For each galaxy, we use the $R_{\rm e,MGE}$ aperture spectrum. This is a binned spectrum, summed over a synthetic elliptical aperture of area $\pi R^2_{\rm e,MGE}$, where $R_{\rm e,MGE}$ is the effective radius of the galaxy determined via multi-Gaussian expansion (MGE) fitting (see Section 1.3.3.1, also Scott et al., 2018 and Croom et al., 2021 for more details).

3.1.1 Quality cuts

We make a series of quality cuts to our sample, based on the reliability of our measurements of [α/Fe]. Figure 3.1 shows the positions of the full sample in the σ_e-signal/noise ratio (S/N) plane, where we have measured the S/N per spectral pixel between 4600-4800 Å on the original R_e aperture spectra, and used the velocity dispersions measured within one effective radius, σ_e, from SAMI DR3 (see Section 1.3.3.5 for more details). We reject spectra with a S/N $< 20\,\mathrm{pix}^{-1}$, as this is not sufficient to adequately constrain [α/Fe], as demonstrated in previous studies such as Gallazzi et al., 2005. We also consider the dependence on σ_e. If a galaxy has a sufficiently high uncertainty on σ_e, this should increase the uncertainty on our index measurements, since the convolution to the Lick/IDS resolution depends on the measured velocity dispersion. In general, we have not considered this effect for our analysis, since the errors on most measurements of σ_e are negligible compared to the errors on the indices themselves. However, since the velocity dispersion uncertainties are considerably higher at low σ_e, in part due to the correlation with S/N visible in Fig. 3.1, we find it prudent to also introduce a cut here, at $\log_{10}\left(\sigma_e/\mathrm{km\,s}^{-1}\right) = 1.6$. This is supported by the quality cuts of van de Sande et al., 2017b, who suggest removing any galaxy for which $\log_{10}\left(\sigma_e/\mathrm{km\,s}^{-1}\right) \leq 1.54$, due to the systematic uncertainties as a result of the instrumental resolution.

3.1.2 Completeness

In total, 971 unique galaxies were removed from the sample due to the cumulative quality cuts outlined in this section. We reject 292 galaxies with $z > 0.0732$ due to possible sky line contamination, detailed in Section 2.3.2, leaving a redshift-limited sample of 2776 galaxies. We remove a further 330 galaxies with a spectral S/N $<$ 20 summed over the R_e aperture, and 154 with $\log_{10}\left(\sigma_e/\mathrm{km\,s}^{-1}\right) < 1.6$. Finally, 195 galaxies either fall on the outer limits of the parameter space in [α/Fe] or have

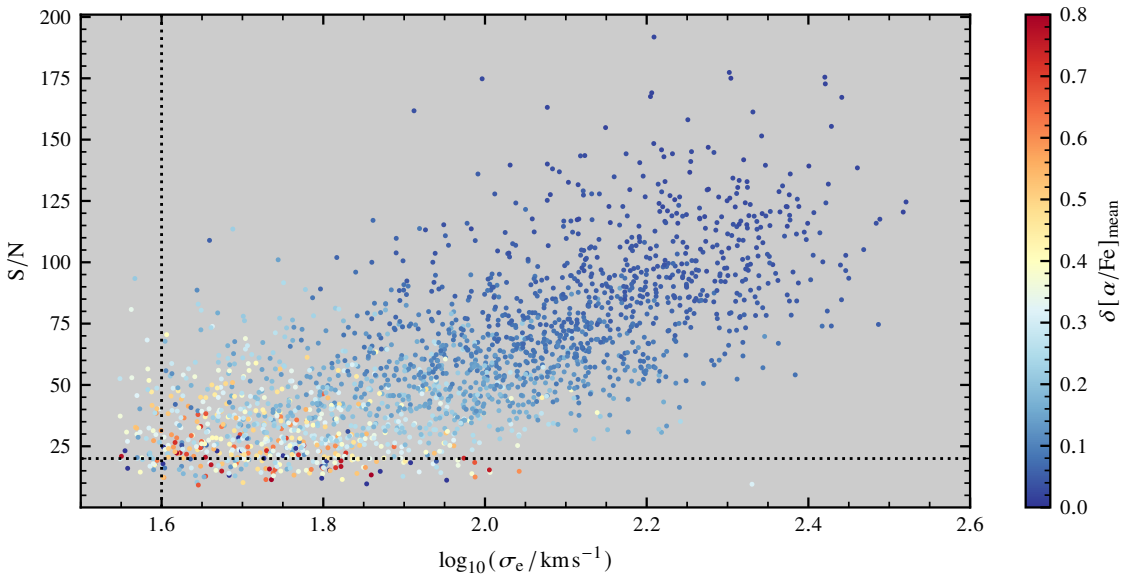


Figure 3.1: The distribution of the SAMI R_e aperture spectra in the velocity dispersion-S/N plane, coloured by the mean of the upper and lower uncertainties on $[\alpha/\mathrm{Fe}]$, $\delta[\alpha/\mathrm{Fe}]_{\mathrm{mean}}$. Galaxies with $\sigma_e \leq 35\,\mathrm{km\,s^{-1}}$ have already been removed from the sample, due to the quality cuts of van de Sande et al., 2017b. We also note the strong correlation between σ_e and S/N for our sample, and display the additional quality cuts via the dotted lines.

uncertainties spanning the entire range. We note that these numbers are given as an indication only – since there is a significant degree of overlap between galaxies cut at each stage, the exact numbers will vary significantly depending on the order of the cuts. For example, galaxies removed with $\log_{10}\left(\sigma_e/\mathrm{km\,s^{-1}}\right) < 1.6$ could also have been rejected in the first instance for having a S/N < 20, as shown in Fig. 3.1. The number of galaxies of each morphological type remaining are summarised in Table 3.1.

We also note that the total number of galaxies differs between sections of the paper, due to the limitations of the prerequisite measurements. Quantities such as the local number surface density Σ_5 cannot be measured for all galaxies, for a variety of reasons expanded upon in the relevant papers. As such, not all of the 2097 galaxies that remain are utilised in each element of our analysis, with the exact decompositions tabulated in Table 3.1.

Figure 3.2 displays how the cumulative quality cuts have affected the completeness

Sample	Total	Optical Morphology					Section
		E	S0	Sa/b	Sc	Unclassified	
All Observations	3426	603	785	682	1182	174	
Unique Galaxies	3068	561	728	605	1026	148	
$z \leq 0.0732$	2776	462	630	544	1002	138	2.3.2
Quality Cuts	2097	456	623	524	405	89	3.1.1
Red Sequence	1314	427	569	218	38	62	3.2.1
Blue Cloud	783	29	54	306	367	27	3.2.1
$\log_{10}\left(\Sigma_5/\mathrm{Mpc}^{-2}\right) \leq 1.15$	1413	218	363	424	357	51	3.2
$\log_{10}\left(\Sigma_5/\mathrm{Mpc}^{-2}\right) > 1.15$	659	229	252	95	46	37	3.2
		Early-type Galaxies					
		E		E/S0		S0	
$\log_{10}\left(\Sigma_5/\mathrm{Mpc}^{-2}\right) \leq 1.15$	393	119		108		166	3.2.2
$\log_{10}\left(\Sigma_5/\mathrm{Mpc}^{-2}\right) > 1.15$	375	130		99		146	3.2.2

Table 3.1: The total number of galaxies used for each stage of the analysis, separated by optical morphological type. Intermediate classifications have been grouped with the earlier of the two types, *e.g.* E/S0 galaxies contribute to the total under the E column. For analyses of early-type galaxies, we use only galaxies classified as E, E/S0, and S0. Note that the total number of galaxies differs slightly between sections, since the required properties cannot be measured for all galaxies.

of the sample. We measure the completeness of our final 2097 galaxies against the redshift-limited sample. Visually, it is clear that the completeness of the sample suffers at low σ_e, and reaches 50% above $\log_{10}\left(\sigma_e/\mathrm{km\,s}^{-1}\right) \approx 1.7$. Above $\log_{10}\left(\sigma_e/\mathrm{km\,s}^{-1}\right) = 2$, the sample is almost complete relative to galaxies below $z = 0.0732$, not falling below 90%. Similarly, looking at the magnitude distribution using M_r (the absolute magnitude in the r-band), we find $> 80\%$ of galaxies fainter than $M_r = -18$ are cut, although nearly all galaxies brighter than $M_r = -20$ remain in the sample.

Looking at Table 3.1, we can see the effect of the quality cuts on the sample morphology distribution. These appear to almost exclusively affect those galaxies classified as Sc, although this is not entirely surprising given that we have introduced a cut-off in velocity dispersion.

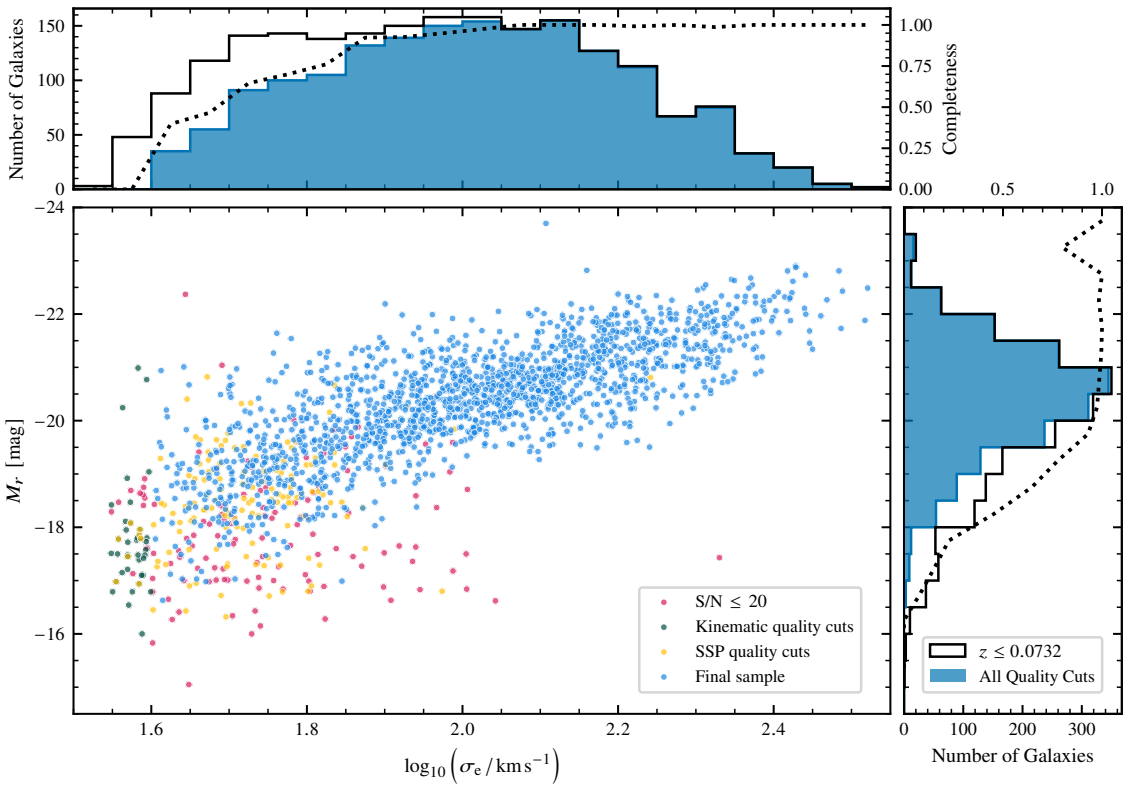


Figure 3.2: The distribution of our sample galaxies in the σ_e-M_r plane. We show the impact of the cumulative quality cuts relative to the redshift-limited sample, noting that galaxies for which $\sigma_e \leq 35\,\mathrm{km\,s^{-1}}$ have already been removed from the sample. In the side histograms, we overlay the completeness of our final sample after all quality cuts, relative to the number of unique galaxies with $z \leq 0.0732$.

3.1.3 DR3 Consistency Checks

We show a comparison between our measurements of [α/Fe] and those released as part of SAMI DR3 in Figure 3.3. Whilst the analyses of the $R_{e,MGE}$ aperture spectra could have been performed with either set of measurements, this comparison is necessary to validate our method, which will be applied later to spectra for which there are no counterparts in SAMI DR3 (see Chapters 5 and 6). We compare only the 2097 galaxies included in our final sample, to reduce the effect of outliers which would not be considered in any analysis. A visual inspection indicates a good agreement between the two versions, which is reinforced by the underlying data. The scatter in the offset increases towards lower S/N, although we do not observe any significant shift

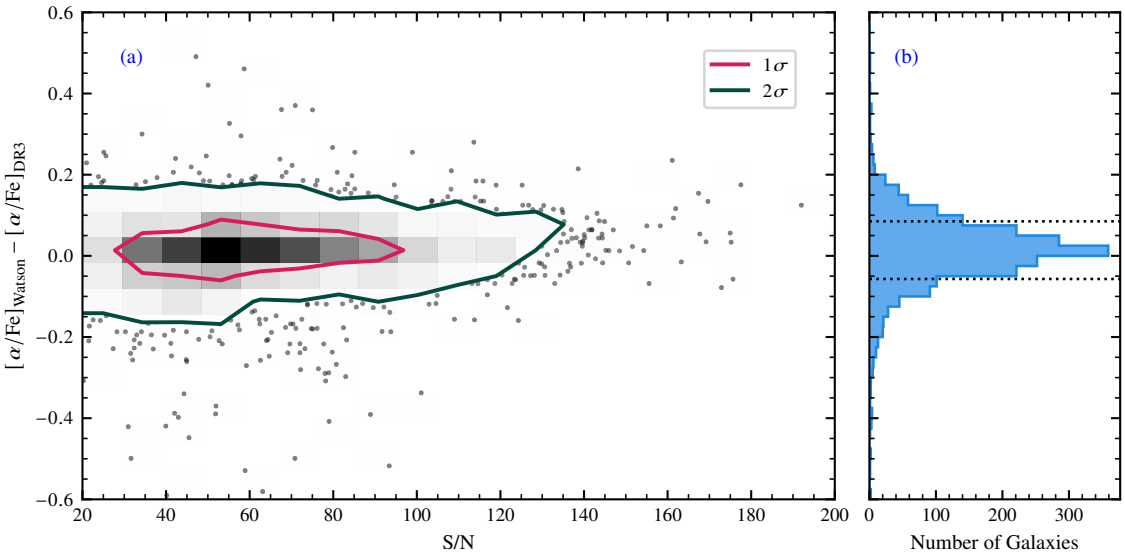


Figure 3.3: The offsets between the measurements of $[\alpha/\mathrm{Fe}]$ in this chapter, denoted by $[\alpha/\mathrm{Fe}]_{\mathrm{Watson}}$, and those included in SAMI DR3, $[\alpha/\mathrm{Fe}]_{\mathrm{DR3}}$. We display in (a) the offset as a function of the spectral signal-to-noise ratio, S/N. The contours denote the 1σ and 2σ confidence intervals of the distribution, enclosing $\approx 68\%$ and $\approx 95\%$ of points respectively. In (b), we marginalise along S/N to show the projection of the offset. The dashed lines delineate the 16^{th} and 84^{th} percentiles of the distribution.

in the distribution, which remains centred around approximately zero offset. Across all galaxies, we find a median offset of 0.014 dex, with the 16^{th} and 84^{th} percentiles occurring at -0.057 dex and 0.085 dex respectively, and hence our measurements are shifted slightly higher than those released in SAMI DR3. However, this is not statistically significant – given the median uncertainty of $\delta[\alpha/\mathrm{Fe}]_{\mathrm{Watson}} = 0.11$ dex, 85.5% of our measurements lie within $\pm 1\sigma$ of the DR3 measurements. We therefore consider our results in excellent agreement with the preceding measurements at a population level.

3.1.4 Line Fitting

Throughout this chapter, we fit multiple linear correlations of the form $y = ax + b$. In order to estimate the best-fitting values of a and b, and their associated uncertainties,

we aim to minimise the quantity

$$\chi^2 = \sum_{j=1}^{N} \frac{[a(x_j - x_0) + b - y_j]^2}{(a\sigma_{x_j})^2 + (\sigma_{y_j})^2}, \tag{3.1}$$

adopted from Press et al., 1992, where σ_{x_j} and σ_{y_j} are the measurement uncertainties on N measurements x_j and y_j respectively, and x_0 is a constant offset. In the limit where the errors on x_j are negligible, this reduces to the simple χ^2 estimator, shown in Eq. 2.17. We make use of the Python library LMFIT by Newville et al., 2021 to calculate this quantity. We set x_0 to zero unless otherwise stated, to simplify comparisons throughout the paper and with other studies.

3.2 Environmental Dependence

3.2.1 Separation by Colour

We focus on the dependence of [α/Fe] on σ_e, the velocity dispersion measured within the effective radius R_e, as studies such as S17 have previously demonstrated that this provides a tighter correlation than the stellar mass M_*. Several previous studies, among them Baldry et al., 2006, have found that the most significant change with environment is the fraction of red galaxies, f_r, and that many environmental correlations can instead be attributed to a change in f_r. To consider the dependence of the [α/Fe]-σ_e relation on the environment, we therefore control for this variable by isolating samples of both red and blue galaxies, and separately analysing their stellar populations.

We begin by dividing our full sample into a red sequence and a blue cloud, shown in Fig. 3.4, and composed of 1314 and 783 galaxies respectively (the full morphological decomposition is shown in Table 3.1). The division between the two samples for the SAMI survey was derived by Owers et al., 2017, and depends upon the K-

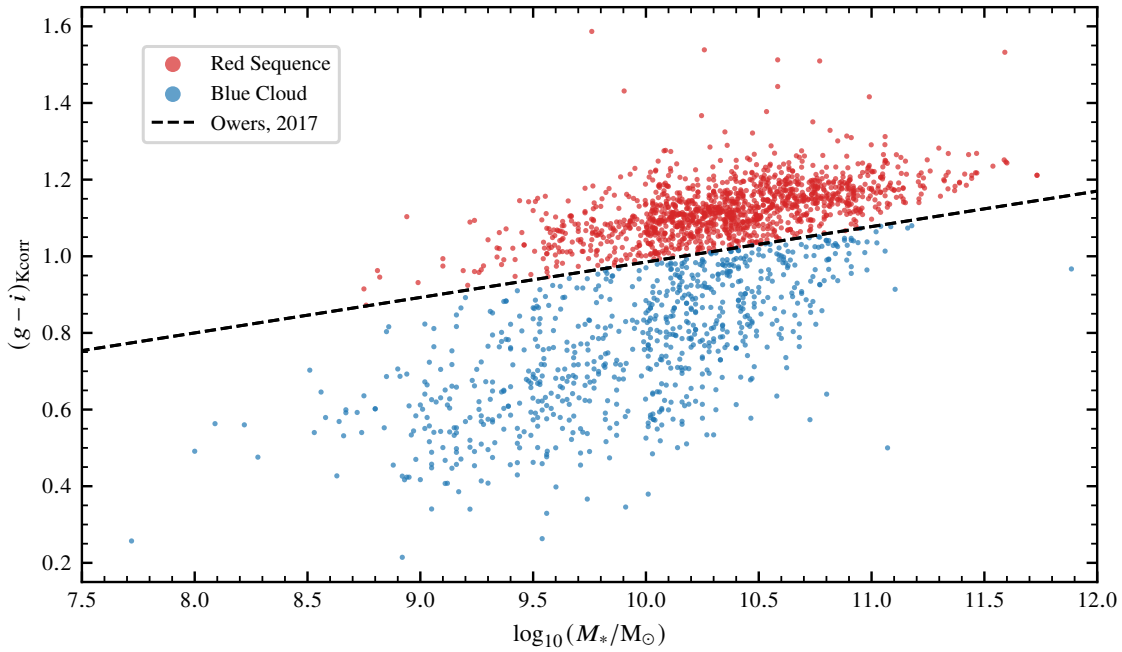


Figure 3.4: The distribution of K-corrected $(g-i)$ galaxy colours as a function of stellar mass, for our final sample. The dividing line between the red sequence and blue cloud is taken from Owers et al., 2017.

corrected $(g-i)$ colour, $(g-i)_{\rm Kcorr}$, where the K-corrections have been determined using the CALC_KCOR code from Chilingarian et al., 2010. Figure 3.5 shows the corresponding distribution of galaxies in $\log_{10}\left(\Sigma_5/{\rm Mpc}^{-2}\right)$, our primary measure of the environmental density, taken from SAMI DR3 (see Section 1.3.3.2 for more details). Whilst both samples are well represented at the lowest number surface densities, above $\log_{10}\left(\Sigma_5/{\rm Mpc}^{-2}\right) \approx 1$ the SAMI survey is dominated by red sequence galaxies.

Following Section 3.1.4, we fit separate weighted linear relations between $[\alpha/{\rm Fe}]$ and $\log_{10}\left(\sigma_{\rm e}/{\rm km\,s}^{-1}\right)$ for both the red sequence and blue cloud, shown in Fig. 3.6a,c. For the red sequence, we derive

$$[\alpha/{\rm Fe}] = (0.342 \pm 0.011)\log_{10}\left(\sigma_{\rm e}/{\rm km\,s}^{-1}\right) - (0.50 \pm 0.02), \tag{3.2}$$

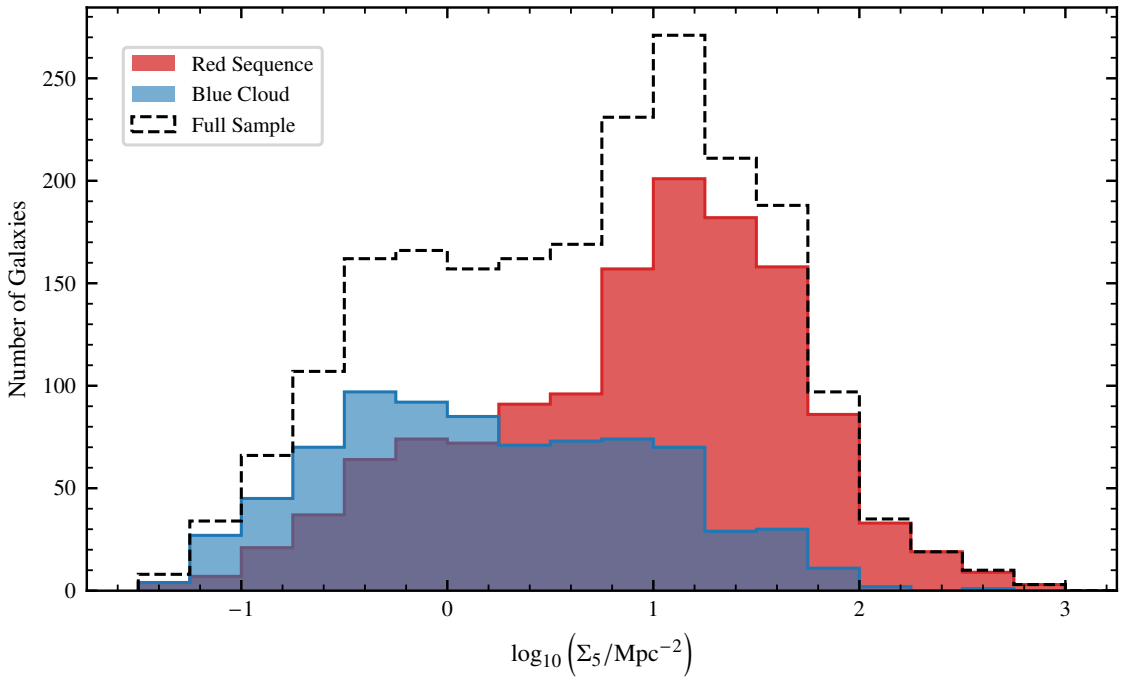


Figure 3.5: The distribution of $\log_{10}\left(\Sigma_5/\mathrm{Mpc}^{-2}\right)$ for red sequence and blue cloud galaxies, alongside the full sample. At the highest values of $\log_{10}\left(\Sigma_5/\mathrm{Mpc}^{-2}\right)$, galaxies almost exclusively belong to the red sequence, whereas we find a more balanced distribution towards lower values of $\log_{10}\left(\Sigma_5/\mathrm{Mpc}^{-2}\right)$.

and for the blue cloud,

$$[\alpha/\mathrm{Fe}] = (0.382 \pm 0.017)\log_{10}\left(\sigma_\mathrm{e}/\mathrm{km\,s}^{-1}\right) - (0.64 \pm 0.04). \tag{3.3}$$

From this, we deduce that galaxies in the red sequence are systematically α-enhanced over those in the blue cloud, which is supported visually by Fig. 3.6. The steeper relationship with σ_e for blue galaxies means that this effect manifests itself predominantly at low velocity dispersions, with an offset of $\approx 0.07\,\mathrm{dex}$ in $[\alpha/\mathrm{Fe}]$ at $\log_{10}\left(\sigma_\mathrm{e}/\mathrm{km\,s}^{-1}\right) = 1.6$ compared to $\approx 0.04\,\mathrm{dex}$ at $\log_{10}\left(\sigma_\mathrm{e}/\mathrm{km\,s}^{-1}\right) = 2.3$ (the maximum velocity dispersion of galaxies in the blue cloud).

To compare the environmental influence for each sample, we express the residuals $\Delta\,[\alpha/\mathrm{Fe}]$ as a function of Σ_5, and refit a linear relation, shown in Fig. 3.6b,d. We

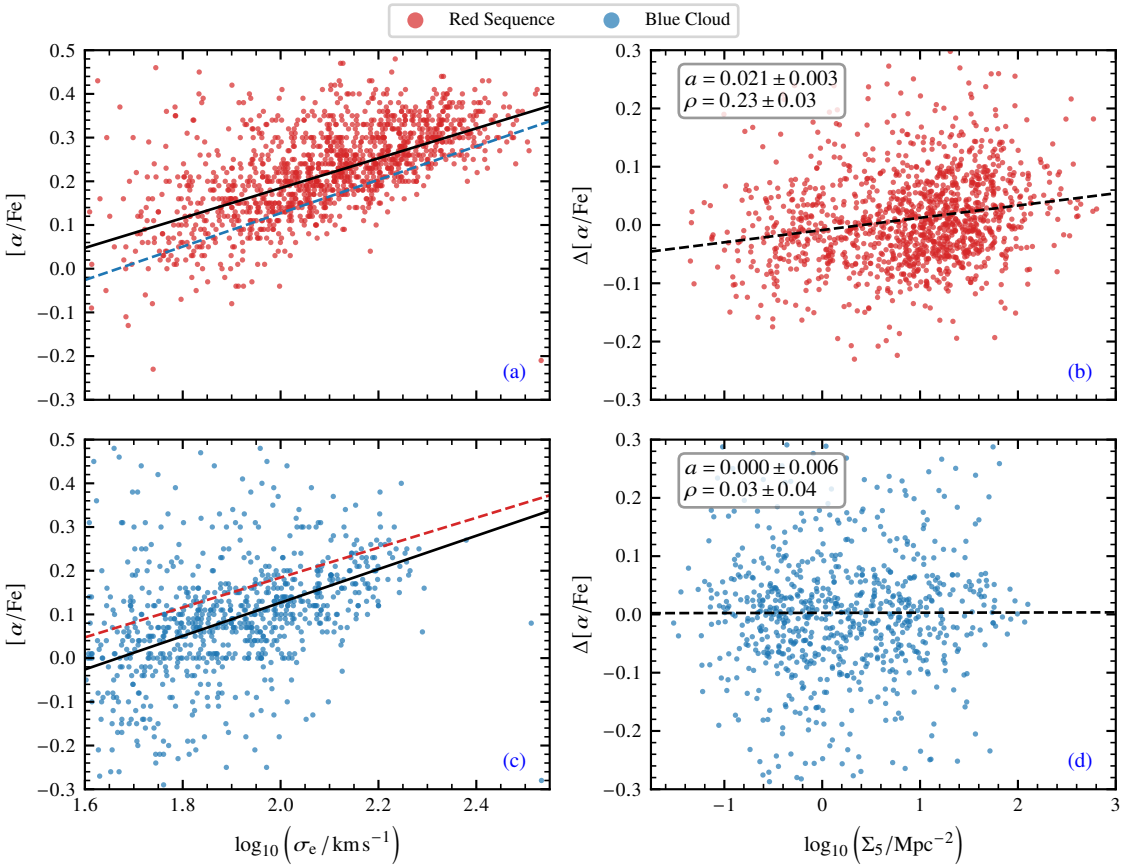


Figure 3.6: The left-hand figures display the $[\alpha/\mathrm{Fe}]$-σ_e relation for both the blue cloud and red sequence, with separate best-fitting relationships shown as solid black lines. For each sample, we overlay the linear relationship for the other sample as a dashed line, to allow a direct comparison. We then fit a second linear trend line to the residuals $\Delta\,[\alpha/\mathrm{Fe}]$, expressed as a function of the local number surface density Σ_5, and displayed as a dashed line in the figures on the right. The gradient a and the Spearman correlation coefficient ρ are inset in the relevant plots. The extent of the $\Delta\,[\alpha/\mathrm{Fe}]$ axis has been truncated to display $\approx 99\%$ of galaxies, whilst allowing for a clear visual comparison between the samples.

also calculate the Spearman rank correlation coefficient ρ, to assess the reliability of the linear fit. We estimate the uncertainty on ρ using a bootstrapping procedure, whereby we generate 1000 iterations of each sample, with each datapoint drawn from a Gaussian distribution of width equal to the measurement uncertainty. For galaxies in the blue cloud, we find that both the correlation and fitted line are consistent with $\Delta\,[\alpha/\mathrm{Fe}]$ having no dependence on Σ_5, given the uncertainties and large degree

of scatter in the residuals. For red sequence galaxies, the scatter in the residuals is reduced, although still substantial. However, we find a positive correlation for the red sequence, with $\rho \approx 0.2$, which we derive as

$$\Delta\,[\alpha/\mathrm{Fe}] = (0.021 \pm 0.003)\log_{10}\left(\Sigma_5/\mathrm{Mpc}^{-2}\right) - (0.009 \pm 0.003). \tag{3.4}$$

Hence, at a fixed velocity dispersion, red sequence galaxies in high density environments (HDEs) have higher $[\alpha/\mathrm{Fe}]$ than their counterparts in low density environments (LDEs).

3.2.2 Early-type Galaxies

For ease of comparison with other studies, we investigate a sample of early-type galaxies (ETGs), defined here as galaxies with a morphological type of E, E/S0, and S0 (MTYPE ≤ 1; see Section 1.3.3.3 and also Cortese et al., 2016). This sample, containing 768 galaxies, can broadly be considered a subset of the red sequence discussed in Section 3.2.1, with only 3% of ETGs being drawn from the blue cloud. As such, the relations derived for the red sequence hold true for ETGs. We fit the whole ETG population to a single linear relationship, shown in Fig. 3.7a, and calculated as

$$[\alpha/\mathrm{Fe}] = (0.307 \pm 0.015)\log_{10}\left(\sigma_\mathrm{e}/\mathrm{km\,s}^{-1}\right) - (0.41 \pm 0.03).$$

From this, we measure the absolute residuals in $[\alpha/\mathrm{Fe}]$, and as before, derive the relation

$$\Delta\,[\alpha/\mathrm{Fe}] = (0.023 \pm 0.003)\log_{10}\left(\Sigma_5/\mathrm{Mpc}^{-2}\right) - (0.012 \pm 0.004),$$

with a correlation coefficient $\rho = 0.27 \pm 0.04$. Although this indicates a slightly stronger correlation than the full red sequence sample, we also investigate alternative

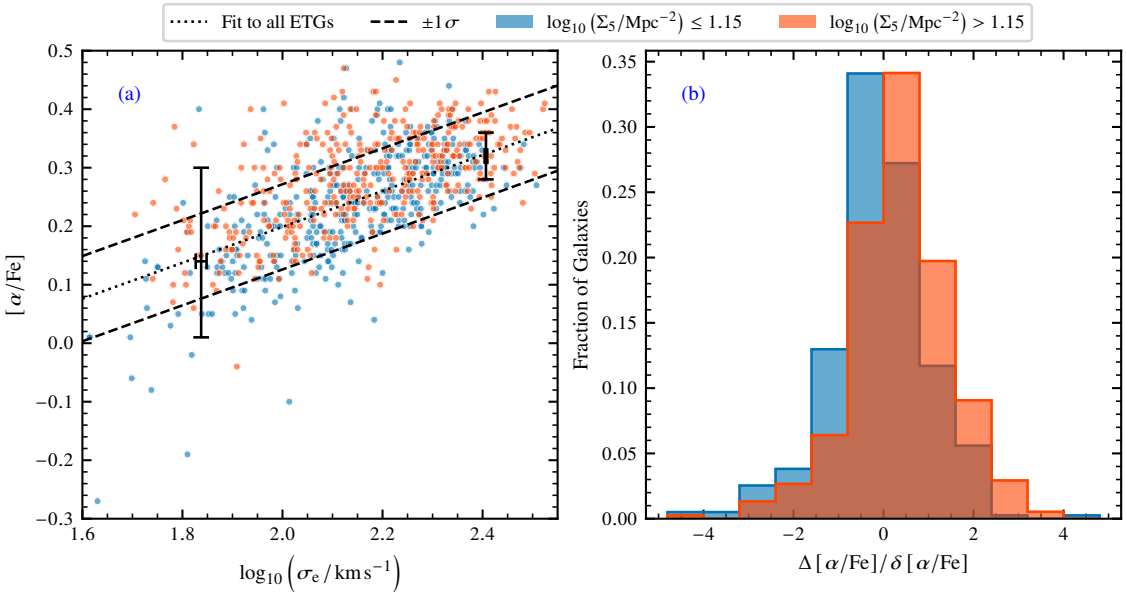


Figure 3.7: (a) The distribution of ETGs in the $[\alpha/\mathrm{Fe}]$-σ_e plane, with the best-fitting linear relationship shown as a dotted line. The error bars show the median uncertainties on $[\alpha/\mathrm{Fe}]$ and σ_e for the 5$^{\mathrm{th}}$ and 95$^{\mathrm{th}}$ percentile of ETGs, ordered by velocity dispersion, and the dashed lines the ±1 standard deviation of galaxies from the best-fitting line. Galaxies are coloured according to their local environmental number surface density, Σ_5. The normalised residuals from the linear relationship are shown in (b).

methods to test the statistical significance of our findings.

We divide the ETGs into two samples of approximately equal size, based on the local environmental number surface density of each galaxy, giving high, $\log_{10}\left(\Sigma_5/\mathrm{Mpc}^{-2}\right) > 1.15$, and low, $\log_{10}\left(\Sigma_5/\mathrm{Mpc}^{-2}\right) \leq 1.15$, environmental density samples (see Section 1.3.3.2). We normalise the residuals $\Delta\,[\alpha/\mathrm{Fe}]$ by the associated error, $\delta[\alpha/\mathrm{Fe}]$, and show the residual distributions in Fig. 3.7b. Visually, we find that the distribution of galaxies with high local number surface densities is shifted to slightly higher values of $[\alpha/\mathrm{Fe}]$, compared to galaxies in lower density environments, with the median value of $[\alpha/\mathrm{Fe}]$ increasing by 0.025 dex.

We first conduct a Kolmogorov-Smirnov test (Hodges, 1958), which allows us to reject the null hypothesis that these two samples are drawn from the same parent population, to a very high degree of certainty ($p \ll 0.01$). The Mann-Whitney test

(Mann et al., 1947) similarly concludes that the locations of the distributions are significantly different, also with $p \ll 0.01$. However, since the actual difference in the sample medians is small, on the order of half the median measurement uncertainty, this offset is dwarfed by the scatter visible in the overall relationship. Based on this, we cannot rule out the primary cause of the offset being the well known morphology-density relation of Dressler, 1980. Indeed, in Table 3.1, we show the breakdown of the constituent morphologies in the ETG sample. The fraction of galaxies labelled as E/S0 remains almost constant across the two environments. In contrast, the fraction of ellipticals increases from 30.3% in LDEs to 34.7% in HDEs. As such, the correlations between α-enhancement and morphology shown in the following section are of the right order to explain this difference in distributions.

3.2.3 Morphology Dependence

Our results in Fig. 3.7b satisfy us that a simple division by environmental density is sufficient to show a divergence in the population, without forcing the residuals to a fit against Σ_5. We therefore further examine the environmental offset by simultaneously testing the underlying dependence on morphology. We separate all 2,097 galaxies in the full sample by visual morphology, using the MTYPE attribute from SAMI DR3, leaving four similarly-sized groups (see Table 3.1). For galaxies for which the classification is split between two morphological types, we group these with the earlier type of the two, such that an E/S0 galaxy would be included in the E sample. We use the same cut-off value for environmental density as before, $\log_{10}\left(\Sigma_5/\mathrm{Mpc}^{-2}\right) = 1.15$, for consistency across comparisons, and discuss this further in Section 1.3.3.2. The results are shown in Fig. 3.8, with the best-fitting parameters in Table 3.2.

For galaxies in LDEs, there is little change in the best fit relation with morphology, with the S0 and Sa/b groups entirely consistent within the stated errors. The slope of the relation is slightly shallower for elliptical galaxies, with the change driven by ellip-

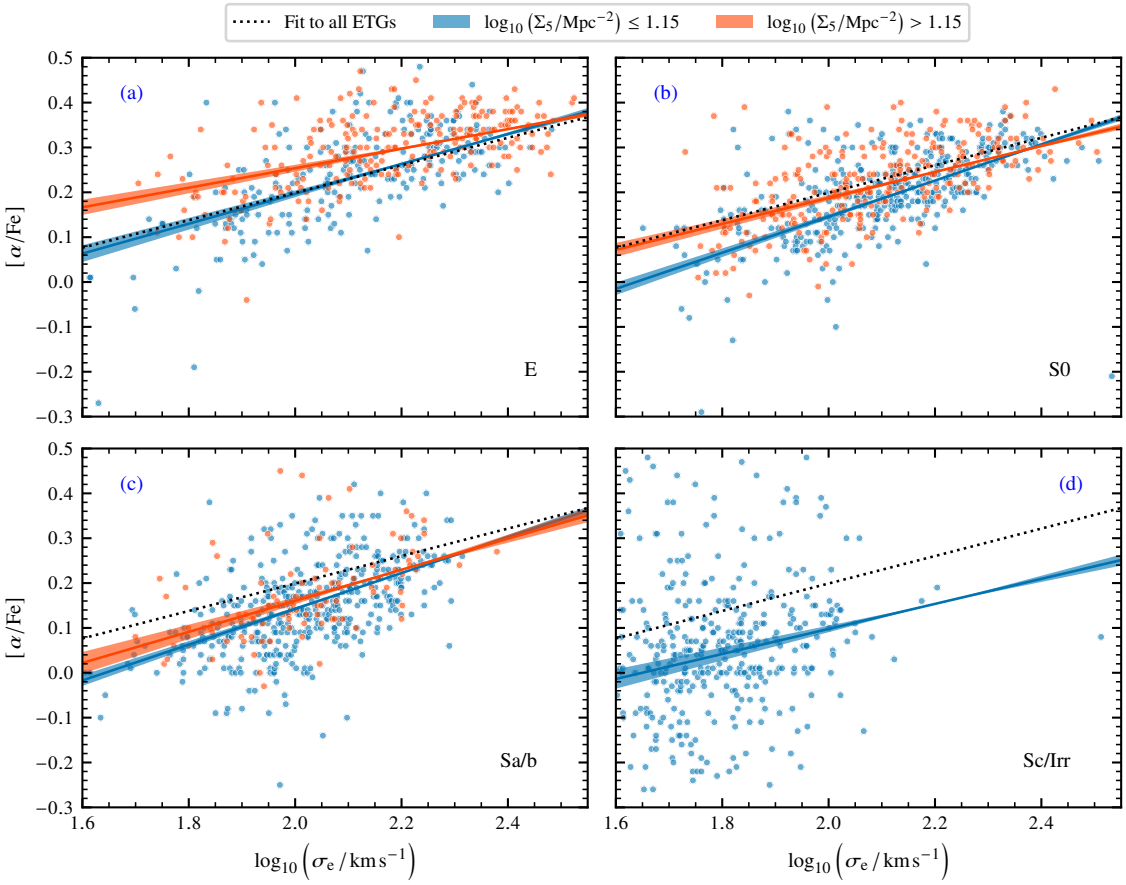


Figure 3.8: The distribution of SAMI galaxies in the [α/Fe]-σ_e plane, separated by morphological type and environment. Using the full sample of galaxies, we also fit each environment and morphology separately, without constraining the fit in any way, and show the results in (a), (b), (c), and (d). Since we do not consider the result for Sc galaxies with high local densities to be as reliable as the other groups due to the large difference in sample size, we do not display it here. We use the relationship for ETGs as a point of reference, represented by the dotted black line.

ticals at low velocity dispersion, $\log_{10}\left(\sigma_e/\mathrm{km\,s^{-1}}\right) < 2$, being α-enhanced over other morphological types. Conversely, at high velocity dispersion, $\log_{10}\left(\sigma_e/\mathrm{km\,s^{-1}}\right) > 2$, the measured [$\alpha$/Fe] ratio is consistent across most morphological types in LDEs. The exception to this is the Sc/Irr group, which shows some evidence for a shallower relationship than all other morphologies. This may be partially caused by the limited sampling, with only 6.9% of Sc/Irr galaxies having $\log_{10}\left(\sigma_e/\mathrm{km\,s^{-1}}\right) > 2$.

For galaxies in high-density environments (HDEs), the picture is more compli-

Morphology	$\log_{10}\left(\Sigma_5/\mathrm{Mpc}^{-2}\right) \leq 1.15$		$\log_{10}\left(\Sigma_5/\mathrm{Mpc}^{-2}\right) > 1.15$	
	a	$[\alpha/\mathrm{Fe}]_{100}$	a	$[\alpha/\mathrm{Fe}]_{100}$
E	0.33 ± 0.03	0.197 ± 0.008	0.22 ± 0.02	0.254 ± 0.008
S0	0.40 ± 0.02	0.146 ± 0.005	0.29 ± 0.02	0.188 ± 0.006
Sa/b	0.40 ± 0.02	0.143 ± 0.004	0.35 ± 0.04	0.160 ± 0.008
Sc/Irr	0.279 ± 0.036	0.098 ± 0.007	-	-

Table 3.2: The best-fitting parameters for the relationships shown in Fig. 3.8, in the form $[\alpha/\mathrm{Fe}] = a \log_{10}(\sigma_\mathrm{e}/100\,\mathrm{km\,s^{-1}}) + b$, where we use the notation $b \equiv [\alpha/\mathrm{Fe}]_{100}$. Note the substantially larger uncertainties on the parameters for Sc galaxies with high local number surface densities.

cated. In Table 3.2, for all morphologies earlier than Sc, there is little observable difference between the HDE samples at high velocity dispersions. The difference here occurs primarily at lower σ_e, with galaxies classified as S0 being α-enhanced over their Sa/b counterparts by approximately 0.04 dex at $\log_{10}\left(\sigma_\mathrm{e}/\mathrm{km\,s^{-1}}\right) = 1.6$. This offset increases further when considering the elliptical galaxies, which are α-enhanced by an additional 0.09 dex over S0 galaxies at $\log_{10}\left(\sigma_\mathrm{e}/\mathrm{km\,s^{-1}}\right) = 1.6$. This is supported by the fiducial values of $[\alpha/\mathrm{Fe}]_{100}$, where we see a consistent decrease in $[\alpha/\mathrm{Fe}]$ with increasing morphological type, across both environments.

In Sc galaxies, recent bursts of star formation will strongly influence the integrated light, making it difficult to evaluate the abundance ratio. Thus, no conclusions can be drawn from the small sample of Sc galaxies.

Comparing now the same morphological types across environments, in the high-σ_e regime, we find no significant difference between galaxies in HDEs or LDEs, irrespective of morphological type. Hence, for galaxies with an earlier type than Sc, at high velocity dispersions there is little evidence here to support a difference in the relative abundance of α-elements across environments. Conversely, at low σ_e, there is a substantial offset between the best-fitting relations for the low- and high-density samples, with galaxies in HDEs being α-enhanced over those in LDEs. At $\log_{10}\left(\sigma_\mathrm{e}/\mathrm{km\,s^{-1}}\right) = 1.6$, the lower limit of our selection, we find an offset of 0.09 dex

in $[\alpha/\mathrm{Fe}]$ for elliptical galaxies, 0.08 dex for S0, and narrowing to 0.05 dex for the Sa/b grouping. This offset narrows at our fitted intercepts of $[\alpha/\mathrm{Fe}]_{100}$, but supports this interpretation, with offsets of 0.06 dex, 0.04 dex, and 0.02 dex for E, S0, and Sa/b respectively. There therefore appear to be two components. The first is that low-σ_e galaxies residing in a similar environment show an increase in $[\alpha/\mathrm{Fe}]$ when looking along the Hubble sequence from spirals to ellipticals. The second is that when comparing galaxies of the same morphological type, those residing in denser environments are likely to be α-enhanced over their LDE counterparts.

3.2.4 Separation by Velocity Dispersion

It is worth considering however, that the offsets at low σ_e discussed in the previous section may vary depending on the exact routine and weighting used to simultaneously fit both the intercept and gradient for each subsample. For this reason, we also utilise a similar method to Liu et al., 2016, shown in Fig. 3.9. For a given morphological type, we fit all galaxies with $\log_{10}\left(\sigma_\mathrm{e}/\mathrm{km\,s^{-1}}\right) > 2$ to a single linear relationship, due to the limited differences between high-σ_e galaxies across environments. Galaxies for which $\log_{10}\left(\sigma_\mathrm{e}/\mathrm{km\,s^{-1}}\right) \leq 2$ are then divided into high- and low-density environments as before, and the gradient of their best-fitting relationships is fixed to the value derived at high σ_e. The resulting parameters are summarised in Table 3.3.

One obvious result from this method, as opposed to that used in Section 3.2.3, is that the fits to the Sc sample no longer appear anomalous compared to the other morphologies, despite the relatively small sample of galaxies with $\log_{10}\left(\sigma_\mathrm{e}/\mathrm{km\,s^{-1}}\right) > 2$. The overall results are largely consistent with the conclusions drawn from Fig. 3.8, with the largest offset in $[\alpha/\mathrm{Fe}]$ occurring in elliptical galaxies, with $\Delta[\alpha/\mathrm{Fe}]_{100} = (0.06 \pm 0.01)$ dex. For Sa/b/c galaxies, we find that the fitted intercepts $[\alpha/\mathrm{Fe}]_{100}$ show only minimal differences between environments – whilst the offset $\Delta[\alpha/\mathrm{Fe}]_{100}$ is larger for Sc/Irr galaxies, the uncertainty on this measurement is greater than for

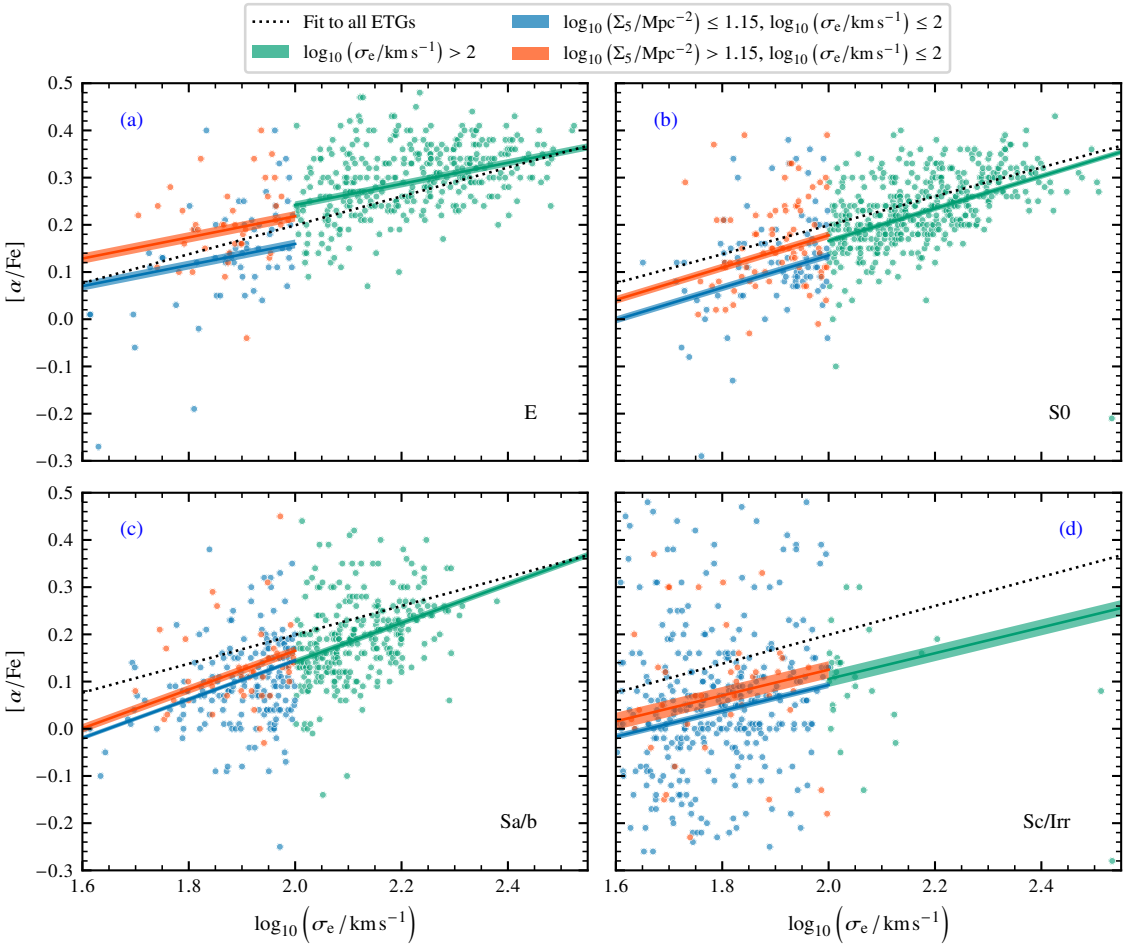


Figure 3.9: As Fig. 3.8, but for each morphological type, the gradient of the linear trend line is set by fitting only to galaxies with $\log_{10}\left(\sigma_{\rm e}/{\rm km\,s^{-1}}\right) > 2$, shown in green. The gradient is then held fixed for the fits to galaxies with $\log_{10}\left(\sigma_{\rm e}/{\rm km\,s^{-1}}\right) \leq 2$, allowing only the intercept, $[\alpha/{\rm Fe}]_{100}$, to vary. The dotted line is the fit for ETGs, shown in Fig 3.7a.

the Sa/b sample. In combination with Fig. 3.8, we take this as evidence that there is little measurable difference between the stellar populations of late-type galaxies with low and high local number surface densities. Conversely, for ETGs, we find that there is sufficient evidence for low-$\sigma_{\rm e}$ galaxies in high-density environments having a truncated period of star formation relative to their counterparts in lower-density environments.

Morphology	a	$[\alpha/\mathrm{Fe}]_{100}$		
		$\log_{10}\left(\sigma_\mathrm{e}/\mathrm{km\,s^{-1}}\right) > 2$	$\log_{10}\left(\sigma_\mathrm{e}/\mathrm{km\,s^{-1}}\right) \leq 2$	
			LDE	HDE
E	0.22 ± 0.03	0.242 ± 0.008	0.160 ± 0.009	0.218 ± 0.011
S0	0.34 ± 0.02	0.166 ± 0.006	0.135 ± 0.008	0.178 ± 0.008
Sa/b	0.41 ± 0.04	0.142 ± 0.007	0.145 ± 0.005	0.165 ± 0.009
Sc/Irr	0.27 ± 0.13	0.105 ± 0.017	0.093 ± 0.007	0.125 ± 0.018

Table 3.3: The best-fitting parameters for the relationships shown in Fig. 3.9, where the gradient a is fixed by fitting to galaxies where $\log_{10}\left(\sigma_\mathrm{e}/\mathrm{km\,s^{-1}}\right) > 2$. LDE and HDE refer to galaxies with $\log_{10}\left(\Sigma_5/\mathrm{Mpc^{-2}}\right) \leq 1.15$ and $\log_{10}\left(\Sigma_5/\mathrm{Mpc^{-2}}\right) > 1.15$ respectively.

3.2.4.1 Non-linear Behaviour

In Fig. 3.9a, the fiducial value of $[\alpha/\mathrm{Fe}]_{100}$ for high-σ_e elliptical galaxies is higher than either of the values of $[\alpha/\mathrm{Fe}]_{100}$ for low-σ_e galaxies, indicating a potential departure from the assumed linear relationship. Investigating this, we fit to a parabolic function of the form $[\alpha/\mathrm{Fe}] = a \log_{10}^2\left(\sigma_\mathrm{e}/\mathrm{km\,s^{-1}}\right) + b \log_{10}\left(\sigma_\mathrm{e}/\mathrm{km\,s^{-1}}\right) + c$, and show the results in Fig. 3.10, where we again separate out galaxies in LDEs and HDEs. To compare against the linear model of Fig. 3.8, we utilise the Bayesian Information Criterion (BIC; Schwarz, 1978) to determine which model is more appropriate. The BIC includes a penalty term for the number of free parameters k to prevent overfitting, and is defined in terms of the χ^2 statistic as

$$\mathrm{BIC} \equiv \chi^2 + k \ln(n) \tag{3.5}$$

for n data points. Generally, the model with the lowest BIC is preferred. We calculate the difference in the criterion as $\Delta\mathrm{BIC} \equiv \mathrm{BIC}_\mathrm{linear} - \mathrm{BIC}_\mathrm{parabolic}$. The difference in favour of the parabolic model is substantial, with $\Delta\mathrm{BIC} = 11.8$ for galaxies in HDEs, and $\Delta\mathrm{BIC} = 9.3$ for those in LDEs. An interpretation of these $\Delta\mathrm{BIC}$ values can be found in Raftery, 1995, who defined "strong" evidence as corresponding to $\Delta\mathrm{BIC} >$

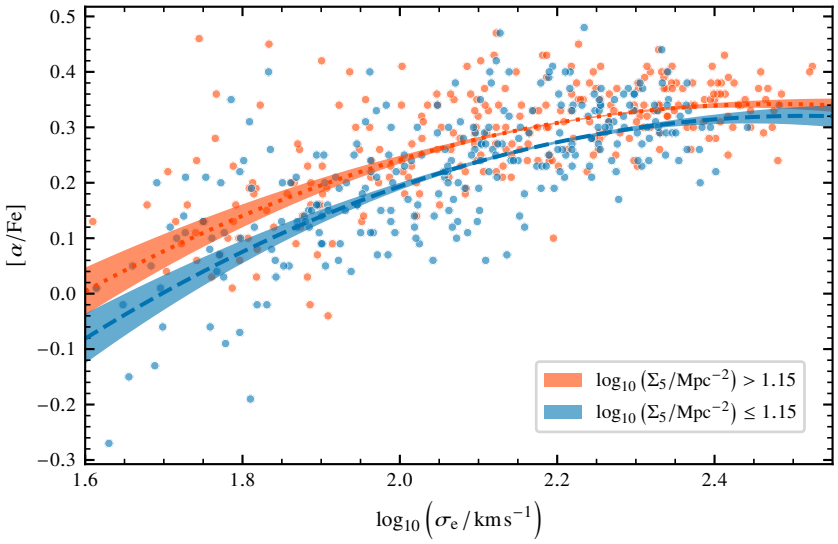


Figure 3.10: For each environmental subsample of elliptical galaxies, we fit a parabolic relationship of the form $[\alpha/\mathrm{Fe}] = a\ \log_{10}^2\left(\sigma_\mathrm{e}/\mathrm{km\,s^{-1}}\right) + b\log_{10}\left(\sigma_\mathrm{e}/\mathrm{km\,s^{-1}}\right) + c$, with further details given in the main text.

6, or equivalently to a posterior odds ratio of 20:1 (analogous to the conventional $p = 0.05$ significance level, for which p is the probability of obtaining a result if the null hypothesis is correct). Our values instead correspond to posterior odds ratios of 105:1 and 284:1 in favour of the parabolic model, when applied to elliptical galaxies in LDEs and HDEs respectively.

We interpret this as strong support for a flattening of the $[\alpha/\mathrm{Fe}]$-σ_e relationship towards high velocity dispersions in elliptical galaxies. We find no such support for other morphological classifications. Although the offset is now greater than 0.03 dex even at high σ_e, we stress that the choice of a linear or parabolic function does not affect our conclusions regarding offsets in α-enhancement at low velocity dispersions. This is an area which would benefit substantially from further study.

3.3 Discussion

3.3.1 Comparisons to Previous Studies

The multitude of methods of calculating the values of simple stellar population (SSP)-equivalent age, metallicity and α-abundance complicates any comparisons of absolute values across different studies. Small changes in the method, such as a different set of stellar population models, or the procedure for removing emission lines, can cascade into larger systematic offsets in the final results. Hence, we only consider here the relative trends and scaling relations.

One of the most obvious comparisons is to Scott et al., 2017 (hereinafter S17), since we are both working with galaxies drawn from the SAMI Galaxy Survey and using a similar method to determine the stellar populations (a full comparison of the measurements themselves is contained in Section 3.1.3). However, where S17 predominantly consider the SSP-equivalent parameters as a function of mass, we instead use σ_e throughout this chapter, limiting direct comparisons. We do not explicitly compare morphological types agnostic of environment, but our results in Fig. 3.9 would indicate that we find a similar offset in [α/Fe] ranging from E to Sc galaxies, of the order of 0.066 ± 0.011 dex in LDEs, and 0.093 ± 0.021 dex in HDEs. In contrast to S17, we find the morphology dependence occurring predominantly at low σ_e, and similarly for our environmental dependence, which we estimate at ≈ 0.06 dex, for galaxies with $\log_{10}\left(\sigma_e/\mathrm{km\,s^{-1}}\right) < 2$. This may simply be a function of our distinct sample selection. We have simultaneously separated the dependence on morphology and environment, using a sample of over 2000 galaxies, an option which was not available to S17 at the time as the SAMI survey was still in progress.

Another study using the SAMI survey is that of Pak et al., 2021, which investigated passive spirals, using S0 galaxies as a control sample. We reach markedly different conclusions for the S0 group; where we find a divergence in [α/Fe] at low σ_e, Pak

et al. found an offset occurring predominantly at $\sigma_e \gtrsim 100\,\mathrm{km\,s^{-1}}$. We note that Pak et al., 2021 retained field galaxies with the highest recession velocities, which we show in Section 2.3.2 to have an offset in $[\alpha/\mathrm{Fe}]$ caused by sky line contamination, and believe to be anomalous. Since these are also high-velocity dispersion galaxies, we are confident that this hypothesis accounts for the erroneous conclusions.

Comparing to the ETG sample of McDermid et al., 2015, our results in Fig. 3.8 are in excellent agreement. For the derived best-fitting relations, we find both the gradients and intercepts are consistent within the stated errors. Similarly, we fit our ETG sample to a single relationship, and separate the residuals $\Delta\,[\alpha/\mathrm{Fe}]$ by environmental density. Performing a Kolmogorov-Smirnov test on these residuals, our results also show a very high probability of the HDE and LDE samples being drawn from distinct parent distributions, in good agreement with McDermid et al., 2015. Both our samples cover a consistent range in velocity dispersion, $\log_{10}\left(\sigma_e/\mathrm{km\,s^{-1}}\right) < 2.5$, and importantly both show the divergence between environmental classifications increasing towards low σ_e, an important result in our analysis.

3.3.2 Physical Implications

In agreement with previous studies, we reproduce the well-known linear relationship between $[\alpha/\mathrm{Fe}]$ and $\log_{10}\left(\sigma_e/\mathrm{km\,s^{-1}}\right)$, which is often taken to mean that star formation in massive galaxies was quenched relatively faster than in less massive galaxies. However, we have also found substantial evidence to suggest that the $[\alpha/\mathrm{Fe}]$ ratio has a strong dependence on the local environmental density. Consistent with the observations of Hirschmann et al., 2014, where the quiescent fraction increases with local environmental density, Fig. 3.8 shows that on average, ETGs in HDEs are α-enhanced over their counterparts in LDEs. Controlling for the correlation with stellar velocity dispersion, this appears to manifest itself primarily at low σ_e, and we stress that this simple division does not appear to extend to the high σ_e regime. From

our own analysis, we infer that the integrated star-formation timescales cannot differ substantially between high-σ_e galaxies across varied environments and morphologies, limiting the formation pathways.

This interpretation appears to support the work of Peng et al., 2010 (hereinafter P10), who found strong evidence for the environment and galaxy mass being independently associated with two distinct quenching processes. Their work divided galaxies into "red passive" and "blue star forming", using the fraction of red galaxies as an indicator of the quenched fraction at a given environmental density and stellar mass. Throughout this chapter, we have interpreted galaxies with the highest values of [α/Fe] as having a rapidly-quenched burst of star formation, and those with solar to sub-solar α-enhancement as having ongoing, or an extended duration of star formation. Hence, although [α/Fe] is not directly linked to the red fraction f_{red} used by P10, we consider it a useful comparison.

We show in Fig. 3.11 the distribution of [α/Fe] in the σ_e-Σ_5 plane. Although the raw data shows a considerable degree of scatter, the locally-smoothed values display a similar symmetry to the red fraction plotted in Fig. 6 of P10, with a line of constant [α/Fe] stretching from medium-σ_e galaxies in LDEs, to low-σ_e galaxies in HDEs. Assuming that [α/Fe] is directly related to the quenching timescale in some manner, this simple symmetry appears to support the independence of both the mass and environmental quenching mechanisms.

We also consider the implications of Fig. 15 in P10, which suggests that the dominant quenching mechanism at low redshift depends on the stellar mass of the galaxy. In particular, environmental quenching is predicted to be dominant for low-mass galaxies. This seems to be consistent with our results, wherein the α-enhancement of low-σ_e galaxies appears to be strongly influenced by the local environmental number surface density, whereas only a faint imprint exists for galaxies at high-σ_e. Further support for the mass dependence of the dominant quenching mechanism comes

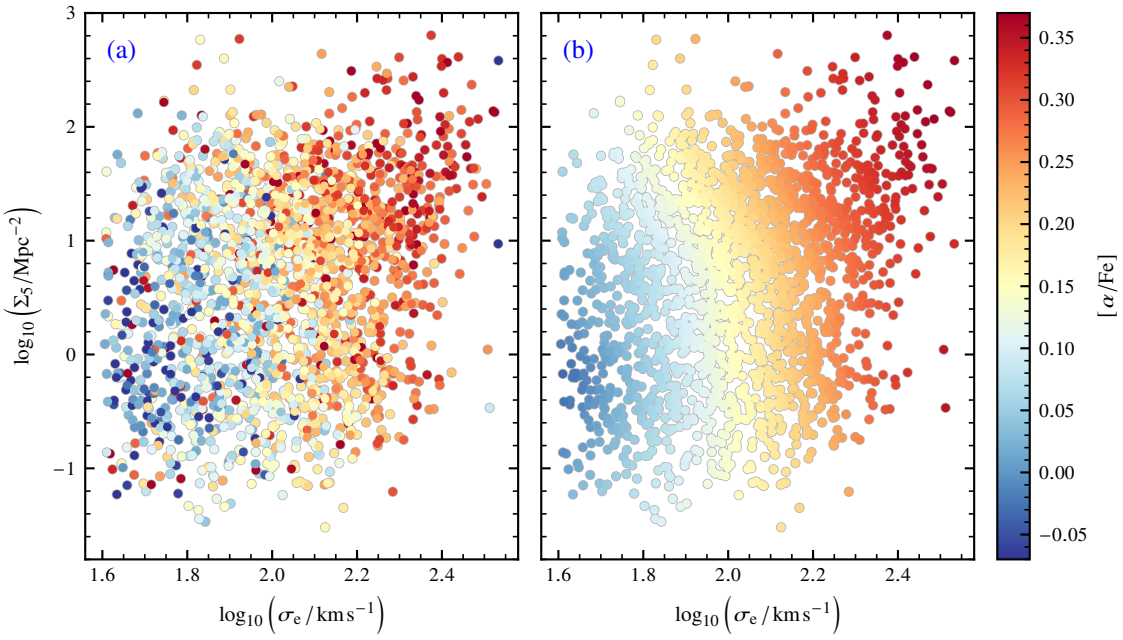


Figure 3.11: The distribution of galaxies in σ_e-Σ_5 space. In (a), galaxies are coloured by their associated measurements of [α/Fe]. In (b), we show the same plot, but we use a locally-smoothed value of [α/Fe], determined using the locally-weighted regression technique (LOESS) of Cappellari et al., 2013. An underlying symmetry is clearly visible in this plane, with high-σ galaxies in HDEs having the highest average values of [α/Fe].

from considering the parabolic relationship in Fig. 3.10. At $\log_{10}\left(\sigma_\mathrm{e}/\mathrm{km\,s}^{-1}\right) = 1.8$, there is an enhancement of 0.07 dex in [α/Fe], which falls to just over half that at $\log_{10}\left(\sigma_\mathrm{e}/\mathrm{km\,s}^{-1}\right) = 2.4$. Thus, whilst all elliptical galaxies show the imprint of environmental quenching, it is still more pronounced at low velocity dispersion. We suggest that our results also align with the naïve expectation, that the shallower potentials in low-σ_e galaxies may make them more susceptible to environmental disruption.

Separately, we consider the flattening observed at high velocity dispersions. The well-known mass-metallicity relation (Lequeux et al., 1979) is also found to flatten towards higher stellar masses ($\log_{10}\left(M_*/\mathrm{M}_\odot\right) > 10.5$), and we suggest that this may have some correlation with the effect that we have observed. This effect appears to be independent of environment, although strongly related to morphology. Further

research in this area is clearly needed, to confirm that the observed flattening is a physical effect rather than an artefact of the SSP models or our sample selection, and to discern the extent to which it depends on morphological type rather than velocity dispersion or stellar mass.

We estimate the effect of the low-σ_e α-enhancement using the empirical relationship from de La Rosa et al., 2011 (hereinafter dLR11), which relates [α/Fe] to the half-mass time $T_{M/2}$, the time interval over which half of the total stellar mass is formed. These were obtained by utilising full-spectrum fitting in a sample of elliptical galaxies to determine non-parametric star-formation histories, and comparing to the abundance ratios derived from line indices, using the same models as we have in this paper (Thomas et al., 2011). One of these formulae considers the half-mass formation time ($T_{M/2}$) as a function of α-abundance,

$$T_{M/2}(\mathrm{Gyr}) = -15.3[\alpha/\mathrm{Fe}] + 5.2. \tag{3.6}$$

For elliptical galaxies, the measurements of [α/Fe] in Table 3.3 would imply $T_{M/2} = (1.86 \pm 0.17)$ Gyr for galaxies in HDEs, compared to $T_{M/2} = (2.75 \pm 0.14)$ Gyr for those in LDEs – or equivalently, the α-enhancement of 0.058 dex leads to an estimated $\Delta T_{M/2} = (0.9 \pm 0.2)$ Gyr. Similarly, we also use dLR11 to estimate the stellar mass fraction contributed by stars older than 10 Gyr, denoted as f_{old}. For low-σ_e ellipticals, we find $f_{old} = (56.8 \pm 1.3)\%$ for those in LDEs, and $f_{old} = (64.7 \pm 1.5)\%$ in HDEs. There appears to be a strong residual dependence on morphological type here as well, with the environmental offsets greatest in ellipticals, and statistically insignificant in Sc/Irr galaxies. We hypothesise that this may be due in part to the effects of ongoing star formation, since a clear picture of the star-formation timescale would be obscured by any more recent starbursts.

3.4 Conclusions

Using the method detailed in Chapter 2, we have made a new set of measurements of [α/Fe] for all galaxies in the SAMI Galaxy Survey. These are an improvement over previous studies, primarily by utilising the variance-weighted method of C01 to measure the underlying Lick/IDS indices. Based on our subsequent analysis we make the following observations, with novel results highlighted in bold:

1. Separating galaxies by their K-corrected $(g-i)$ colour, we find **red sequence galaxies are consistently α-enhanced over those in the blue cloud**, at fixed velocity dispersion σ_e. The relationship for red sequence galaxies can be described by the equation

$$[\alpha/\mathrm{Fe}] = (0.342 \pm 0.011)\log_{10}\left(\sigma_e/\mathrm{km\,s^{-1}}\right) - (0.50 \pm 0.02).$$

2. Taking the residuals $\Delta\,[\alpha/\mathrm{Fe}]$ from a linear relationship with σ_e, and investigating the variation with the local number surface density, Σ_5, we find a **weak correlation for red sequence galaxies**,

$$\Delta\,[\alpha/\mathrm{Fe}] = (0.021 \pm 0.003)\log_{10}\left(\Sigma_5/\mathrm{Mpc^{-2}}\right) - (0.009 \pm 0.003). \tag{3.7}$$

   In contrast, **no such correlation exists for blue cloud galaxies**.

3. At low velocity dispersion, $\sigma_e < 100\,\mathrm{km\,s^{-1}}$, and controlling for morphological type, we find that galaxies in high-density environments ($\log_{10}\left(\Sigma_5/\mathrm{Mpc^{-2}}\right) > 1.15$) are α-enhanced by up to ≈ 0.07 dex compared to their counterparts in low-density environments ($\log_{10}\left(\Sigma_5/\mathrm{Mpc^{-2}}\right) \leq 1.15$).

4. **This enhancement includes a strong morphological dependence**, with the offset increasing from 0.025 ± 0.010 dex in spirals to 0.058 ± 0.014 dex in

ellipticals. Using the models of de La Rosa et al., 2011, we estimate the inferred reduction in half-mass formation time for ellipticals as $\Delta T_{\mathrm{M}/2} = 0.88 \pm 0.22\,\mathrm{Gyr}$.

5. **Controlling for the environment, we find some indication of an additional morphological dependence**. Considering galaxies in high-density environments at $\log_{10}\left(\Sigma_5/\mathrm{Mpc}^{-2}\right) = 1.6$, we expect ellipticals to be α-enhanced by 0.09 dex over S0s, and by 0.13 dex over Sa/b galaxies. The evidence for this is weaker than the environmental effect, and would benefit greatly from further study.

6. **There is evidence to suggest a flattening of the $[\alpha/\mathrm{Fe}]$-σ_e relation at high velocity dispersions in elliptical galaxies. This flattening exists independently of the environment. However, we find no support for such a relationship for later morphological types.**

Chapter 4

The Dependence of Global Stellar Populations on Kinematic Morphology

In this chapter, we explore the variations in the [α/Fe]-$\sigma_{\rm e}$ relation for a sample of galaxies drawn from the Sydney-Australian-Astronomical-Observatory Multi-object Integral-field Spectrograph (SAMI) Galaxy Survey, focussing on residual correlations with the spin parameter proxy, $\lambda_{R_{\rm e}}$. The results presented in this chapter were previously published in Watson et al., 2022b.

4.1 Sample Selection

Our underlying sample is the same used in Chapter 3. This contains galaxies drawn from the third public data release (DR3) of the SAMI Galaxy Survey (Croom et al., 2021), itself containing 3068 unique galaxies. For each galaxy, we estimate the equivalent simple stellar population (SSP) age, metallicity [Z/H], and relative α-element abundance [α/Fe] from the $R_{\rm e,MGE}$ aperture spectrum, using the method detailed in Chapter 2.

4.1.1 Quality Cuts

As in Chapter 3, we make a series of quality cuts to the full sample of 3068 galaxies. Having established that galaxies at redshifts $z > 0.0732$ show strong signs of sky line contamination in Section 2.3.2, affecting our measurements of [α/Fe], we remove these galaxies from consideration. This leaves a redshift-limited sample of 2776 galaxies, which we use as our reference for sample completeness.

We apply the recommended quality cuts from van de Sande et al., 2017b to the kinematic measurements. These include Q_1, which requires the mean line-of-sight velocity v to have a maximum uncertainty $v_{\rm error} < 30\,{\rm km\,s^{-1}}$, and Q_2, that the uncertainty on the velocity dispersion σ follows $\sigma_{\rm error} < 0.1\sigma + 25\,{\rm km\,s^{-1}}$. Whilst we also require that a measurement of the spin proxy $\lambda_{R_{\rm e}}$ exists, we do not place any further constraints on this (see Section 1.3.3.5 for more details). The cumulative effect of these constraints reduces the sample size to 1408 galaxies. We also apply similar quality cuts to our measurements as in Section 3.1.1, removing seven galaxies with a spectral signal/noise ratio (S/N) $< 20\,{\rm pix^{-1}}$. We reject a further 14 galaxies which either fall on the outer limits of the parameter space in [α/Fe], or have 1σ uncertainties spanning the entire model grid. Compared to Section 3.1.1, we introduce a more stringent requirement on velocity dispersion, rejecting all galaxies with $\sigma_{\rm e} < 56\,{\rm km\,s^{-1}}$.

4.1.2 Completeness

After applying these quality cuts to the initial redshift-limited sample, a total of 1317 galaxies remain. We refer to this as the "kinematic sample", with the distribution shown in Fig. 4.1. We measure the sample completeness against the 2776 galaxies with $z \leq 0.0732$. By construction, the final sample is $> 50\%$ complete throughout the chosen range of velocity dispersion, and $> 80\%$ complete for $\sigma > 70\,{\rm km\,s^{-1}}$. Conversely, the sample only achieves a completeness of $\geq 50\%$ for $-21 < M_r <$

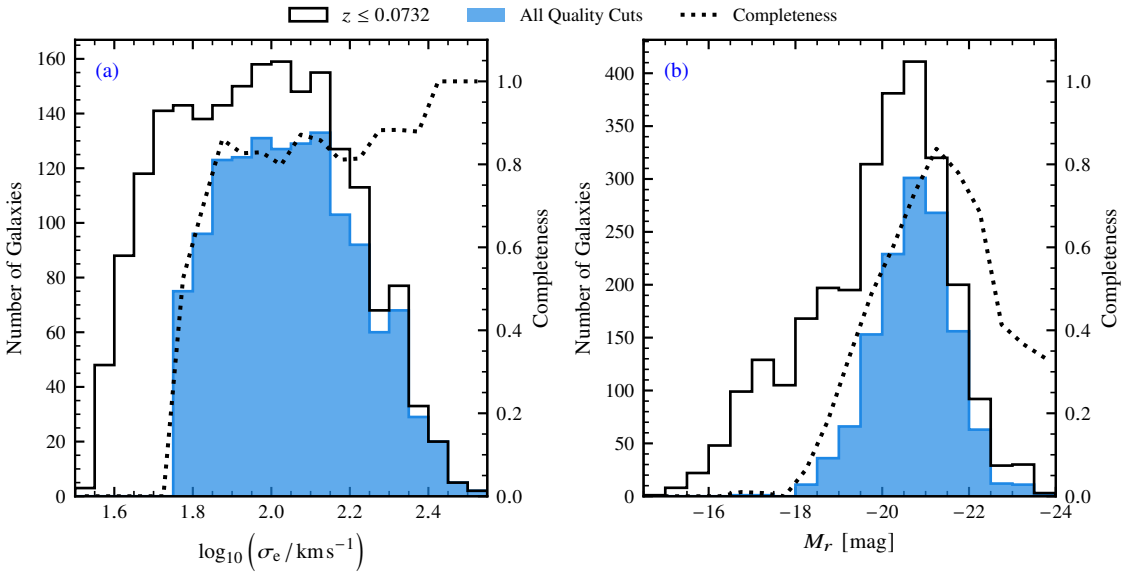


Figure 4.1: The distribution of our kinematic sample as a function of effective velocity dispersion σ_e, and absolute magnitude in the r-band M_r. The dotted lines indicate the completeness of this sample, relative to the number of unique galaxies with $z \leq 0.0732$.

-19, with a significant number of galaxies removed at all luminosities. Many of the brightest galaxies are removed as these also typically have the largest on-sky areas, and hence are not fully covered by the SAMI integral-field unit (IFU) bundles. For some fraction of these, it is thus not possible to a derive an accurate aperture correction for λ_{R_e} (see van de Sande et al., 2021a for more details).

Comparing against the sample of 2097 galaxies used in Chapter 3, we have cut a substantially higher number of galaxies at low velocity dispersions, due to the additional constraints from both van de Sande et al., 2017b and our own selection criteria. The number of galaxies of each morphological type are summarised in Table 4.1, where we can see the effect of the quality cuts on the sample morphology distribution. Galaxies classified as Sc are largely removed from the sample, because they typically have $\log_{10}\left(\sigma_e/\mathrm{km\,s^{-1}}\right) < 1.75$.

Sample	Total	Optical Morphology					Section
		E	S0	Sa/b	Sc	Unclassified	
$z \leq 0.0732$	2776	462	630	544	1002	138	2.3.2
Kinematic Sample	1317	293	470	394	135	25	4.1.3
Star-forming	692	68	165	322	129	8	4.2.3
Quenched	625	225	305	72	6	17	4.2.3
		Kinematic Morphology					
		SR	I	II	III	IV	
Kinematic Sample	1317	91	202	279	391	345	4.1.3
Star-forming	692	21	82	88	220	276	4.2.3
Quenched	625	70	120	191	171	69	4.2.3

Table 4.1: The samples of galaxies used in this chapter, separated by both optical and kinematic morphology. Intermediate classifications have been grouped with the earlier of the two types, *e.g.* E/S0 galaxies contribute to the total under the E column. The selection criteria for the kinematic classifications can be found in Section 4.1.3.

4.1.3 Kinematic Classification

We begin by separating out the slow rotators (SRs), using the selection criteria from van de Sande et al., 2021a, which have been optimised for use with galaxies observed as part of the SAMI survey, accounting for the observed area and atmospheric seeing. With these criteria, galaxies are classified as SRs if they lie in the region of the λ_{R_e}-ellipticity plane delineated by

$$\begin{aligned} \lambda_{R_e} &< \lambda_{R_{start}} + \epsilon_e/4, \\ 8\epsilon_e &< 0.35 + \frac{\lambda_{R_{start}}}{1.538}, \end{aligned} \tag{4.1}$$

where $\lambda_{R_{start}} = 0.12$. We show this in Fig. 4.2a, noting that our results do not substantially change if we use instead the more generic selection criteria of Cappellari, 2016. We remove from our analysis nine galaxies identified as SRs by these criteria,

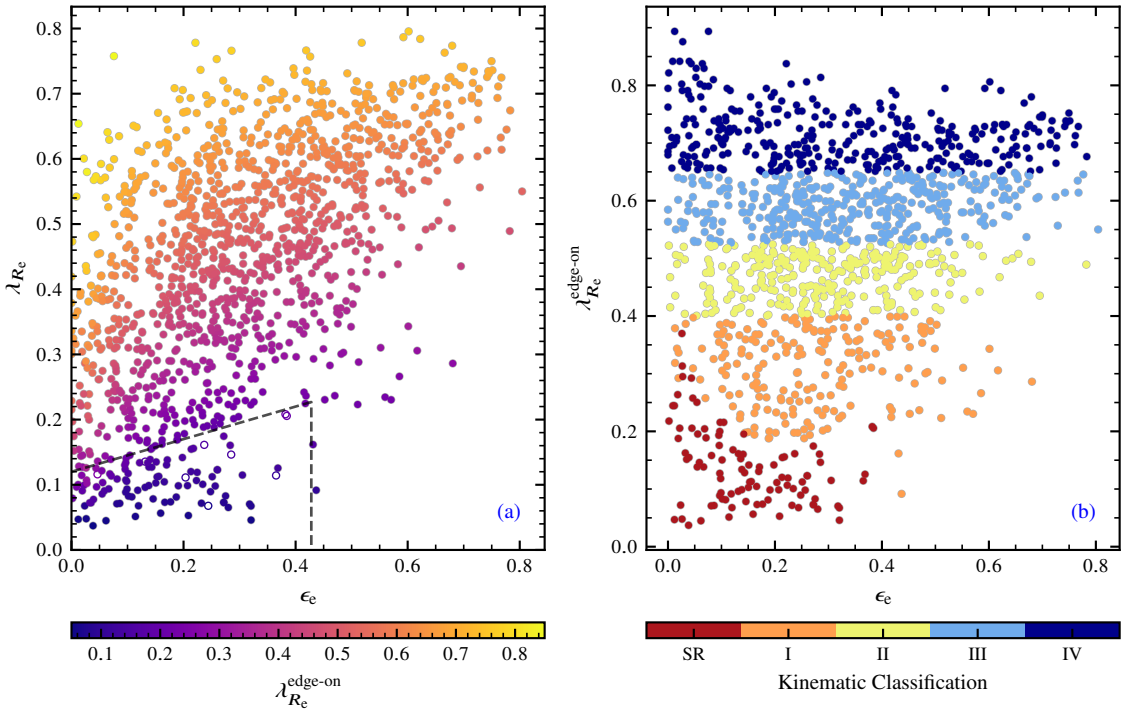


Figure 4.2: (a) The distribution of the kinematic sample in the observed spin proxy (λ_{R_e})-ellipticity (ϵ_e) plane. Galaxies are coloured according to their derived values for the intrinsic spin proxy, $\lambda_{R_e}^{edge-on}$. The dashed lines delineate the slow rotator (SR) classification from van de Sande et al., 2021a. Open circles represent nominal SRs which were revealed to be face-on spirals in a visual inspection, and as such are not included in our analysis. (b) The division of fast rotators into four kinematic classifications, based on their values of $\lambda_{R_e}^{eo}$ (see the text for more details).

but which are revealed to be face-on spirals by a visual inspection (MTYPE$\geq$2). This orientation accounts for the low observed spin and ellipticity. The remaining galaxies are typically classified as fast rotators (FRs). For our analysis, rather than treating the FRs as a monolithic block, we further subdivide them into four separate groups, sorted by the intrinsic λ_{R_e}, $\lambda_{R_e}^{edge-on}$, and denoted by Region I-IV as follows:

- Region I: $\lambda_{R_e}^{eo} \leq 0.4$
- Region II: $0.4 < \lambda_{R_e}^{eo} \leq 0.525$
- Region III: $0.525 < \lambda_{R_e}^{eo} \leq 0.65$
- Region IV: $0.65 < \lambda_{R_e}^{eo}$

These criteria were chosen such that a similar range of $\lambda_{R_e}^{eo}$ was surveyed in each group, with a full decomposition of the kinematic sample available in Table 4.1, and the distribution displayed in Fig. 4.2b alongside the SRs.

4.2 Results

4.2.1 Global Relations

Using the method outlined in Section 3.1.4, we fit a weighted linear relationship between $[\alpha/\mathrm{Fe}]$ and $\log_{10}\left(\sigma_e/\mathrm{km\,s^{-1}}\right)$ to all 1317 galaxies in our final kinematic sample, resulting in

$$[\alpha/\mathrm{Fe}] = (0.388 \pm 0.011)\log_{10}\left(\sigma_e/\mathrm{km\,s^{-1}}\right) - (0.61 \pm 0.02). \tag{4.2}$$

We show this result and the distribution in Fig. 4.3a, alongside the residuals $\Delta\,[\alpha/\mathrm{Fe}]$ as a function of σ_e in Fig. 4.3b. Considering the overall distribution of the residuals, it is clear that the scatter in the relation decreases with increasing galaxy velocity dispersion. We attribute this to the positive correlation between σ_e and S/N observed previously in Fig. 3.1. Aside from this, there is no underlying structure evident, and the residuals are evenly distributed around zero, as we would expect from minimisation of the χ^2 statistic in Eq. 2.17.

Throughout Fig. 4.3, galaxies are coloured according to their measurements of the inclination-corrected spin proxy $\lambda_{R_e}^{eo}$, using the region classification scheme from Section 4.1.3. From this, we can see that there is a clear dependence on $\lambda_{R_e}^{eo}$ in the residuals in Fig. 4.3b, with Region III and IV galaxies predominantly having $\Delta\,[\alpha/\mathrm{Fe}] \lessapprox 0$. Conversely, albeit less pronounced, Region I galaxies appear to be distributed towards higher values of $\Delta\,[\alpha/\mathrm{Fe}]$. Therefore, if we instead present the residuals $\Delta\,[\alpha/\mathrm{Fe}]$ as a function of $\lambda_{R_e}^{eo}$, as in Fig. 4.3c, we find a statistically-significant

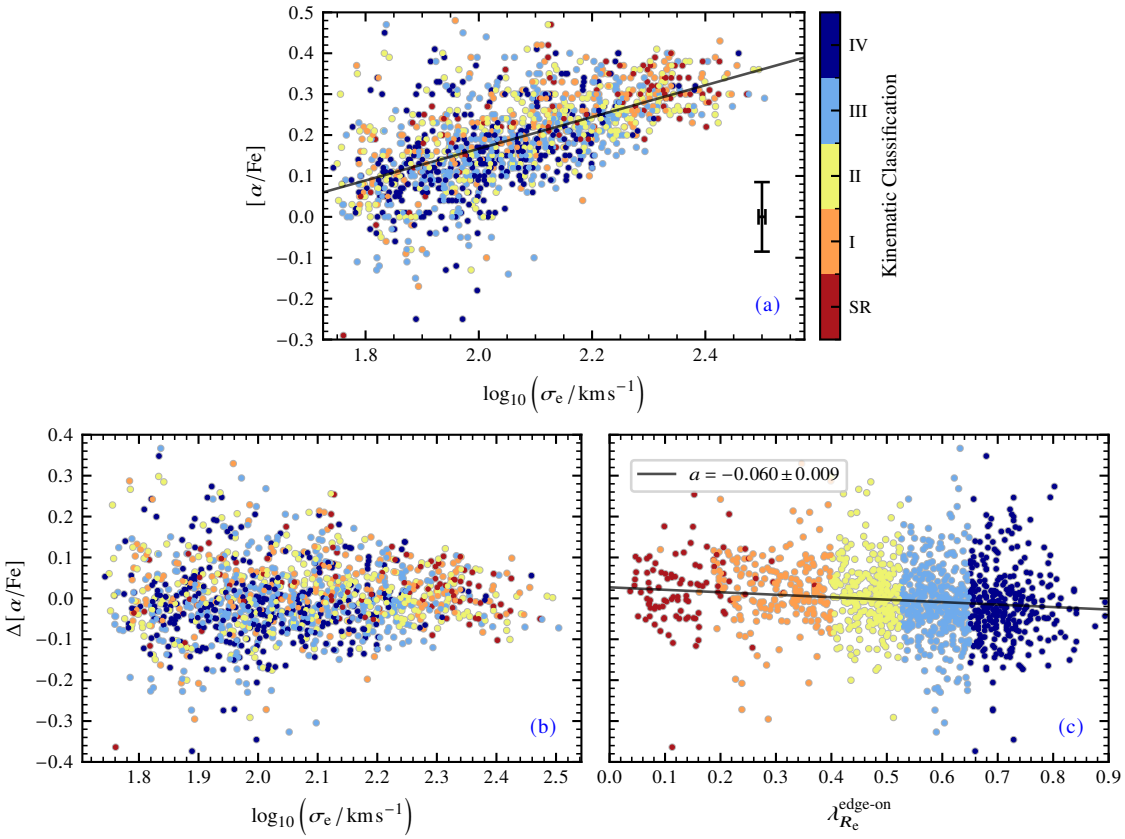


Figure 4.3: (a) The σ_e-[α/Fe] relation for our kinematic sample, with the best-fitting linear relation represented by the dashed line. (b) The residuals Δ [α/Fe], as a function of $\log_{10}\left(\sigma_e/\mathrm{km\,s^{-1}}\right)$. There is no correlation, as expected, although the scatter increases at lower values of σ_e due to the decrease in S/N. (c) The residuals as a function of $\lambda^{eo}_{R_e}$. The best-fitting relation is shown as the dashed line, with the gradient a inset. Galaxies are coloured according to their $\lambda^{eo}_{R_e}$ values, using the region classification scheme from Table 3.1, with slow rotators (SRs) marked in red, and Region IV galaxies in dark blue. The colour scheme is consistent across all three plots.

anti-correlation. Fitting a linear trendline to this gives the result

$$\Delta\,[\alpha/\mathrm{Fe}] = (-0.060 \pm 0.009)\lambda^{eo}_{R_e} + (0.027 \pm 0.004). \tag{4.3}$$

The scatter around this relationship increases slightly towards higher values of $\lambda^{eo}_{R_e}$, although this is not as pronounced as the effect seen in Fig. 4.3b. We caution that using the projected measurements of λ_{R_e} rather than the inclination-corrected values

of $\lambda^{\rm eo}_{R_{\rm e}}$ leads to a derived gradient $\approx 50\%$ steeper than in Eq. 4.3. As shown in Fig. 4.2a, this is merely the expected outcome of applying the correction. Whilst the correction shifts all galaxies to higher $\lambda^{\rm eo}_{R_{\rm e}}$, high-$\lambda_{R_{\rm e}}$ galaxies are shifted more than low-$\lambda_{R_{\rm e}}$ galaxies, so all correlations will appear shallower.

4.2.2 Slow Rotators

We consider the effect of including SRs in this relationship, as they are kinematically distinct from the FRs in the remainder of the sample. We begin by a comparison against galaxies denoted as "Region I", as discussed in Section 4.1.3, as these ought to be the closest physical match, with very low levels of rotational support. In Fig. 4.4, we display the distribution of several structural parameters for each group, such as the physical effective radius $R_{\rm e}$, the stellar mass $\log_{10}(M_*/{\rm M}_\odot)$, and the ellipticity within $1R_{\rm e}$, $\epsilon_{\rm e}$. The medians for each sample are tabulated in Table 4.2. Whilst there is considerable overlap in these parameters, SRs are slightly larger and more massive than Region I galaxies, but significantly rounder, with the median ellipticity differing by a factor of two between the two groups. By construction, the distributions of $\lambda^{\rm eo}_{R_{\rm e}}$ are clearly distinct, emphasising the physical differences between the samples.

The differing distributions of galaxy stellar mass complicates the comparison of $[\alpha/{\rm Fe}]$ across the two groups. Since we know *a priori* that galaxies with higher stellar mass, or velocity dispersion, have a higher α-enhancement on average, we expect the median $[\alpha/{\rm Fe}]$ of the SRs to be higher (see Sections 1.2.1). The measured difference of 0.05 dex, whilst significant, is therefore not unexpected. To make a fair comparison, we instead look at the distribution of the residuals $\Delta\,[\alpha/{\rm Fe}]$, from the global $[\alpha/{\rm Fe}]$-$\sigma_{\rm e}$ relation displayed in Fig. 4.3a. These distributions are shown in Fig. 4.4 for SRs and Region I galaxies, and the medians for all subsamples are given in Table 4.2. We notice that despite having a higher $[\alpha/{\rm Fe}]_{\rm med}$, the median $\Delta\,[\alpha/{\rm Fe}]$ for SRs is almost identical to that of Region I galaxies. Thus, in the region of parameter space where the

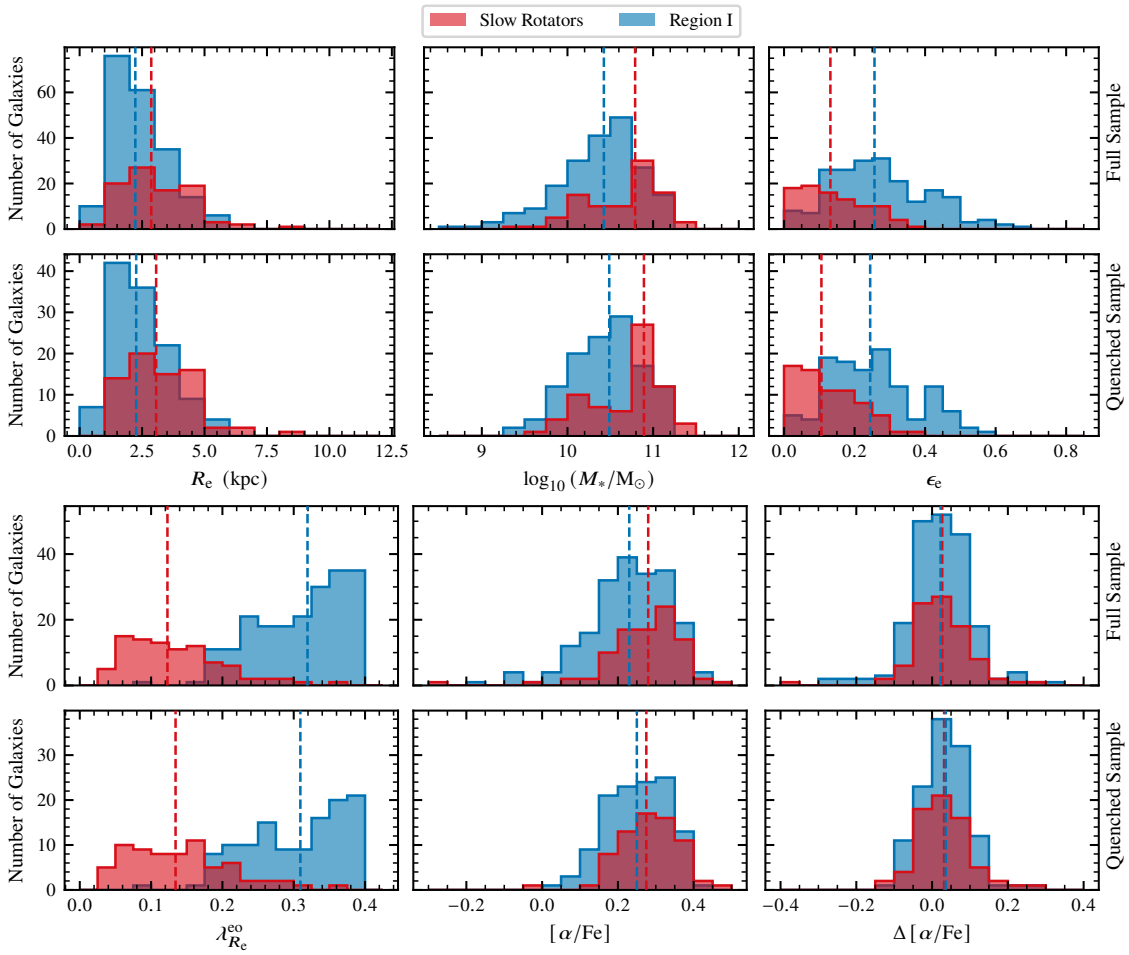


Figure 4.4: A comparison of the distributions of the structural and SSP-equivalent parameters for SRs and galaxies in Region I. The dashed lines indicate the medians of each distribution. On alternate rows, we show the same properties after we have isolated the quenched population (see Section 4.2.3), illustrating that the two populations still show distinct distributions of physical parameters, but no measurable offset in the residual α-enhancement, $\Delta[\alpha/\mathrm{Fe}]$.

distributions of galaxy velocity dispersion σ_e overlap, there is no measurable difference between the $[\alpha/\mathrm{Fe}]$ ratios of SRs and Region I galaxies, in contrast to the relation seen across the fast rotators. We therefore infer that at low $\lambda_{R_e}^{eo}$ ($\lambda_{R_e}^{eo} < 0.4$), any further separation of galaxies by their degree of rotational support, *i.e.* Region I galaxies and slow rotators, has no bearing on the $[\alpha/\mathrm{Fe}]$ ratio (beyond that arising from the correlation with velocity dispersion), and hence the most probable evolutionary pathway of the stellar component.

Sample	Median Value					
	R_e (kpc)	$\log_{10}(M_*/M_\odot)$	ϵ_e	$\lambda^{eo}_{R_e}$	$[\alpha/Fe]$	$\Delta[\alpha/Fe]$
SR	$2.87^{+1.39}_{-1.06}$	$10.8^{+0.3}_{-0.7}$	$0.13^{+0.12}_{-0.09}$	$0.12^{+0.08}_{-0.05}$	$0.28^{+0.08}_{-0.09}$	$0.027^{+0.068}_{-0.071}$
Reg. I	$2.23^{+1.21}_{-0.75}$	$10.4^{+0.4}_{-0.5}$	$0.26^{+0.16}_{-0.12}$	$0.32^{+0.06}_{-0.09}$	$0.23^{+0.10}_{-0.10}$	$0.022^{+0.074}_{-0.064}$
Reg. II	$2.06^{+1.12}_{-0.62}$	$10.4^{+0.4}_{-0.5}$	$0.28^{+0.16}_{-0.14}$	$0.48^{+0.03}_{-0.05}$	$0.22^{+0.08}_{-0.13}$	$0.002^{+0.073}_{-0.064}$
Reg. III	$2.36^{+1.10}_{-0.68}$	$10.4^{+0.4}_{-0.4}$	$0.34^{+0.18}_{-0.16}$	$0.59^{+0.04}_{-0.05}$	$0.19^{+0.10}_{-0.11}$	$-0.017^{+0.078}_{-0.064}$
Reg. IV	$2.76^{+1.67}_{-0.87}$	$10.3^{+0.4}_{-0.2}$	$0.31^{+0.29}_{-0.23}$	$0.71^{+0.05}_{-0.04}$	$0.14^{+0.12}_{-0.08}$	$-0.020^{+0.080}_{-0.077}$

Table 4.2: For each kinematic classification, we present the median values of the structural parameters R_e, $\log_{10}(M_*/M_\odot)$, ϵ_e, and $\lambda^{eo}_{R_e}$, as well as the SSP-equivalent $[\alpha/Fe]$, and the residual $\Delta[\alpha/Fe]$ measured from the global relation shown in Fig. 4.3a. The uncertainties listed are measured from the 16th and 84th percentiles.

We also draw attention to the median values of the measured parameters for galaxies in the other regions, shown in Table 4.2. The distributions for Region I galaxies are generally consistent with galaxies in Regions II-IV, and are distinct from SRs. As we move from $\lambda^{eo}_{R_e}|_{med} \approx 0.3$ to higher values, we find that $\Delta[\alpha/Fe]_{med}$ decreases monotonically. Taken on its own, this would seem to imply a link between the duration of star formation and the angular momentum of galaxies in Regions I-IV.

4.2.3 Relations for the Quenched Sample

To assess this conclusion, we isolate a "quenched" subsample of the galaxies, utilising the measurements of the star-formation rate (SFR) from SAMI DR3 (Croom et al., 2021; see Section 1.3.3.4 for more details). We display all SAMI galaxies in the SFR-M_* plane in Fig. 4.5, where we have colour-coded galaxies by their optical morphological type. We select late-type spirals (Sc+) as being the best tracer of the star-forming main sequence (SFMS), in line with previous works such as Medling et al., 2018. We therefore fit the SFMS as a simple linear relationship to the Sc population, using the same procedure as detailed previously in Section 3.1.4 with an

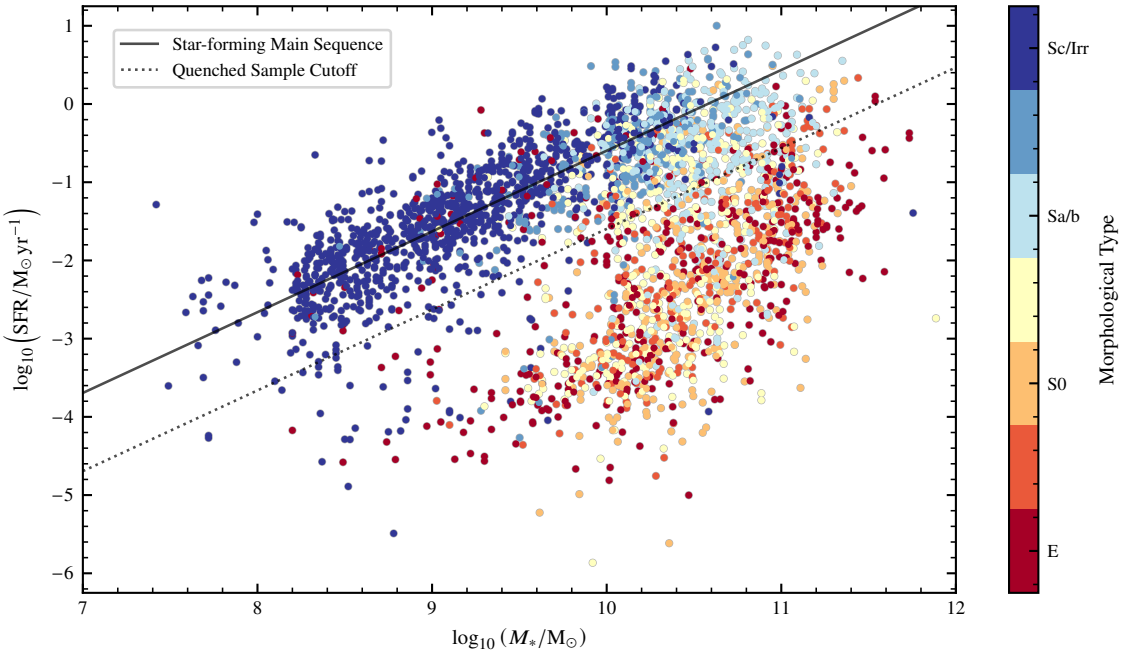


Figure 4.5: The distribution of SAMI galaxies in the SFR-M_* plane. Galaxies are coloured according to their optical morphological type. The SFMS (denoted as the solid black line) is fit only to those galaxies classified as Sc/Irr. The dotted black line shows the 1 dex cutoff in SFR, below which we classify galaxies as quenched.

offset of $\log_{10}(M_*/\mathrm{M}_\odot) = 9.1$, giving

$$\log_{10}\left(\mathrm{SFR}/\mathrm{M}_\odot\,\mathrm{yr}^{-1}\right) = (1.03 \pm 0.03)\log_{10}(M_*/9.1\mathrm{M}_\odot) - (1.52 \pm 0.02). \quad (4.4)$$

From the SFR-M_* plane, we define quenched galaxies as having a SFR more than 1 dex below the SFMS. Despite the somewhat arbitrary nature of this threshold, which is in line with literature values (Renzini et al., 2015; Bluck et al., 2020), we note that the results in this section are robust against a wide range of selection criteria, even using an offset of just 0.5 dex. We apply the 1 dex selection criterion to our previous $\lambda_{R_\mathrm{e}}^{\mathrm{eo}}$-based samples, and note that this substantially reduces the sample size available for all our groups, although the effect is not uniform. Region II now consists of 191 galaxies, whilst Region IV contains just 69 galaxies (previously 279 and 345 galaxies respectively, with the full decomposition available in Table 4.1). Although this limits

our analysis somewhat, it is not unexpected. Galaxies known as "anaemic spirals", with little ongoing star formation but a visual spiral structure, are known to be only a small fraction of late-type spiral galaxies (van den Bergh, 1976).

In light of this, we revisit the comparison of SRs and Region I galaxies established in Section 4.2.2. In Fig. 4.4, we compare both the structural parameters, and the absolute and residual α-enhancements for the quenched subsamples. Although there are small shifts in the distributions, and the sample sizes, the overall conclusions are unchanged. SRs are larger, rounder, and more massive than Region I galaxies, and correspondingly more α-enhanced. As before though, when comparing the residuals $\Delta\,[\alpha/\mathrm{Fe}]$ to account for the difference in the mass distributions, we find no such distinction. In fact, quenched Region I galaxies are enhanced by ≈ 0.01 dex in $\Delta\,[\alpha/\mathrm{Fe}]$ compared to SRs, although we do not consider this significant due to the uncertainties on the measurements. These results appear to be consistent with the unquenched sample, although the sample of unquenched slow rotators is too small to draw any firm conclusions.

Considering all kinematic classifications, we again analyse the residuals from the global $[\alpha/\mathrm{Fe}]$-σ_e relationship in Fig. 4.3a, shown as a function of $\lambda^{\mathrm{eo}}_{R_\mathrm{e}}$ in Fig. 4.6a. In the top panel, we refit a linear relationship to the residuals, with the SRs excluded from the fit, following the discussion in Section 4.2.2. In comparison to Fig. 4.3c, the gradient is $\approx 50\%$ steeper. Due to the reduction in the sample size, the uncertainty on the fit has also increased, and hence the statistical significance of the relationship is exactly as before. We note that reusing the fit from Fig. 4.3a, compared to refitting the $[\alpha/\mathrm{Fe}]$-σ_e relationship without SRs, has no measurable impact when calculating the residuals, and so this can be excluded as a potential source of bias.

In Fig. 4.6b, we consider only the quenched galaxies. Comparing to the correlation using the full sample, it is immediately clear that the statistical significance of the $\Delta\,[\alpha/\mathrm{Fe}]$-$\lambda^{\mathrm{eo}}_{R_\mathrm{e}}$ relation has been substantially reduced. There are two components

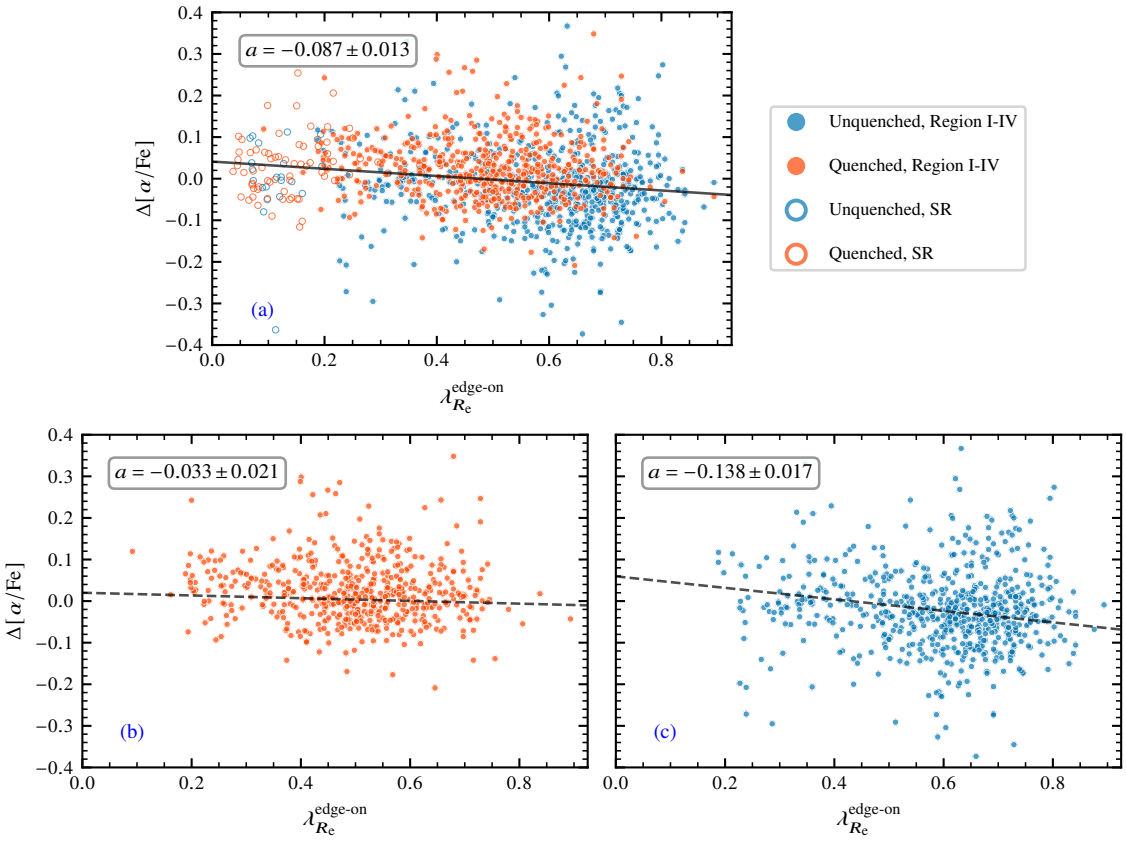


Figure 4.6: (a) The correlation between the residuals $\Delta\,[\alpha/\mathrm{Fe}]$ and $\lambda^{\mathrm{eo}}_{R_\mathrm{e}}$, using the global $[\alpha/\mathrm{Fe}]$-σ_e relation from Fig. 4.3a. The solid line shows the best-fitting linear relation, with the gradient a inset. Following the discussion in Section 4.2.2, slow rotators are not included in the derivation of this relation, but are displayed here as open circles for reference. Galaxies are coloured according to their classification as "quenched" or "unquenched" (see the text for details). (b, c) As above, but the linear trend lines are fitted only to the quenched and unquenched galaxies respectively.

to this. Firstly, the sample size has decreased by approximately a factor of two, from 1317 galaxies to only 625. We therefore expect the uncertainty on our fits to increase, and we note that the ratio of the uncertainties scales with the square root of the sample sizes. Secondly, the removed unquenched galaxies are likely those with ongoing or recent episodes of star formation. As such, we anticipate these galaxies to be substantially less α-enhanced than those in the quenched sample, which would also translate to lower $\Delta\,[\alpha/\mathrm{Fe}]$. By comparing the distribution of galaxies between Fig. 4.6b and Fig. 4.6c, we see that a large proportion of galaxies have been removed

from the high $\lambda^{\rm eo}_{R_{\rm e}}$ regime. The strong gradient for the unquenched galaxies is therefore the clear cause of the flattening of this $\Delta\,[\alpha/{\rm Fe}]$-$\lambda^{\rm eo}_{R_{\rm e}}$ relationship in the quenched sample.

4.3 Discussion

4.3.1 Comparisons to Previous Studies

As previously mentioned in Section 3.3.1, the multitude of methods of calculating the values of age, metallicity and α-abundance complicates any comparisons of absolute values across different studies. Small changes in the method, such as a different set of stellar population models, can cascade into larger systematic offsets in the final results. Hence, we only consider here the relative trends and scaling relations.

There are few studies directly linking the kinematic morphologies to stellar populations. McDermid et al., 2015 (hereinafter M15) briefly considered the difference between regular and non-regular rotators (analogous to our Regions I-IV and slow rotators), and found no significant change in the relative abundance of α-elements. This may be partially caused by the differing sample selection, with the ATLAS3D sample utilised by M15 consisting only of early-type galaxies (ETGs). For reference, we show in Fig. 4.7 the limited distribution of ETGs in the $\lambda^{\rm eo}_{R_{\rm e}}$-$\epsilon_{\rm e}$ plane for the kinematic sample of SAMI galaxies, where we see that the full distribution samples galaxies with both higher $\lambda^{\rm eo}_{R_{\rm e}}$, and higher ellipticities. By focussing on ETGs, M15 would have also been limited to a similar sample as in Fig. 4.6b, considering the morphological mixture shown in Table 4.1. This is only a weak relationship, and as such, it is highly likely that any correlation between $\Delta\,[\alpha/{\rm Fe}]$ and $\lambda_{R_{\rm e}}$ would be drowned out by the scatter in the $[\alpha/{\rm Fe}]$-$\sigma_{\rm e}$ relation, depending on the precise sample selection.

A similar study is Bernardi et al., 2019 (hereinafter B19), which primarily focussed on the radial gradients of galaxies in the Mapping Nearby Galaxies at Apache

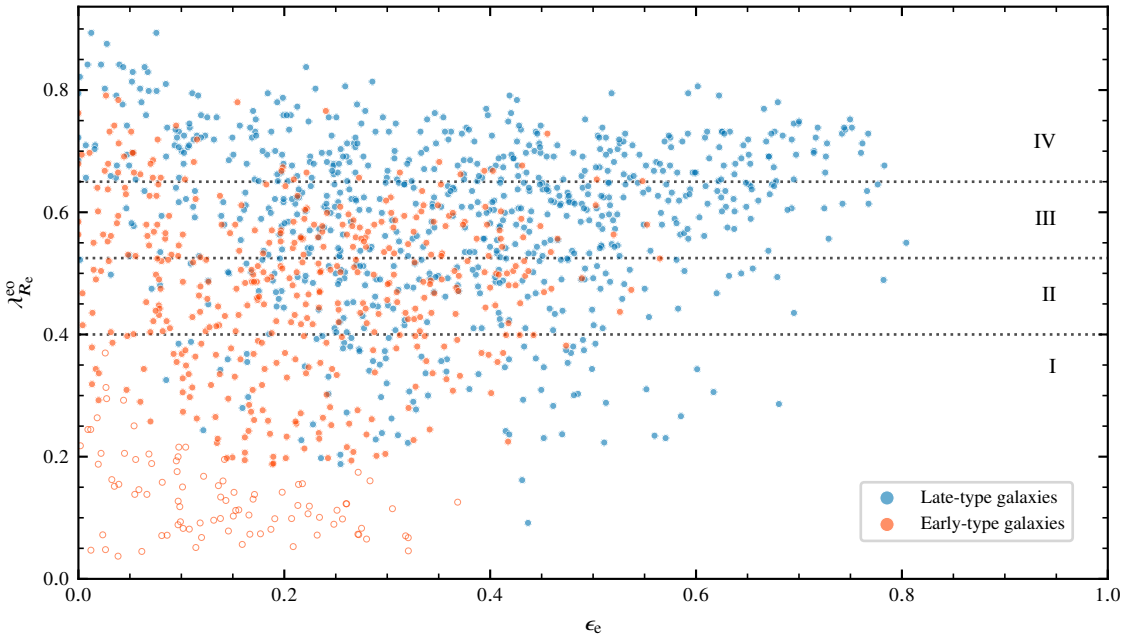


Figure 4.7: The distribution of our kinematic sample in the $\lambda^{eo}_{R_e}$-ϵ_e plane, where we have highlighted visually-classified ETGs in orange. Slow rotators are represented as open circles, whilst all other galaxies are shown as filled markers. The dotted lines show the selection criteria for Regions I-IV (see Section 4.1.3), as indicated on the right.

Point Observatory (MaNGA) survey (Bundy et al., 2015). The sample used by B19 contained almost exclusively ETGs, with the slow rotators separated by means of a simple cut at $\lambda_{R_e} = 0.2$, rather than the selection criteria first defined by Cappellari, 2016 (see Section 4.1.3 for more details). In each bin of size, luminosity, and velocity dispersion, B19 found offsets of approximately 0.01-0.05 dex in [α/Fe] between fast and slow rotators, depending on the galactocentric radius. Whilst the integrated properties within a given radius (as measured in this chapter) are not directly equivalent to those measured at said radius, the [α/Fe] gradients are uniformly shallow, and unlikely to introduce any noticeable bias. The measured offsets are in broad agreement with our own results, although we note that a similar limitation applies to this as to M15, in that results drawn from a binary kinematic classification are strongly dependent on the distribution of galaxies in the λ_{R_e}-ϵ plane.

To the best of our knowledge, no other work to date has sought to disentangle the relationship between the spin parameter proxy λ_{R_e} and the abundance of α elements, whilst simultaneously mitigating the effects of ongoing star formation, and so we cannot make any further comparisons here.

4.3.2 Physical Implications

As in Chapter 3, we reproduce the correlation between [α/Fe] and σ_e, an indicator that star formation ceased relatively faster in more massive galaxies than their low mass counterparts.

Analysing residuals from the [α/Fe]-σ_e relation for the entire sample, we find a statistically significant anti-correlation with the inclination-corrected spin proxy, $\lambda^{eo}_{R_e}$. This indicates that the kinematic structure of a galaxy plays a role in the quenching mechanism, with disc-dominated systems having a longer duration of star formation. This is in good agreement with van de Sande et al., 2018, who found an analogous relationship between the luminosity-weighted stellar age, and (V/σ), the ratio of ordered rotation to random motion, although the different quantities measured mean that our results are not directly comparable.

Considering the wider astronomical context in Section 1.2.3, we suggest that this behaviour is largely consistent with a picture in which classical bulges (CBs) form over considerably shorter periods of time than extended galactic discs (Larson, 1974; Bender et al., 1992). The decrease in the temporal extent of star formation would lead to a relatively higher [α/Fe] in the CB compared to the disc. Considering galaxies at some fixed velocity dispersion, any increase in the bulge-to-disc ratio would correspond to a decrease in the overall rotational support, and hence the measured $\lambda^{eo}_{R_e}$. The relatively larger bulge would produce a greater fraction of the integrated light, and so a global measurement of [α/Fe] would be seen to increase. When taken over a range of velocity dispersion, such a formation scenario would therefore be able

to qualitatively explain the observed anti-correlation between $\lambda^{\mathrm{eo}}_{R_\mathrm{e}}$ and the residuals $\Delta\,[\alpha/\mathrm{Fe}]$ shown in Fig. 4.3.

However, we note that galaxies containing CBs are not likely to account for the majority of our sample. Taking a survey of the local 11 Mpc volume, Fisher et al., 2011 found only $(17 \pm 10)\%$ of galaxies had an observed CB, relative to $(45 \pm 12)\%$ with a pseudo-bulge (PB). This is supported by observational evidence from previous studies using the SAMI Galaxy Survey, with Barsanti et al., 2021 finding 23% of galaxies contained bulges that were older than their discs (probable CBs), and 34% where the bulges were younger (probable PBs). Pseudo-bulges are thought to form out of gas brought to the central regions from the galactic disc, via secular evolution over long timescales (Athanassoula, 2005). In contrast to CBs, which exhibit a wide range of SFRs, PBs are almost universally star-forming (Luo et al., 2020). Integrated over a galaxy, this longer extent of star formation in PBs would suggest a noticeably lower measurement of $[\alpha/\mathrm{Fe}]$ compared to CBs. Since PBs do not have substantially different star-formation histories to their surrounding discs, we do not expect the host galaxies to show any clear relationship between their degree of rotational support, and their α-enhancement.

From Fig. 4.5, we can see that our sample contains a considerable fraction of actively star-forming galaxies. Whilst Luo et al., 2020 demonstrated that CBs themselves have a wide range of SFRs, a large share of their host galaxies are still star-forming, depending on the morphology and environment (Mishra et al., 2019). As such, when investigating the quenched sample, we remove a considerable proportion of galaxies for which we expect $\lambda^{\mathrm{eo}}_{R_\mathrm{e}}$ and $\Delta\,[\alpha/\mathrm{Fe}]$ to be correlated, leading to the relationship displayed in Fig. 4.6b. By comparison, our unquenched sample most probably consists of a mixture of CBs and PBs. Whilst Fig. 4.6c demonstrates a clear anti-correlation between the degree of rotational support and α-enhancement, we suggest that the scatter is largely driven by galaxies hosting PBs.

There is considerable support in existing literature for differing quenching mechanisms as a function of kinematic morphology, such as Smethurst et al., 2015. In particular, for disc-dominated galaxies, which would have high $\lambda^{\rm eo}_{R_{\rm e}}$, Smethurst et al. found that the dominant quenching mechanisms were those taking place over long timescales (*i.e.* quenching timescales $\tau > 2\,$Gyr). These are likely to be secular processes, i.e. those internal to the galaxy, such as bar formation in spiral galaxies funnelling gas towards central PBs (Cheung et al., 2013). By comparison, the dominant mechanisms for smooth galaxies (those with lower $\lambda^{\rm eo}_{R_{\rm e}}$) are those taking place over the shortest time-scales ($\tau < 1\,$Gyr), such as dry major mergers, perhaps in combination with feedback from active galactic nuclei (AGN; Springel et al., 2005). We would expect the relatively longer quenching timescales for disc-dominated systems to lead to a lower α-abundance. However, whilst there is some evidence for this in Section 4.2.3, this is not statistically significant enough for us to draw any firm conclusions. In particular, we cannot conclude whether the observed relationship in Fig. 4.6b is due to morphology-dependent quenching mechanisms, or a weak residual effect from galaxies containing CBs. We suggest that further study with a larger sample size would be very helpful, especially in order to clarify the statistical significance of this relation. Disentangling the relative contribution of bulges to the overall α-enhancement of galaxies requires a spatially-resolved view, and whilst this specific area is out of scope of this thesis, we hope that it will be explored in greater depth in future studies, such as follow-up papers to Barsanti et al., 2021.

Although there is only weak evidence for this $\Delta\,[\alpha/{\rm Fe}]$-$\lambda^{\rm eo}_{R_{\rm e}}$ anti-correlation persisting in the quenched sample, we show in Fig. 4.6c that the relationship in the full sample is largely driven by unquenched galaxies. To estimate the physical implications of this result, we use the empirical formulae of de La Rosa et al., 2011, as in Section 3.3.2 (see Eq. 3.6). Looking at the relationship in Fig. 4.6c, we can therefore

predict how $T_{\mathrm{M}/2}$ varies at some fixed velocity dispersion,

$$\Delta T_{\mathrm{M}/2}\,(\mathrm{Gyr})\Big|_{\mathrm{unquenched}} = (-2.11 \pm 0.26)\Delta\lambda^{\mathrm{eo}}_{R_\mathrm{e}}. \tag{4.5}$$

As an example, considering the median galaxy in each group, we would expect a Region IV galaxy to have a half-mass formation time $\approx 0.8\,\mathrm{Gyr}$ longer than a galaxy in Region I. To put this in context, at a fixed velocity dispersion of $200\,\mathrm{km\,s^{-1}}$, considering the global relationship in Fig. 4.3a, a Region I galaxy would have $T_{\mathrm{M}/2} = 0.64\,\mathrm{Gyr}$, whereas a Region IV galaxy would have $T_{\mathrm{M}/2} = 1.46\,\mathrm{Gyr}$.

4.3.2.1 Similarities Between Slowly-spinning Systems

Turning our attention to the slow rotators (SRs), the offsets in the distributions in Fig. 4.4 support the concept that slow and fast rotators form distinct populations, at least as far as their structural parameters are concerned. However, we find little evidence for such a binary classification in the stellar populations, with the SRs having a residual α-enhancement consistent with Region I galaxies (see Table 4.2). Considering similar population parameters such as the mean stellar age, we note that studies such as van de Sande et al., 2018 have previously shown a smooth variation of stellar populations across the slow/fast rotator boundary. Therefore, the unexpected result here is that the residual α-enhancement appears to level off for $\lambda^{\mathrm{eo}}_{R_\mathrm{e}} < 0.4$. We illustrate this more clearly in Fig. 4.8, where we show the distribution of residuals in the $\lambda^{\mathrm{eo}}_{R_\mathrm{e}}$-$\epsilon_\mathrm{e}$ plane, after local smoothing using the LOESS algorithm (Cappellari et al., 2013). Whilst there is a clear trend towards lower values of $\Delta\,[\alpha/\mathrm{Fe}]$ for $\lambda^{\mathrm{eo}}_{R_\mathrm{e}} > 0.4$, there is no appreciable difference in the residuals below this point as a function of $\lambda^{\mathrm{eo}}_{R_\mathrm{e}}$, either in the smoothed values or the binned raw values.

One hypothesis is that this may be partially due to the difficulty in determining a clean separation between the two groups. van de Sande et al., 2021a expands

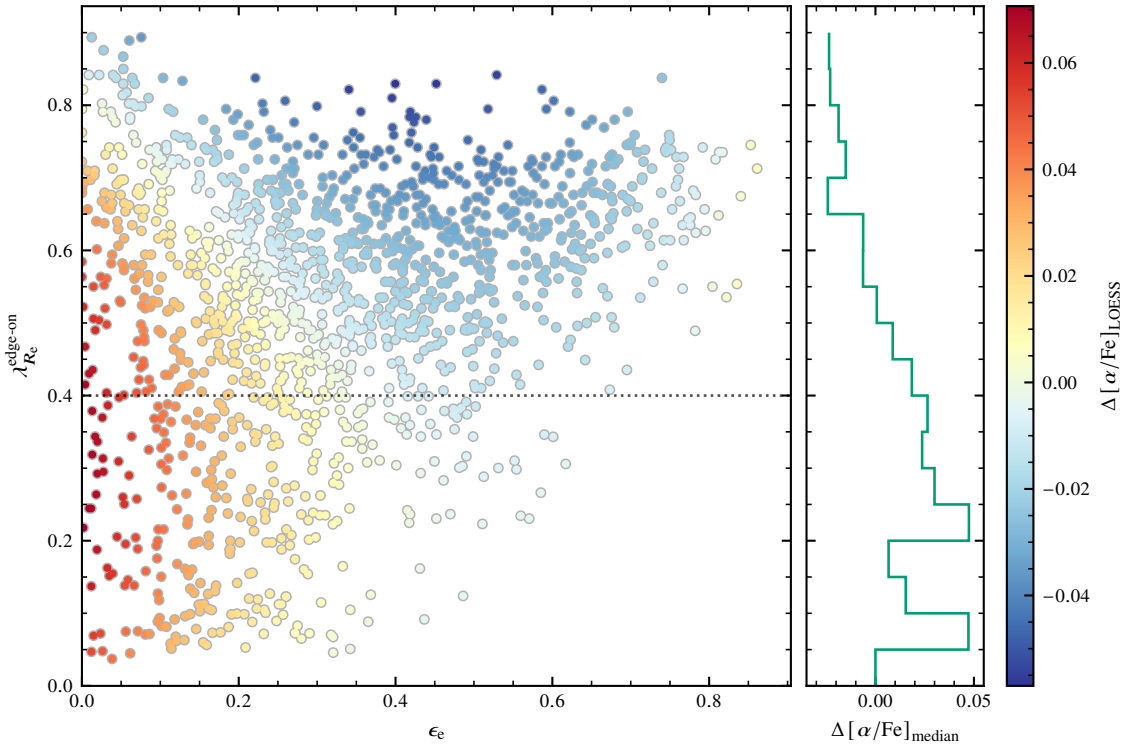


Figure 4.8: The distribution of SAMI galaxies in the $\lambda_{R_e}^{\mathrm{eo}}$-$\epsilon_e$ plane. Galaxies are coloured according to their residual α-enhancement, measured relative to the best-fitting relation displayed in Fig. 4.3a. These values have been smoothed using the locally-weighted regression technique (LOESS) of Cappellari et al., 2013. The dotted line indicates the division between Region I galaxies and more rotationally-supported systems, below which $\Delta\,[\alpha/\mathrm{Fe}]$ shows little variation with $\lambda_{R_e}^{\mathrm{eo}}$. The stepped function in the right panel displays the median $\Delta\,[\alpha/\mathrm{Fe}]$ in bins of 0.05 $\lambda_{R_e}^{\mathrm{eo}}$, as measured from the raw values prior to smoothing.

upon this problem of how to accurately determine distinct kinematic classifications in considerable detail, and although we refer any interested readers there, it is clear that any solution contains a certain degree of compromise. Simplistically, we can see in Fig. 4.2a the density of galaxies in λ_{R_e}-ϵ_e space around the SR cutoff. However, from Fig. 4.3c, we can also see that the distribution of $\Delta\,[\alpha/\mathrm{Fe}]$ is consistent between SRs and Region I across a range of $\lambda_{R_e}^{\mathrm{eo}}$. It is not clear that these distributions can be separated in any substantial way by selection criteria based upon λ_{R_e} and so we reject this selection effect as the driver behind our results.

An additional factor that we consider is that the SAMI sample is known to contain

a non-zero number of galaxies with counter-rotating discs (Rawlings et al., 2020), also referred to as 2σ galaxies. When integrated over a wide enough aperture, these will have a anomalously low measured spin proxy due to the summation of the separate disc components, and may be misidentified as SRs. Although most of these galaxies have $\epsilon > 0.4$, and would be caught by the selection criteria introduced in Cappellari, 2016, a few may still remain in our sample. We visually inspect the resolved kinematic maps (both velocity and velocity dispersion) from SAMI DR3, for all SRs and Region I galaxies. For each subsample, we find two 2σ galaxies, and one with an embedded disc (SR catalogue IDs: 300787, 9388000124, and 536454 respectively; Region I: 178197, 239560, and 492690 respectively). The inclusion or removal of these specific galaxies does not affect our results either way. However, we highlight that this is likely an underestimate of the true number of kinematically-anomalous galaxies, when compared to surveys such as ATLAS3D which found $\approx 11\%$ of SRs contained two counter-rotating discs (Emsellem et al., 2011). Thus, whilst we consider it unlikely to have a substantial effect on our analysis, we cannot rule out that this may influence the exact relationship.

As before for the general anti-correlation described in Fig. 4.3, the similarity between the residual α-enhancement distributions of SRs and Region I galaxies cannot be easily attributed to differing stellar populations across bulge and disc components. Whilst there are bulge-disc decompositions for the SAMI Galaxy Survey, these have been limited so far to subsamples, such as the lenticular cluster sample explored in Barsanti et al., 2021 and the Galaxy and Mass Assembly (Driver et al., 2011, GAMA,) regions in Lah et al. (in prep.), or with stringent quality cuts (Oh et al., 2020). We instead look at the optical morphological classifications of Cortese et al., 2016 (see Section 1.3.3.3 for further details), presented in Fig. 4.9 for SRs and Region I galaxies drawn from our quenched sample. Whilst SRs are heavily bulge-dominated systems, with about two-thirds unambiguously classified as ellipticals, Region I galaxies show

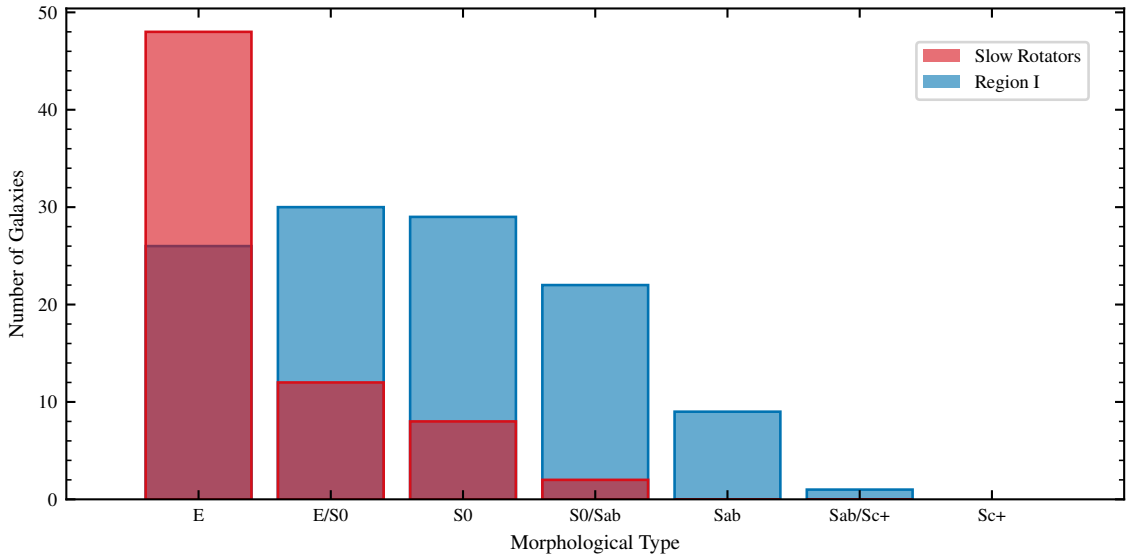


Figure 4.9: The morphological distribution of slow rotators and Region I galaxies in the quenched sample. Slow rotators are almost exclusively ellipticals, whereas Region I galaxies show a much wider distribution of optical morphologies.

a much greater variation in their morphological classifications. This is in line with the other structural parameters explored in Fig. 4.4. Hence, despite the limitations discussed previously, we maintain that the similar residual α-enhancements of SRs and Region I galaxies in our sample is a real phenomenon, and one that we expect to be replicated across other spectroscopic surveys.

To explain the likely reasons behind this phenomenon, we explore the slow rotator formation scenarios espoused by Naab et al., 2014. Although the selection criteria for SRs differs slightly from our approach, we see that there are two likely pathways that agree with observations:

- Class C: Late ($z \lesssim 1$), gas-rich major mergers. The high fraction of stars formed in the galaxy, relative to those accreted through a merger, would likely result in a low integrated [α/Fe] ratio.

- Class F: Repeated minor mergers, from at least $z \approx 2$. These would likely have significantly higher [α/Fe] than Class C galaxies.

Clearly, these two formation scenarios would likely result in a broad spread of [α/Fe] relative to fast rotators, and hence we consider the possible mix of Class C and F galaxies as the most probable cause for slow rotators not following the residual anti-correlation between Δ [α/Fe] and $\lambda_{R_e}^{eo}$. We further speculate that under the formation pathway of Class F galaxies, a recent minor merger with a late-type galaxy may also depress the integrated [α/Fe] ratio, and result in measurements closer to solar values. In addition, the sample used by Naab et al. predicts both an increase in the median stellar mass and effective radius of slow rotators relative to fast rotators, in good agreement with our results from Fig. 4.4.

More recently, these results have been reinforced by Lagos et al., 2022, who investigated slow rotator formation scenarios in the Evolution and Assembly of GaLaxies and their Environments (EAGLE) simulation. They explicitly computed the expected chemical abundances for each assembly history, as a function of galaxy radius. All slow rotators that formed via mergers were α-enhanced, relative to main sequence galaxies, whereas those that formed without mergers, and hence had little disruption to ongoing star formation, were predicted to have considerably lower [α/Fe] towards the centre. Similarly, investigating slow rotators that have had any merger in the last 10 Gyrs, those with gas-rich mergers were $\approx$ 0.1 dex lower in [α/Fe] than the average, in agreement with the expectations from Naab et al., 2014. Both the "no merger" and "gas-rich merger" scenarios could explain the comparable residual α-enhancements of SRs and Region I galaxies. Further work on this area is clearly needed however, to explore whether the spatial information in the kinematic maps is able to reveal which formation pathway is dominant.

4.4 Conclusions

We utilise measurements of $\lambda^{\rm eo}_{R_{\rm e}}$ from van de Sande et al., 2021a, and [α/Fe] from the method in Chapter 2 to analyse galaxies in the SAMI Galaxy Survey. Based on our analysis of the kinematic properties across the sample, we make the following observations, with novel results highlighted in bold:

1. For all 1317 galaxies with measurements of $\lambda_{R_{\rm e}}$, we fit a global [α/Fe]-$\sigma_{\rm e}$ relation to obtain the result

$$[\alpha/\mathrm{Fe}] = (0.388 \pm 0.011)\log_{10}\left(\sigma_{\rm e}/\mathrm{km\,s^{-1}}\right) - (0.61 \pm 0.02).$$

   We find that the residuals Δ [α/Fe] display a strong ($> 6\sigma$) anti-correlation with the inclination-corrected $\lambda^{\rm eo}_{R_{\rm e}}$,

$$\Delta\,[\alpha/\mathrm{Fe}] = (-0.060 \pm 0.009)\lambda^{\rm eo}_{R_{\rm e}} + (0.027 \pm 0.004).$$

   If we use $\lambda_{R_{\rm e}}$ rather than $\lambda^{\rm eo}_{R_{\rm e}}$, the gradient of this relationship is over 50% higher.

2. We isolate the quenched population based on a 1 dex offset in SFR from the SFMS. This substantially reduces the statistical significance of this anti-correlation, which now has a gradient $a = -0.033 \pm 0.021$. However, **the persistence of this relation, whilst weak, demonstrates that the offset cannot unambiguously be attributed to ongoing star formation.**

3. Compared against the quenched sample, **unquenched galaxies demonstrate a much more significant relationship,**

$$\Delta\,[\alpha/\mathrm{Fe}] = (-0.138 \pm 0.017)\lambda^{\rm eo}_{R_{\rm e}} + (0.060 \pm 0.010).$$

4. This anti-correlation would therefore imply a link between the duration of star formation and the angular momentum of the galaxy. Utilising the empirical formulae of de La Rosa et al., 2011, we derive the half-mass formation time of unquenched galaxies as

$$\Delta T_{\mathrm{M}/2}\,(\mathrm{Gyr}) = (-2.11 \pm 0.26)\Delta\lambda^{\mathrm{eo}}_{\mathrm{R_e}}.$$

Thus, we estimate the half-mass formation time for the average galaxy in Region IV to be extended by $\approx 0.7\,\mathrm{Gyr}$ relative to that in Region I. We hope to further explore this link in future studies.

5. Comparing slow rotators to the lowest $\lambda^{\mathrm{eo}}_{R_\mathrm{e}}$ fast rotators (Region I), we find that the difference in α-enhancement is determined to first order by σ_e. Accounting for this, by looking at the residuals $\Delta\,[\alpha/\mathrm{Fe}]$, we find the slow rotators and Region I galaxies are indistinguishable. **The star-formation histories of these two groups ($\lambda^{\mathrm{eo}}_{R_\mathrm{e}} \lessapprox 0.4$) are therefore similar, despite a substantial difference in their structure and kinematics. This contrasts with galaxies in Regions II-IV, which show increasingly extended star-formation histories, correlated with their degree of rotational support.**

Chapter 5

Measuring Radial Gradients

In this chapter, we discuss the methods used to extract the radial gradients of stellar populations in integral-field unit (IFU) observations of galaxies, with a specific focus on galaxies drawn from the Sydney-Australian-Astronomical-Observatory Multi-object Integral-field Spectrograph (SAMI) Galaxy Survey Data Release 3 (DR3).

5.1 Binning Methods

Although there exist many studies to date on the radial gradients of stellar populations, across many different samples of galaxies, there is no clear consensus as to the optimum method of deriving these gradients. Some studies, such as González Delgado et al., 2015, extract spectra binned within elliptical annuli of a fixed axis ratio, where the radius of each annulus is a constant fraction of the galaxy effective radius $R_{\rm e}$ (or less commonly, as a fraction of the observed angular diameter, *e.g.* Ferreras et al., 2019, hereinafter F19). The annuli from multiple galaxies can then be stacked for each division in $R_{\rm e}$, in order to increase the signal/noise ratio (S/N; Greene et al., 2015; Bernardi et al., 2019). Others, among them Ferreras et al., 2019 and Santucci et al., 2020, prefer to trade off a reduction in the S/N in order to avoid the loss of information from stacking independent galaxies. Alternative binning methods such

as Voronoi tessellation have also seen use (Goddard et al., 2017b; Zheng et al., 2017), and are often utilised in stellar population studies with larger IFUs like the Multi-Unit Spectroscopic Explorer (MUSE; Bacon et al., 2010).

When applied to large-scale surveys using compact IFUs, these existing methods may unnecessarily limit the amount of useful information that can be retrieved. This prompted the investigation of which binning procedure is optimal for use with data drawn from the SAMI Galaxy Survey. In particular, under the assumption that our data are S/N-limited, we aim to find the best compromise between the useful extent of the radial information and the loss of spatial resolution. We rule out stacking spectra from different galaxies, as this presents significant obstacles to disentangling higher-order relationships, and considering the wide distribution of morphologies present in the SAMI survey, we look to methods that make as few prior assumptions as possible regarding the shape and symmetry of galaxies.

5.1.1 Fixed Annuli

The first method we consider, and in many ways the simplest, is to extract spectra binned within elliptical annuli from each galaxy. Even here, there are different approaches - where Ferreras et al., 2019 extract a fixed number of annuli across the width of the IFU, Bernardi et al., 2019 and others prefer to fix the radii of the annuli as a proportion of the galaxy effective radius, R_e. We show the distribution of $R_{e,c}$ across the SAMI survey in Fig. 5.1a, where we use $R_{e,c}$ to refer to the circularised radius $R_{e,circ} \equiv \sqrt{a_e b_e}$, taken from the multi-Gaussian expansion (MGE) fits of D'Eugenio et al., 2021. Here, a_e and b_e are the semi-major and semi-minor axes of the ellipse containing half of the total flux in the best-fitting MGE model, and we use the notation $R_e = a_e$ throughout. Comparing the median $R_{e,c} = 2''.68$ against the nominal IFU radius of $7''.5$, we see that the majority of galaxies are well-sampled radially, with only 4% not covered by the IFU bundle up to $1\,R_{e,c}$. We also plot

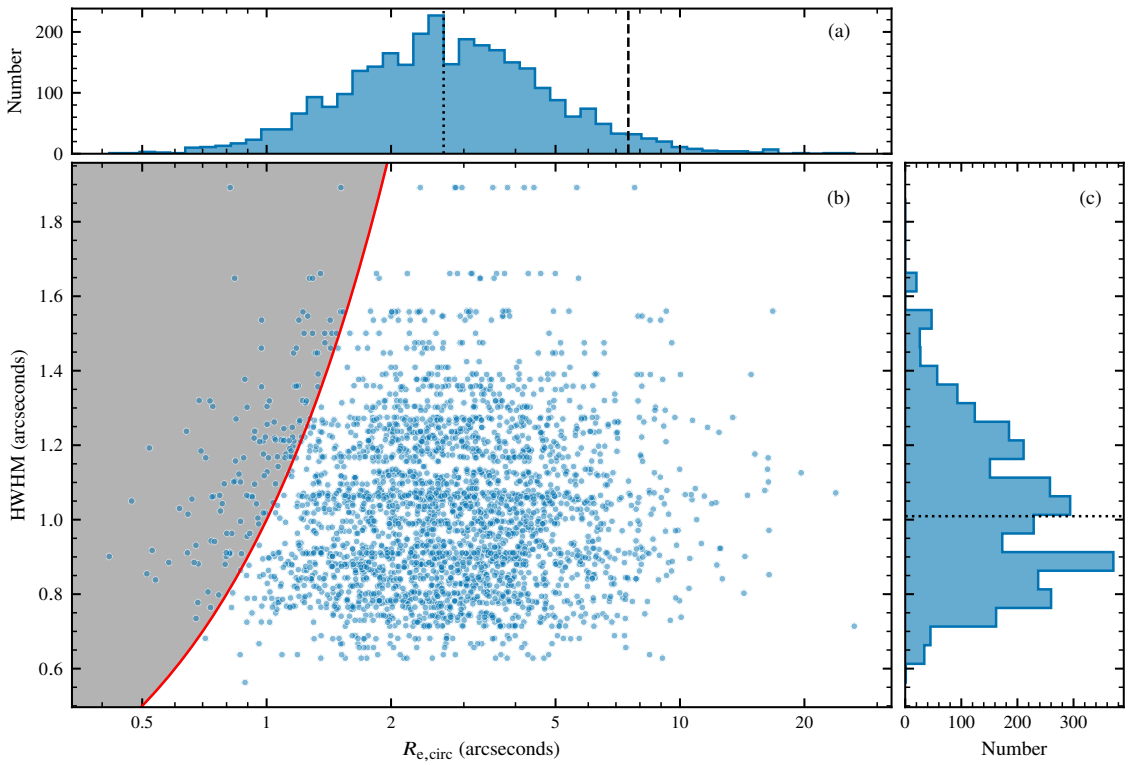


Figure 5.1: The distribution of galaxies in the SAMI survey in the $R_{e,circ}$-HWHM plane. In (b), the red line delineates $R_{e,circ}$ = HWHM, and the shaded region indicates $R_{e,circ}$ < HWHM. In (a) and (c), we display the projected distribution as a function of $R_{e,circ}$ and HWHM respectively, with the dotted lines denoting the sample median. The dashed line in (a) indicates the nominal IFU radius of 7.″5.

$R_{e,c}$ against the half-width at half-maximum (HWHM) of the spatial point-spread function (PSF) of the SAMI datacubes, and highlight in the shaded region of Fig. 5.1 the set of galaxies where $R_{e,c}$ < HWHM. For these 135 galaxies it will be impossible to obtain any reliable stellar population gradients, and so we exclude this set from further analysis, and from any sample size quoted in the remainder of this section.

Given the wide variation in projected galaxy sizes, we investigate elliptical annuli as a function of the IFU radius, rather than R_e. We define the elliptical radial distance of a spaxel as the semi-major axis of the ellipse on which it lies, utilising the ellipticity (ε) and position angle (PA) measurements from the MGE fits in D'Eugenio et al., 2021, with an example shown in Fig. 5.2a for SAMI 302657. We also display the

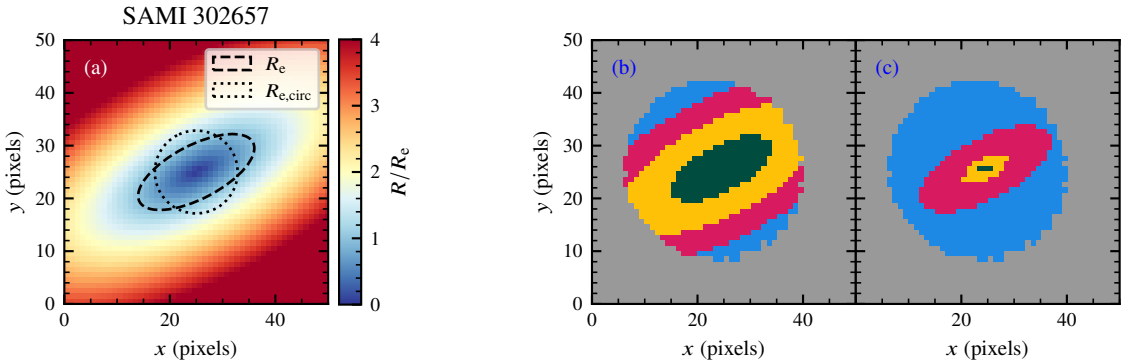


Figure 5.2: (a) The elliptical radial distance of every spaxel from the centre, scaled to the semi-major effective radius R_e for SAMI galaxy 302657. R_e and $R_{e,circ}$ are overlaid as dashed and dotted lines respectively. (b) The bin mask resulting from linearly-scaled elliptical annuli. (c) The bin mask from logarithmically scaling the annuli.

different definitions of effective radius, contrasting the semi-major effective radius R_e with the circularised radius $R_{e,circ}$. We then find the maximum observed radius, and assign each spaxel to one of a fixed number of bins. For our work, we test both linearly- and logarithmically-scaled sampling, with examples shown in Fig. 5.2b and Fig. 5.2c respectively.

5.1.2 Voronoi Tessellation

A significant disadvantage of the annular binning method is that the annuli are fixed, regardless of the galaxy being observed. Given two galaxies with identical R_e, but differing surface brightness profiles, the S/N in each bin for the fainter galaxy may fall below the threshold necessary to perform our stellar populations analysis. We therefore consider an adaptive binning scheme, namely the Voronoi tessellation method of Cappellari et al., 2003.

Compared to earlier binning methods such as the Quadtree algorithm (Samet et al., 1984), the Voronoi binning method aims to satisfy three fundamental requirements:

- **Topology:** The bins should tessellate across the region of interest, *i.e.* partition the data without overlapping each other or leaving holes.
- **Morphology:** Each bin should be as compact (or round), as possible, so that the spatial position of the bin is well-defined.
- **Uniformity:** Given a target S/N, $\mathrm{S/N_{target}}$, the scatter around this value should be as small as possible.

In Fig. 5.3, we show two example galaxies binned using this method to $\mathrm{S/N_{target}} = 20$, alongside the bin S/N as a function of radius. We display a composite *gri* image of SAMI 136842, a bright high-mass galaxy ($m_r = 13.8$, $M_* = 10^{10.8}\,\mathrm{M}_\odot$, $R_{\mathrm{e,circ}} = 8\farcs72$), in Fig. 5.3a, made by collapsing the blue-arm datacube over 3 equal spectral regions. The bin mask, corresponding to the 191 distinct bins from the Voronoi method, is displayed alongside in Fig. 5.3b. For each bin, we calculate the median S/N along the spectral axis, and the median bin radius scaled to the galaxy effective radius, and show the resulting distribution in Fig. 5.3e. In the region $0.3 < R/R_\mathrm{e} < 0.5$, a floor is clearly visible in the bin S/N, traced by the target S/N. Some "overshoot" and scatter is inevitable due to the discrete nature of the underlying data. This is highlighted by the inner regions of the galaxy, where the bin S/N increases with decreasing radius. This is caused by the individual spaxels exceeding the target S/N, and hence it is not possible to combine spaxels in this region to achieve a S/N closer to the target – in other words, the spaxel grid in the centre of the galaxy is already the optimal binning scheme.

To contrast, we show a similar set of plots in Figs. 5.3c,d,f for SAMI 49702, a fainter, more compact galaxy ($m_r = 15.5$, $M_* = 10^{10.6}\,\mathrm{M}_\odot$, $R_{\mathrm{e,circ}} = 4\farcs38$). Whilst it is immediately clear that the lower signal in the original datacube results in fewer Voronoi bins (48 bins, compared to 191 bins), the distribution and morphology of the bins presents another problem for extracting radial gradients. Because the Voronoi

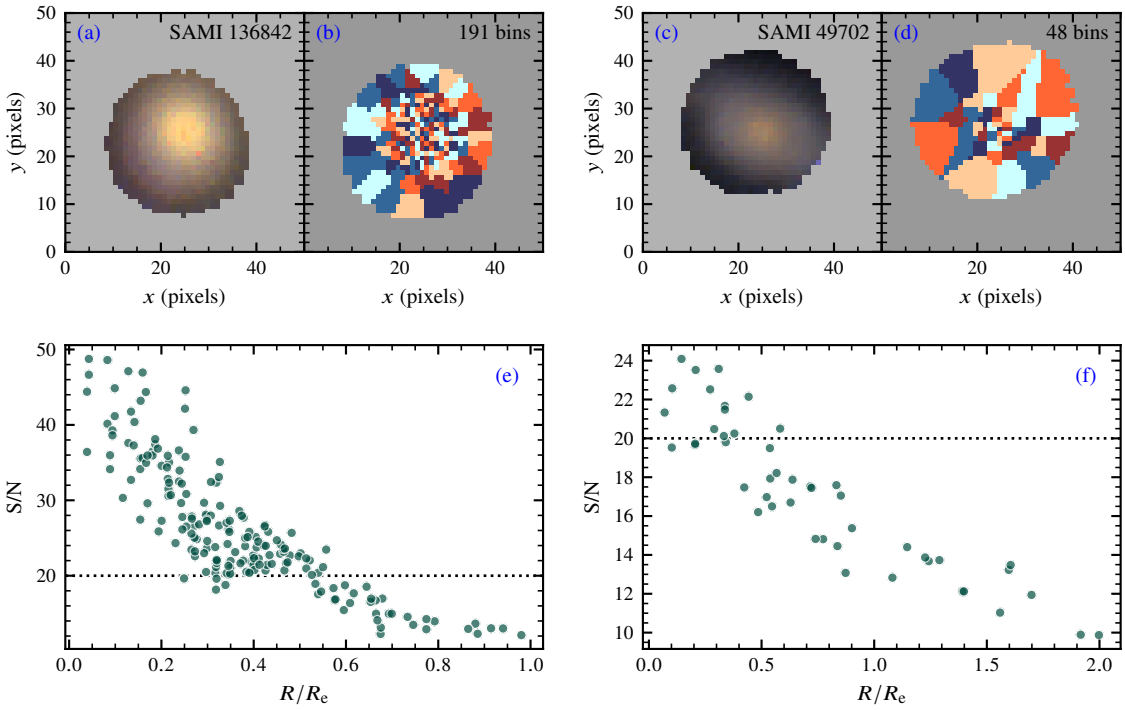


Figure 5.3: (a) A composite *gri* image made by collapsing the blue-arm datacube for SAMI galaxy 136842 along the spectral axis. (b) The bin mask resulting from a Voronoi tessellation to a target S/N = 20. (e) The S/N of each bin as a function of radius, scaled by the galaxy effective radius. (c), (d), and (f) display the same content as (a), (b), and (e) respectively, for the lower surface brightness galaxy SAMI 49702.

algorithm aims to make each bin as compact as possible, towards the outer regions of a field, these bins will preferentially deform radially rather than azimuthally. Fig. 5.3f shows the consequence of this – whilst there may be enough signal to reach the target S/N in an annuli covering the inner regions of several bins, the radial deformation results in very few bins exceeding the threshold. Compared to Fig. 5.3e, we see that despite the field-of-view extending to double the effective radius, the radial extent of the outermost bin is almost identical: $R_{\rm last} = 0.56\,R_{\rm e}$ for SAMI 136842, and $R_{\rm last} = 0.58\,R_{\rm e}$ for SAMI 49702.

5.1.3 Flux Contours

Considering the significant drawbacks of both the fixed elliptical annuli and Voronoi tessellation binning methods for extracting radial gradients, we propose to use a new method – binning spaxels based on the isophotal contours of the continuum flux. What we will refer to as *contour binning* is not in itself a novel method (Sanders, 2006), but it is almost exclusively used to bin X-ray data, rather than optical/near-infrared (NIR) IFU data. A similar method was utilised by Barsanti et al., 2021, in order to separate the stellar populations of bulges and disks for double-component galaxies in the SAMI cluster sample. There, the source images were the total flux from two-dimensional bulge-disk decomposition models, derived using PROFIT and PROFOUND (Robotham et al., 2017; Robotham et al., 2018), from Sloan Digital Sky Survey (SDSS; Ahn et al., 2012) and Very Large Telescope Survey Telescope (VST) ATLAS photometry (Shanks et al., 2013; Shanks et al., 2015).

Here, we present a generalised implementation of this method, which does not require any specific modelling beyond a characterisation of the PSF in the source photometry and the IFU datacubes. For the SAMI survey there is no single homogeneous source for the underlying photometry. We therefore include a method based on SExtractor and PSFEx (Bertin et al., 1996; Bertin, 2011) to extract the PSF from the imaging data, and calculate the required convolution kernel to match the IFU resolution, detailed in Section 5.1.3.2. The binning procedure itself is explained in Section 5.1.3.3.

A brief overview of the procedure for one galaxy is as follows, assuming the availability of both a reference image and a datacube:

- All sources in the image are located using SExtractor, and a small cut-out is extracted for each of them.
- PSFEx determines which extracted sources are point sources, and it uses the

cut-outs of the point sources to construct a model of the PSF of the reference image.

- PSFEx calculates the 'homogenisation kernel', which is applied to the original image to degrade it to the lower spatial resolution of the datacube.
- Using the isophotal contours of the PSF-matched reference image, spaxels in the datacube are radially accreted into bins, up to some arbitrary S/N threshold.

5.1.3.1 Source Images

The contour binning method requires a source image, from which the isophotal contours can be measured. Whilst the contours can be measured directly from the data to be binned, this is not always an optimal solution for IFU data, which can suffer from spaxel-to-spaxel variations in the flux calibration (a more detailed description of this can be found in Section 5.1.3.3). The source surveys and their characteristics are listed in Table 5.1. Whilst all SAMI galaxies selected from the Galaxy and Mass Assembly (GAMA) survey (Driver et al., 2011) are fully covered by the Kilo-Degree Survey (KiDS; de Jong et al., 2015), this survey has only patchy coverage of the cluster galaxies. For the $\approx$ 800 galaxies in the cluster sample, we opt to use a combination of different sources, all observed using the Dark Energy Camera (DECam; Flaugher et al., 2015).

The combination of sources was chosen to ensure that all galaxies had a similar depth for observations in the g band. A comparison of the relative system throughput of each instrument is shown in Fig. 5.4. The $g'_{\rm SDSS}$ filter, used in conjunction with the OmegaCAM camera for KiDS (Kuijken, 2011), has a very flat transmission profile as a function of wavelength. In contrast, the DECam system throughput with the $g_{\rm DECam}$ filter peaks at longer wavelengths, and drops off by a factor of two at the blue end of the spectrum. The spectral coverage of both instruments in the g band is

Source	Survey	Instrument	$t_{\rm exp}$	5σ Limit
SAMI-GAMA	KiDS	2.6m VST/OmegaCAM	900 s	$g = 25.4$
Abell 85, 2399	DECaLS	4m Blanco/DECam	≈ 270 s	$g \approx 24.7$
Abell 119, 168; EDCC442	DES	4m Blanco/DECam	≈ 270 s	$g \approx 24.6$
APMCC917; Abell 3880, 4038	Oh et al., 2020	4m Blanco/DECam	800 s	$g = 25.5$

Table 5.1: The sources for the imaging used in the contour binning method. KiDS refers to the Kilo-Degree Survey (de Jong et al., 2013; Kuijken et al., 2019), DECaLS to the Dark Energy Camera Legacy Survey (Dey et al., 2019), and DES to the Dark Energy Survey (Morganson et al., 2018; Abbott et al., 2021).

substantially less than the region sampled by SAMI, with KiDS covering about 60% of the range, compared to $\approx 70\%$ for the wider DECam filter. However, we consider this an acceptable compromise for our purposes, as the photometric observations are fully contained within the IFU spectral range. Whilst similar depth observations are available in the r-band, the coverage would then extend beyond our region of interest by ≈ 1500 Å. Whilst the u band may increase the depth towards shorter wavelengths, and would extend beyond the SAMI coverage by only ≈ 200 Å, not all SAMI galaxies have been observed in this bandpass.

5.1.3.2 PSF Matching

We begin by extracting a square region around the galaxy, of side length $360''$. This area was chosen as a compromise between ensuring that enough non-saturated point sources are visible, particularly in the relatively crowded cluster fields, but also to avoid any significant spatial variations in the PSF across the instrumental field-of-view. Throughout this section, we utilise SAMI galaxy 136842 as an example, with the corresponding field displayed in Fig. 5.5.

We first make use of SExtractor (Bertin et al., 1996), to locate and extract

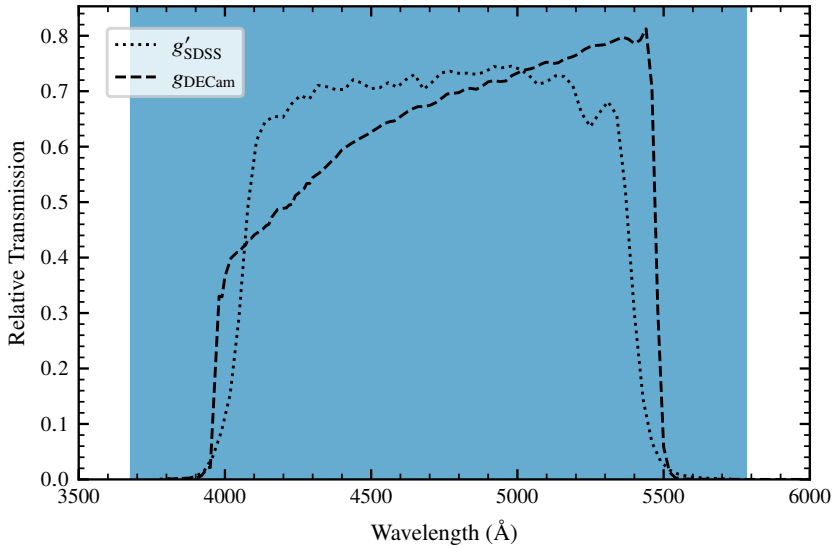


Figure 5.4: The relative system throughput using the g-band filters on each instrument, without accounting for the additional reduction from atmospheric transmission. The shaded region indicates the approximate spectral coverage of the blue arm of the SAMI datacubes.

all sources visible in this field. SExtractor works by estimating the sky background level, and the standard deviation σ of this background, and then extracting all objects for which the flux lies above a 3σ threshold. Although there are many different parameters and configuration options available, such as for deblending and measuring magnitudes in a variety of adaptive apertures, for the most part we do not change these values from their defaults. As we do not intend to re-measure any of the photometric properties for which ancillary measurements already exist, such as $R_{\rm e}$ (D'Eugenio et al., 2021), for each source we record only the properties needed to characterise the source PSF. These are detailed below, with the appropriate SExtractor keywords:

- VIGNET(X,Y). A small cut-out of the source, of pixel width x and height y. For all galaxies in this work, we use (63,63), matching the DES pipeline (Morganson et al., 2018). At the pixel scales of DECam and OmegaCAM, this corresponds to an on-sky square window of side length $8\farcs25$ and $6\farcs3$ respectively.

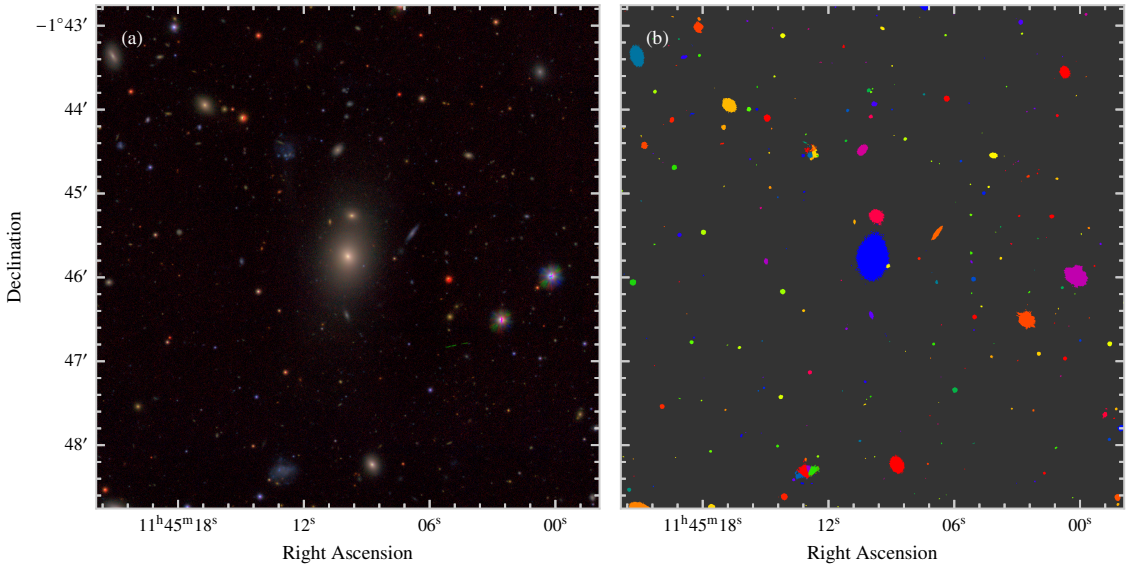


Figure 5.5: (a) A colour image of a $6' \times 6'$ window centred on SAMI 136842, using KiDS *gri* imaging. (b) An example of a SExtractor segmentation map, based on (a), showing the detected sources.

- X_IMAGE, Y_IMAGE. The pixel coordinates of the centroid of the object, along x and y.
- FLUX_RADIUS. The circularised half-light radius of the object.
- FLUX_APER, FLUXERR_APER. The source flux, and associated uncertainty, measured through a fixed circular aperture. As before, we follow DES and use an aperture size of $5''.55$.
- ELONGATION. For historical reasons, this is defined within SExtractor as $(1 - b/a)$, for the semi-major axis a and the semi-minor axis b.
- SNR_WIN. The signal/noise ratio measured within a weighted Gaussian window.
- FLAGS. A record of any extraction flags (*e.g.* a saturated object, or an object containing bad pixels).

The output from SExtractor is a catalogue containing all of these measured properties for each detected source. We can also generate diagnostic plots, such as a

segmentation map displayed in Fig. 5.5b. This displays the most probable detected object ID to which each pixel belongs, and can be used to mask out nearby objects, as well as a consistency check if there are any problems with source masking further down the line.

The next step is to utilise PSFEx (Bertin, 2011) to characterise the PSF of any unresolved sources in the image. This software makes two assumptions in order to select suitable sources from those extracted previously:

- For unresolved, unsaturated sources, the shape of the light profile is flux-independent.
- Unresolved sources will have the smallest full-width at half-maximum (FWHM).

Point sources are therefore selected from a rectangular cut in the magnitude vs. half-light radius plane (Kaiser et al., 1995), followed by a further iterative process to remove low S/N, highly elliptical, or contaminated sources.

The recovered PSF is represented in the PIXEL basis, where each pixel is treated as a free parameter, and an example is shown in Fig. 5.6c. This basis makes fewer assumptions about the shape of the PSF as opposed to a Gauss-Laguerre basis, at the cost of requiring more samples to generate a robust model (see Bertin, 2011 for more details). For our images, with a large number of point sources and a heterogeneous PSF, dependent upon on the source survey, we consider the choice of this basis to be a good compromise.

One of the primary motivations for using PSFEx is the ability to calculate a "PSF homogenisation kernel" for any input catalogue. This is a convolution kernel, which can be applied to the original image in order to smooth the PSF of any point source to an arbitrary shape. In the current version of PSFEx (3.17.1), the target shape is limited to a Moffat profile (Moffat, 1969), parameterised below as a function

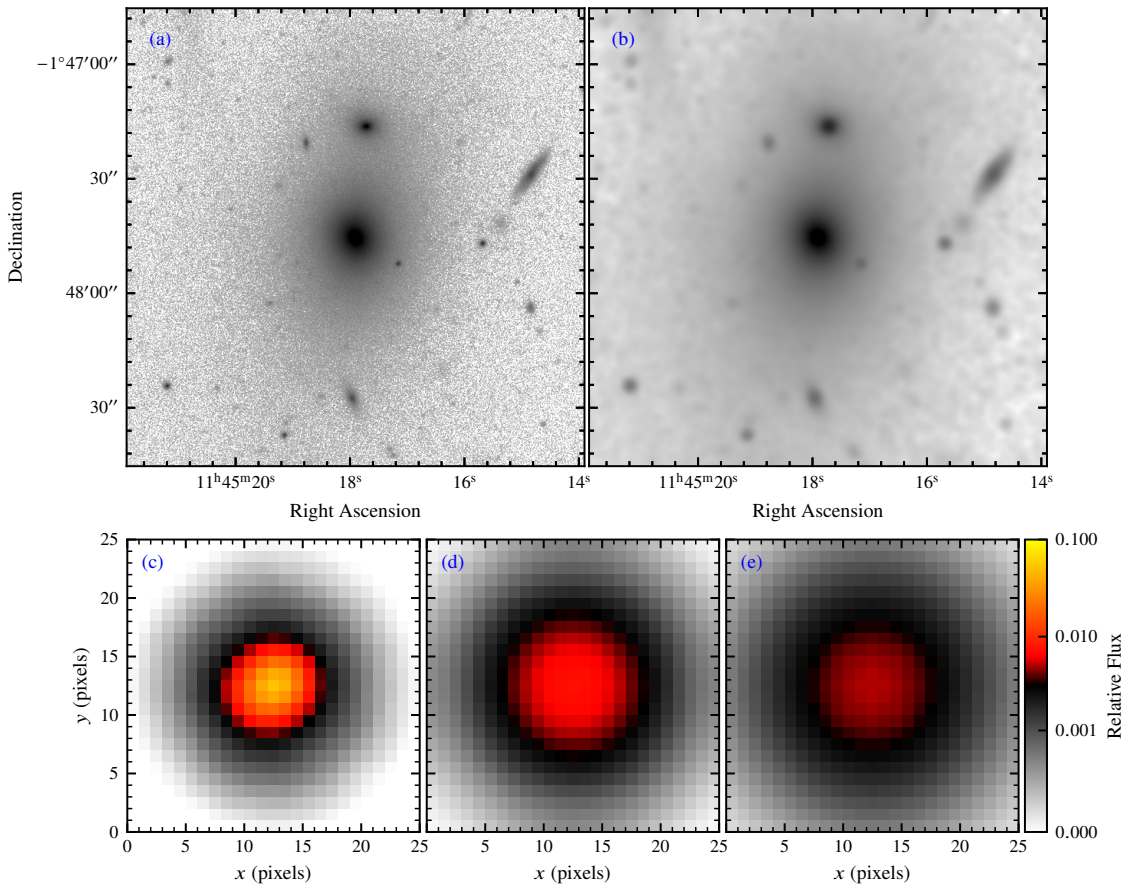


Figure 5.6: (a) A $2' \times 2'$ window centred around SAMI 136842, from KiDS g-band imaging. (b) The same field-of-view as (a), but convolved to the resolution of the SAMI datacube. (c) The PSF measured from (a), using PSFEx, with the sum of flux normalised to unity. (d) The "homogenisation kernel" derived by PSFEx, convolved with (a) to produce (b). (e) The spatial PSF of the SAMI datacube, and the PSF of the degraded image in (b).

of radius r:

$$\mathrm{PSF}\,(r) = \frac{\beta - 1}{\pi \alpha^2} \left[1 + \left(\frac{r}{\alpha} \right)^2 \right]^{-\beta}, \tag{5.1}$$

where the parameters α and β represent the width and power-law index of the profile respectively. The FWHM of this function is given by $\mathrm{FWHM} = 2\alpha\sqrt{2^{1/\beta} - 1}$, and the total flux has been normalised to unity.

For each field in the SAMI Galaxy Survey, a calibration star was observed in one of the 13 IFUs. During the data reduction process for SAMI DR3, the PSF for

each field was measured from this secondary star, by fitting the flux around 5000 Å to a Moffat profile. The α and β parameters of each profile are saved in the galaxy datacube headers, and after correcting for the differing pixel scales between each cube and the corresponding imaging, we pass these parameters to PSFEx during the fit. In Fig. 5.6e, we show an example of the target Moffat profile, reconstructed from the SAMI datacube, alongside the derived homogenisation kernel in Fig. 5.6d. For all galaxies in the SAMI survey, the FWHM of the datacube PSF is greater than the imaging PSF. The result of this is displayed in Fig. 5.6b, where we have convolved the original image in Fig. 5.6a with the homogenisation kernel in Fig. 5.6d. The flux limits for the colour map have been kept consistent across both plots, to highlight the reduction in resolution.

5.1.3.3 Binning Procedure

Given a suitable source image, at the correct resolution, the next stage is to rebin the IFU data, following the flux contours. Whilst there are several possible methods to perform this (*e.g.* adaptively growing the bins one spaxel at a time, as with Voronoi binning), our method is motivated by a desire to avoid the computationally expensive S/N calculations of the SAMI data, due to the need to account for covariance. The covariance data for SAMI is reconstructed as a 5×5 array for each pixel (spatial and spectral) in the datacube. When binning, the variance for each pixel must be multiplied by the sum of the covariances for all the nearby pixels with which it is covariant. A more detailed discussion can be found in Sharp et al., 2015. As such, we aim to limit the number of these calculations performed for each galaxy.

Given a discrete sampling of the radial light profile, for each isophote we check which IFU spaxels are fully contained within the bounds of the contour, and calculate their S/N, accounting for covariance. If the S/N in that isophote does not exceed the target, which in our case is set to $\mathrm{S/N_{target}} = 20$, then we include the spaxels bounded

by the next isophote, moving outwards in radius until the target S/N is reached. We do not consider fractional spaxels to avoid degenerate bins (*i.e.* the same spaxels appearing in multiple bins due to closely-spaced isophotes). This procedure is then repeated until all spaxels have been assigned to a bin. The specific implementation of this that we have written includes the possibility of setting a minimum number of spaxels for each bin, and the requirement for all spaxels in a given bin to be contiguous. For this research, taking into account the IFU size, we require a minimum of 4 spaxels per bin, and enforce contiguity for each bin, allowing for a single break. This means that topologically, a bin must have less than or equal to one hole, but cannot consist of two or more disconnected subsets. This is enforced before checking whether a given spaxel has any signal, to minimise disruption from any dead spaxels.

There are several distinct approaches to this procedure. The first is to derive the isophotal contours on the source image, then transform the pixel coordinates of the bounds to the IFU spaxel space before calculating membership of the bins. This introduces an additional overhead for every isophotal sample, and the computational cost scales commensurately. The advantage of this approach is that it reduces any discretisation effects, especially where the spaxel scale of the IFU data is heavily undersampled compared to the imaging pixel scale.

The second is to reproject the source image on to the IFU spaxel grid, resampling the original image using a flux-conserving method such as the spherical polygon intersection used in Montage (Berriman et al., 2017). Whilst this has a clear advantage in being able to calculate the contours directly on the same coordinate grid, it also incurs a heavy computational penalty by requiring the initial resampling step.

The choice of method depends largely on the number of samples taken along the light profile, compared to the size of the IFU datacube. During our testing, the limited size of the SAMI datcubes (covering at most a 50 x 50 spaxel grid) meant that the repeated overhead of the round-trip coordinate transformations led to a lower

computational cost than the large initial overhead of reprojecting the image to the IFU spaxel grid.

A final possibility is to eschew the requirement for a separate reference image, and use the median flux of the IFU datacube, collapsed along the spectral axis. In Fig. 5.7, we show why this was not considered to be a viable option for the SAMI datacubes. The SAMI IFUs, known as *hexabundles*, used circular optical fibres packed into a bundle, combined with a 7-point dither pattern, for each observation. One major disadvantage of this approach, as opposed to image slicers, or a lenslet array, is that it is substantially more complicated to reduce the raw data and produce a regularly-gridded datacube (a thorough discussion can be found in Sharp et al., 2015). The sparse sampling of the original fibre bundles presents difficulties in accounting for uneven exposure duration in each output spaxel, as well as introducing significant covariances between adjacent spaxels. This can be seen in Fig. 5.7, where the cubing algorithm has resulted in significant residual structure when compared to the reference image, convolved to the same PSF. Whilst this approach has considerable benefits, including considerably reduced complexity and no ancillary data requirement, we consider that it is best suited to IFU observations with a more regularly-sampled field-of-view, such as Mapping Nearby Galaxies at Apache Point Observatory (MaNGA; Bundy et al., 2015), and/or with deeper observations which allow for an increased accuracy of the spaxel-to-spaxel flux calibration, such as MUSE (Bacon et al., 2010). For the SAMI data used throughout this chapter, we prefer to rely on the reference images as previously described.

The calculation of the isophotal contours also requires some consideration. It is not possible to know *a priori* how many contours will be required, or indeed the light profile of any individual galaxy relative to the IFU field-of-view. We therefore evaluate two variables to establish the most efficient procedure – linear *vs.* logarithmic sampling, and the number of samples, shown in Fig. 5.8 for a high S/N galaxy. The

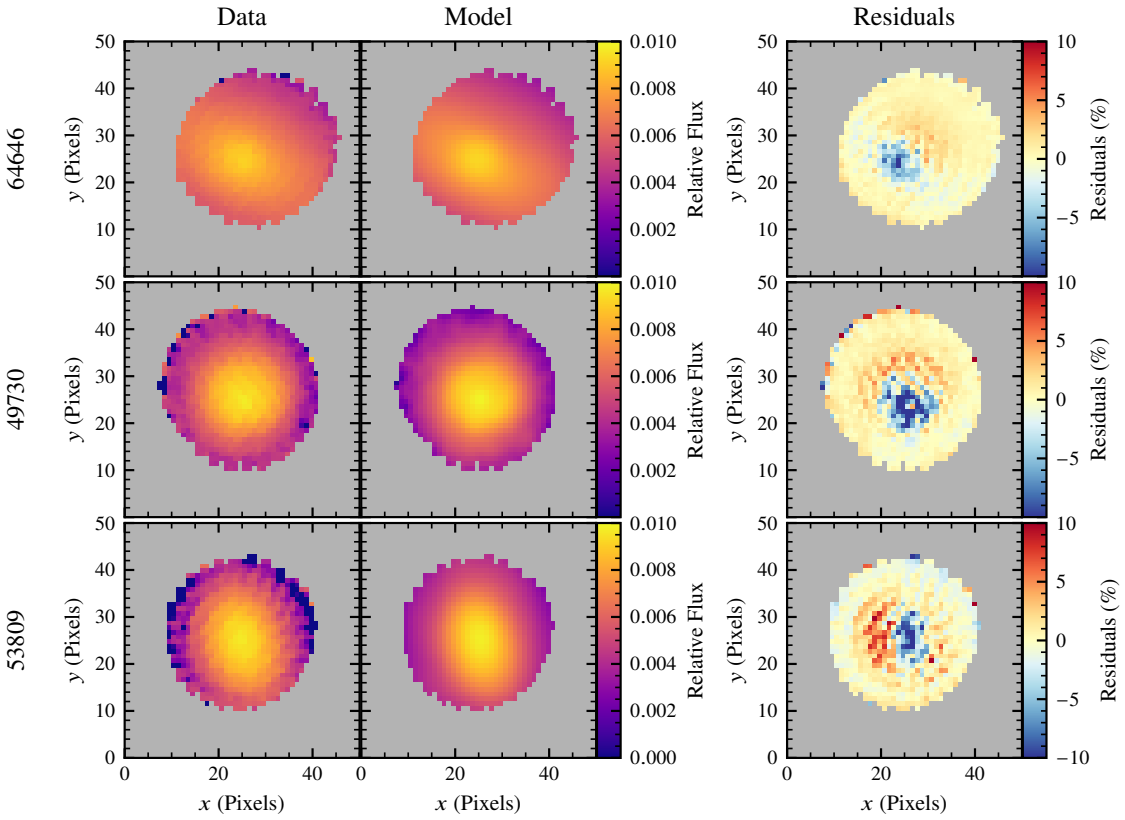


Figure 5.7: Three example SAMI galaxies, in order of increasing structure in the residuals from top to bottom. In the left column, we show the median flux in the blue-arm datacube, in the middle column, the convolved and rebinned imaging data, with the sum of fluxes normalised to unity. In the right column, we show the residuals after subtracting the model from the data, with the colour map limits set to ±10%.

maximum and minimum flux values are calculated from a cut-out of the reference image matching the extent of the IFU spaxel grid. In the linear case, the contours are derived from n evenly spaced samples, whereas the logarithmic method returns n samples, with each a constant multiple of the previous.

The logarithmic sampling consistently returns a higher number of bins, with a more even spacing as a function of radius. For severely undersampled data, $n = 5$ in Fig. 5.8, the logarithmic sampling returns bins almost linearly spaced in radius, as expected for a galaxy with an exponential light profile. The logarithmic scheme also shows swiftly diminishing returns with increasing n, relative to the linear scheme.

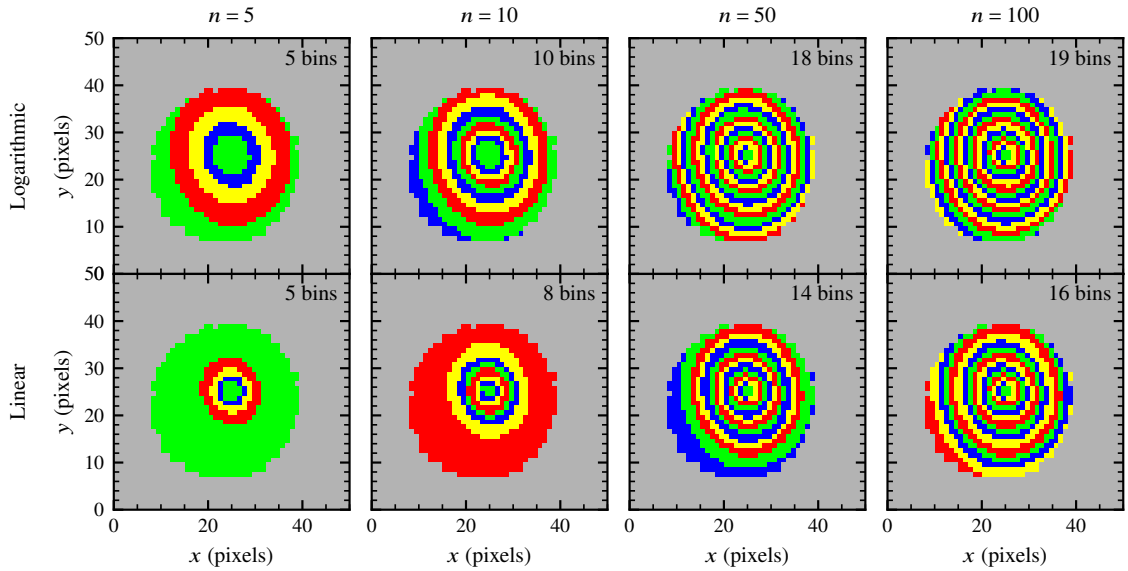


Figure 5.8: On the top row, the bin layout from logarithmically-sampled isophotal contours, for increasing number of samples n from left to right. The bottom row follows the same layout, but for linearly-sampled isophotal contours.

Whilst one could evaluate an even higher number of isophotes to ensure a perfect sampling, the computational cost scales linearly with the number of contours evaluated. Additionally, it is possible to place some further constraints on the number of samples required. For a properly-centred SAMI datacube, the theoretical maximum number of bins for a high-S/N galaxy is ≈ 35, although this assumes the galaxy light profile is perfectly described by a logarithmic function. To account for this, and for observations where the IFU bundle is not centred on the galaxy, we calculate the bin mask for all SAMI galaxies using 100 logarithmically-spaced contours.

5.1.4 A Comparison of Methods

For our comparison, we apply each binning method to every galaxy in the SAMI survey that has a reliable measurement of R_e (a more detailed discussion on the sample selection can be found in Section 6.1). For each bin, we use the line-of-sight mean velocity maps from SAMI DR3 to shift all spectra to a common rest frame,

before summing the fluxes, and adding the variances in quadrature, with a factor to account for the strong covariance between adjacent pixels (see Sharp et al., 2015 for more details). We then measure both the S/N and mean elliptical radius of each bin, scaling the radius by the semi-major effective radius R_e.

We show the resulting distributions in Fig. 5.9, for linearly-sampled annuli as shown in Fig. 5.2b. Although it has been used for many previous studies, we demonstrate here that it is perhaps the least useful method when applied to IFU surveys such as SAMI. Considering the S/N distribution, an extraordinary amount of information is lost, with only 33.1% of binned spectra exceeding our target S/N threshold, S/N = 20. The median S/N of the distribution is merely 10.7, with the 16^{th} and 84^{th} percentiles occurring at S/N = 1.5 and 36.9 respectively. Whilst this is not entirely unexpected, as the method does not consider the signal of the galaxy at all when generating the bins, it presents severe difficulties when attempting to extract radial gradients. In Fig. 5.9b, we show the distribution of bin radii. Of the spectra with S/N < 20, the overwhelming majority of these are drawn from the outermost annuli, where $R > R_e$, introducing a significant bias into our sample.

Considering that the flux profile of a galaxy is not a linear function with radius, we expect that a logarithmic sampling of annuli should produce more consistent results. We show the S/N distribution in Fig. 5.10a, following the binning scheme introduced in Fig. 5.2c. The binned spectra are much more evenly distributed compared to Fig. 5.9a, with 49.8% of galaxies exceeding S/N = 20 (16^{th} percentile: S/N = 5.8; 84^{th} percentile: S/N = 42.4). As before, the S/N distribution has a pronounced extended tail. This is driven by spaxels at the centres of bright galaxies, which are combined in the central annulus to produce bins with S/N > 100. Whilst such high S/N bins are unnecessary for our analysis, it is a consequence of fixing the bin radius without adapting to each galaxy.

We also consider the distribution of bin radii in Fig. 5.10b, where we see a rather

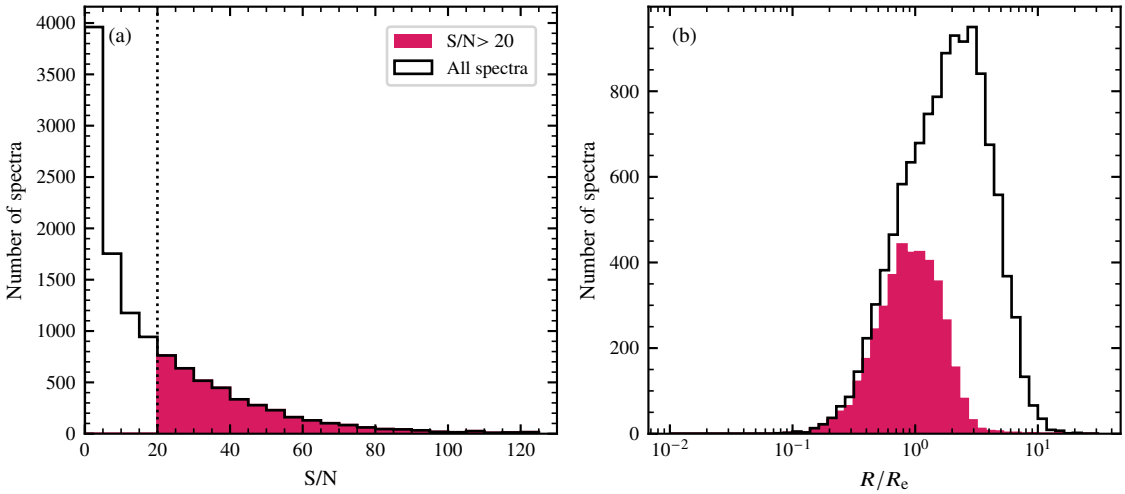


Figure 5.9: (a) The distribution of S/N in binned spectra, using linearly-sampled elliptical annuli. The target S/N = 20 is shown as a dashed vertical line, with the shaded region denoting spectra that exceed this threshold. (b) The distribution of the mean radius of each bin, scaled to the galaxy effective radius. We also show the distribution for only the spectra with S/N > 20.

flat, and possibly bimodal distribution, with a dip at $\approx 0.7R/R_e$. The reasons for this unusual shape are not immediately apparent. Compared to Fig. 5.9b, this shape is far more consistent between the full sample, and those spectra with S/N > 20. However, although a greater proportion of binned spectra reach our threshold at $R > R_e$, 43% have S/N < 20 at relative radii $R/R_e \leq 0.1$. This is caused by the central annuli not covering enough spaxels for the fainter galaxies, leading to the scenario where the central bin is not included in the analysis, but the outer bins are.

In Fig. 5.11, we consider the first adaptive method, namely Voronoi tessellation as shown in Fig. 5.3. An immediate consequence is the vastly increased number of binned spectra – whereas the previous methods both produced 12,068 bins, the Voronoi method produces a total of 78,510 bins from 3017 input galaxies. Whilst it may be tempting to subsequently assume that we are underestimating the potential number of bins by a factor of ≈ 6 when using either linearly- or logarithmically-spaced bins, we show in Fig. 5.11a that this is merely the inevitable outcome of being able to adapt the bin size to target a particular S/N. Whilst the median S/N is

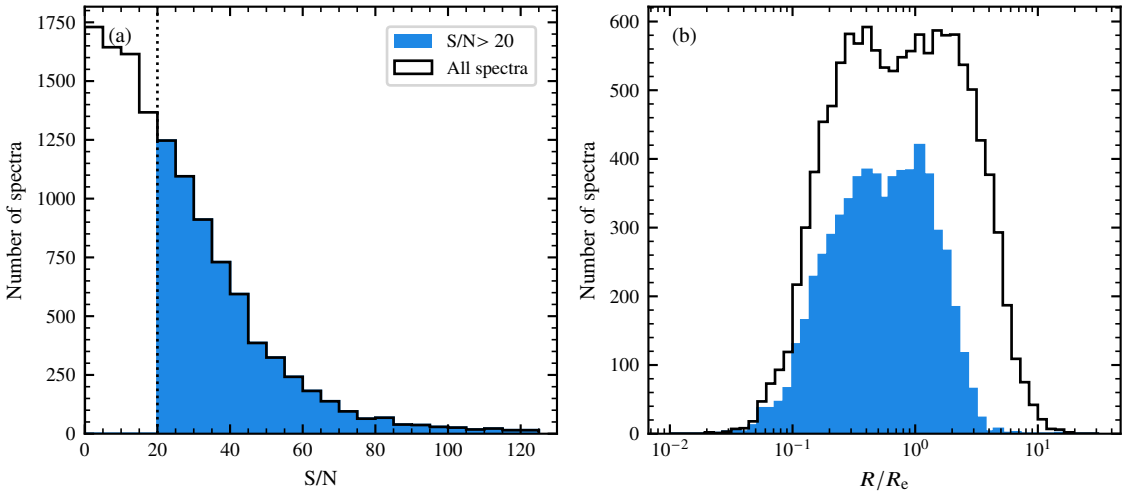


Figure 5.10: The distributions of (a) bin S/N, and (b) bin radius, for galaxies binned using logarithmically-sampled elliptical annuli. The histogram bin widths are consistent with Fig. 5.9, for ease of comparison of the shape of each distribution.

almost unchanged at 21.4, compared with using logarithmically-spaced annuli, the distribution itself is much more sharply peaked around $S/N_{target} = 20$, with the 16^{th} and 84^{th} percentiles occurring at S/N = 12.1 and 29.7 respectively. As a result, 57% of binned spectra exceed the threshold. However, we draw attention to Cappellari et al., 2003, where the authors note that a scatter of $\approx 6\%$ around S/N_{target} is typical for real data. As such, there will be a degree of compromise between the target S/N, and applying a strict threshold.

A secondary consideration with the Voronoi binning scheme is the proportion of bins at higher radii that fail to reach S/N_{target}. As with the linearly-sampled annuli, we see in Fig. 5.11b that the majority of bins are cut for $R > R_e$. The cause of this is the same limitation highlighted previously in Fig. 5.3d. In the faint outskirts of galaxies, the Voronoi method compromises on the S/N of each bin, in an attempt to keep them as compact as possible. Whilst this may be useful for bright galaxies binned to a high S/N, with a more relaxed threshold, in our analysis it results in discarding a significant amount of information.

Finally, we present a similar analysis for the contour binning method in Fig. 5.12.

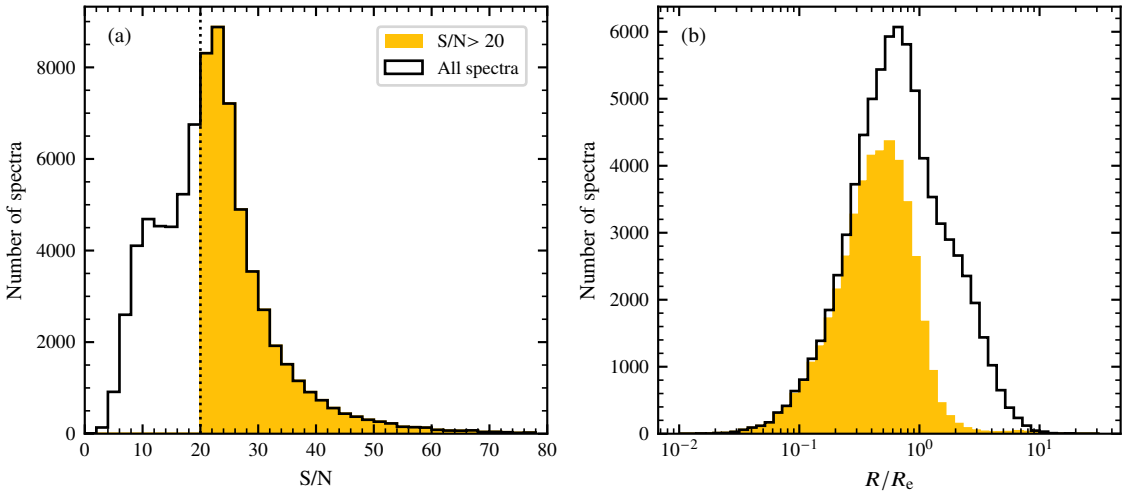


Figure 5.11: The bin S/N and bin radii distributions for galaxies binned using the Voronoi method, presented in the same manner as in Fig. 5.9. Note that the scale in (a) has been truncated, for ease of viewing.

By design, this method should ensure that no spectra is binned to a S/N less than S/N_{target}, as seen by the very sharp peak in Fig. 5.12a ($S/N_{median} = 31.5$; 16^{th} percentile: $S/N = 21.0$; 84^{th} percentile: $S/N = 52.9$). However, there are a few spectra that fall below our threshold. These are in fact entire galaxies, for which it is not possible to bin up to S/N_{target} through any combination of spaxels, least of all to have multiple bins, and which account for approximately 10% of the sample. Note that these galaxies will also have fallen below the threshold in the previous binning schemes, but are more visible here by design. For the remaining galaxies, we have a total of 21224 binned spectra, or an average of 8 radial bins per galaxy.

The radial distribution in Fig. 5.12b shows a significantly improved coverage compared to the previous methods. Whilst we include the galaxies which fail to meet our S/N threshold again, we note that the radii of these bins is in fact the average radius over the observed fibre bundle, and therefore has little physical meaning. As before, these spectra fall in the region $R > R_e$.

We now compare the radius of the outermost radial bin, R_{last}, for each of the four methods, as shown in Fig. 5.13. We consider only galaxies with at least three

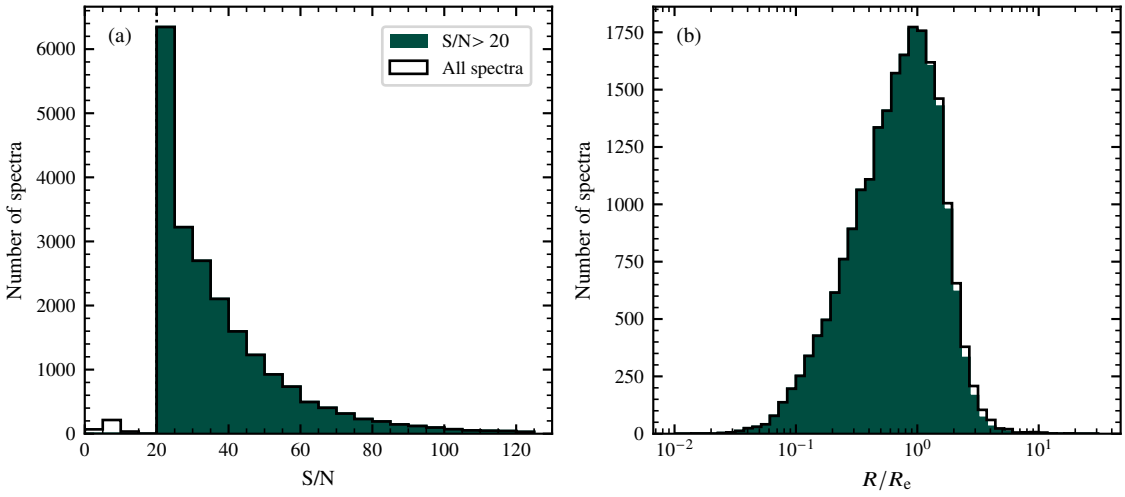


Figure 5.12: The bin S/N and bin radii distributions for galaxies binned using the contour binning method presented in Section 5.1.3.

spectra with S/N > 20, and as such, the number of galaxies available is not consistent across the four methods. Whilst the two annular methods give very similarly-shaped distributions, with the logarithmic sampling showing a slight shift towards larger radii, the number of galaxies differs by almost a factor of four (linear: 402 galaxies; logarithmic: 1559). As mentioned earlier, this is clear evidence that matching the bin spacing to the flux light profile gives a more consistent S/N distribution between bins. Whilst a linear spacing may be useful for analyses looking at properties as a linear function of radius, or where a logarithmic spacing would lead to annuli sizes smaller than a single spaxel, we suggest that this method should in general be reserved for bright galaxies, or deep observations.

Considering the two adaptive binning schemes, we note that selecting a minimum of three bins is not strictly equivalent for the Voronoi binning method. If we take the theoretical limit of hexagonal packing (Cappellari et al., 2003), then with a singular bin at the centre of the galaxy, a minimum of 19 bins would be required to achieve three radial samples. We show the two different distributions in Fig. 5.13, noting that adopting the more conservative bin limit reduces the number of available galaxies from

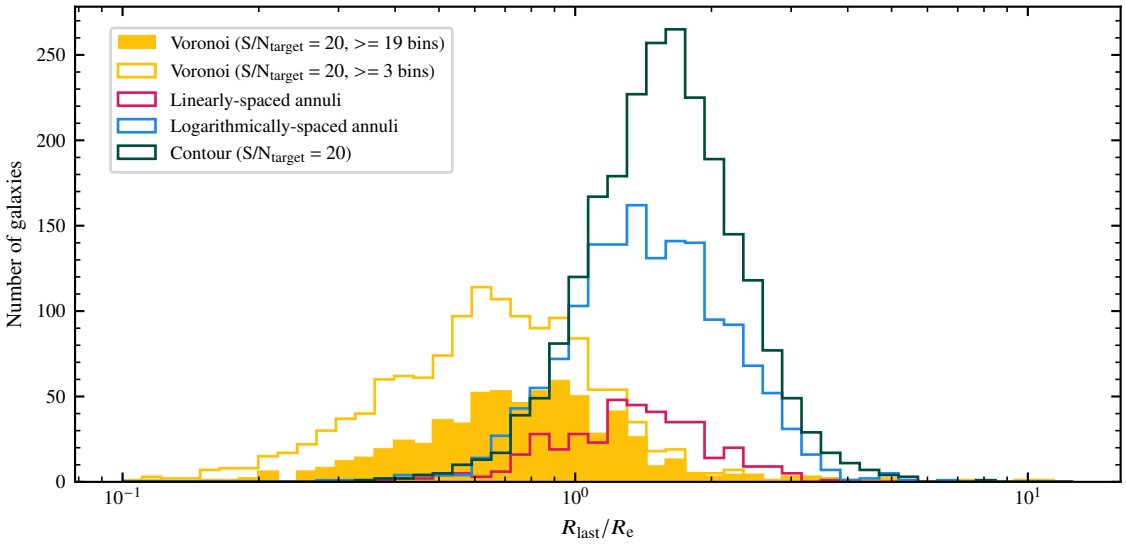


Figure 5.13: The distribution of the radius of the outermost radial bin $R_{\rm last}$, scaled by the galaxy semi-major effective radius, for the four binning methods considered in this section. Galaxies are only included if they contain at least three spectra with a S/N > 20. Two histograms are included for the Voronoi method, where the stepped histogram shows the distribution of galaxies with at least three bins, and the filled histogram the sample with at least 19 bins. Note that the total number of galaxies is not consistent across each histogram.

1351 to 642. It is also abundantly clear that a substantial amount of information is lost in the outskirts of galaxies binned in this manner. The median radial ratio is $R_{\rm last} = 0.77\,R_{\rm e}$, compared to $R_{\rm last} = 1.45\,R_{\rm e}$ when using logarithmically-spaced annuli. By constrast, binning galaxies using the contour binning method produces both the highest number of galaxies with at least 3 bins (2314), and the highest radial ratio ($R_{\rm last} = 1.54\,R_{\rm e}$). As covered in Fig. 5.12, this method also returns bins with a very consistent S/N, by construction, and so we select this binning scheme for our analysis going forward.

5.2 Seeing Corrections

For this subsection, we display results from galaxies binned using the contour binning scheme in Section 5.1.3, although we note that the methods and discussion are appli-

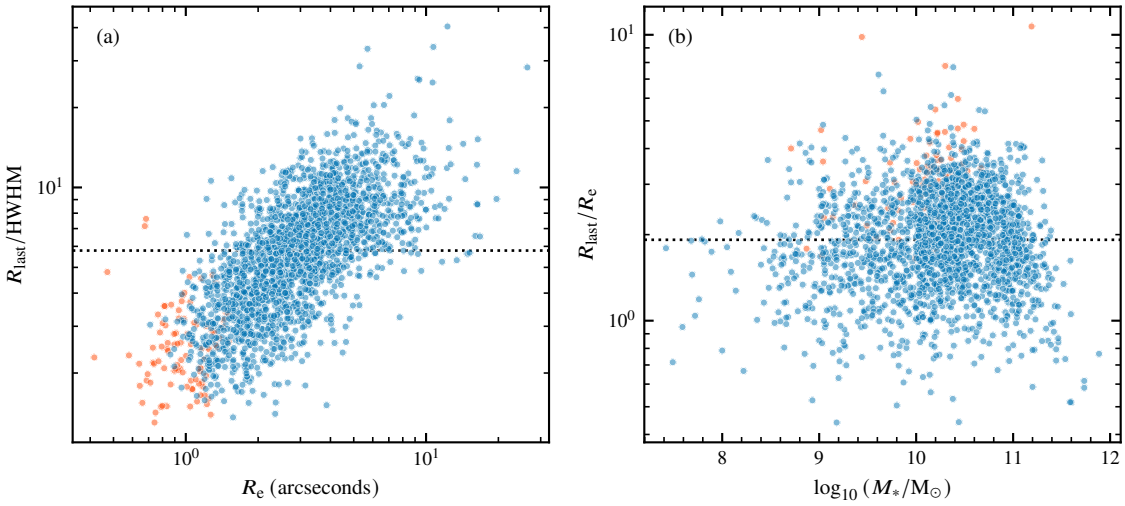


Figure 5.14: (a) The ratio of the radius of the outermost radial bin $R_{\rm last}$ to the HWHM of the cube PSF, against the effective radius of the galaxy. (b) The ratio of $R_{\rm last}$ to $R_{\rm e}$, against the galaxy stellar mass. Orange points denote galaxies where $R_{\rm e} <$ HWHM. The dotted lines show the median ratios.

cable more generally. For each binned spectrum, we measure the stellar populations using the same method as before, detailed in Chapter 2. However, whilst it would be convenient to simply fit these measurements to some parameterisation of the galaxy radius, this neglects the significant impact from atmospheric seeing. In Fig. 5.14a, we display the ratio of the radius of the outermost bin, $R_{\rm last}$, to the HWHM of the cube PSF. With a median value of $R_{\rm last}/{\rm HWHM} = 6.3$, this represents a small but significant impact on any derived gradients. Considering Fig. 5.1, an additional concern is that the HWHM can vary by more than a factor of two between any two galaxies, and so it is not possible to draw valid comparisons between galaxies without first accounting for this.

We require a galaxy to have reliable stellar population measurements in at least three bins to derive a meaningful gradient with uncertainties. The procedure we use to correct for seeing is adapted from Ferreras et al., 2019. We display a graphical representation of this method in Fig. 5.15.

We begin by generating a model, following a linear relationship between the log-

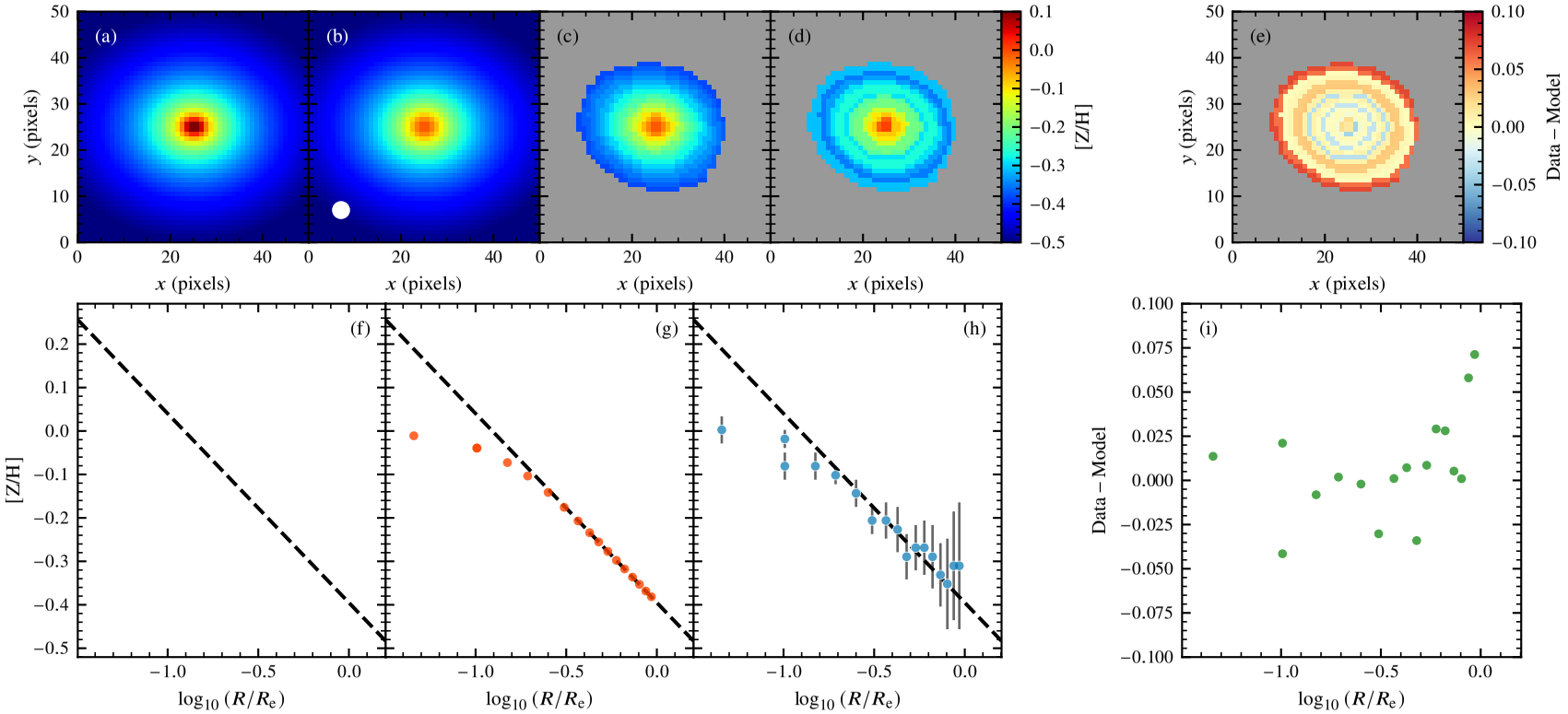


Figure 5.15: (a) A linear model of a radial metallicity gradient, of the form $[\mathrm{Z/H}] = a \log_{10}(R/R_\mathrm{e}) + [\mathrm{Z/H}]\big|_{R=R_\mathrm{e}}$. (b) The gradient model, after convolution with a Moffat profile to match the IFU PSF (the FWHM of the PSF is inset, as a filled white circle). (c) The convolved gradient model, rebinned to match the contour binned observations. (d) The measured [Z/H] values, from the contour-binned observations. (e) The residuals, from (d) − (c). (f) The gradient model from (a), shown as a function of $\log_{10}(R/R_\mathrm{e})$. This line is reproduced in (g) and (h) as a visual reference. (g) The rebinned gradient model, also shown in (c), against $\log_{10}(R/R_\mathrm{e})$. (h) The radial [Z/H] measurements, also shown in (d). (i) The residuals from (h) − (g), expressed as a function of $\log_{10}(R/R_\mathrm{e})$.

scaled radius (normalised to the effective radius of each galaxy), $\log_{10}(R/R_e)$, and the given stellar population parameter, y, of the form

$$y = a \log_{10}(R/R_e) + b\,. \tag{5.2}$$

An example of this is shown in Figs. 5.15a and 5.15f. The model is convolved with the datacube PSF, in our case the Moffat function previously described in Section 5.1.3.2, to reproduce an observation of the intrinsic gradient model (Fig. 5.15b). We note that this procedure currently assumes a uniform surface brightness distribution, whereas observations are luminosity-weighted. Correctly accounting for this additionally requires a model of the intrinsic surface brightness profile of each galaxy, and is an excellent opportunity for future improvements.

This model observation can then be rebinned, using the same bin layout as the real observations, to produce a set of model observations m_i (Fig. 5.15c, g). The log-likelihood is then given by

$$\begin{aligned} \ln(\mathcal{L}) &= -\frac{\chi^2}{2}\,, \\ &= -\frac{1}{2}\sum_i \left(\frac{o_i - m_i}{\sigma_i}\right)^2\,, \end{aligned} \tag{5.3}$$

for the measured population parameters o_i and their associated uncertainties σ_i, summed over bins i.

From Eq. 5.3, it straightforward to solve for the maximum log-likelihood using LMFIT (Newville et al., 2021), and therefore identify the best estimate for the unbiased population gradient. This can also be expressed as finding the *intrinsic* stellar population gradient. To estimate the uncertainties on this, we use a Markov-Chain Monte Carlo (MCMC) sampler, EMCEE (Foreman-Mackey et al., 2013). We use 32 walkers, and initialise them using the solution from LMFIT, with flat priors. We run the sampler for 5,000 steps, with typical autocorrelation times of ≈ 50 steps.

Two examples of the resulting distribution are shown in Fig. 5.16. When looking at the metallicity gradient, we adopt the notation

$$\nabla[\mathrm{Z/H}] \equiv \frac{\Delta[\mathrm{Z/H}]}{\Delta \log_{10}(R/R_\mathrm{e})} \tag{5.4}$$

for the gradient a, and $[\mathrm{Z/H}]\Big|_{R=R_\mathrm{e}}$ for the intercept b. In Fig. 5.16a, we show a strong negative metallicity gradient for SAMI galaxy 8487, with a well-constrained solution. We overlay the 1σ and 2σ contours on the scatter plot, and show the marginalised distributions with the 1σ deviations in the histograms on the side. In Fig. 5.16c we display the corresponding radial profile, including the naïve least-squares fit (LS). As expected, the least-squares fit returns a shallower gradient than the unbiased estimator from EMCEE, as the PSF smooths over the central values. Looking at the radial sampling, the distribution of points lies almost exclusively within $\log_{10}(R/R_\mathrm{e}) < 0$. This constraint leads to a strong covariance between the gradient and intercept, although the marginalised distributions for both parameters still follow a normal distribution.

In contrast, Fig. 5.16b displays the MCMC samples for a poorly-constrained solution, using SAMI galaxy 49784. In Fig. 5.16d, we see that the radial sampling is more evenly distributed around $\log_{10}(R/R_\mathrm{e}) = 0$, relaxing the constraints on the intercept. However, in the same plot we can also see that the uncertainties on the individual metallicity measurements are comparable to the radial variation across all measurements. Whereas the least-squares fit gives a negative metallicity gradient at the 2σ confidence level, the EMCEE fit shows that the uncertainty on this has been substantially underestimated, and the measurements are instead consistent with a flat metallicity profile.

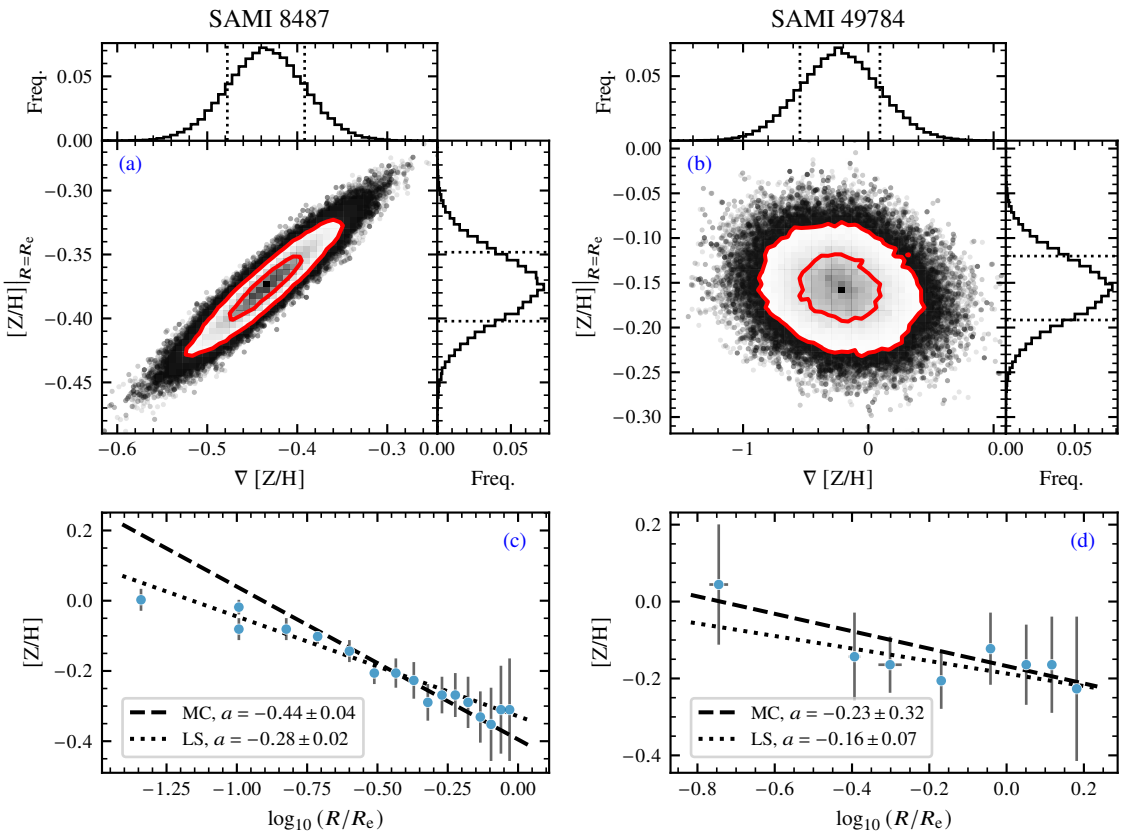


Figure 5.16: The distribution of MCMC samples for the seeing-corrected metallicity gradient and intercept are shown in (a) and (b), for SAMI galaxies 8487 and 49784 respectively. The red contours show the extent of the 1σ and 2σ levels, with the 1σ levels also overlaid as dotted lines in the projected histograms. In (c) and (d), [Z/H] is shown against the log-scaled bin radius, with the best-fitting gradients displayed. "LS" denotes the naïve least-squares fit, and "MC" the MCMC seeing-corrected fit, displayed as dotted and dashed lines respectively.

5.3 Conclusions

Throughout this chapter, we used data drawn from the SAMI Galaxy Survey to discuss the methods used to retrieve radial gradients from compact, seeing-limited IFU surveys. We summarise our work in this chapter as follows:

- For galaxies with a poor spaxel-to-spaxel flux calibration, we demonstrated a workflow using ancillary photometry to produce a PSF-matched reference image. Whilst this ought to be unnecessary for the majority of IFU surveys, we

used this method here due to the significant number of artefacts in the SAMI datacubes from the dithering procedure.

- We showed an implementation of the contour-binning procedure, whereby IFU data are binned following the isophotal contours – either of the datacube itself, or in our case of the reference image. This is by no means the only possible implementation of this procedure, and our specific method is aimed at reducing the number of S/N evaluations required, due to the costly covariance calculations necessary for SAMI data (and other similar surveys).

- We evaluated commonly-used binning schemes for the purpose of extracting radial gradients of IFU data. The ubiquitous Voronoi binning scheme, whilst able to adapt to differing surface brightness profiles, probes smaller radii than all other schemes considered. This is due to preferential radial deformations of the outermost bins, which result in a significant loss of radial information when applying a hard cut-off in S/N. This behaviour is particularly prevalent in more compact IFUs, with a small total number of spaxels.

- By comparison, fixed-width annuli can lead to a smaller loss of radial information. Despite its popularity in other studies of radial gradients, linear sampling is the poorest-performing sampling, when evaluated by the fraction of bins reaching a given S/N threshold. As expected, logarithmically-sampled annuli are better matched to the surface brightness profiles of most galaxies compared to linearly-sampled annuli, resulting in higher proportions of bins reaching the S/N threshold. However, logarithmic sampling can limit the total number of bins due to the discrete nature of IFU data, with the sizes of the central bins set by the spaxel scales.

- The contour binning method, by construction, ensures all bins reach a given S/N threshold, giving it a significant advantage over other binning schemes. It

also allows us to use bins at the largest radii covered by the IFU, maximising the retrieval of radial information. We therefore selected this method for our analysis.

- We showed the application of the seeing-correction method of Ferreras et al., 2019 to our contour-binned data, highlighting the reasons for poorly-constrained fits in some of our galaxies. Whilst there is still room for improvement in this method (*e.g.* accounting for the non-uniform intrinsic surface brightness profiles), the seeing corrections are necessary to ensure an unbiased comparison across the full SAMI survey.

Chapter 6

Radial Gradients of Stellar Populations

In this chapter, we derive the radial stellar population gradients for up to 1453 galaxies. We show the distribution of these radial profiles and seeing-corrected gradients in the size-mass plane, separating our sample by both morphological type and environment simultaneously.

6.1 Sample Selection

Our initial sample is drawn from the third public data release (DR3) of the Sydney-Australian-Astronomical-Observatory Multi-object Integral-field Spectrograph (SAMI) Galaxy Survey (Croom et al., 2021). Of the 3426 pairs of datacubes, covering the red and blue arms of the AAOmega spectrograph (Saunders et al., 2004; Smith et al., 2004; Sharp et al., 2006), there are 3068 unique galaxies. We select the unique datacubes using the ISBEST flag in the DR3 "CubeObs" catalogue, which indicates the highest quality datacube in the case of repeat observations, based on the seeing full-width at half-maximum (FWHM) and signal/noise ratio (S/N).

From this, we take the intersection of galaxies with both reliable measurements

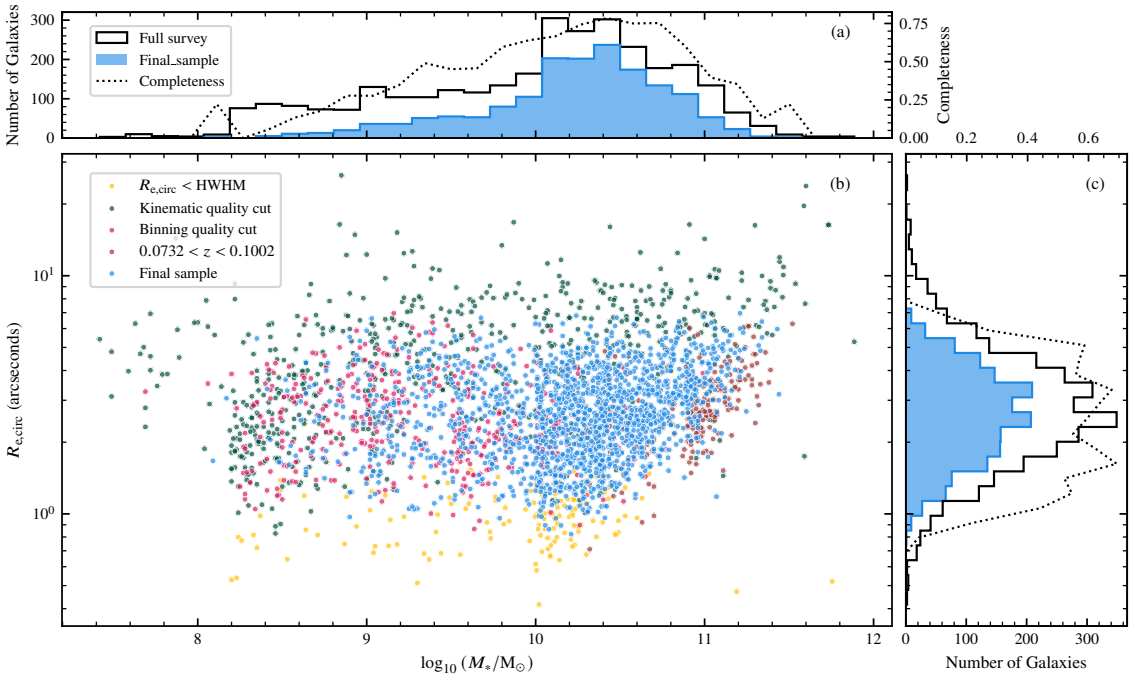


Figure 6.1: The distribution of our sample in the R_e-M_* plane. In (b), we show the contribution of the multiple quality cuts. In (a) and (c), we display the projection of our full and final samples as a function of $\log_{10}(M_*/M_\odot)$ and $R_{e,circ}$ respectively. The dashed lines indicate the completeness of our final sample.

of the stellar kinematics and morphological parameters. A total of 51 galaxies were unsuccessfully fit by the multi-Gaussian expansion (MGE) method of Cappellari, 2002, used by D'Eugenio et al., 2021 to measure the effective radius (R_e), the position angle (PA), and ellipticity (ε). We show the remainder of the sample in Fig. 6.1, where we highlight the contribution of all additional quality cuts. As previously mentioned in 5.1.1, and highlighted in Fig. 5.1, for 135 galaxies the circularised effective radius $R_{e,circ}$ is smaller than the half-width at half-maximum (HWHM) of the atmospheric seeing disc, and so these galaxies are also excluded. A further 676 galaxies fail to meet the stringent kinematic quality cuts imposed by van de Sande et al., 2017b, leaving a total of 2206 galaxies for which we attempt to extract radial population gradients.

We apply the contour binning method (Section 5.1.3) to these remaining galaxies, in order to obtain a series of radial bins, with a minimum S/N = 20. For each

bin, we shift all flux and variance spectra to a common rest-frame before stacking, using the mean line-of-sight velocity maps of van de Sande et al., 2017b. We then extract the stellar populations from each binned spectrum, using the same method as in Chapter 2, and with an identical treatment of the measurement errors. The same quality cuts are applied to the stellar populations as before, namely that measurements where the uncertainty extends over the width of the model parameter grid are discarded. To extract the radial gradients themselves, we require a minimum of three radial bins, at a S/N $\geq$ 20, with reliable stellar population measurements. A total of 402 galaxies fail to meet this criterion. We also apply the same redshift quality cut as in Section. 2.3.2, removing a further 193 galaxies, and leaving 1611 galaxies for which we have measurements of the stellar population gradients.

Considering the distribution of these galaxies displayed in Fig. 6.1, we note that our final sample is not entirely representative of the full survey. The completeness of our sample suffers heavily at low masses, and only reaches 50% at $\log_{10}(M_*/\mathrm{M}_\odot) = 9.6$, before dropping off again for $\log_{10}(M_*/\mathrm{M}_\odot) > 11.0$. A similar number of galaxies are cut throughout the mass range, with the highest proportion removed at low masses, consistent with our sample selection for the aperture spectra in Section 3.1.2.

The distribution is not uniform for each quality cut, however. The majority of galaxies that fail to meet our binning scheme S/N requirement have low masses, whereas the redshift quality cut almost exclusively affects high-mass galaxies. In contrast, the distributions are almost reversed for the quality cuts as a function of $R_{\mathrm{e,circ}}$. Whilst the redshift and binning requirements affect a broad range of galaxy sizes, the kinematic quality cuts are focussed on some of the largest galaxies, particularly those for which $R_{\mathrm{e,circ}} > 7\farcs5$ (the nominal integral-field unit (IFU) radius; see Section 4.1.1 for more details). As expected, the galaxies for which $R_{\mathrm{e,circ}} <$ HWHM are amongst the smallest in our sample. Considering the completeness with respect to $R_{\mathrm{e,circ}}$, our sample is only $> 50\%$ complete in the range $1\farcs1 < R_{\mathrm{e}} < 5\farcs9$.

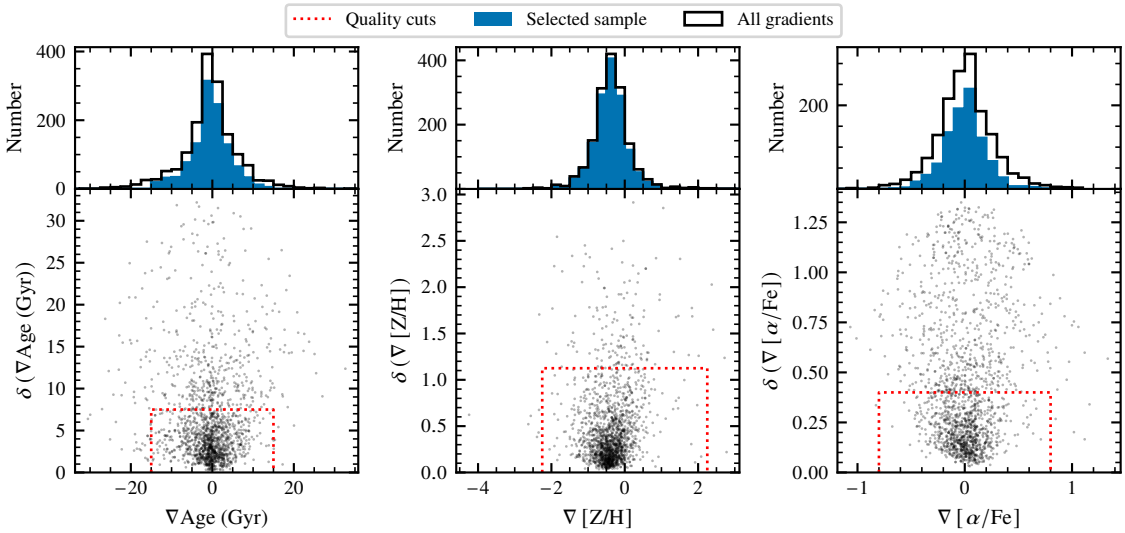


Figure 6.2: The selection criteria for reliable gradient measurements, for each measured stellar population parameter. In the lower panels, we display the bounding region (red dashed lines) from which we draw the gradient samples. In the upper panels, we show the gradient distribution both before and after the cuts. Note that the scatter for each parameter relative to the bounding box leads to a different number of galaxies in each selection, tabulated in Table 6.1.

6.1.1 Gradient Quality Cuts

We apply further quality cuts to the measured gradients. The aim here is to remove low-quality fits, without introducing additional biases into our final sample. We consider the gradients of each stellar population property separately – whilst the selection criteria in the previous section would affect all gradients equally, such as $R_{\rm e,circ} <$ HWHM, we do not assume that a galaxy with a poorly-fit age gradient will also necessarily lead to rejecting the metallicity and [α/Fe] gradients, for example.

The first cut we apply is to limit the absolute value of the gradient to the width of the model parameter space, *i.e.* $|\nabla{\rm Age}| < 15\,{\rm Gyr}$, $|\nabla[{\rm Z/H}]| < 2.25$, and $|\nabla[\alpha/{\rm Fe}]| < 0.8$, shown graphically in Fig. 6.2. For all three population parameters, the extent of the Thomas et al., 2011 (hereinafter TMJ11) model grids is an excellent match to the physical observations, with extremely subsolar and supersolar [Z/H] and [α/Fe] stars being exceedingly rare. We consider that a seeing-corrected gradient indicates

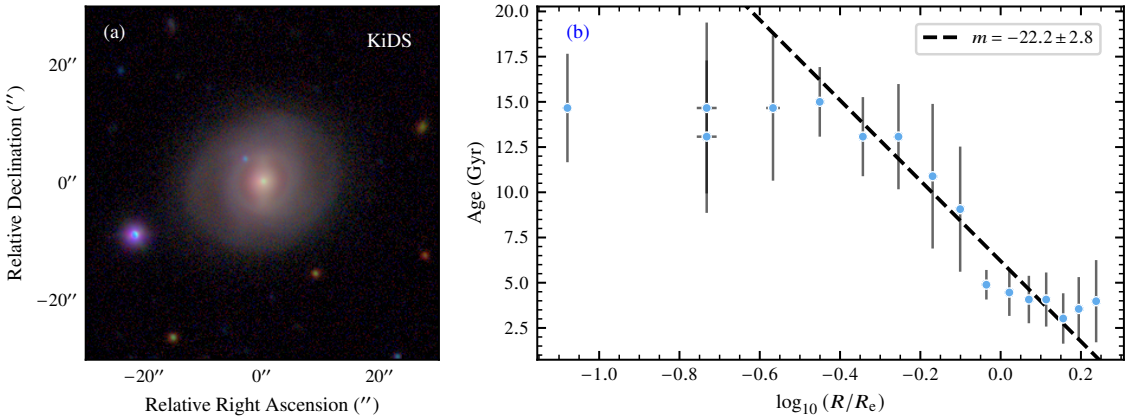


Figure 6.3: In (a), we display a colour image of SAMI galaxy 610846, using KiDS *gri* imaging. There is a clear colour shift between the centre of the galaxy, and the blue outer regions. In (b), we show the measured ages as a function of radius, scaled by R_e. The dashed line indicates the derived gradient, and is a poor fit to the bins at both large and small radii.

the change in that parameter on a logarithmic radial spacing. As such, a galaxy with supersolar abundances at $0.1\,R_e$, and subsolar abundances at $1\,R_e$ appears unlikely to be physical, and is much more likely to indicate a problem with the fit. We show an example of such an outlier in Fig. 6.3, with an extremely low nominal age gradient. Upon inspection, the derived gradient is clearly non-physical, as a result of overfitting the steep transition between the older centre and younger outer regions, where the derived ages plateau rather than decrease monotonically. Whilst these may be interesting galaxies, this behaviour cannot be accounted for with our current method of fitting linear gradients. We therefore exclude these galaxies, noting that this will remove both low-quality data, and real data that cannot be adequately described. This affects only a small number of galaxies, with a total of 29 galaxies removed due to excessively steep age gradients, that would not also be removed due to large fitting uncertainties.

We further restrict our sample of galaxies based on the estimated uncertainties for the gradients. In a similar manner as for the global stellar populations in Section 2.3.1, we do not intend to use galaxies for which the 1σ uncertainty on the gradient spans

SSP Parameter	Full Sample		Quality Cuts	
	n	Median Gradient	n	Median Gradient
Age	1611	-0.33 Gyr	1098	-0.32 Gyr
[Z/H]	1611	-0.39	1453	-0.40
[α/Fe]	1611	0.00	912	0.00

Table 6.1: The sample sizes and median gradients for each stellar population parameter, before and after the quality cuts shown in Fig. 6.2.

the model parameter grid, as this measurement contains no useful information. To account for asymmetric uncertainties stemming from the fitting method in Section 5.2, we implement this by requiring that the mean 1σ uncertainty, denoted as $\delta(X)$ for population parameter X, must be less than half the extent of the parameter space, again shown in Fig. 6.2. We do not apply any additional cuts based on the intercept, as these measurements are typically much better constrained.

To assess the impact of these cuts on our sample, we show the distributions of measured gradients in the upper panels of Fig. 6.2, and tabulate them in Table 6.1. Whilst the measurements of ∇[Z/H] are quite concentrated within the bounding box, leading to a reduction in sample size of less than 10%, the age and [α/Fe] gradients are significantly more scattered. The age gradients are reasonably well localised around the median, giving a sharp peak in the distribution in Fig. 6.2, but have errors up to twice the extent of the model grid. This is likely driven by the saturation in the models, discussed further in Section 2.3.1. As with the global measurements in Fig 2.8, we find a considerable scatter in our measurements of ∇[α/Fe]. Only $\approx 57\%$ of galaxies remain after applying our selection criteria, and the galaxies that do remain show a much wider distribution compared to ∇Age or ∇[Z/H].

We see in Table 6.1 that these quality cuts have a negligible effect on the median gradients of the samples. Additionally, the error-weighted fits we perform for our subsequent analysis mean that the inclusion of these galaxies would not change our

conclusions in any measurable way. As such, whilst we cannot claim that our final samples are fully representative of the full sample (considering that galaxies with reliable $\nabla[\alpha/\mathrm{Fe}]$ constitute less than a third of the original sample), we have not knowingly introduced any significant bias into our sample from these additional cuts.

6.1.2 Bayesian Line Fitting

Compared to Section 3.1.4, we improve our method for fitting linear relationships between quantities x and y, by the inclusion of a term accounting for the intrinsic scatter, $\varepsilon_{\mathrm{intr}}$. Adopting $\mathcal{N}(\mu, \sigma^2)$ as shorthand for "the Gaussian distribution with mean μ and variance σ^2", the true relationship can then be parameterised as

$$y = ax + b + \mathcal{N}\left(0, \varepsilon_{\mathrm{intr}}^2\right) . \tag{6.1}$$

As before, we have a set of observations $\{x_i, y_i\}_{i=1}^{N}$, where each observation (x_i, y_i) has known Gaussian uncertainties $(\sigma_{x_i}, \sigma_{y_i})$, and some covariance σ_{xy_i}. This gives a covariance matrix

$$S_i \equiv \begin{pmatrix} \sigma_{x_i}^2 & \sigma_{xy_i} \\ \sigma_{xy_i} & \sigma_{y_i}^2 \end{pmatrix} . \tag{6.2}$$

Assuming that the uncertainties are independent[1], the off-diagonal covariances are all zero, *i.e.* $\sigma_{xy_i} = 0$. We can then follow Hogg et al., 2010 and derive the log-likelihood up to some constant K as

$$\ln(\mathcal{L}) = K - \frac{1}{2}\sum_{i=1}^{N} \frac{\Delta_i^2}{\Sigma_i^2 + \varepsilon_{\mathrm{intr}}^2} - \frac{1}{2}\sum_{i=1}^{N} \ln\left(\Sigma_i^2 + \varepsilon_{\mathrm{intr}}^2\right) , \tag{6.3}$$

[1]As mentioned in Section 3.1.1, this is not necessarily true when fitting simple stellar population (SSP) parameters as a function of velocity dispersion. Nevertheless, we still assume that the covariance is negligible in all cases throughout this chapter.

where

$$\Sigma_i^2 \equiv (a\sigma_{x_i})^2 + \sigma_{y_i}^2 \,, \tag{6.4}$$

$$\Delta_i \equiv ax_i + b - y_i \,. \tag{6.5}$$

We estimate the best-fitting parameters a, b, and $\varepsilon_{\rm intr}$, and their associated uncertainties in the same manner as in Section 5.2. The only difference here is that we modify our choice of priors, to obtain maximally uninformative priors[2]. We therefore follow Jeffreys, 1946 and VanderPlas, 2014 in constructing flat priors p in the transformed variables $(\theta, b_\perp) \equiv (\arctan(a), b\cos(\theta))$. We also select a log-uniform prior on $\varepsilon_{\rm intr}$, resulting in

$$p(a,b) \propto \left(1+a^2\right)^{-3/2} , \tag{6.6}$$

$$p(\ln \varepsilon_{\rm intr}) \propto \begin{cases} 1 & \text{if } -3 < \ln\left(\varepsilon_{\rm intr}/k\right) < 3 \,, \\ 0 & \text{otherwise} \,, \end{cases} \tag{6.7}$$

where k is a constant depending on the SSP parameter,

$$k = \begin{cases} 1\,\text{Gyr} & \text{for Age}, \\ 0.1 & \text{for [Z/H]}, \\ 0.05 & \text{for } [\alpha/\text{Fe}]. \end{cases} \tag{6.8}$$

Compared to the EMCEE sampler in Section 5.2, typical autocorrelation times for fits using this method are $\sim$100 steps.

[2] A flat prior on the gradient of a line, *i.e.* drawing samples evenly-spaced in terms of the gradient, will highly favour very steep gradients.

Measurement	a	b	$\varepsilon_{\rm intr}$
∇Age	-1.9 ± 0.7	3.4 ± 1.4	3.23 ± 0.11
$\text{Age}\big\vert_{\text{R=R}_\text{e}}$	-	-	-
∇[Z/H]	-0.21 ± 0.06	0.02 ± 0.12	0.294 ± 0.009
$\text{[Z/H]}\big\vert_{R=R_\text{e}}$	0.54 ± 0.05	-1.31 ± 0.11	0.158 ± 0.004
$\nabla[\alpha/\text{Fe}]$	0.04 ± 0.04	-0.08 ± 0.08	0.072 ± 0.006
$[\alpha/\text{Fe}]\big\vert_{R=R_\text{e}}$	0.389 ± 0.015	-0.614 ± 0.033	0.058 ± 0.002

Table 6.2: The best-fitting linear relations of the form $y = ax + b$, for all measurements as a function of the velocity dispersion σ_e, displayed in Fig. 6.4. $\varepsilon_{\rm intr}$ is the intrinsic scatter in the relationship, and is covered in more detail in Section 6.1.2. We do not fit to $\text{Age}\big\vert_{\text{R=R}_\text{e}}$ due to the considerable scatter, and similarly, the fit for $\text{[Z/H]}\big\vert_{R=R_\text{e}}$ only includes galaxies where $\log_{10}\left(\sigma_\text{e}/\text{km s}^{-1}\right) \geq 2.0$.

6.2 Correlations With Velocity Dispersion

We begin by considering the dependence of both the stellar population gradients (∇X) and the intercepts at $R = R_\text{e}$ ($X|_{R=R_\text{e}}$) on σ_e, the stellar velocity dispersion measured within R_e. The resulting distributions are displayed in Fig. 6.4. For each measured parameter, we fit a linear relationship, using the method detailed in Section 6.1.2, with the results shown in Table 6.2. Due to the large intrinsic scatters, and complex behaviours, we do not attempt to fit the $\text{Age}\big\vert_{\text{R=R}_\text{e}}$-$\sigma_\text{e}$ relationship, and only fit to $\text{[Z/H]}\big\vert_{R=R_\text{e}}$ for $\log_{10}\left(\sigma_\text{e}/\text{km s}^{-1}\right) \geq 2$.

For the age gradients, we find that there is no clear relation with σ_e. Whilst the gradients show a slight trend towards negative values at higher velocity dispersions, there is a considerable amount of uncertainty on the intercept, and a large intrinsic scatter in the relation. Whilst the median 1σ uncertainty is considerable ($\delta\left(\nabla\text{Age}\right) = 3\,\text{Gyr}$), there is no clear correlation between the magnitude of the uncertainties and either σ_e or ∇Age. Considering these measurement uncertainties, and the scatter in the relation, we conclude that this is consistent with our sample being drawn from an underlying population with flat age gradients.

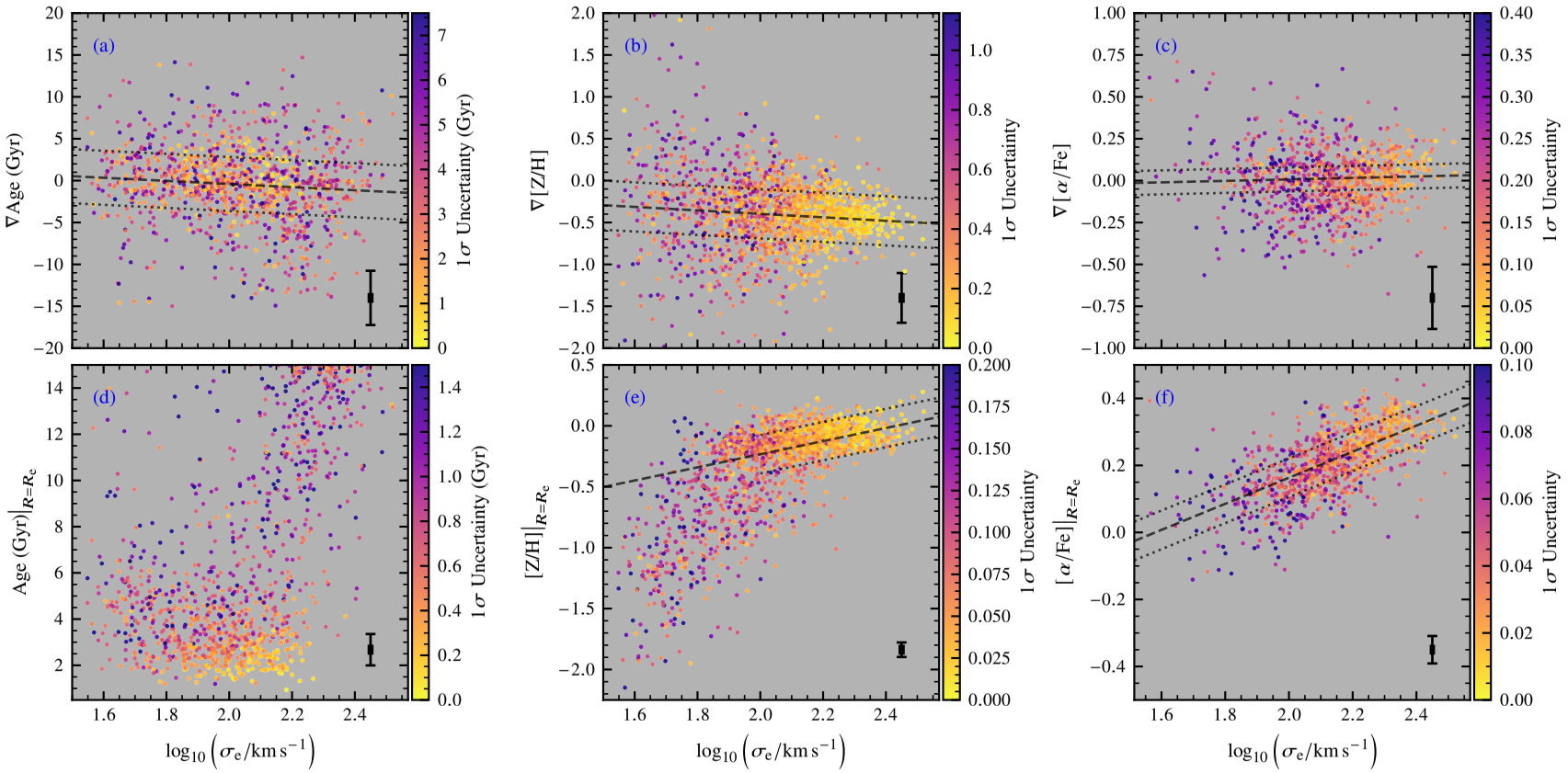


Figure 6.4: The seeing corrected gradients, and their intercepts at $R = R_e$, for age, [Z/H] and [α/Fe] for all possible galaxies in the SAMI survey. We fit each parameter to a linear relationship against the velocity dispersion within 1 R_e, as shown by the dashed lines. The dotted lines delineate the derived intrinsic scatter in each relationship. We colour all points by the magnitude of the 1σ uncertainty on each measurement, and show the median uncertainty in the lower right-hand corner of each panel. We do not fit $[\mathrm{Z/H}]\big|_{R=R_e}$ for $\log_{10}\left(\sigma_e/\mathrm{km\,s^{-1}}\right) < 2$, or $\mathrm{Age}\big|_{\mathrm{R=R_e}}$, as these parameters are not well described by a simple linear relation.

The dependence of the projected intercept at R_e on σ_e is rather more complicated. We see here that the best-fitting results are those at low projected ages, which occur at intermediate velocity dispersions ($1.9 < \log_{10}\left(\sigma_e/\mathrm{km\,s^{-1}}\right) < 2.2$). At lower σ_e, the scatter in the projected ages increases, although the ages themselves remains low. Conversely, at high velocity dispersions, we see the projected ages extending upward, with a clustering at $\mathrm{Age}\big|_{R=R_e} \approx 15\,\mathrm{Gyr}$. We draw attention to previous studies utilising the TMJ11 models, which found a propensity for old galaxies, particularly at low metallicities, to saturate the model grid for the age of the stellar population (Kuntschner et al., 2010). This clustering is therefore an artefact of the models, although we note that the relative behaviour of the stellar populations is still valid. Considering the flat age gradients, this would imply that at higher velocity dispersions, the stellar populations of galaxies are uniformly older than at lower velocity dispersions.

The metallicity gradients are predominantly negative, which can be seen in both Fig. 6.4b and Fig. 6.2. In addition, there is a small but significant negative correlation between $\nabla[\mathrm{Z/H}]$ and σ_e. Following the best-fitting relation described in Table 6.2, $\nabla[\mathrm{Z/H}]$ steepens from -0.34 at $\log_{10}\left(\sigma_e/\mathrm{km\,s^{-1}}\right) = 1.7$, to -0.46 at $\log_{10}\left(\sigma_e/\mathrm{km\,s^{-1}}\right) = 2.3$. However, this correlation is smaller than the intrinsic scatter in the relation, and so it is difficult to draw any firm conclusions. Additionally, the uncertainty on the gradient measurements shows a strong inverse correlation with stellar velocity dispersion, which matches the increased scatter in the relation at low σ_e.

The projected metallicity at R_e shows a complex dependence on the effective velocity dispersion σ_e. Above $\log_{10}\left(\sigma_e/\mathrm{km\,s^{-1}}\right) \approx 2$, the measurements have small uncertainties, and are well fit by a positive linear relation. At lower velocity dispersions, the scatter and measurement uncertainties both increase, whilst $[\mathrm{Z/H}]\big|_{R=R_e}$ decreases sharply. At all velocity dispersions, $[\mathrm{Z/H}]\big|_{R=R_e}$ rarely goes above the solar value of $[\mathrm{Z/H}] = 0$.

The best-fitting linear relation between $\nabla[\alpha/\mathrm{Fe}]$ and σ_e is completely consistent with there being no dependence. Although both the measurement uncertainties and scatter decrease as a function of σ_e, there is a less marked correlation between the two when compared to $\nabla[\mathrm{Z/H}]$. The median uncertainty is considerable, at $\delta\left(\nabla[\alpha/\mathrm{Fe}]\right) = 0.19$, and we suggest that this may have contributed to the lower intrinsic scatter, compared to the other SSP gradients. The effects of the reduced sample size are also evident here, with far fewer galaxies at $\log_{10}\left(\sigma_\mathrm{e}/\mathrm{km\,s^{-1}}\right) < 1.8$ than in the age or metallicity samples.

For the projected $[\alpha/\mathrm{Fe}]$ at R_e, we find a clear correlation between $[\alpha/\mathrm{Fe}]\Big|_{R=R_\mathrm{e}}$ and σ_e, with the estimated slope of 0.389 ± 0.015 consistent with previous measurements using R_e aperture spectra (see Eq. 4.2). This is not unexpected – with predominantly flat radial gradients, we intuitively expect the projected abundance at $1\,R_\mathrm{e}$ to very closely correlate with the integrated abundance within $1\,R_\mathrm{e}$, and detail this further in Appendix A.

6.3 The Stellar Mass-size Plane

We explore the distribution of stellar population gradients on the stellar mass-size plane. Galaxy sizes are taken as the effective elliptical radius, R_e, converted from arcseconds to kpc using the distance determined from the spectroscopic redshift for each galaxy. In Fig. 6.5, we show the distribution of the best-fitting projected SSP parameters at R_e. In the upper panels, we display the raw value, where each point is coloured by the derived SSP parameter. In the lower panels, the points are coloured by a locally-smoothed value, determined using the locally-weighted regression technique (LOESS) of Cappellari et al., 2013. We show both colour schemes here, as they are often complementary – whilst the LOESS method can reveal underlying trends in noisy data, by construction it smooths over both small variations and sharp bound-

aries in a sample. Assuming that the stellar population is virialised, and that the galaxy has a constant density, it can be described by the equation

$$R \approx \frac{GM}{5\sigma^2}, \tag{6.9}$$

where G is the gravitational constant, M the enclosed mass, and σ the velocity dispersion within some radius R (see Appendix B for a detailed derivation). We therefore overlay lines of constant velocity dispersion in Fig. 6.5, at $\sigma_e = 20, 30, 50, 100$, and $200\,\mathrm{km\,s^{-1}}$. Note that these are approximations, and should be used only as an indication of the direction of increasing/decreasing velocity dispersions.

For the full sample, the inferred ages, metallicity, and α-abundance at R_e all increase with increasing stellar mass, and decreasing effective radius. Considering the stellar ages, we see a sharp dichotomy in the raw values that is smoothed over by the LOESS method. This binary distribution is a close match to the behaviour seen in Fig. 6.4. We see that the dividing line between the two populations is parallel to the lines of constant velocity dispersion. However, there appears to be very little large-scale variation outside of this distinction.

In Fig. 6.5e, the contours of constant metallicity very closely follow the lines of constant σ_e. As with $\mathrm{Age}\big|_{R=R_e}$, towards low masses and larger radii, $[\mathrm{Z/H}]\big|_{R=R_e}$ decreases sharply. This metallicity distribution also supports our earlier results, showing the dependency on velocity dispersion in Fig. 6.4. We can see here that the sharp decrease in $[\mathrm{Z/H}]\big|_{R=R_e}$ observed previously is a real feature of our measurements, and not simply a consequence of projecting the R_e-M_* plane to a function of σ_e. The results for $[\alpha/\mathrm{Fe}]\big|_{R=R_e}$ are similar. Whilst the sample covers a much more limited area of the size-mass plane, the projected α-abundance monotonically increases with σ_e, with the scatter in Fig. 6.4 appearing to be driven by the intrinsic scatter rather than projection effects.

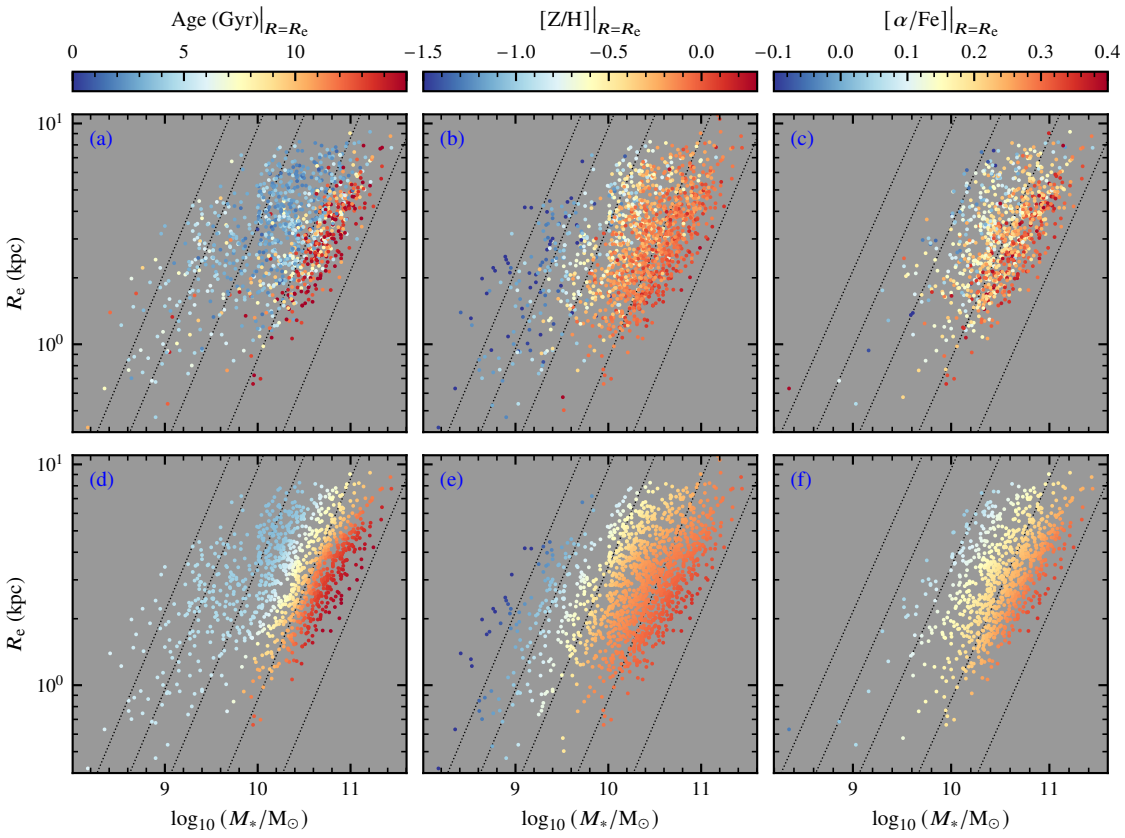


Figure 6.5: The distributions of the best-fitting projected SSP parameters at R_e, in the size-mass plane. The dashed lines indicate lines of constant velocity dispersion, at $\sigma_e = 20, 30, 50, 100$, and $200\,\mathrm{km\,s^{-1}}$ from left to right. In the upper panels, we show the raw results. In the lower panels, all points are coloured by the locally-smoothed values using the LOESS method of Cappellari et al., 2013.

Similar to Fig. 6.5, in Fig. 6.6, we show the distributions of the radial gradients. Where the best-fitting projected SSP parameters at $R = R_e$ showed a simple increase across the plane, the behaviour of the best-fitting gradients is far more complex. Compact, low-mass galaxies typically have very small positive age gradients, flat-to-positive metallicity gradients, and strongly positive [α/Fe] gradients, implying either more recent star formation in the galaxy centres, or a process of outside-in quenching. The variation in ∇Age appears to occur predominantly along the lines of constant velocity dispersion. ∇[Z/H], whilst also decreasing from compact low-mass galaxies towards extended high-mass galaxies, varies primarily along lines of slopes shallower

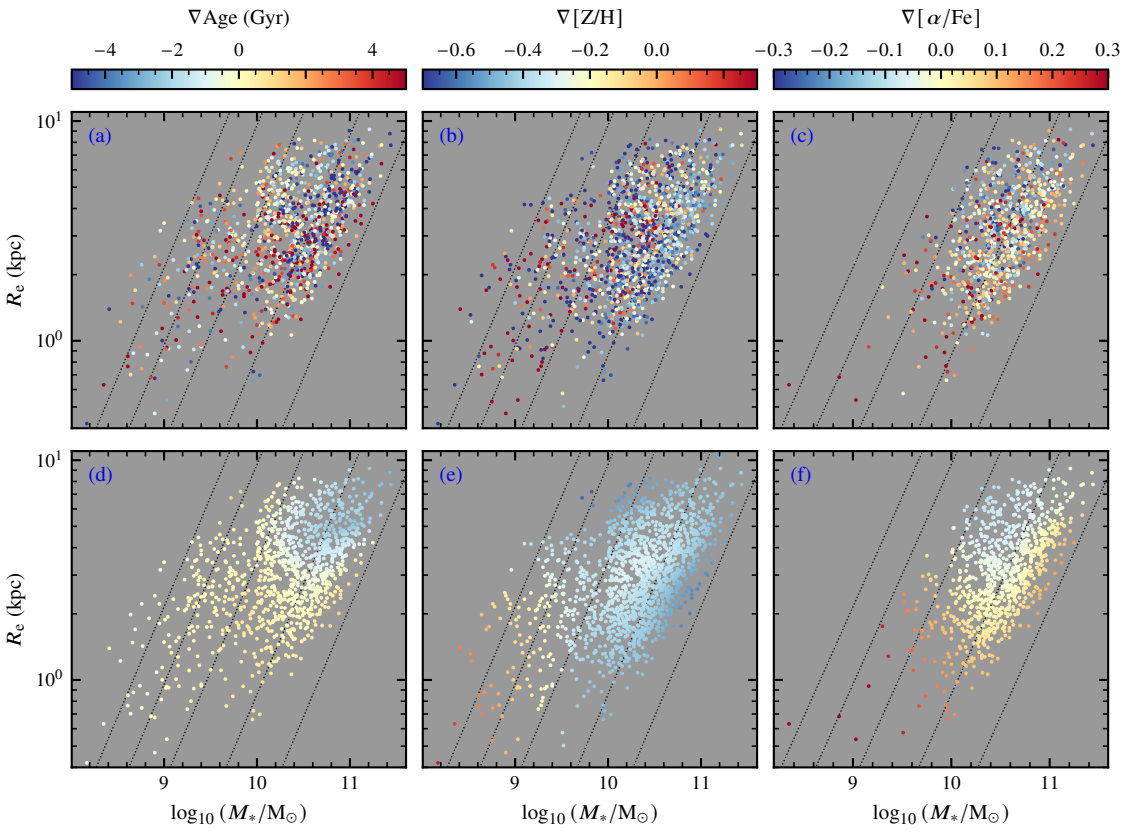


Figure 6.6: As Fig. 6.5, but for the best-fitting stellar population gradients. The limits of the colour maps are chosen to highlight the variations in the gradients, and have truncated the ranges of the raw values.

than that of the lines of constant σ_e. We highlight the small additional variation, which appears to show a secondary local maximum in ∇[Z/H] at intermediate velocity dispersions. Given the significant scatter in the underlying values, we suggest that this is most likely an artefact of the LOESS method, although cannot rule out that it indicates an unexplored extra parameter.

The [α/Fe] gradients show variation in two distinct directions, in different areas of the size-mass plane. At low masses and small effective radii, galaxies show positive [α/Fe] gradients, indicating lower central values. This decreases at fixed velocity dispersion, where intermediate-mass galaxies with large radii show negative ∇[α/Fe]. For galaxies with large radii, ∇[α/Fe] flattens, and eventually becomes positive again at the highest stellar masses. Behaviour similar to this has been seen before in other

studies (Li et al., 2018), and typically indicates the sample consists of a combination of two different populations, each with a distinct behaviour in the size-mass plane (*e.g.* early- and late-type galaxies). At a fixed intermediate velocity dispersion (*e.g.* $\sigma_e = 100\,\mathrm{km\,s^{-1}}$), the variation in $\nabla[\alpha/\mathrm{Fe}]$ is ≈ 0.15. This variation in the size-mass plane can therefore account for the estimated intrinsic scatter $\varepsilon_{\mathrm{intr}} \approx 0.06$ observed after projection to the $[\alpha/\mathrm{Fe}]$-σ_e space in Fig. 6.4.

6.3.1 Optical Morphology

Our first check is to separate the full gradient sample into early-type galaxies (ETGs), and late-type galaxies (LTGs), following our analysis in Section 3.2.3 which demonstrated that these populations had distinct stellar populations after controlling for velocity dispersion. The samples are separated based on the optical morphological classifications from Cortese et al., 2016, and we define ETGs as E-S0 ($\mathrm{MTYPE} \leq 1$), and LTGs as Sa+ ($\mathrm{MTYPE} \geq 2$). We aim for sample purity over size, and as such do not include the S0/Sa galaxies ($\mathrm{MTYPE} = 1.5$) in either sample, due to the ambiguity over their precise classification. We stress that the conclusions drawn are not affected by the presence of these galaxies in either subsample.

The distributions of the best-fitting projected SSP intercepts are shown in Fig. 6.7, where we display the locally-smoothed values for each separate sample. Metallicity and α-abundance show little difference from the results for the full sample in Fig. 6.5, with ETGs and LTGs both showing a monotonic increase of the SSP intercept with increasing stellar velocity dispersion. Considering the SSP values themselves, ETGs and LTGs appear to form a continuous distribution here, with no distinction between the two samples in the region where they overlap. In contrast, $\mathrm{Age}\big|_{\mathrm{R=R_e}}$ is clearly distinct in each sample, with Figs. 6.7a and d displaying almost no overlap in colour. In LTGs, we see no obvious variation across any part of the size-mass plane, with galaxies uniformly having $\mathrm{Age}\big|_{\mathrm{R=R_e}} < 6\,\mathrm{Gyr}$, with a median age of 3.3 Gyr. ETGs,

whilst being uniformly older (median of 10.9 Gyr), even in the region of overlap, show a slight progression towards younger ages with decreasing σ_e, although this is highly uncertain due to the sparse sampling at lower masses.

The best-fitting gradients, displayed in Fig. 6.8, show a similar distinction between ETGs and LTGs. For LTGs, the steepest negative SSP gradients all occur at high masses and large effective radii, although the variation is not quite so uniform. For ∇Age, gradients appear to flatten and turn slightly positive with decreasing stellar mass, and display less variation with R_e. For ∇[Z/H] and $\nabla[\alpha/\mathrm{Fe}]$, the gradients increase with both decreasing stellar mass and decreasing effective radius, and therefore show significant variation at fixed velocity dispersion. For ETGs, the direction of maximum variation (for all three SSP parameters) is almost perpendicular to that for LTGs. ∇Age is lowest for ETGs with large effective radii, but trends weakly positive for more compact galaxies, again showing only minimal variation with R_e. The median age gradient is slightly shallower in ETGs (-0.2 *vs.* -0.4 in ETGs and LTGs respectively), although not by a significant margin. Whilst metallicity gradients in ETGs display little to no variation across the size-mass plane, the gradients are in general steeper (median of -0.44) than in LTGs (median of -0.36). Similarly, in ETGs $\nabla[\alpha/\mathrm{Fe}]$ flattens from slightly positive gradients, with both decreasing mass and increasing effective radii, and the median gradient of 0.03 is again higher than in LTGs (-0.03).

6.3.2 Environmental Density

We also separate galaxies by their local environmental density in the same manner as in Section 3.2, showing the best-fitting projected intercepts and gradients in Figs. 6.7 and 6.8 respectively. In general, the results for the environmental separation largely track the previous results for morphological separation, due to the high degree of crossover between ETGs and high-density environments, and LTGs and low-density

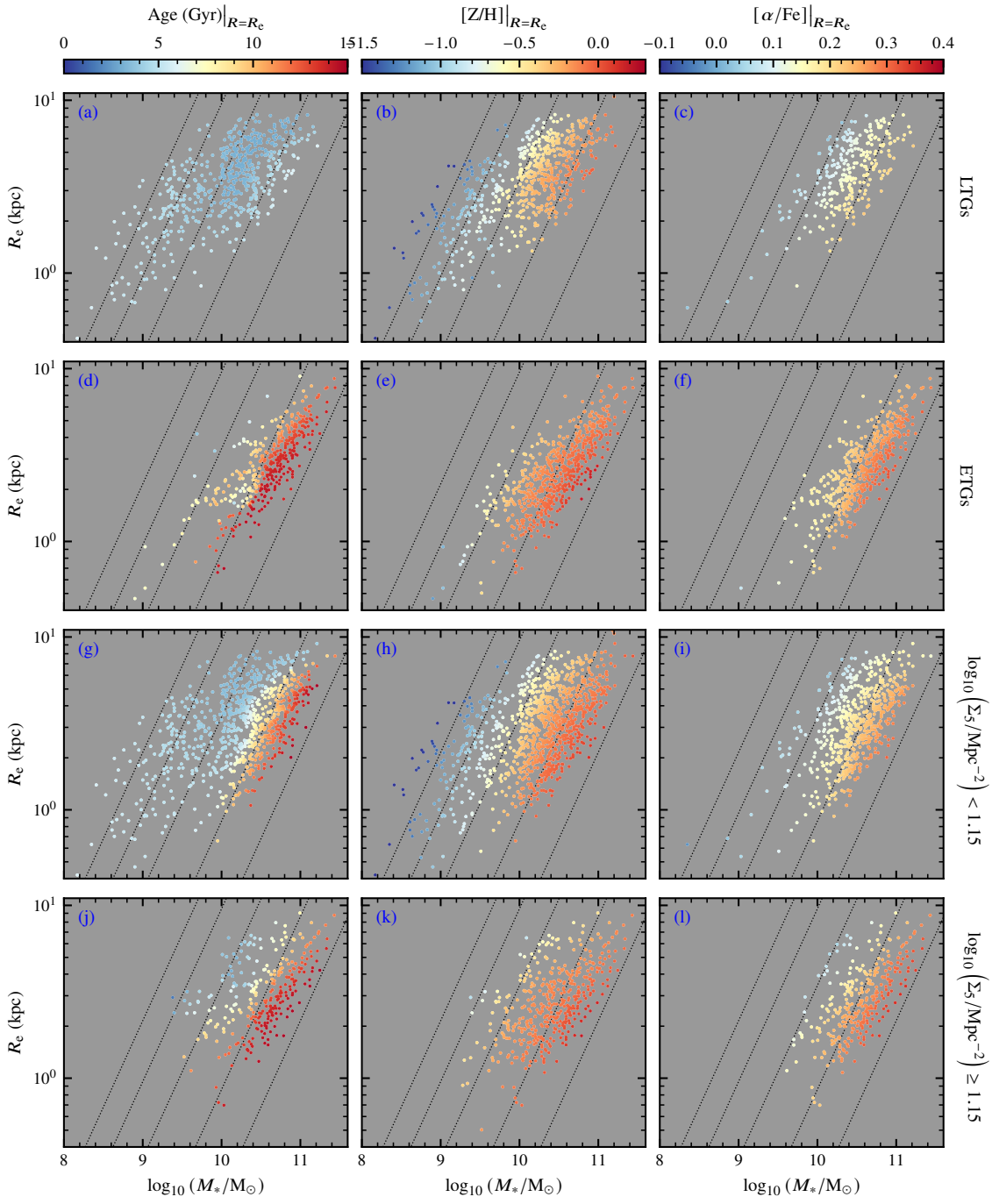


Figure 6.7: As Fig. 6.5, showing the distribution of the best-fitting projected SSP parameters at R_e, but separated into LTGs (a-c), ETGs (d-f), and galaxies in low- and high-density environments (g-i, and j-l respectively). All values are locally-smoothed using the LOESS method.

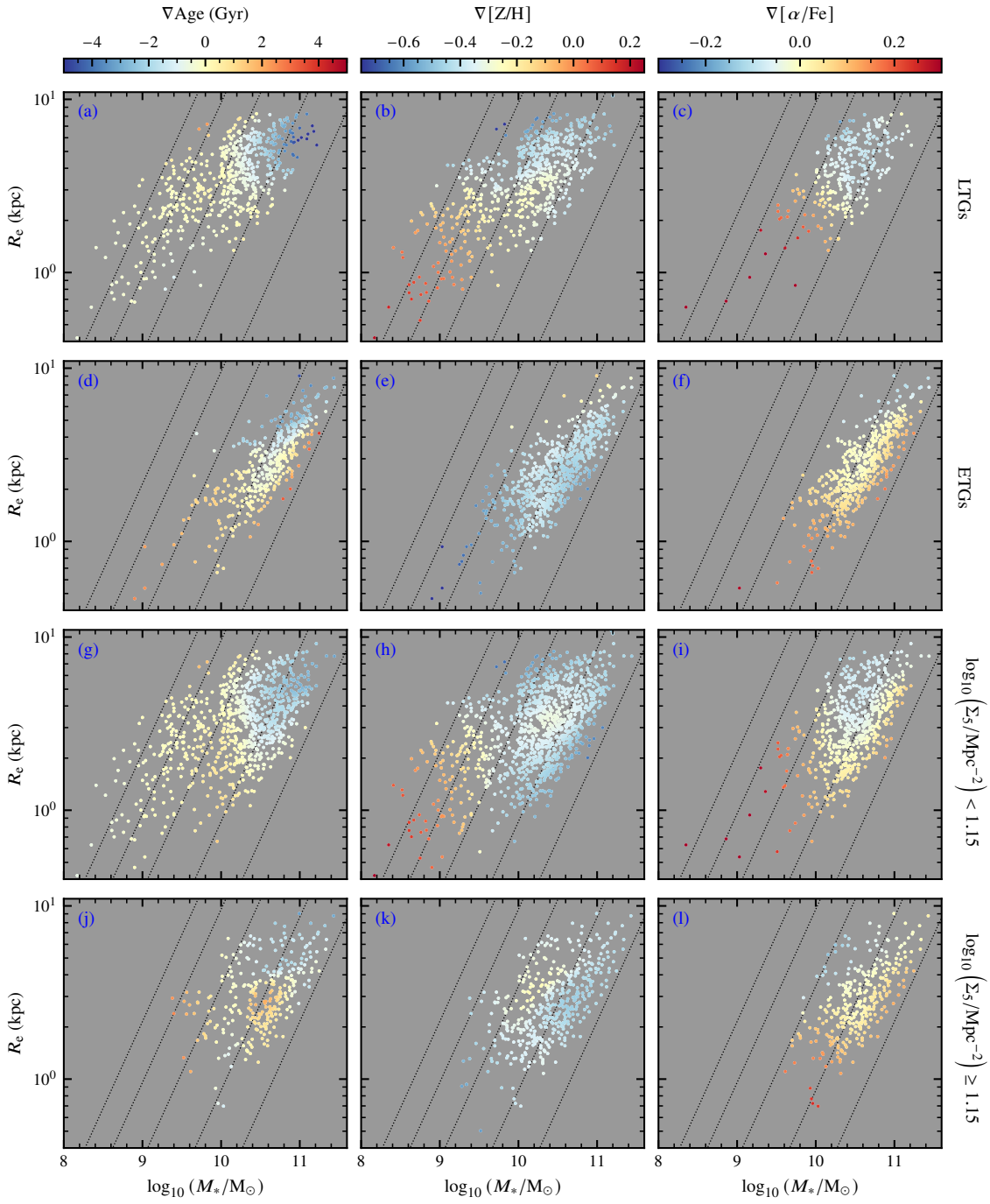


Figure 6.8: As Fig. 6.6, showing the distribution of the best-fitting SSP gradients, but separated into LTGs (a-c), ETGs (d-f), and galaxies in low- and high-density environments (g-i, and j-l respectively). All values are locally-smoothed using the LOESS method.

environments. Notable exceptions include the best-fitting projected ages at $R = R_e$, where galaxies in both environments are older with increasing velocity dispersion, in the same manner as in Fig. 6.5. In addition, although there is significant variation in the age gradients in Fig. 6.8j, there is no clear structure or direction.

6.4 Radial Profiles

To assess the reliability of our results in Section 6.3, and provide a point of comparison with other studies, we examine the radial profiles of the stellar populations in detail. Since we are relying on the underlying stellar population measurements, rather than the derived gradients, the results we present here use the sample selection from Fig. 6.1, rather than the reduced samples displayed in Fig. 6.2, although this does not affect the results. As before, we group galaxies by their optical morphology into ETGs and LTGs, and simultaneously separate these by their local environmental density, giving four non-overlapping groups:

1. ETGs in high-density environments (HDEs): MTYPE ≤ 1 and $\log_{10}\left(\Sigma_5/\mathrm{Mpc}^{-2}\right) \geq 1.15$.
2. ETGs in low-density environments (LDEs): MTYPE ≤ 1 and $\log_{10}\left(\Sigma_5/\mathrm{Mpc}^{-2}\right) < 1.15$.
3. LTGs in HDEs: MTYPE ≥ 2 and $\log_{10}\left(\Sigma_5/\mathrm{Mpc}^{-2}\right) \geq 1.15$.
4. LTGs in LDEs: MTYPE ≥ 2 and $\log_{10}\left(\Sigma_5/\mathrm{Mpc}^{-2}\right) < 1.15$.

The distribution of these groups in the stellar mass-size plane is shown in Fig. 6.9.

Since we know that the SSP gradients vary across the stellar mass-size plane, we aim to group together similar galaxies to avoid smoothing over underlying trends. We separate galaxies into nine distinct bins, with three mass bins,

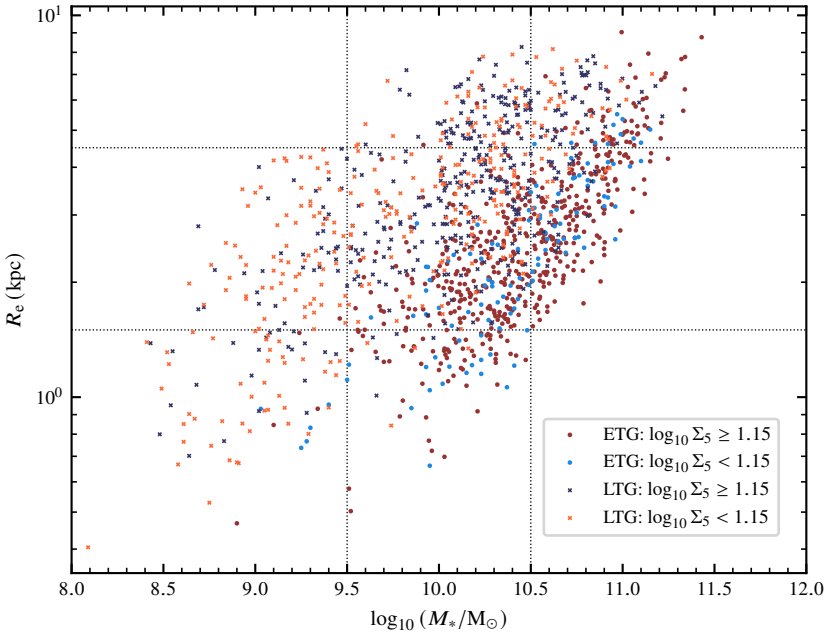


Figure 6.9: The distribution of galaxies in the size-mass plane. The colour and shape of each point indicate the morphology and environment of the galaxy, as described in the legend (inset). The dotted lines indicate the bounding regions used to generate subsamples across the size-mass plane.

- Low-mass: $\log_{10}(M_*/\mathrm{M}_\odot) < 9.5$,
- Intermediate-mass: $9.5 \leq \log_{10}(M_*/\mathrm{M}_\odot) < 10.5$,
- High-mass: $\log_{10}(M_*/\mathrm{M}_\odot) \geq 10.5$,

and three radii bins,

- Compact: $R_\mathrm{e} < 1.5\,\mathrm{kpc}$,
- Intermediate: $1.5 \leq R_\mathrm{e} < 4.5\,\mathrm{kpc}$,
- Extended: $R_\mathrm{e} \geq 4.5\,\mathrm{kpc}$.

We display these selection criteria in Fig. 6.9. As a result of the existing sample selection, there are no extended low-mass galaxies, nor are there any compact high-mass galaxies for any of the subsamples we consider.

For each of the seven remaining bins, we calculate the average radial profile for each subsample of morphology and environment as follows. First, we take the raw stellar population parameters, and apply the same cuts as before, *i.e.* removing any measurements where the errors span the model grid. Second, we use a linear radial sampling of $0.2\,R_{\rm e}$, and take the mean of both the bin galactocentric radii and the SSP parameters, weighted by the inverse variance as

$$\bar{x} = \frac{\sum_{i=1}^{N} w_i x_i}{\sum_{i=1}^{N} w_i}\,, \tag{6.10}$$

for N values x_i with weights $w_i = 1/\sigma_{x_i}^2$, where σ_{x_i} is the uncertainty on each x_i. The uncertainty on the mean is calculated in a similar manner,

$$\sigma_{\bar{x}} = \frac{1}{\sum_{i=1}^{N} w_i} \sqrt{\sum_{i=1}^{N} \left(w_i \sigma_{x_i}\right)^2}, \tag{6.11}$$

which reduces to the well known standard uncertainty on the mean, if all $w_i = 1$ and all measurements have the same uncertainty $\sigma_i = \tilde{\sigma}$.

We note that some caution must be applied when examining the radial profiles. The differing physical extents of galaxies in every region of the size-mass plane means that the number of galaxies contributing to each radial bin is not constant. We mitigate this by requiring a minimum of 10 galaxies in each subsample of the size-mass plane before calculating the radial profile, in order to avoid outliers biasing the results. We also note that the selection in physical effective radius leads to grouping galaxies together with a similar angular extent, and hence large variations in size are extremely unlikely.

An additional caveat is that the results here are not corrected for seeing, as they are calculated from the raw SSP measurements, and hence the slope is not guaranteed to match the derived gradients in earlier sections. The compact galaxies will be more heavily affected than the extended galaxies, due to their small angular sizes relative

to the FWHM of the seeing. There is no simple mitigation for this, and hence we present the results as they are, with the radial profiles of age, [Z/H], and [α/Fe] shown in Figs. 6.10, 6.11, and 6.12 respectively. We also focus on the relative behaviour of the stellar populations rather than the absolute offsets between galaxies in different regions of the size-mass plane. For comparison, in each region throughout Figs. 6.10, 6.11, and 6.12, we show the equivalent mean gradient, calculated from the seeing-corrected values discussed in Section 6.3, as a point of reference.

We begin by considering the radial profiles of light-weighted stellar ages. For ETGs, in all bins in the size-mass plane, galaxies in high-density environments are consistently older than those in low-density environments. This discrepancy is largest for both compact intermediate-mass galaxies, and extended high-mass galaxies. The gradients of the radial profiles appear to evolve with both effective radius and stellar mass. Compact ETGs in LDEs show a slightly positive age gradient, although this is not fully corroborated by those in HDEs. At intermediate sizes, ETGs have nearly flat age profiles, with only a small difference ($\approx 2\,\mathrm{Gyr}$) between environments. At this fixed size, the galaxies are older and have slightly negative age gradients with increasing stellar mass. Finally, extended, high-mass galaxies show negative age profiles, with the centres of ETGs in HDEs having the oldest populations observed in our entire sample. This trend in gradients matches our observations in Figs. 6.8d, where the age gradients invert at intermediate sizes and masses, irrespective of environment. Due to the progression of ∇Age across the plane, the oldest stellar populations at R_e are found in compact high-mass galaxies, consistent with Fig. 6.7d.

For LTGs, the overall trend in age gradients is similar. Compact, low-mass galaxies have positive age gradients, whereas extended, high-mass galaxies decrease in age as a function of galactocentric radius. However, we do not see such a clear variation of the mean ages at $R = R_\mathrm{e}$ with any parameter. Whilst the lowest-mass LTGs have the highest mean ages at $R = R_\mathrm{e}$, there is no clear monotonic trend of decreasing

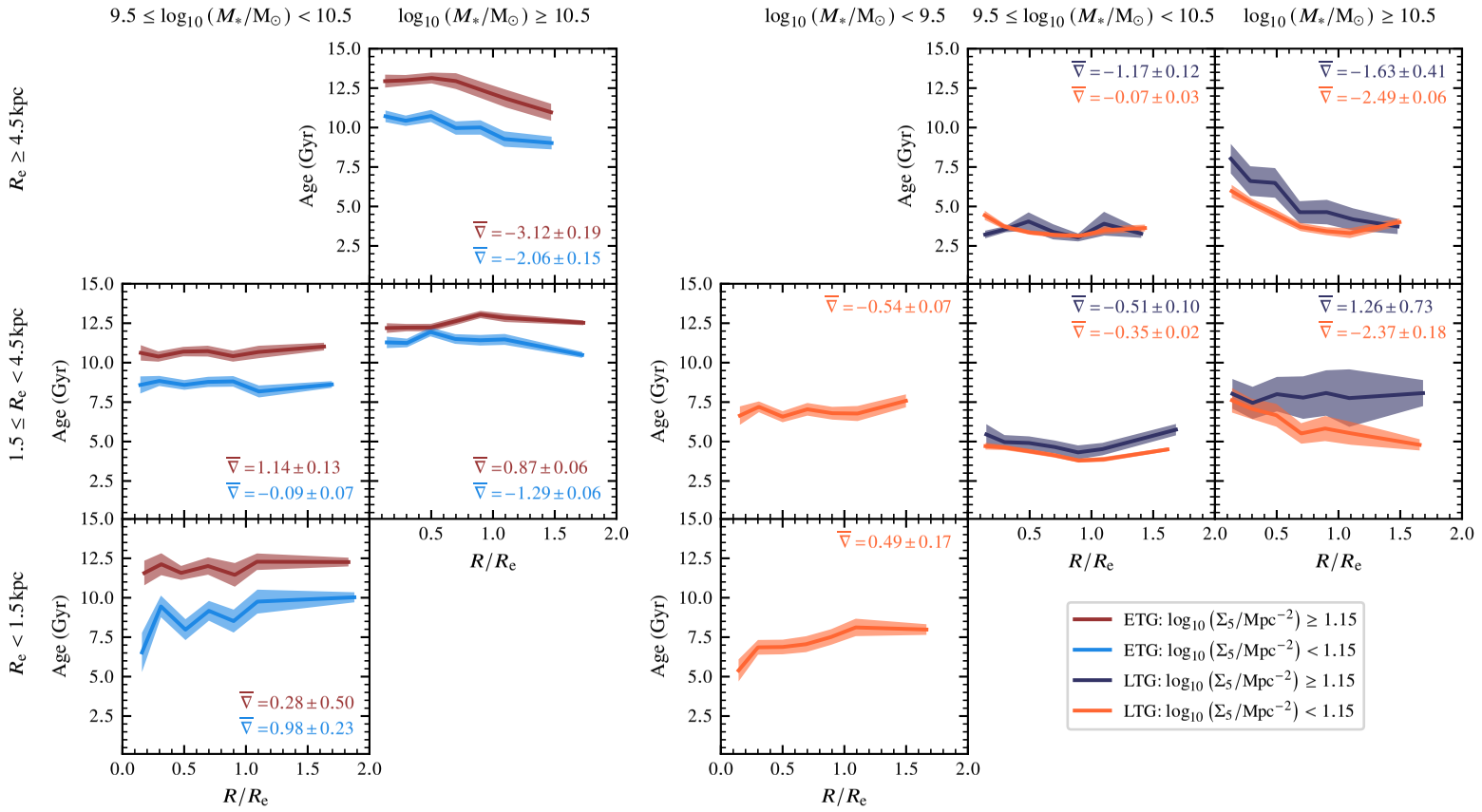


Figure 6.10: The mean SSP-equivalent ages as a function of galactocentric radius, for different bins of stellar mass and effective radius (see the row and column labels). The shaded regions denote the standard error on the mean age, calculated at each radius. Galaxies are separated by morphology and environment, as indicated in the legend, with further details given in the text. Inset in each panel, we quote the mean best-fitting seeing-corrected gradients from Section 6.3, for the same sample.

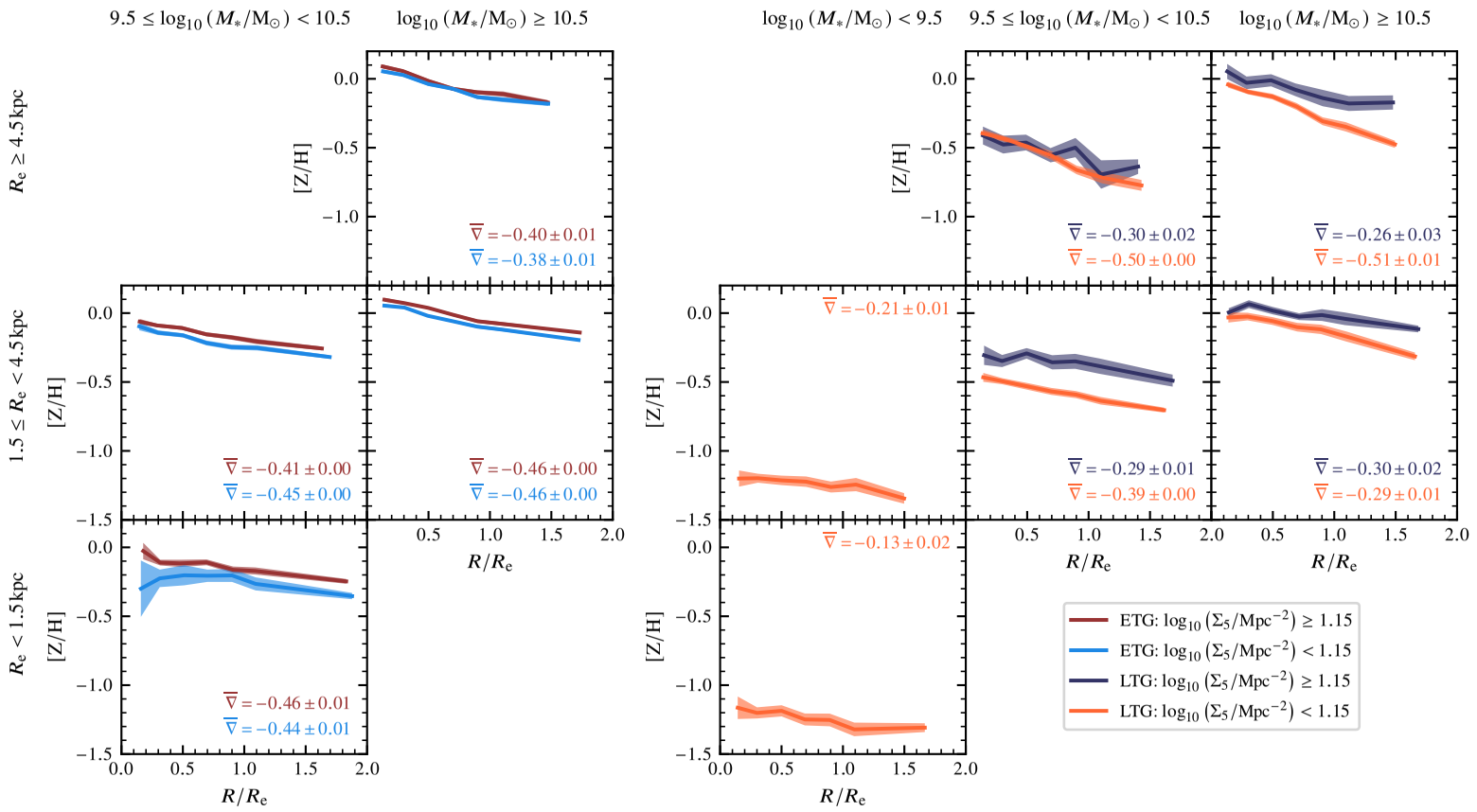


Figure 6.11: As Fig. 6.10, but for the SSP-equivalent metallicity, [Z/H].

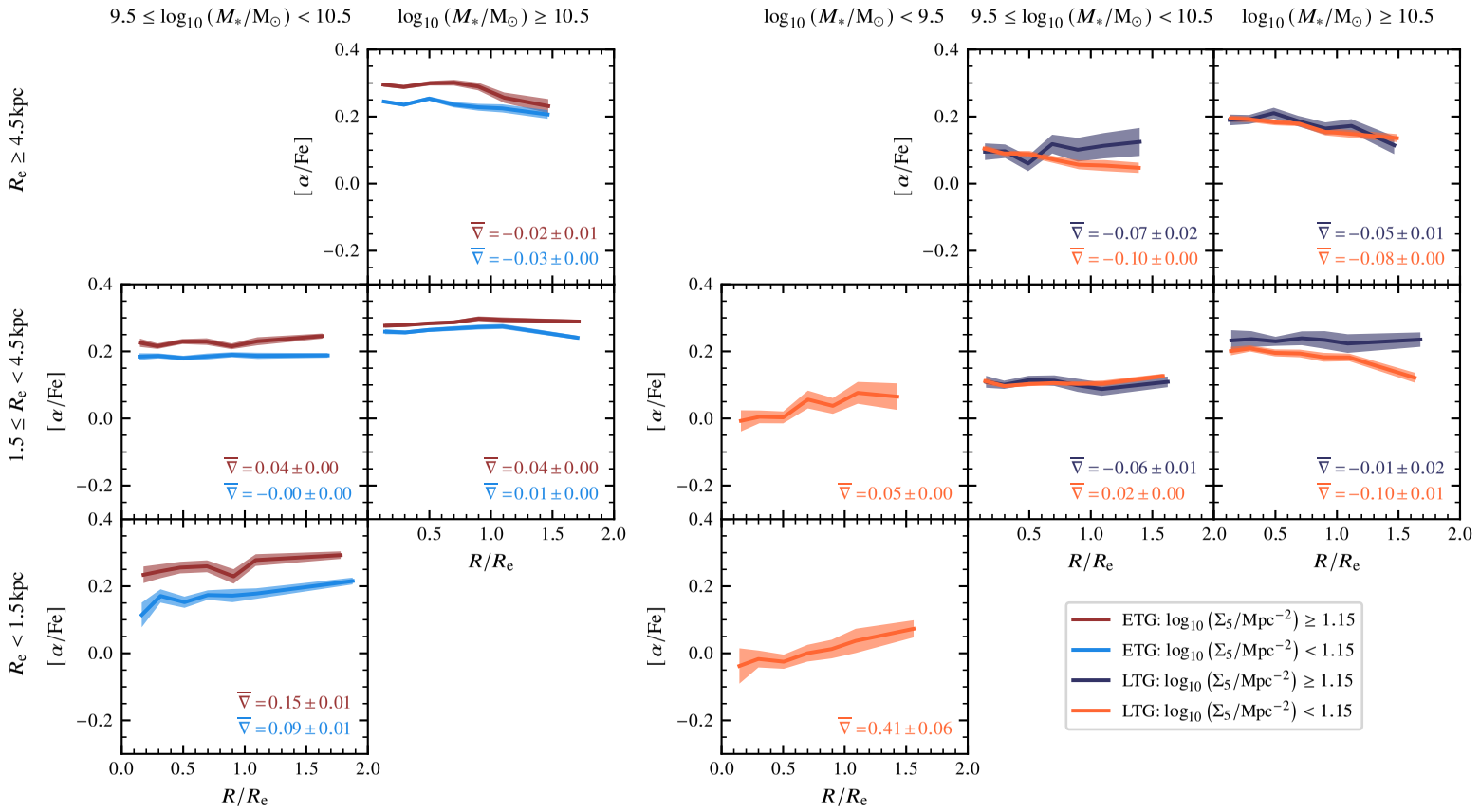


Figure 6.12: As Fig. 6.10, but for the SSP-equivalent α-abundance, [α/Fe].

ages at $R = R_e$ with increasing stellar mass. The ages of LTGs in low and high density environments are mostly indistinguishable, except intermediate-sized galaxies at high mass, where those in low-density environments are increasingly younger as a function of galactocentric radius. However, across the entire size-mass plane, and in all environments, LTGs are uniformly younger than ETGs, by $\gtrsim 2$ Gyr. We also draw attention to the non-linearity in the age profiles of high-mass LTGs (see Section 6.5.2 for a more detailed discussion), noting that the fitted gradients are therefore less likely to be reliable in this region.

For the radial metallicity profiles in Fig. 6.11, we find very little variation in the gradients of ETGs, matching our seeing-corrected measurements in Fig. 6.8e. Whilst ETGs in high density environments have slightly higher metallicities on average, the difference is small (Δ[Z/H] < 0.1). For LTGs, we find a slight correlation between the metallicity gradient and both size and mass, but only for galaxies in LDEs. Compact, low-mass LTGs show nearly flat metallicity profiles, which become increasingly negative as both stellar mass and effective radius increase, as in Fig. 6.8b. LTGs in HDEs have higher metallicities on average than those in LDEs, although this offset is not uniform, and displays no clear trend across the size-mass plane. The greatest offset is for intermediate-size and mass galaxies, with Δ[Z/H] ≈ 0.2.

We find a significant shift in the mean metallicities at $R = R_e$ across the size-mass plane, primarily driven by LTGs. In ETGs the shift is small, and correlates with increasing stellar mass and decreasing R_e. This can also be seen in Fig. 6.7e for the best-fitting $[\mathrm{Z/H}]\big|_{R=R_e}$, where we note that the change is ≈ 0.2 dex across the ETG sample. Conversely, in LTGs, for decreasing stellar mass [Z/H] drops substantially at all galactocentric radii, and to a lesser extent for increasing R_e. At fixed mass, the mean [Z/H] is consistent across all galaxy sizes in the centres. Moving from compact to extended galaxies, we find that the steepening metallicity gradient causes a decrease in the mean [Z/H] at $R = R_e$, driving the relationship seen in Fig. 6.7b.

At fixed size and mass, we find that ETGs display consistently higher [α/Fe] than LTGs, shown in Fig. 6.12. ETGs in HDEs are significantly α-enhanced over those in LDEs in all size and mass bins, with the greatest offset found for compact galaxies, consistent with our results in Section 3.2.4. Beyond that, the variations in [α/Fe] across the size-mass are small, and more uncertain. The radial profiles, alongside the quoted means for the seeing-corrected gradients, suggest that for both ETGs and LTGs, ∇[α/Fe] moves from positive to negative, going from compact low-mass galaxies to high-mass extended galaxies, consistent with the behaviour of ∇Age. At intermediate sizes and stellar masses, where the majority of galaxies in our sample lie, the gradients are nearly flat. This corroborates the results of Fig. 6.8c,f, where intermediate-size and mass galaxies have flat gradients, steepening towards either extreme of the size-mass plane. This leads to $[\alpha/\mathrm{Fe}]\big|_{R=R_\mathrm{e}}$ increasing as M_* increases, and R_e decreases.

6.5 Discussion

6.5.1 Comparison with Previous Studies

6.5.1.1 Global Properties

As in Section 3.3.1, we note that the absolute values of stellar population models are not always well constrained, and can suffer from systematic offsets between models (McDermid et al., 2015; Scott et al., 2017, hereinafter S17). We therefore focus on the trends and scaling relations, as the relative behaviour of the derived populations remains consistent, and a full evaluation of the quantitative offsets is out of scope of this research.

Our projected SSP parameters at R_e will not be an exact match to properties integrated within an effective aperture due to the radial variation of the populations,

even if the light distributions are identical. However, in the case where the SSP radial gradients show only small variations, as demonstrated in Fig. 6.8, the global properties should correlate with our measurements, offering a useful point of comparison (for more details, see Appendix A). Considering the dependence of our measurements on the effective velocity dispersion σ_e in Fig. 6.4, we find a close match to Fig. 5 of S17. The derived linear relations (displayed in Table 6.2) fall between the estimates from S17 for both the Galaxy and Mass Assembly (GAMA; Driver et al., 2011) and cluster samples. However, whilst the scatter on our [α/Fe]-σ_e relationship is significantly reduced, we find remarkably different distributions for the stellar ages. Where S17 find a continuous relationship (albeit expressed as log Age), we see instead a strong dichotomy between younger galaxies, and older galaxies with high σ_e. As noted previously, this may be due to our choices of stellar population models – whilst S17 switched to the S07 models for measuring ages, we used the models of TMJ11 throughout.

There are a great many other studies on global stellar populations, both as a function of mass, or in the full size-mass plane. We focus here on some of the more recent literature, including research from other members of the SAMI team, such as S17, Barone et al., 2022 (hereinafter B22), and Vaughan et al., 2022 (hereinafter V22). We also compare to studies utilising Mapping Nearby Galaxies at Apache Point Observatory (MaNGA; Li et al., 2018, hereinafter L18), and Large Early Galaxy Astrophysics Census (LEGA-C; Beverage et al., 2021, hereinafter B21). Whilst S17 use a line-index method to measure the stellar populations, in a very similar manner to our own method (a full comparison can be found in Section 3.1.3), B22, V22, L18, and B21 all use complementary, but different, full-spectrum fitting methods.

Figs. 9 and 10 in S17 are a good analogue to our separation by environment in the lower panels of Fig. 6.7, although there is some overlap, since our HDE sample also includes a fraction of the highest density groups from GAMA (see Section 1.3.3.2).

Where S17 find that age shows a strong trend with galaxy stellar mass surface density ($\propto M_*/{R_\mathrm{e}}^2$) in their full sample, we find that the projected ages of galaxies in both environments, shown in Fig. 6.7g,j, appear to correlate most strongly with effective velocity dispersion σ_e. B22, focussing only on quiescent galaxies, reach a similar conclusion to S17, finding that age correlates most strongly with $M_*/{R_\mathrm{e}}^2$. The evidence from L18 suggests that the variation is primarily with σ_e, whereas at higher redshifts, B21 find no significant correlation with any structural parameter.

To assess this, we separate our gradient samples by both morphology and environment, following the divisions established in Section 6.4. For each sample, we calculate the Spearman rank correlation coefficient ρ between our seeing-corrected best-fitting SSP intercepts at R_e, $X|_{R=R_\mathrm{e}}$, and the structural parameters $\log_{10}(M_*/\mathrm{M}_\odot)$, $\log_{10}\left(\frac{M_*/R_\mathrm{e}}{\mathrm{M}_\odot\,\mathrm{kpc}^{-1}}\right)$, and $\log_{10}\left(\frac{M_*/{R_\mathrm{e}}^2}{\mathrm{M}_\odot\,\mathrm{kpc}^{-2}}\right)$. We note the proportionality between $\log_{10}\left(\frac{M_*/R_\mathrm{e}}{\mathrm{M}_\odot\,\mathrm{kpc}^{-1}}\right)$ and velocity dispersion σ_e (see Eq. 6.9), and that this parameter can also be used as a proxy for the depth of the gravitational potential Φ. The uncertainties on ρ are estimated following a bootstrapping procedure, where we generate 1000 iterations of each sample, drawing each datapoint from a Gaussian distribution with width equal to the uncertainty on each measurement. We take the standard deviation of the distribution of ρ as the 1σ uncertainty, σ_ρ, with the results shown in Table. 6.3.

Considering only the ages, we find that although the full sample shows the strongest correlation with mass surface density, this is an artefact of the differing behaviour of the subsamples. The ages of ETGs in HDEs correlate closely with M_*/R_e and $M_*/{R_\mathrm{e}}^2$, whereas the ages of those in LDEs correlate best with M_*/R_e. However, whilst there is no clear correlation for LTGs in HDEs, those in LDEs show an anti-correlation with stellar mass instead. Whilst this might seem unexpected based on the predominantly flat relationship shown in Fig. 6.7a, we note that it is consistent with the radial profiles in Fig. 6.10, where the age at $R = R_\mathrm{e}$ decreases with increasing M_*.

SSP Parameter	Sample		$n_{\rm gal}$	$\log(M_*/\mathrm{M}_\odot)$	$\log\left(\frac{M_*/R_\mathrm{e}}{\mathrm{M}_\odot\,\mathrm{kpc}^{-1}}\right)$	$\log\left(\frac{M_*/{R_\mathrm{e}}^2}{\mathrm{M}_\odot\,\mathrm{kpc}^{-2}}\right)$
Age	All		1098	0.32 ± 0.03	0.50 ± 0.02	$\mathbf{0.53 \pm 0.02}$
	ETG	HDE	161	0.21 ± 0.08	0.36 ± 0.07	0.43 ± 0.07
		LDE	227	0.41 ± 0.06	$\mathbf{0.52 \pm 0.05}$	0.31 ± 0.06
	LTG	HDE	76	0.01 ± 0.12	0.23 ± 0.11	0.30 ± 0.12
		LDE	481	$\mathbf{-0.45 \pm 0.04}$	-0.38 ± 0.04	-0.20 ± 0.04
[Z/H]	All		1453	0.60 ± 0.02	$\mathbf{0.75 \pm 0.01}$	0.71 ± 0.02
	ETG	HDE	266	0.35 ± 0.06	0.52 ± 0.05	$\mathbf{0.58 \pm 0.04}$
		LDE	348	0.41 ± 0.05	$\mathbf{0.56 \pm 0.04}$	0.51 ± 0.04
	LTG	HDE	87	0.55 ± 0.09	0.67 ± 0.08	0.62 ± 0.08
		LDE	520	0.76 ± 0.02	0.78 ± 0.02	0.62 ± 0.03
[α/Fe]	All		912	0.40 ± 0.03	$\mathbf{0.60 \pm 0.02}$	0.54 ± 0.02
	ETG	HDE	212	0.29 ± 0.07	$\mathbf{0.36 \pm 0.06}$	0.29 ± 0.06
		LDE	261	0.36 ± 0.06	$\mathbf{0.48 \pm 0.05}$	0.26 ± 0.05
	LTG	HDE	50	0.43 ± 0.11	0.60 ± 0.09	0.54 ± 0.10
		LDE	237	0.28 ± 0.06	0.42 ± 0.06	0.36 ± 0.06

Table 6.3: The Spearman rank correlation coefficients (ρ), for correlations between the seeing-corrected best-fitting SSP intercepts at R_e, $X|_{R=R_\mathrm{e}}$, and the structural parameters M_*, M_*/R_e, and $M_*/{R_\mathrm{e}}^2$. The morphological and environmental definitions of the samples are the same as in Section 6.4. For each relation, we highlight in bold the parameter with the highest correlation coefficient, if this is greater than $1\sigma_\rho$ from the other correlations.

This is supported by Fig. 11 of S17, which separates GAMA galaxies in the size-mass plane by morphology – whilst ETGs show little variation with mass or radius, LTGs show a clear trend towards older ages with decreasing mass. We therefore posit that the apparent structural dependence of stellar ages is highly dependent on the exact morphological mix in the sample, accounting for the somewhat contradictory results across different studies.

Comparing the stellar metallicities, the results here are far more consistent. Both S17 and L18 find a strong dependence of [Z/H] on velocity dispersion, for fixed morphological type. For their quiescent sample, B22 find that M_*/R_e is the structural

parameter leading to the highest correlation coefficient ρ, in concordance with both Beverage et al., 2021 and the majority of our results in Table 6.3 (note that ETGs in HDEs correlate slightly better with $M_*/{R_e}^2$ than with M_*/R_e, and the uncertainties for LTGs are too large to infer a definitive correlation). V22 likewise conclude that the gravitational potential depth proxy M_*/R_e is a better fit than M_* alone.

There are fewer studies which examine the relative chemical abundances across the size-mass plane. At higher redshifts, B21 examine [Mg/Fe] (see Section 2.3.3 for a discussion of the nomenclature), and find no correlations with either M_* or M_*/R_e. Using the SAMI survey, S17 demonstrate that contours of constant [α/Fe] fall between lines of constant σ_e and lines of constant stellar surface mass density, when separating the sample by either environment or morphology. Our results agree more closely with S17, although in all subsamples we find the strongest support for a correlation between $[\alpha/\mathrm{Fe}]\big|_{R=R_e}$ and M_*/R_e. However, we note that the coefficients displayed in Table 6.3 are considerably more uncertain than those for age and [Z/H], with only ETGs having a correlation coefficient more than $1\sigma_\rho$ greater than for the other structural parameters.

6.5.1.2 Gradients

The comparison of radial gradients is complicated somewhat by the effects of seeing on each sample. Whilst we have made every effort to correct for this (see Section 5.2), this is not always the case in existing literature, creating further difficulties for quantitative comparisons. Ferreras et al., 2019, hereinafter F19, analyse the gradients of ETGs in the SAMI survey, applying a similar correction for the spatial resolution as we do in Section 5.2. Focussing initially on the metallicity gradients ∇[Z/H], they find high-mass galaxies have marginally steeper gradients. Santucci et al., 2020, hereinafter S20, follow the same method, albeit calculating the gradients as a function of log-scaled R_e as in our analysis, looking at the stellar populations of passive central and

satellite galaxies. Whilst we agree that metallicity gradients are typically negative, their results indicate a weak positive trend with stellar mass, such that ∇[Z/H] is shallower at high stellar masses. Our observations instead support the analysis of L18, who found increasingly steeper gradients as a function of M_* using galaxies drawn from the MaNGA survey, although we note that this is merely a projection, and hence simplification, of the full behaviour in the size-mass plane. This is consistent with the results of Goddard et al., 2017b, hereinafter G17b, who also examined ETGs and LTGs in MaNGA to find a weak negative correlation of metallicity gradients with stellar mass, more pronounced in LTGs. However, as S20 note, the observation of this behaviour is likely to be strongly dependent on the exact morphological mix and sampling in stellar mass. Whilst our observations extend over several orders of magnitude in mass ($8.5 \lesssim \log_{10}(M_*/\mathrm{M}_\odot) \gtrsim 11.5$), this trend may be far less significant over a restricted mass range.

At fixed morphological type, we find no support for varying metallicity gradients as a function of environment. This is consistent with S20, Goddard et al., 2017a (hereinafter G17a), and Tortora et al., 2012, although in minor disagreement with F19. We suggest that the observed differences are driven by small variations in the selection criteria for low- and high-density environments. Whilst F19 separate their HDE and LDE samples by GAMA and cluster membership, our definitions include a portion of the GAMA groups in the HDE sample (see Fig. 1.3.3.2).

There is no clear consensus on the behaviour of age gradients in the literature. Looking at ∇Age, our full sample shows predominantly flat age gradients, with a small decrease from positive to negative gradients as both size and mass increase. This behaviour is consistent with F19, who looked at the dependency of the gradients on M_* and $\log_{10}\left(\sigma_\mathrm{e}/\mathrm{km\,s^{-1}}\right)$, finding negative correlations for both. Similarly, Fig. 7 of L18, one of the few studies to place the age gradients on the size-mass plane, is in good agreement with our Fig. 6.6d. However, neither S20 nor G17b find any

correlation with stellar mass, and in addition the sample of S20 has generally positive age gradients. For fixed morphology, we find little difference in the age gradients across environments, consistent with G17a and Tortora et al., 2012, although again differing from F19. As before, we note that the samples of S20 and F19 do not consider a full range of morphologies and have differing environmental metrics, and hence the differences between our three studies are likely due to non-representative sampling from the parent SAMI survey.

Looking at our results for $\nabla[\alpha/\mathrm{Fe}]$, the gradients of the full sample are overall consistent with flat $[\alpha/\mathrm{Fe}]$ profiles, although this obscures the underlying trend of positive to negative gradients with increasing size and mass, similar to ∇Age. This is in qualitative agreement with F19 and S20, who find negative $[\alpha/\mathrm{Fe}]$ gradients with increasing M_*. However, where we find consistent behaviour of $\nabla[\alpha/\mathrm{Fe}]$ between HDEs and LDEs, irrespective of morphological type, F19 find galaxies in clusters have flatter gradients overall. We note that the same issues apply to the environmental selection criteria as before, with the additional confounding factor that F19 explicitly measure [Mg/Fe], rather than $[\alpha/\mathrm{Fe}]$ (see Section 2.3.3).

6.5.1.3 Radial Profiles and Kinematic Morphology

An additional comparison can be made to studies which examine the radial profiles, rather than linear gradients, such as González Delgado et al., 2015 (hereinafter GD15), Domínguez Sánchez et al., 2019 (D19), and Bernardi et al., 2019 (B19). There is a subtle difference to note in the methodology of these studies. In Section 6.4, we derive the stellar populations in radial bins for each individual galaxy, then take the mean of the populations in a series of radial bins for multiple galaxies. This is a very similar process to GD15, who take the radial profiles from each galaxy, and average them as a function of morphological type. In B19 and D19, the galaxy spectra are first stacked in annuli scaled as a function of R_e, then the stellar populations are measured

from these stacked spectra, each with S/N $\geq$ 100. The primary effect of this is that neither B19 nor D19 quote the SSP parameters with any associated measurement uncertainties, as these are too small to be significant.

GD15 separate their sample based on morphological type, distinguishing between Hubble types rather than simply ETGs and LTGs as in our analysis. Across all galaxies, they find generally negative age and metallicity gradients within 1 R_e, with age flattening at larger radii, consistent with our observations in Fig. 6.10. Their Sd sample shows flatter age profiles, with slightly positive gradients within 0.5 R_e, and positive [Z/H] gradients. We note that this galaxy type occurs primarily at $\log_{10}(M_*/M_\odot) < 10$ in the Calar Alto Legacy Integral Field Area (CALIFA; Sánchez et al., 2012) sample (see Fig. 11 in GD15). We suggest that this may be a contributing factor to our flatter metallicity gradients at low mass, seen in Fig. 6.11, if the morphological mix in this region also favours Sd galaxies over other LTGs.

D19 separate ETGs based on their velocity dispersions and luminosities. For their most massive galaxies, they find positive age gradients, and the steepest (most negative) metallicity gradients. B19 further divide this sample into "large" and "small" galaxies, based on whether they are larger or smaller than the mean R_e-luminosity relation for each sample. Whilst this is not a perfect analogue to our bins across the size-mass plane, it allows a more direct comparison. For the highest mass galaxies, the age gradients are instead flat, with the majority of their sample displaying negative age gradients and steep negative metallicity gradients. They also find that in all bins, larger galaxies are older, more metal poor, and more α-enhanced, attributing this to the distinction between fast and slow rotators (FRs; SRs).

To allow for a more direct comparison, we separate our ETG sample into FRs and SRs, using the definitions established in Section 4.1.3, with sample sizes of 348 and 78 galaxies respectively. We display the locally-smoothed seeing-corrected best-fitting SSP intercepts at R_e in Fig. 6.13, across the size-mass plane. One of the results of

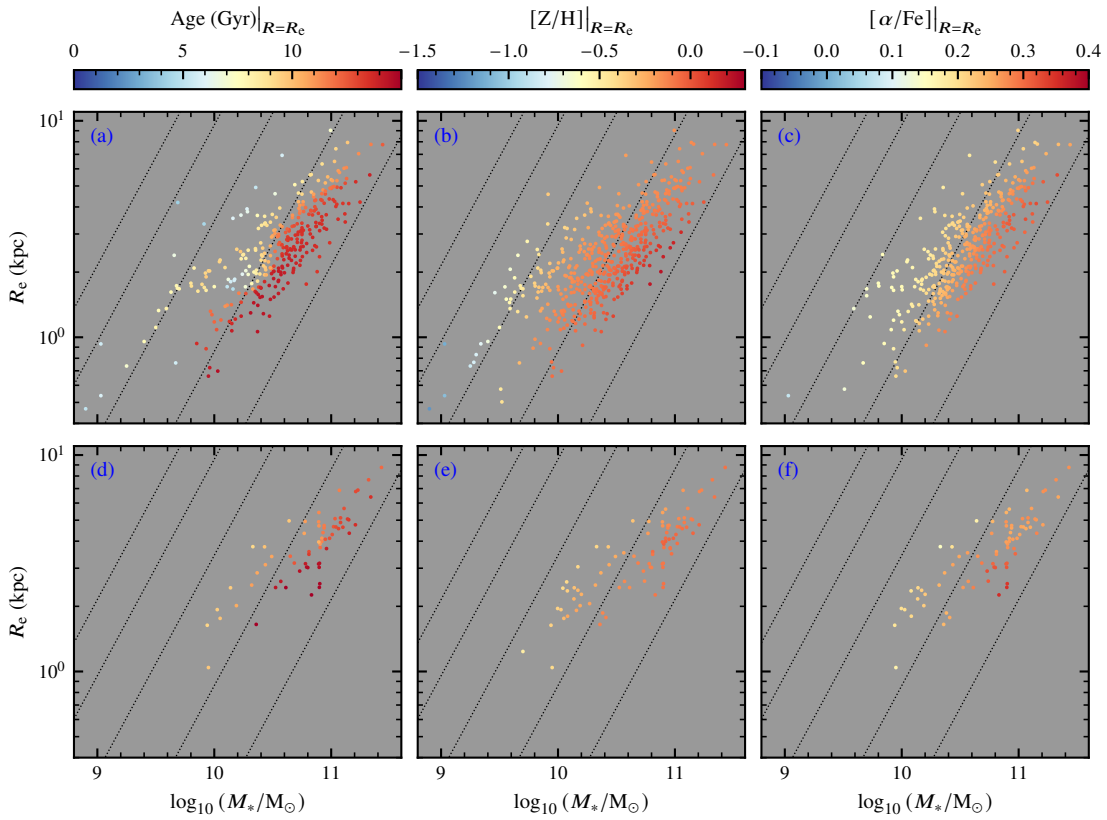


Figure 6.13: As Fig. 6.5, showing the distribution of seeing-corrected best-fitting SSP intercepts at R_e. Here we display the ETG sample separated into fast and slow rotators (see the text for details), shown in (a-c) and (d-f) respectively. All values are locally-smoothed using the LOESS method.

B19 is that at fixed luminosity and velocity dispersion, FRs are younger, with higher [Z/H] and lower [α/Fe]. We evaluate this by selecting galaxies from each group with $\log_{10}\left(\sigma_e/\mathrm{km\,s^{-1}}\right) > 2.3$. Considering the sparse distribution of SRs in the size-mass plane, and to mitigate any bias towards compact ETGs, which are primarily FRs, we introduce a secondary cut at $R_e > 2\,\mathrm{kpc}$. For all FRs and SRs in these samples, we calculate the median SSP parameter, and take the standard deviation as the uncertainty on these measurements, with the results displayed in Table 6.4.

We find that for a fixed velocity dispersion σ_e, extended ETGs show almost no difference in their stellar populations, whether they are classified as SRs or FRs. FRs have slightly higher metallicities, but this is not at all significant given the quoted

Sample	$n_{\rm gal}$	Median SSP Parameter		
		$\text{Age}\big\vert_{\text{R=R}_\text{e}}$ (Gyr)	$[\text{Z/H}]\big\vert_{R=R_\text{e}}$	$[\alpha/\text{Fe}]\big\vert_{R=R_\text{e}}$
Fast Rotators	82	13.8 ± 2.6	-0.06 ± 0.11	0.31 ± 0.07
Region I	32	13.7 ± 3.4	-0.10 ± 0.08	0.32 ± 0.09
Slow Rotators	33	13.2 ± 2.7	-0.10 ± 0.07	0.29 ± 0.07

Table 6.4: The sample sizes and median seeing-corrected best-fitting SSP intercepts at R_e, taken from the galaxy samples displayed in Fig. 6.13 for only those galaxies with $R_\text{e} > 2\,\text{kpc}$ and $\log_{10}\left(\sigma_\text{e}/\text{km}\,\text{s}^{-1}\right) > 2.3$. For completeness, we also show the results for galaxies defined as Region I in Section 4.1.3.

uncertainties. Considering Fig. 18 in B19, we note that their distribution of ages is inconsistent with our Fig. 6.13. For both FRs and SRs, the oldest galaxies are those with the highest velocity dispersion, or equivalently, high-mass compact galaxies are on average the oldest in our sample. As noted by B19, the difference between their results and others in the existing literature appears to be driven by their FRs having much younger ages. Our results in Fig. 6.13, drawn from our existing ETG sample, are instead consistent with studies such as McDermid et al., 2015, where galaxies with $\log_{10}\left(\sigma_\text{e}/\text{km}\,\text{s}^{-1}\right) > 2.3$ are considerably older than the rest of the population.

6.5.2 Physical Implications

We first consider the impact of the environment on the resolved stellar populations, taking the median values of the seeing-corrected best-fitting gradients and intercepts for each sample, and displaying the results in Table 6.5. Consistent with our previous analysis of the global properties in Section 3.2.4, we find that low-mass, compact ETGs have higher $[\alpha/\text{Fe}]$ ratios in HDEs, which do not appear to vary significantly with galactocentric radius. More generally, regardless of galaxy mass or size, ETGs in HDEs are consistently older, and generally more metal-rich, than their counterparts in LDEs. LTGs in higher density environments also tend to have higher [Z/H] but are not measurably older than those in lower density environments. For both

morphological types, at any given mass and size, there is no appreciable difference between the median radial gradients across environments. This places considerable constraints on the possible formation pathways, and supports previous studies (*e.g.* G17a; Tortora et al., 2012; Greene et al., 2015; Zheng et al., 2017) that indicate the internal properties of galaxies matter more than the surrounding environment in determining the stellar population gradients.

Current cosmological models favour a two-phase "inside-out" formation process for galaxies, common across morphological types (Kauffmann et al., 1993; Aumer et al., 2013). In this context the bulge, or central stellar component, formed rapidly at a high redshift ($z \gtrsim 2$), followed by a second phase of evolution dominated by dissipationless mergers. The merger mass ratios, and the presence of gas (dry *vs.* wet mergers) are still a cause for considerable debate, as the formation history should lead to distinguishing features in the radial variations of the stellar populations of galaxies at the present day. Minor dissipationless mergers, for example, are expected to steepen existing negative metallicity gradients, as stars are accreted in the outer regions from low-mass, metal-poor satellite galaxies (Hilz et al., 2013). Conversely, the disruption from a major merger tends to wash out gradients, as stars are redistributed throughout the galaxy (Roškar et al., 2008a; Sánchez-Blázquez et al., 2009). The effects of gas inflows, suggested by studies such as Grisoni et al., 2018 as being a fundamental component of disk galaxy formation, are highly dependent on both the source and infall location of the gas. Pristine gas infalling on the outskirts of galaxies may steepen metallicity gradients whilst flattening age gradients, whilst the reverse may be true for "fountain" gas previously ejected from the galaxy (Roberts-Borsani et al., 2019).

In our research, we find support for steep negative metallicity gradients in both ETGs and LTGs, and very shallow negative age profiles (albeit with considerable scatter). These quantities are tabulated in Table 6.5, including for the individual

Morphology	Environment	∇Age (Gyr)	$\text{Age}\big\vert_{R=R_e}$ (Gyr)	∇[Z/H]	$[\text{Z/H}]\big\vert_{R=R_e}$	$\nabla[\alpha/\text{Fe}]$	$[\alpha/\text{Fe}]\big\vert_{R=R_e}$
			(a) Median values				
All		-0.32 ± 4.73	4.72 ± 4.35	-0.40 ± 0.46	-0.19 ± 0.42	0.00 ± 0.18	0.21 ± 0.10
ETG	HDE	-0.17 ± 5.20	12.87 ± 3.30	-0.44 ± 0.32	-0.10 ± 0.15	0.04 ± 0.16	0.28 ± 0.07
	LDE	-0.31 ± 5.25	9.09 ± 4.25	-0.44 ± 0.39	-0.14 ± 0.23	0.02 ± 0.16	0.24 ± 0.08
LTG	HDE	-0.59 ± 4.01	3.32 ± 2.85	-0.31 ± 0.44	-0.23 ± 0.40	-0.04 ± 0.18	0.16 ± 0.10
	LDE	-0.41 ± 4.30	3.29 ± 2.21	-0.37 ± 0.57	-0.63 ± 0.48	-0.03 ± 0.22	0.14 ± 0.09
			(b) Best-fitting slopes for correlations with $\log_{10}(M_*/\text{M}_\odot)$				
All		-1.07 ± 0.26	2.57 ± 0.23	-0.05 ± 0.02	0.58 ± 0.02	-0.06 ± 0.02	0.10 ± 0.01
ETG	HDE	-0.15 ± 0.64	2.08 ± 0.77	0.05 ± 0.04	0.15 ± 0.02	0.00 ± 0.03	0.06 ± 0.01
	LDE	-0.75 ± 0.65	3.70 ± 0.64	-0.09 ± 0.05	0.30 ± 0.02	-0.07 ± 0.03	0.09 ± 0.01
LTG	HDE	-0.74 ± 0.80	0.29 ± 0.52	0.05 ± 0.11	0.57 ± 0.08	-0.01 ± 0.07	0.12 ± 0.04
	LDE	-1.55 ± 0.35	-1.47 ± 0.16	-0.11 ± 0.05	0.63 ± 0.02	-0.26 ± 0.04	0.04 ± 0.02
			(c) Best-fitting slopes for correlations with $\log_{10}\left(\sigma_e/\text{km s}^{-1}\right)$				
All		-1.89 ± 0.72	11.38 ± 0.53	-0.21 ± 0.06	1.46 ± 0.04	0.04 ± 0.04	0.39 ± 0.02
ETG	HDE	0.05 ± 0.82	11.24 ± 1.37	-0.01 ± 0.10	0.41 ± 0.04	0.21 ± 0.07	0.26 ± 0.03
	LDE	-0.66 ± 1.11	14.05 ± 1.29	-0.39 ± 0.12	0.76 ± 0.05	-0.05 ± 0.06	0.36 ± 0.03
LTG	HDE	-0.56 ± 1.10	0.77 ± 1.08	0.04 ± 0.24	1.44 ± 0.18	-0.06 ± 0.17	0.37 ± 0.09
	LDE	-4.57 ± 1.20	-3.22 ± 0.55	-0.41 ± 0.14	1.97 ± 0.08	-0.44 ± 0.09	0.23 ± 0.04

Table 6.5: (a) The median SSP gradients and intercepts at R_e, for each sample in morphology and environment defined in Section 6.4. The quoted uncertainties are the standard deviations of the measurements. (b) The best-fitting slopes of the fitted linear relationships with $\log_{10}(M_*/\text{M}_\odot)$, following the MCMC method described in Section 6.1.2. (c) As in (b), but for the fitted linear relationships with $\log_{10}\left(\sigma_e/\text{km s}^{-1}\right)$. The fits to the full sample were previously shown in Fig. 6.4.

subsamples used in Section 6.4. The negative age gradients observed support the inside-out formation scenario, where the inner regions of a galaxy are the first to form.

A closer examination of the LTG radial profiles in Fig. 6.10 reveals that for higher-mass extended galaxies the SSP-equivalent ages tend towards some constant at larger galactocentric radii, and in some bins, the ages even increase again. This "U-shaped" age profile has been seen before in other studies using light-weighted stellar population measurements, notably Parikh et al., 2021, Zheng et al., 2017, and G17b. These studies show that at approximately 1 R_e, the SSP-equivalent age plateaus, and begins to increase again. This is in good agreement with our results, although we highlight that this upturn in age shows some environmental dependence. Whilst the effect is most visible in extended high-mass LTGs in LDEs, intermediate-mass and size LTGs show a similar behaviour. We do not find this behaviour in low-mass compact LTGs. Consistent with the observations of González Delgado et al., 2015, we note that there is also no evidence in our results for a similar upturn in ages in ETGs.

One explanation of these U-shaped age profiles comes from stellar radial migration, in which stars formed in the inner disc of a galaxy migrate to the outer disc, washing out the radial age gradient and leading to a shallow or constant age profile in the outskirts (Roškar et al., 2008a). This scenario supports the distinction seen between early- and late-type galaxies, as ETGs do not have structures such as bars or spiral arms, which are sometimes considered prerequisites for stellar migration in numerical simulations (Sellwood et al., 2002; Roškar et al., 2008b). This is by no means the only explanation though. Sánchez-Blázquez et al., 2009 argue that although radial migration plays a role, the upturn in light-weighted stellar ages is due to a decrease in star formation in the external parts of the disc, which is itself caused by a decrease in the volume density of the gas. Ruiz-Lara et al., 2016b, using cosmological simulations of Milky Way-mass discs, suggest that although radial motions contribute to the older

ages at large radii, the old stars are primarily populated by accretion of satellites.

González Delgado et al., 2015 and Ruiz-Lara et al., 2016a, both examining CALIFA galaxies, find clear evidence for an 'inside-out' pattern of *quenching*, in which an extended disc is formed earlier, and a smaller region of ongoing star formation is gradually quenched towards the outskirts. This pattern of inside-out quenching is very likely to be necessary to explain the negative age gradients observed in the central regions of extended high-mass LTGs in our sample. Radburn-Smith et al., 2012, examining the galaxy NGC 7793, found that the older stars extend significantly farther than the underlying HI disc, and are therefore unlikely to have all formed at their current radii, favouring stellar radial migration as the most probable explanation. Whilst our light-weighted stellar population measurements do not allow a determination of the radial variation of the mass-weighted stellar age distribution necessary to conclusively rule out many of these hypotheses, we revisit this discussion later alongside the [α/Fe] gradients.

In our research, we find that LTGs display increasingly negative age and metallicity gradients within $1\,R_{\rm e}$, as a function of increasing size and stellar mass (see Fig. 6.8a,b and Table 6.5). Looking at the metallicity gradients, we see that ∇[Z/H] is generally negative for all morphological types, with the median $\nabla[\mathrm{Z/H}] = -0.40 \pm 0.46$ (see Table 6.5). These are ≈ 0.1 dex steeper than other studies using the SAMI survey (F19; S20), although we note that our sample selection and methodology differ substantially. The large uncertainty stems from the considerable evolution of ∇[Z/H] across the size-mass plane. Our measurements show a weak anticorrelation with mass, and a much stronger relationship with velocity dispersion (bearing in mind that $\sigma_{\rm e} \propto M_*/R_{\rm e}$), with a slope of $\nabla[\mathrm{Z/H}] \propto (-0.21 \pm 0.06) \log_{10}\left(\sigma_{\rm e}/\mathrm{km\,s^{-1}}\right)$, consistent with hydrodynamical simulations (Tortora et al., 2011).

The median [α/Fe] gradients are consistent with zero across our full sample. ETGs have slightly positive gradients on average, compared to shallow negative gradients

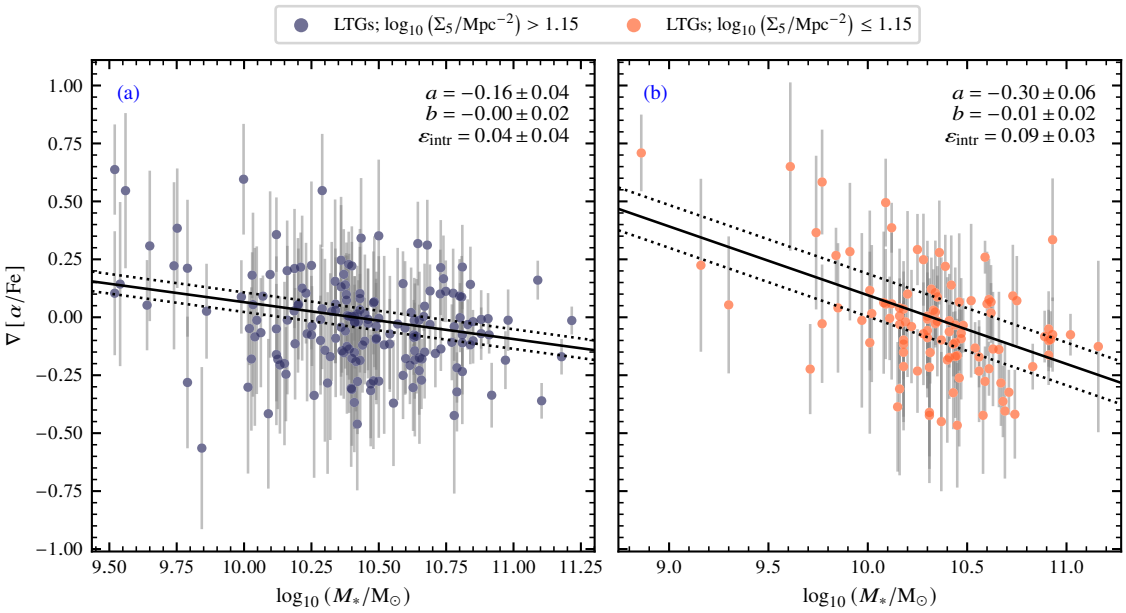


Figure 6.14: The distribution of $\nabla[\alpha/\mathrm{Fe}]$ against M_* for LTGs, separated by environment. The solid lines show the best-fitting linear relationships, derived following the MCMC method in Section 6.1.2, with the resulting parameters inset. The dotted lines indicate the estimated intrinsic scatters, $\varepsilon_{\mathrm{intr}}$.

for LTGs, but this is not a statistically-significant offset. However, in LTGs $\nabla[\alpha/\mathrm{Fe}]$ displays a $> 3\sigma$ anti-correlation with M_* for galaxies in LDEs, leading to negative $[\alpha/\mathrm{Fe}]$ gradients in the highest mass spiral galaxies, highlighted in Fig. 6.14. Making the same assumption as detailed in Section 1.1.4, that $[\alpha/\mathrm{Fe}]$ correlates with the star-formation timescale, this would suggest that galaxies in this part of the size-mass plane quench considerably faster in their central regions relative to the outskirts. We take this to infer support for the inside-out quenching hypothesis proposed by Ruiz-Lara et al., 2016a to explain the negative central age gradients, although we highlight the caveat that our light-weighted analysis does not distinguish between late quenching and recent rejuvenation. With the measurements we have, we also cannot discern whether the upturn in ages at larger radii is due to stellar radial migration, satellite accretion, or any other factor.

6.6 Conclusions

Using the methods detailed in Chapter 2 and 5, we have measured the radial stellar population gradients of 1611 galaxies drawn from the SAMI Galaxy Survey. We summarise our observations and interpretations here, with novel results highlighted in bold:

1. Across the full sample, galaxies display flat age and [α/Fe] gradients, but steep negative metallicity gradients (∇[Z/H] ≈ -0.4). Taken as a function of effective velocity dispersion σ_e, there is a weak negative correlation for both ∇Age and ∇[Z/H], but no relation for ∇[α/Fe].

2. Separating by morphological type into early- and late-type galaxies (ETGs and LTGs), we find that at fixed mass and size, ETGs are significantly older, more metal-rich, and α-enhanced compared to LTGs.

3. The local environmental density has very little effect on the stellar population gradients, once morphological type is accounted for, in line with previous studies (Tortora et al., 2012; S20; G17a). The main exception to this is ∇[α/Fe] in LTGs, which is uniformly close to zero for galaxies in HDEs, and yet displays a highly significant anti-correlation with $\log_{10}(M_*/M_\odot)$ in LDEs. Therefore, **whilst low-mass LTGs have broadly positive** [α/Fe] **gradients, in high-mass LTGs,** [α/Fe] **decreases as a function of galactocentric radius.**

4. The local environmental density has a significant impact on the SSP-equivalent parameters, as measured by both the best-fitting seeing-corrected intercept at R_e, and the mean radial profile around $R = R_e$. **For ETGs in a given region of the size-mass plane, those in HDEs are older by $\gtrsim 2$ Gyr, and more metal-rich and α-enhanced by ≈ 0.05 dex. Conversely, LTGs appear to have little difference in their measurements of age or** [α/Fe]**, but**

show increases of up to ≈ 0.15 dex in [Z/H] in HDEs.

5. We compare the projected stellar populations at R_e of fast and slow rotators (FRs and SRs) across a common region of the size-mass plane. In contrast to B19, but in concordance with results from M15, we find no difference between the SSP parameters of FRs and SRs for fixed R_e and velocity dispersion.

6. Examining the radial age profiles of high-mass LTGs, we find negative age gradients in the central regions, followed by an upturn in SSP-equivalent ages at large galactocentric radii, consistent with previous studies (G17b; Zheng et al., 2017; Parikh et al., 2021). Taken in concert with our observations of negative [α/Fe] gradients for the same galaxies, we suggest that **our results support the proposed inside-out quenching mechanism of Ruiz-Lara et al., 2016a**, although we cannot distinguish between the different mechanisms that may cause the outer U-shaped profiles.

"*Pippin: I didn't think it would end this way.*

Gandalf: End? No, the journey doesn't end here."

– J.R.R. Tolkein

Chapter 7

Conclusions

In this thesis, we have studied the stellar populations of a sample of low-redshift galaxies, across a range of morphological types and environments. We summarise here our results from previous chapters, and detail areas with potential for further research.

In Chapter 2, we developed and detailed the tools necessary to extract stellar populations from individual spectra, in a method which can be trivially parallelised for large-scale surveys. This approach leverages the information contained in up to 20 line indices, deriving the best-fitting simple stellar population (SSP)-equivalent parameters of age, [Z/H], and [α/Fe] through minimisation of the χ^2 statistic (Proctor et al., 2004). Our method maintains a significant lead in efficiency over alternatives such as full-spectrum fitting, as we focus only on particular spectral regions of interest. The specific improvements we made over previous methods used in the Sydney-Australian-Astronomical-Observatory Multi-object Integral-field Spectrograph (SAMI) survey include the adoption of a variance-weighted measurement of the individual indices (Cenarro et al., 2001), and a thorough analysis of the effects of model grid discreti-

sation on the SSP uncertainties. We highlighted contamination of the Mg complex from the [OI] atmospheric sky line resulting in anomalously low [α/Fe] measurements, which affects $\approx$10% of the SAMI sample, primarily galaxies drawn from the Galaxy and Mass Assembly (GAMA) regions.

In Chapter 3, we initially focussed our efforts on exploring variations in the [α/Fe]-$\sigma_{\rm e}$ relation, an empirical correlation between the effective velocity dispersion of a galaxy $\sigma_{\rm e}$ and the relative abundance of α-elements, which is typically interpreted as an indication of the duration of star formation. We measured the stellar populations for 3068 unique galaxies in the SAMI survey, using spectra summed within an elliptical aperture scaled to the effective radius $R_{\rm e}$. After the application of quality cuts to ensure the reliability of the measurements, the sample size was restricted to 2097 galaxies. Dividing our sample on the basis of $(g-i)$ colour into a red sequence and a blue cloud, we found that at fixed velocity dispersion, redder galaxies had on average higher [α/Fe] by (0.06 ± 0.01) dex. We fitted both subsamples to a linear correlation with velocity dispersion $\sigma_{\rm e}$, and discovered a slightly steeper relationshp for blue galaxies – meaning that as $\sigma_{\rm e}$ decreased, the gap in α-enhancement between the two subsamples grew wider. We measured the residuals $\Delta\,[\alpha/{\rm Fe}]$ separately for each sample, and plotted both against the fifth-nearest-neighbour number surface density Σ_5, a measure of the surrounding environment. Whilst blue galaxies displayed no dependence on Σ_5, galaxies in the red sequence showed a statistically-significant positive correlation. Red galaxies residing in the densest environments therefore appeared to have shorter star-formation timescales than their low-density environment counterparts.

We continued this investigation into the influence of the local environment by considering a sample of early-type galaxies (ETGs). We defined our high-density environment (HDE) sample as $\log_{10}\left(\Sigma_5/{\rm Mpc}^{-2}\right) > 1.15$, and our low-density environment (LDE) sample with $\log_{10}\left(\Sigma_5/{\rm Mpc}^{-2}\right) \leq 1.15$. We compared the distribution of

residuals from a single linear relationship between [α/Fe] and $\sigma_{\rm e}$, and found that both Kolmogorov-Smirnov and Mann-Whitney tests rejected the null hypothesis that the HDE and LDE samples were drawn from the same parent population, with $p \ll 0.01$.

We extended this analysis to encompass all morphological types in the SAMI survey, through a variety of methods. The takeaway results were that at fixed velocity dispersion, earlier morphological types showed a consistently higher abundance of α-elements than later types, with the magnitude of this offset greatest at low velocity dispersions. At a fiducial value of $\sigma_{\rm e} = 100\,{\rm km\,s^{-1}}$, elliptical galaxies were α-enhanced by $\gtrsim 0.05\,{\rm dex}$ compared to spirals, and even by as much as $\approx 0.14\,{\rm dex}$ in certain circumstances (see Table 3.3). Taking the lower bound of $(0.05 \pm 0.01)\,{\rm dex}$ from Table 3.2, we used the empirical models of de La Rosa et al., 2011 to estimate the difference in half-mass formation time as $\Delta T_{\rm M/2} \approx (0.8 \pm 0.1)\,{\rm Gyr}$.

Additionally, we demonstrated that the offset in [α/Fe] between ETGs in LDEs and HDEs was reproducible to an extent across all morphological types. This behaviour showed a strong dependence on both morphology and velocity dispersion, and the offset was largest in low-$\sigma_{\rm e}$ ellipticals at $(0.06 \pm 0.01)\,{\rm dex}$. This corresponds to a decrease in half-mass formation time of $\Delta T_{\rm M/2} = (0.9 \pm 0.2)\,{\rm Gyr}$ for ellipticals in HDEs compared to their LDE counterparts, and is consistent with a picture in which the dominant quenching mechanism depends on the stellar mass of the galaxy. In particular, our results support the dominance of environmental quenching for low-mass galaxies as proposed by Peng et al., 2010.

In Chapter 4 we again investigated the residual variations in the [α/Fe]-$\sigma_{\rm e}$ relation, but with a particular focus on the kinematic classifications of galaxies. We used inclination-corrected measurements of the spin proxy $\lambda_{R_{\rm e}}^{\rm eo}$, kindly provided by Dr. Jesse van de Sande, to classify galaxies as slow rotators (SRs) and fast rotators (FRs), themselves divided into four regions in order of increasing rotational support. We found that after removing the dependence on velocity dispersion, the residuals

$\Delta\,[\alpha/\mathrm{Fe}]$ displayed a statistically-significant anti-correlation with $\lambda^{\mathrm{eo}}_{R_\mathrm{e}}$, $\Delta\,[\alpha/\mathrm{Fe}] \propto (-0.06 \pm 0.01)\lambda^{\mathrm{eo}}_{R_\mathrm{e}}$. We used measurements of the star-formation rates (SFRs) to divide our sample into quenched and unquenched groups, and discovered that the significance of the anti-correlation was greatly reduced in the quenched sample. Whilst there is support in the existing literature for differing quenching mechanisms as a function of kinematic morphology (*e.g.* Smethurst et al., 2015), the quality of the data for our quenched sample was not sufficient to provide new observational constraints. Conversely, the unquenched sample showed a clear relation, with $\Delta\,[\alpha/\mathrm{Fe}] \propto (-0.14 \pm 0.02)\lambda^{\mathrm{eo}}_{R_\mathrm{e}}$. This is consistent with an underlying population of disc galaxies containing classical bulges (CBs), which typically form over much shorter periods of time than the surrounding discs, and hence have both higher $[\alpha/\mathrm{Fe}]$ and lower rotational support. An increase in the bulge-to-disc ratio for these galaxies then directly leads to the observed behaviour in our unquenched sample, and we concluded that this is the most plausible explanation.

An additional, and unexpected, result from Chapter 4 was the equivalence of the measured $[\alpha/\mathrm{Fe}]$ ratio between SRs and Region I galaxies, those with $\lambda^{\mathrm{eo}}_{R_\mathrm{e}} \leq 0.4$. We confirmed that the structural parameters of these two groups were distinct, with SRs being larger, rounder, and more massive, in line with results from van de Sande et al., 2021b. However, the α-enhancement of the two groups displayed only a minimal difference, which vanished entirely once the σ_e dependence was accounted for. Thus, despite clear structural differences, our results suggested the integrated star-formation histories of low-spin galaxies are indistinguishable. This cannot be easily explained by galaxies with counter-rotating cores (Rawlings et al., 2020), which occur in very low numbers equally within SRs and Region I. Our results may support simulations from Naab et al., 2014 and Lagos et al., 2022, who proposed multiple different formation scenarios for SRs, encompassing a range of values for $[\alpha/\mathrm{Fe}]$.

In Chapter 5, we presented a novel application and generalised implementation of

the contour binning method, first proposed by Sanders, 2006 for use with X-ray data. We demonstrated how SExtractor and PSFEx (Bertin et al., 1996; Bertin, 2011) can be leveraged to produce a point-spread function (PSF)-matched reference image from any arbitrary source photometry. We showed the optimisations applied during the binning procedure, and how the spaxel-to-spaxel flux variations in the SAMI datacubes rendered them unsuitable as a self-referential image, an issue specific to the fibre layout and cubing algorithm used by the SAMI survey. Compared to previous binning methods such as Voronoi binning (Cappellari et al., 2003) or fixed annuli, we demonstrated that using the flux contours maximises the retrieved radial information, subject to signal/noise ratio (S/N) constraints.

In Chapter 6, we applied the contour binning method to the SAMI survey, measuring the resolved stellar populations of 1611 galaxies. We derived the seeing-corrected gradients from these measurements, and applied quality cuts to obtain values of ∇Age, ∇[Z/H], and $\nabla[\alpha/\mathrm{Fe}]$ for 1098, 1453, and 912 galaxies respectively. Across the full survey, we found that on average galaxies had flat age and $[\alpha/\mathrm{Fe}]$ gradients, but negative [Z/H] gradients. This meant that the projected intercepts at R_e correlated well with the global properties measured in Chapter 3 (see Appendix A), enabling useful comparisons with other studies.

We followed on from our earlier analysis of the global populations in Chapter 3 by separating our sample by morphological type, this time into ETGs and late-type galaxies (LTGs). Rather than focussing on the dependence of our projected R_e SSP measurements on σ_e, we analysed the distribution of our sample in the size-mass plane. To our knowledge, this is the first time that abundance gradients have been evaluated in this manner. Comparing galaxies with the same stellar mass and effective radius, ETGs were typically older, more metal-rich, and α-enhanced over LTGs, with the latter being consistent with our earlier observations in Chapter 3. We also divided our sample of galaxies into those found in HDEs and LDEs, using the same definitions as

before. Without simultaneously separating by morphology, we found little difference between environments. Stellar population gradients typically became more negative with increasing M_* and R_e.

We then investigated the underlying stellar population measurements, taking the mean values as a function of galactocentric radius in several regions of the size-mass plane. This allowed us to simultaneously separate the sample by both environment and morphological type, establishing that the local environmental density had little effect on the variation of stellar population gradients, in line with previous studies (Tortora et al., 2012; S20; G17a). The only significant exception was for $\nabla[\alpha/\mathrm{Fe}]$ in LTGs. Although the median gradients did not differ significantly across environments, for galaxies in HDEs the gradients are broadly similar across the size-mass plane, while for those in LDEs we found a strong anti-correlation with stellar mass, $\nabla[\alpha/\mathrm{Fe}] \propto (-0.26 \pm 0.04)\log_{10}(M_*/\mathrm{M}_\odot)$.

Considering the radial profiles, local environmental density had a much more significant impact on the stellar populations at R_e. For ETGs, those in HDEs were older by $\gtrsim 2\,\mathrm{Gyr}$, and had higher [Z/H] and $[\alpha/\mathrm{Fe}]$ by $\approx 0.05\,\mathrm{dex}$. These offsets were not uniform across the size-mass plane. Whilst ETGs in different environments showed similar age gaps regardless of R_e or M_*, the differences in $[\alpha/\mathrm{Fe}]$ and [Z/H] were largest for compact, low-mass galaxies. With typical environmental offsets of $\Delta\,[\alpha/\mathrm{Fe}] \approx 0.1\,\mathrm{dex}$ in this regime, this supported our conclusions derived using the integrated stellar populations in Chapter 3. In contrast, LTGs showed very similar age and $[\alpha/\mathrm{Fe}]$ profiles across differing environments, although those in HDEs had higher [Z/H], by up to $\approx 0.15\,\mathrm{dex}$ for more compact lower-mass galaxies.

We also compared the projected stellar populations at R_e for both SRs and FRs. Whilst the sample sizes were too small to investigate any correlation with $\lambda^{\mathrm{eo}}_{R_e}$, as in Chapter 4, we demonstrated that for fixed velocity dispersion and R_e, SRs and Region I galaxies do not have significantly different resolved stellar populations. This

supported our previous conclusions in Chapter 4, with the caveat that our gradient sample here only consisted of ETGs.

Finally, an examination of the radial age profiles revealed that in high-mass LTGs, the measured SSP-equivalent ages initially decrease with increasing galactocentric radii, then show an upturn to older ages in the outskirts. Whilst few of these galaxies were sampled to large radii ($R > 1.5\,R_{\rm e}$), we noted that this behaviour has been observed before (G17b; Zheng et al., 2017; Parikh et al., 2021). There are multiple existing theories in the literature which offer plausible explanations. Roškar et al., 2008a suggested that outwards radial migration of stars, driven by spiral arms, is sufficient to explain constant age profiles at large radii. Sánchez-Blázquez et al., 2009, whilst not disputing the contribution of radial migration, suggested that lower star-formation rates in the outskirts naturally leads to a U-shaped age profile. Our results, in concordance with GD15 and Ruiz-Lara et al., 2016a, appeared to favour a scenario of early disc formation followed by inside-out quenching, which is supported by the negative $\nabla[\alpha/\mathrm{Fe}]$ seen for this population, although we could not discern which, if any, of the proposed mechanisms could also be responsible for the upturn in ages at large radii.

7.1 Future Work

Whilst this thesis represents a comprehensive study of stellar populations in the SAMI Galaxy Survey, it also raises several intriguing questions. We highlight below some of the avenues which could be pursued to expand on the work presented here.

- The research into potential biases in the kinematic classification in Section 4.3.2.1 touched upon the presence of kinematically-anomalous galaxies, such as those with counter-rotating cores, which leads to a distinctive double peak in their velocity dispersion maps. The observed frequency of these 2σ galaxies is significantly lower than in previous surveys such as ATLAS3D (Emsellem et al.,

2011). One possible explanation for this is that the atmospheric seeing in the SAMI observations smears out many of the identifying features. Given a suitable number of these 2σ galaxies, a future analysis could focus on their resolved stellar populations, and hence determine whether these galaxies show any other distinguishing features.

- There are now very detailed simulations of the formation scenarios leading to SRs, such as from Lagos et al., 2022. Whilst the observations from SAMI do not contain enough radial information or signal to adequately constrain the radial stellar population profiles, future integral-field unit (IFU) surveys such as Hector (Lawrence et al., 2012) should improve upon this. In particular, the higher spectral resolution of Hector of 1.3 Å (*c.f.* 2.65 Å for SAMI) will allow much more accurate determinations of the stellar populations, using full-spectrum fitting with models such as those of Verro et al., 2022. With a larger sample size of high S/N observations of SRs, it should then be possible to test observationally the relative proportions forming via each pathway.

- In Section 6.1.1, we discussed that some number of galaxies were removed due to physically implausible gradients, despite having realistic stellar population measurements. On closer inspection, three of these galaxies were discovered to host blue star-forming rings, inside an otherwise quiescent galaxy. We have obtained follow-up observations using the Wide-Field Spectrograph (WiFeS; Dopita et al., 2007) for the galaxy shown in Fig. 7.1, containing a counter-rotating star-forming ring, to ascertain the physical processes that lead to the formation of these structures. In particular, we aim to measure higher-order moments of the velocity distributions, alongside chemical and kinematic properties of the gas inside and outside of the ring, to constrain current models for gas dynamical settling times.

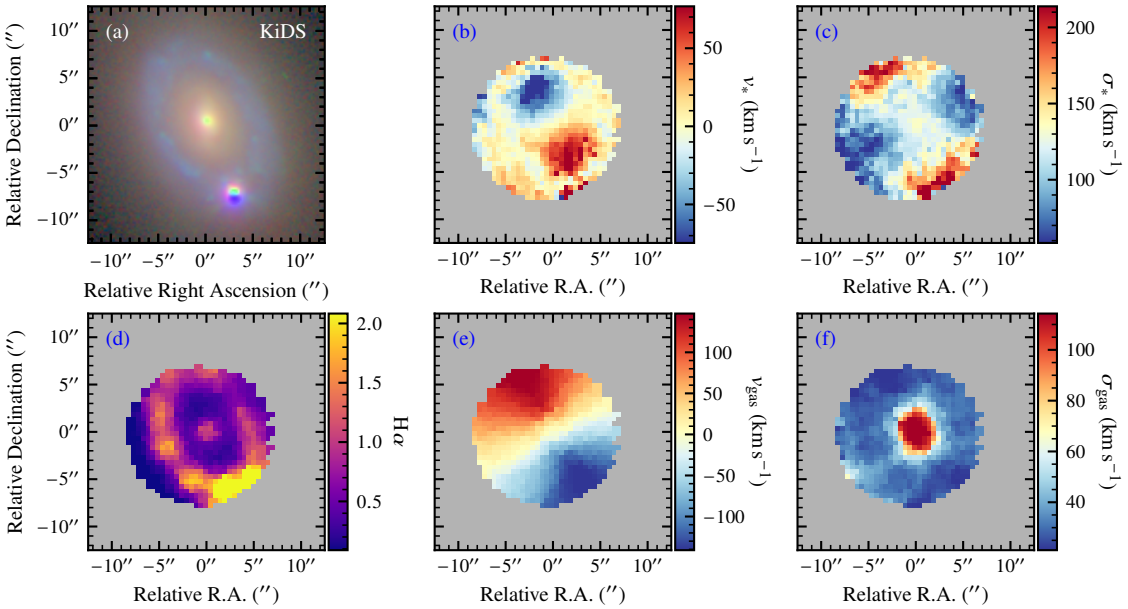


Figure 7.1: (a) A colour image of SAMI galaxy 560238, using KiDS *gri* imaging. (b) The stellar line-of-sight mean velocity. Red indicates positive (recessional) velocities. (c) As (b), but for the stellar line-of-sight velocity dispersion. (d) The Hα flux. Note the clearly visible ring structure. (e) As (b), but for the ionised gas line-of-sight mean velocity. Note that the ionised gas is counter-rotating compared to the stars. (f) As (b), but for the ionised gas line-of-sight velocity dispersion.

- Looking further ahead, the future of this field will be in studying the resolved populations of nearby galaxies, using facilities such as the Extremely Large Telescope[1] (ELT; Gilmozzi et al., 2007), the Giant Magellan Telescope (GMT; Johns, 2008), and the Thirty Meter Telescope (TMT; Szeto et al., 2008). For example, with the adaptive optics in place on the ELT, imaging will be possible down to < 10 milli-arcseconds in the I, J, and K bands using the Multi-Adaptive Optics Imaging Camera for Deep Observations (MICADO; Davies et al., 2010). This will enable direct observations of the stars in galaxies out to the Virgo cluster with a completeness of $\gtrsim 90\%$, allowing an unprecedented reconstruction of the star-formation history via simple star counts (Greggio et al., 2012). Similarly, even in unresolved populations, it may now be possible to recover

[1]Originally known as the European Extremely Large Telescope, or E-ELT.

the spectra of the coolest giant branch stars, using techniques such as Poisson fluctuation spectroscopy (Smith, 2022).

With these suggestions in mind, we look forward to continuing our investigations into stellar populations, and their role in the overall field of galaxy formation and evolution.

Appendix A

Comparing Integrated and Radial SSP Measurements

In Fig. A.1, we evaluate the equivalence of our SSP measurements. We show the distribution of the best-fitting seeing-corrected projected SSP intercepts at $R_{\rm e}$, $X|_{R=R_{\rm e}}$, used throughout Chapter 6, against the SSP parameters measured within an elliptical $R_{\rm e}$ aperture, $X_{\rm PJW}$, taken from Chapter 3. For age and [α/Fe], the offset in the median is very small, and dwarfed by the scatter in the distribution. For [Z/H], we find a proportionally larger shift, where the measurements made within the $R_{\rm e}$ aperture are offset to higher metallicities than the measurements projected to $R_{\rm e}$. We attribute this offset to the stellar population gradients – whilst ∇Age and ∇[α/Fe] are close to zero in our sample (see Table 6.5), ∇[Z/H] is on average negative. Hence, measurements of the metallicity will vary depending on the relative contribution of light from the centre of the galaxy.

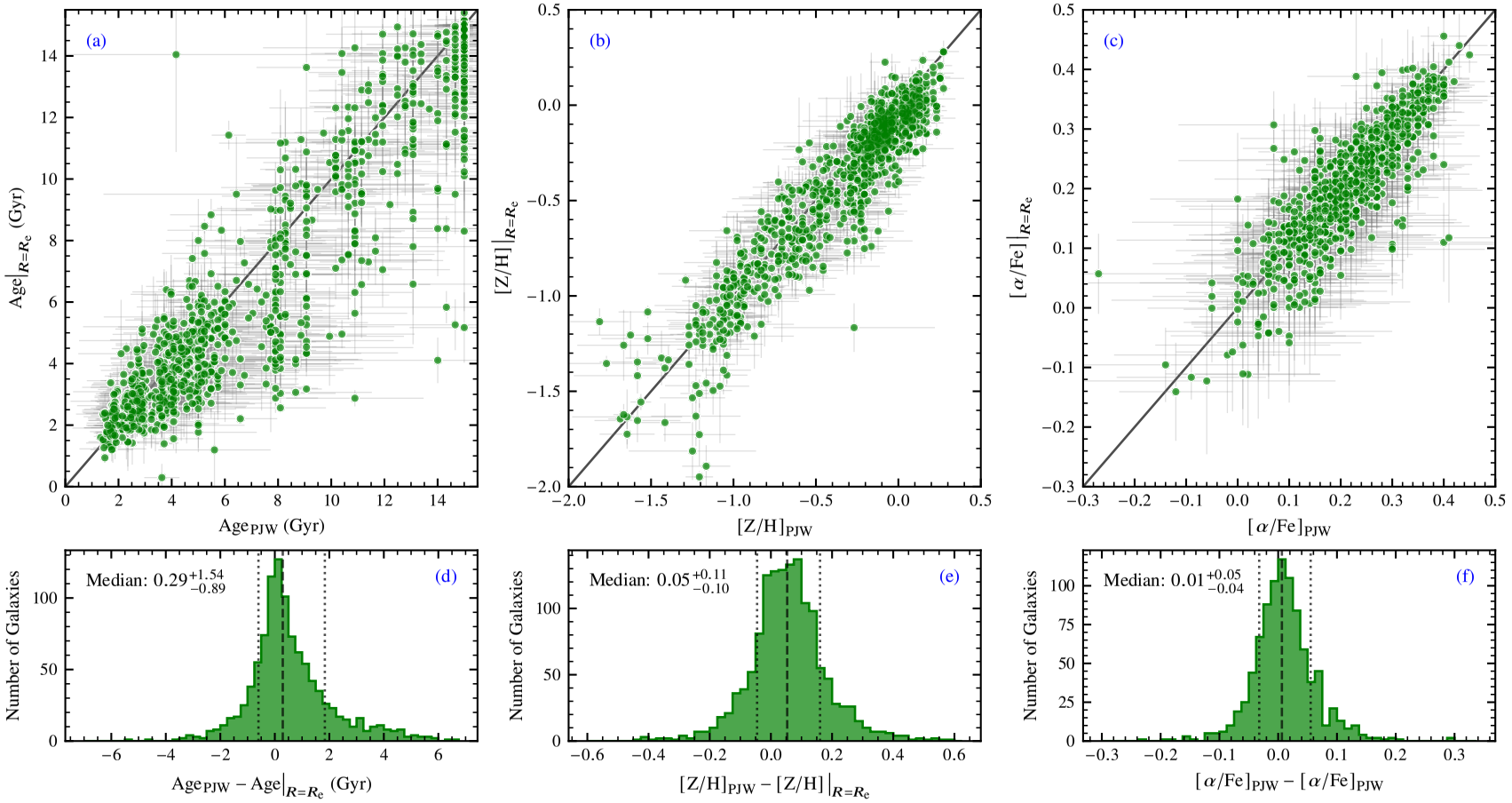


Figure A.1: (a-c) The best-fitting seeing-corrected projected SSP intercepts at R_e, $X|_{R=R_e}$, used throughout Chapter 6, against the SSP parameters measured within an elliptical R_e aperture, X_{PJW}, taken from Chapter 3. The solid line indicates a 1:1 relationship. (d-f) The distribution of the residuals, $X_{PJW} - X\big|_{R=R_e}$. Inset, the median of the distribution, displayed as a dashed line, and the location of the 16th and 84th percentiles, shown as dotted lines.

Appendix B

The Virial Theorem

There exists a basic principle known as the "virial theorem" (Clausius, 1870), which states that for a stable system of particles bound by a potential, the time-averaged kinetic energy $\langle T \rangle$ can be related to the time-averaged potential energy $\langle U \rangle$ as

$$2\langle T \rangle + \langle U \rangle = 0\,. \tag{B.1}$$

In order to apply this to galaxies, we note that the gravitational potential energy U of a spherical density distribution $\rho(r)$ can be written as

$$U = -\int_0^R \frac{GM(r)}{r}\rho(r)4\pi r^2 dr, \tag{B.2}$$

where R is the total radius, G is the gravitational constant, and $M(r)$ is the mass enclosed in a shell of radius r, which in full generality is given by integrating over the density,

$$M(r) = \int_0^r \rho(r')4\pi r'^2 dr'\,. \tag{B.3}$$

We can make the simplifying assumption that the density is constant, and hence the enclosed mass is given by

$$M(r) = \frac{4}{3}\pi r^3 \rho\,, \tag{B.4}$$

such that the total gravitational potential energy in Eq. B.2 becomes

$$U = -\frac{16}{3}\pi G\rho^2 \int_0^R r^4 dr\,, \tag{B.5}$$

$$= -\frac{16}{15}\pi^2 G\rho^2 R^5\,, \tag{B.6}$$

$$= -\frac{3}{5}\frac{GM^2}{R}\,, \tag{B.7}$$

where M is the total mass. The total kinetic energy can be written as

$$\langle T\rangle = \sum_{i=1}^{N} \frac{1}{2} m\langle v\rangle^2, \tag{B.8}$$

$$= \frac{1}{2} Nm\langle v\rangle^2, \tag{B.9}$$

for N stars, each of mass m, and average velocity $\langle v\rangle$. Combining Eqs. B.7 and B.9 by substituting into the virial theorem, we obtain

$$2\left(\frac{1}{2}M\langle v\rangle^2\right) - \frac{3}{5}\frac{GM^2}{R} = 0\,, \tag{B.10}$$

noting that $Nm = M$. In our observations, we cannot directly obtain the average velocity in three dimensions $\langle v\rangle$, but instead measure the one-dimensional velocity dispersion σ. These two quantities are related through $\langle v\rangle = \sqrt{3}\,\sigma$, and hence we obtain

$$R = \frac{GM}{5\sigma^2}\,. \tag{B.11}$$

We stress that this is only an approximation, due to the multiple assumptions made along the way. We note that Eq. B.11 can also be rearranged to find an expression for M,

$$M = \frac{5\sigma^2 R}{G}\,. \tag{B.12}$$

Given measurements of R and σ, one can trivially calculate this quantity, often referred to as the dynamical mass $M_{\rm dyn}$.

Bibliography

Abadi, M. G., B. Moore, and R. G. Bower, 1999. *MNRAS* 308, 947.

Abbott, T. M. C. et al., 2021. *ApJS* 255, 20.

Ahn, C. P. et al., 2012. *ApJS* 203, 21.

Ahn, C. P. et al., 2014. *ApJS* 211, 17.

Albrecht, A. and P. J. Steinhardt, 1982. *Physical Review Letters* 48, 1220.

Allen, J. T. et al., 2015. *MNRAS* 446, 1567.

Aller, L. H., 1942. *ApJ* 95, 52.

Annibali, F., R. Grützbauch, R. Rampazzo, A. Bressan, and W. W. Zeilinger, 2011. *A&A* 528, A19.

Athanassoula, E., 2005. *MNRAS* 358, 1477.

Aumer, M. and S. D. M. White, 2013. *MNRAS* 428, 1055.

Avni, Y., 1976. *ApJ* 210, 642.

Baade, W., 1944. *ApJ* 100, 137.

Babcock, H. W., 1953. *PASP* 65, 229.

Bacon, R. et al., 2001. *MNRAS* 326, 23.

Bacon, R. et al., 2010. *SPIE* 7735, 773508.

Baldry, I. K. et al., 2006. *MNRAS* 373, 469.

Barbosa, C. E. et al., 2021. *A&A* 649, A93.

Barnes, J. and G. Efstathiou, 1987. *ApJ* 319, 575.

Barone, T. M. et al., 2022. *MNRAS* 512, 3828.

Barsanti, S. et al., 2021. *ApJ* 906, 100.

Bell, E. F. and R. S. de Jong, 2001. *ApJ* 550, 212.

Bell, E. F. et al., 2004. *ApJ* 608, 752.

Bender, R., R. P. Saglia, and O. E. Gerhard, 1994. *MNRAS* 269, 785.

Bender, R., D. Burstein, and S. M. Faber, 1992. *ApJ* 399, 462.

— ,1993. *ApJ* 411, 153.

Bending, T. J. R., C. L. Dobbs, and M. R. Bate, 2020. *MNRAS* 495, 1672.

Bernardi, M., H. Domínguez Sánchez, J. R. Brownstein, N. Drory, and R. K. Sheth, 2019. *MNRAS* 489, 5633.

Berriman, G. B. and J. C. Good, 2017. *PASP* 129, 058006.

Bertin, E., 2011. Astronomical Society of the Pacific Conference Series 442, 435.

Bertin, E. and S. Arnouts, 1996. *Astronomy and Astrophysics Supplement* 117, 393.

Best, P. N. and T. M. Heckman, 2012. *MNRAS* 421, 1569.

Beuzit, J. .-. et al., 2019. *A&A* 631, A155.

Beverage, A. G. et al., 2021. *ApJ* 917, L1.

Bigiel, F. et al., 2008. *AJ* 136, 2846.

Bigiel, F. et al., 2011. *ApJ* 730, L13.

Bland-Hawthorn, J. et al., 2011. *Optics Express* 19, 2649.

Bluck, A. F. L. et al., 2020. *MNRAS* 499, 230.

Blumenthal, G. R., S. M. Faber, J. R. Primack, and M. J. Rees, 1984. *Nat* 311, 517.

Bolton, A. S., S. Burles, T. Treu, L. V. E. Koopmans, and L. A. Moustakas, 2007. *ApJ* 665, L105.

Bower, R. G., J. R. Lucey, and R. S. Ellis, 1992. *MNRAS* 254, 601.

Bressan, A., F. Fagotto, G. Bertelli, and C. Chiosi, 1993. *A&AS* 100, 647.

Brough, S. et al., 2013. *MNRAS* 435, 2903.

Brough, S. et al., 2017. *ApJ* 844, 59.

Bruzual, G. and S. Charlot, 2003. *MNRAS* 344, 1000.

Bruzual, G. and S. Charlot, 1993. *ApJ* 405, 538.

Bryant, J. J., J. Bland-Hawthorn, L. M. R. Fogarty, J. S. Lawrence, and S. M. Croom, 2014. *MNRAS* 438, 869.

Bryant, J. J. et al., 2015. *MNRAS* 447, 2857.

Bundy, K. et al., 2015. *ApJ* 798, 7.

Burbidge, E. M. and G. R. Burbidge, 1965. *ApJ* 142, 634.

Burstein, D., 1979. *ApJ* 232, 74.

Burstein, D., S. M. Faber, C. M. Gaskell, and N. Krumm, 1984. *ApJ* 287, 586.

Burstein, D. et al., 1988. *ASSL* 141, 17.

Calura, F. and N. Menci, 2011. *MNRAS* 413, L1.

Cappellari, M., 2002. *MNRAS* 333, 400.

— ,2016. *ARA&A* 54, 597.

— ,2017. *MNRAS* 466, 798.

Cappellari, M. and Y. Copin, 2003. *MNRAS* 342, 345.

Cappellari, M. and E. Emsellem, 2004. *PASP* 116, 138.

Cappellari, M. et al., 2006. *MNRAS* 366, 1126.

Cappellari, M. et al., 2011. *MNRAS* 413, 813.

Cappellari, M. et al., 2013. *MNRAS* 432, 1862.

Carlsten, S. G., G. K. T. Hau, and A. Zenteno, 2017. *MNRAS* 472, 2889.

Carnall, A. C., R. J. McLure, J. S. Dunlop, and R. Davé, 2018. *MNRAS* 480, 4379.

Cenarro, A. J. et al., 2001. *MNRAS* 326, 959.

Chabrier, G., 2003. *PASP* 115, 763.

Chester, C. and M. S. Roberts, 1964. *AJ* 69, 635.

Cheung, E. et al., 2013. *ApJ* 779, 162.

Chilingarian, I. V., A.-L. Melchior, and I. Y. Zolotukhin, 2010. *MNRAS* 405, 1409.

Chilingarian, I. V. and I. Y. Zolotukhin, 2012. *MNRAS* 419, 1727.

Cicone, C. et al., 2014. *A&A* 562, A21.

Cid Fernandes, R. et al., 2014. *A&A* 561, A130.

Clausius, R., 1870. *Annalen der Physik* 217, 124.

Colless, M. et al., 1999. *MNRAS* 303, 813.

Conroy, C., G. J. Graves, and P. G. van Dokkum, 2014. *ApJ* 780, 33.

Conroy, C., A. Villaume, P. G. van Dokkum, and K. Lind, 2018. *ApJ* 854, 139.

Copernicus, N., 1543. *De Revolutionibus Orbium Coelestium*.

Cortese, L. et al., 2016. *MNRAS* 463, 170.

Crabtree, S. A. et al., 2021. *Nature Human Behaviour* 5.10, 1303.

Croom, S. M. et al., 2012. *MNRAS* 421, 872.

Croom, S. M. et al., 2021. *MNRAS* 505, 991.

Curtis, H. D., 1917. *PASP* 29, 206.

D'Eugenio, F. et al., 2021. *MNRAS* 504, 5098.

Darvish, B., B. Mobasher, D. Sobral, N. Scoville, and M. Aragon-Calvo, 2015. *ApJ* 805, 121.

Davies, R. et al., 2010. *SPIE* 7735, 77352A.

Davies, R. L., E. M. Sadler, and R. F. Peletier, 1993. *MNRAS* 262, 650.

Davis, M., G. Efstathiou, C. S. Frenk, and S. D. M. White, 1985. *ApJ* 292, 371.

De Jong, J. T. A., G. A. Verdoes Kleijn, K. H. Kuijken, and E. A. Valentijn, 2013. *Experimental Astronomy* 35, 25.

De Jong, J. T. A. et al., 2015. *A&A* 582, A62.

Dekel, A., J. Devor, and G. Hetzroni, 2003. *MNRAS* 341, 326.

Dekel, A. et al., 2009. *Nat* 457, 451.

De La Rosa, I. G., F. La Barbera, I. Ferreras, and R. R. de Carvalho, 2011. *MNRAS* 418, L74.

De Vaucouleurs, G., 1948. *Annales d'Astrophysique* 11, 247.

Dey, A. et al., 2019. *AJ* 157, 168.

De Zeeuw, P. T. et al., 2002. *MNRAS* 329, 513.

De Zeeuw, T. and M. Franx, 1991. *ARA&A* 29, 239.

Di Matteo, P., A. Pipino, M. D. Lehnert, F. Combes, and B. Semelin, 2009. *A&A* 499, 427.

Djorgovski, S. and M. Davis, 1987. *ApJ* 313, 59.

Domínguez Sánchez, H., M. Bernardi, J. R. Brownstein, N. Drory, and R. K. Sheth, 2019. *MNRAS* 489, 5612.

Dopita, M. et al., 2007. *Ap&SS* 310, 255.

Doppler, C. A., 1843. *Abhandlungen der Königlichen Böhmischen Gesellschaft der Wissenschaften* 2, 465.

Dressler, A., 1980. *ApJ* 236, 351.

Dressler, A. et al., 1987. *ApJ* 313, 42.

Dreyer, J. L., 1888. *Mem. R. Astron. Soc.* 49, 1.

Dreyer, J. L. E., 2014. *History of the Planetary Systems*.

Driver, S. P. et al., 2006. *MNRAS* 368, 414.

Driver, S. P. et al., 2011. *MNRAS* 413, 971.

Eggen, O. J., D. Lynden-Bell, and A. R. Sandage, 1962. *ApJ* 136, 748.

Emsellem, E., G. Monnet, and R. Bacon, 1994. *A&A* 285, 723.

Emsellem, E. et al., 2004. *MNRAS* 352, 721.

Emsellem, E. et al., 2011. *MNRAS* 414, 888.

Faber, S. M., 1973. *ApJ* 179, 731.

Faber, S. M., E. D. Friel, D. Burstein, and C. M. Gaskell, 1985. *ApJS* 57, 711.

Faber, S. M. and R. E. Jackson, 1976. *ApJ* 204, 668.

Faber, S. M. et al., 1987. *Global Scaling Relations for Elliptical Galaxies and Implications for Formation*, 175.

Faber, S. M., 1977. *The Chemical Composition of Old Stellar Populations*, 157.

Falcón-Barroso, J. et al., 2011. *A&A* 532, A95.

Fall, S. M. and G. Efstathiou, 1980. *MNRAS* 193, 189.

Ferreras, I. et al., 2019. *MNRAS* 489, 608.

Fichtner, Y. A., L. Grassitelli, E. Romano-Díaz, and C. Porciani, 2022. *MNRAS* 512, 4573.

Fiore, F. et al., 2017. *A&A* 601, A143.

Fish, R. A., 1963. *AJ* 68, 72.

Fisher, D. B. and N. Drory, 2011. *ApJ* 733, L47.

Flaugher, B. et al., 2015. *AJ* 150, 150.

Foreman-Mackey, D., D. W. Hogg, D. Lang, and J. Goodman, 2013. *PASP* 125, 306.

Franx, M. and G. Illingworth, 1990. *ApJ* 359, L41.

Fraunhofer, J., 1817. *Annalen der Physik* 56, 264.

Freedman, W. L., 2021. *ApJ* 919, 16.

Frenk, C. S. and S. D. M. White, 2012. *Annalen der Physik* 524, 507.

Galilei, G., 1610. *Sidereus Nuncius Magna*.

Gallazzi, A., S. Charlot, J. Brinchmann, S. D. M. White, and C. A. Tremonti, 2005. *MNRAS* 362, 41.

Gilmozzi, R. and J. Spyromilio, 2007. *The Messenger* 127, 11.

Goddard, D. et al., 2017a. *MNRAS* 465, 688.

Goddard, D. et al., 2017b. *MNRAS* 466, 4731.

González Delgado, R. M. et al., 2015. *A&A* 581, A103.

Gorgas, J. et al., 1993. *ApJS* 86, 153.

Gott III, J. R. and M. J. Rees, 1975. *A&A* 45, 365.

Graham, M. T. et al., 2018. *MNRAS* 477, 4711.

Graves, G. J., 2014. *Astrophysics Source Code Library*, ascl:1407.019.

Graves, G. J. and R. P. Schiavon, 2008. *ApJS* 177, 446.

Green, A. W. et al., 2018. *MNRAS* 475, 716.

Greene, J. E. et al., 2015. *ApJ* 807, 11.

Greggio, L., R. Falomo, S. Zaggia, D. Fantinel, and M. Uslenghi, 2012. *PASP* 124, 653.

Greggio, L. and A. Renzini, 1983. *A&A* 118.2, 217.

Grisoni, V., E. Spitoni, and F. Matteucci, 2018. *MNRAS* 481, 2570.

Guiderdoni, B. and B. Rocca-Volmerange, 1987. *A&A* 186, 1.

Gunn, J. E. and J. R. Gott III, 1972. *ApJ* 176, 1.

Guth, A. H. and S. .-. Pi, 1982. *Physical Review Letters* 49, 1110.

Guth, A. H., 1981. *Physical Review D* 23, 347.

Hafez, I., 2010. "Abd Al-Rahman al-Sufi and His Book of the Fixed Stars: A Journey of Re-Discovery".

Haid, S. et al., 2019. *MNRAS* 482, 4062.

Hale, G. E., 1896. *ApJ* 3, 215.

Hamacher, D., 2018. *Indigenous Use of Stellar Scintillation for Predicting Weather and Seasonal Change*, 17.

Harborne, K. E. et al., 2020. *MNRAS* 497, 2018.

Harmand, S. et al., 2015. *Nat* 521, 310.

Hawking, S. W., 1982. *Physics Letters B* 115, 295.

Hearnshaw, J. B., 2014. *The Analysis of Starlight*.

Herschel, W., 1786. *Philosophical Transactions of the Royal Society of London Series I* 76, 457.

— ,1789. *Philosophical Transactions of the Royal Society of London Series I* 79, 212.

— ,1802. *Philosophical Transactions of the Royal Society of London Series I* 92, 477.

Hilz, M., T. Naab, and J. P. Ostriker, 2013. *MNRAS* 429, 2924.

Hirschmann, M. et al., 2014. *MNRAS* 444, 2938.

Hodges, J. L., 1958. *Arkiv for Matematik* 3, 469.

Hogg, D. W., J. Bovy, and D. Lang, 2010. *arXiv e-prints*.

Hopkins, P. F. et al., 2009. *ApJS* 181, 135.

Hoskin, M., 1982. *Journal for the History of Astronomy* 13, 97.

Hubble, E. P., 1926. *Contributions from the Mount Wilson Observatory / Carnegie Institution of Washington* 324, 1.

— ,1927. *Observatory* 50, 276.

— ,1929. *Proceedings of the National Academy of Science* 15, 168.

— ,1936. *Realm of the Nebulae*.

Hunger, H. and J. M. Steele, 2019. *The Babylonian Astronomical Compendium MUL.APIN*.

Hyde, J. B. and M. Bernardi, 2009. *MNRAS* 396, 1171.

Jeffreys, H., 1946. *Proceedings of the Royal Society of London Series A* 186, 453.

Johns, M., 2008. 6986, 698603.

Johnson, H. L. and W. W. Morgan, 1953. *ApJ* 117, 313.

Kaiser, N., G. Squires, and T. Broadhurst, 1995. *ApJ* 449, 460.

Kant, I., 1755. *Allgemeine Naturgeschichte Und Theorie Des Himmels*.

Kauffmann, G., S. D. M. White, and B. Guiderdoni, 1993. *MNRAS* 264, 201.

Kennicutt Jr., R. C., P. Tamblyn, and C. E. Congdon, 1994. *ApJ* 435, 22.

Kepler, J., 1609. *Astronomia Nova*.

Kereš, D., N. Katz, D. H. Weinberg, and R. Davé, 2005. *MNRAS* 363, 2.

Kim, J.-G., W.-T. Kim, and E. C. Ostriker, 2018. *ApJ* 859, 68.

Kleiner, D., K. A. Pimbblet, D. H. Jones, B. S. Koribalski, and P. Serra, 2017. *MNRAS* 466, 4692.

Krajnović, D. et al., 2011. *MNRAS* 414, 2923.

Krajnović, D. et al., 2020. *Astronomy & Astrophysics* 635, A129.

Kuijken, K., 2011. *The Messenger* 146, 8.

Kuijken, K. et al., 2019. *A&A* 625, A2.

Kuntschner, H., 1998. "The Star Formation History of Early-Type Galaxies in the Fornax Cluster".

Kuntschner, H. et al., 2010. *MNRAS* 408, 97.

La Barbera, F. et al., 2012. *MNRAS* 426, 2300.

La Barbera, F. et al., 2014. *MNRAS* 445, 1977.

Lagos, C. d. P. et al., 2022. *MNRAS* 509, 4372.

Larson, R. B. and B. M. Tinsley, 1978. *ApJ* 219, 46.

Larson, R. B., B. M. Tinsley, and C. N. Caldwell, 1980. *ApJ* 237, 692.

Larson, R. B., 1974. *MNRAS* 166, 585.

Lawrence, J. et al., 2012. *SPIE* 8446, 844653.

Leaman, T. M. and D. W. Hamacher, 2019. *Journal of Astronomical History and Heritage* 22, 225.

Leitherer, C. et al., 1999. *ApJS* 123, 3.

Lequeux, J., M. Peimbert, J. F. Rayo, A. Serrano, and S. Torres-Peimbert, 1979. *A&A* 80, 155.

Leroy, A. K. et al., 2008. *AJ* 136, 2782.

Leroy, A. K. et al., 2013. *AJ* 146, 19.

Li, H. et al., 2018. *MNRAS* 476, 1765.

Linde, A. D., 1982. *Physics Letters B* 108, 389.

Liske, J. et al., 2015. *MNRAS* 452, 2087.

Liu, Y., L. C. Ho, and E. Peng, 2016. *ApJ* 829, L26.

Luo, Y. et al., 2020. *MNRAS* 493, 1686.

MacArthur, L. A., 2005. *ApJ* 623, 795.

Mann, H. B. and D. R. Whitney, 1947. *The Annals of Mathematical Statistics* 18.1, 50.

Maoz, D., F. Mannucci, and T. D. Brandt, 2012. *MNRAS* 426, 3282.

McDermid, R. M. et al., 2015. *MNRAS* 448, 3484.

McGaugh, S. S., J. M. Schombert, G. D. Bothun, and W. J. G. de Blok, 2000. *ApJ* 533, L99.

McNamara, B. R. and P. E. J. Nulsen, 2012. *New Journal of Physics* 14, 055023.

Medling, A. M. et al., 2018. *MNRAS* 475, 5194.

Messier, C., 1781. *Catalogue Des Nébuleuses et Des Amas d'Étoiles (Catalog of Nebulae and Star Clusters)*, 227.

Mishra, P. K., Y. Wadadekar, and S. Barway, 2019. *MNRAS* 487, 5572.

Mo, H. J., S. Mao, and S. D. M. White, 1998. *MNRAS* 295, 319.

Moffat, A. F. J., 1969. *A&A* 3, 455.

Moore, B., G. Lake, and N. Katz, 1998. *ApJ* 495, 139.

Moore, B., G. Lake, T. Quinn, and J. Stadel, 1999. *MNRAS* 304, 465.

Morganson, E. et al., 2018. *PASP* 130, 074501.

Mukhanov, V. F. and G. V. Chibisov, 1981. *Soviet Journal of Experimental and Theoretical Physics Letters* 33, 532.

Muldrew, S. I. et al., 2012. *MNRAS* 419, 2670.

Naab, T. et al., 2014. *MNRAS* 444, 3357.

Newton, I., 1687. *Philosophiae Naturalis Principia Mathematica.*

Newville, M. et al., 2021. *Zenodo*.

Norris, R. P., 2016. *PASA* 33, e039.

Norris, R. P., C. Norris, D. W. Hamacher, and R. Abrahams, 2013. *Rock Art Research* 30, 55.

Oh, S. et al., 2020. *MNRAS* 495, 4638.

Owers, M. S. et al., 2017. *MNRAS* 468, 1824.

Pagel, B. E. J. and M. G. Edmunds, 1981. *ARA&A* 19, 77.

Pak, M. et al., 2021. *ApJ* 906, 43.

Parikh, T. et al., 2021. *MNRAS* 502, 5508.

Peebles, P. J. E., 1982. *ApJ* 263, L1.

Peimbert, M., 1968. *ApJ* 154, 33.

Peletier, R. F., 1989. "Elliptical Galaxies - Structure and Stellar Content".

Peng, Y., R. Maiolino, and R. Cochrane, 2015. *Nat* 521, 192.

Peng, Y.-j. et al., 2010. *ApJ* 721, 193.

Perlmutter, S. et al., 1999. *ApJ* 517, 565.

Press, W. H. and P. Schechter, 1974. *ApJ* 187, 425.

Press, W. H., S. A. Teukolsky, W. T. Vetterling, and B. P. Flannery, 1992. *Numerical Recipes in FORTRAN. The Art of Scientific Computing*.

Proctor, R. N., D. A. Forbes, and M. A. Beasley, 2004. *MNRAS* 355, 1327.

Pumfrey, S., 2009. *Notes and Records of the Royal Society*.

Radburn-Smith, D. J. et al., 2012. *ApJ* 753, 138.

Raftery, A. E., 1995. *Sociological Methodology* 25, 111.

Rahman, N. et al., 2012. *ApJ* 745, 183.

Rappenglück, M., 2003. *Uppsala Astronomical Observatory Reports* 59, 51.

Rathjen, T.-E. et al., 2021. *MNRAS* 504, 1039.

Rawlings, A. et al., 2020. *MNRAS* 491, 324.

Renzini, A. and Y.-j. Peng, 2015. *ApJ* 801, L29.

Riess, A. G. et al., 1998. *AJ* 116, 1009.

Ritchey, G. W., 1909. *ApJ* 29, 198.

Roberts-Borsani, G. W. and A. Saintonge, 2019. *MNRAS* 482, 4111.

Robotham, A. S. G., D. S. Taranu, R. Tobar, A. Moffett, and S. P. Driver, 2017. *MNRAS* 466, 1513.

Robotham, A. S. G. et al., 2011. *MNRAS* 416, 2640.

Robotham, A. S. G. et al., 2018. *MNRAS* 476, 3137.

Roediger, J. C., S. Courteau, P. Sánchez-Blázquez, and M. McDonald, 2012. *ApJ* 758, 41.

Roškar, R., V. P. Debattista, T. R. Quinn, G. S. Stinson, and J. Wadsley, 2008a. *ApJ* 684, L79.

Roškar, R. et al., 2008b. *ApJ* 675, L65.

Rousset, G., J. C. Fontanella, P. Kern, P. Gigan, and F. Rigaut, 1990. *A&A* 230, L29.

Rousset, G. et al., 2003. *SPIE* 4839, 140.

Rubin, K. H. R. et al., 2014. *ApJ* 794, 156.

Ruiz-Lara, T. et al., 2016a. *MNRAS* 456, L35.

Ruiz-Lara, T. et al., 2016b. *A&A* 586, A112.

Rupke, D. S. N. and S. Veilleux, 2011. *ApJ* 729, L27.

Samet, H., A. Rosenfeld, C. A. Shaffer, and R. E. Webber, 1984. *Pattern Recognition* 17, 647.

Sánchez, S. F. et al., 2012. *A&A* 538, A8.

Sánchez-Blázquez, P., S. Courty, B. K. Gibson, and C. B. Brook, 2009. *MNRAS* 398, 591.

Sánchez-Blázquez, P., P. Ocvirk, B. K. Gibson, I. Pérez, and R. F. Peletier, 2011. *MNRAS* 415.1, 709.

Sánchez-Blázquez, P. et al., 2006. *MNRAS* 371, 703.

Sánchez-Blázquez, P. et al., 2014. *A&A* 570, A6.

Sandage, A., 1972. *ApJ* 176, 21.

Sandage, A., M. Sandage, and J. Kristian, 1975. *Galaxies and the Universe*.

Sanders, J. S., 2006. *MNRAS* 371, 829.

Sansom, A. E. et al., 2015. *MNRAS* 450, 1338.

Santucci, G. et al., 2020. *ApJ* 896, 75.

Saunders, W. et al., 2004. *SPIE* 5492, 389.

Schaefer, B. E., 2007. *American Astronomical Society Meeting Abstracts* 210, 42.05.

Schiavon, R. P., 2007. *ApJS* 171, 146.

Schwarz, G., 1978. *Annals of Statistics* 6, 461.

Scott, N. et al., 2017. *MNRAS* 472, 2833.

Scott, N. et al., 2018. *MNRAS* 481, 2299.

Searle, L., 1971. *ApJ* 168, 327.

Searle, L., W. L. W. Sargent, and W. G. Bagnuolo, 1973. *ApJ* 179, 427.

Segers, M. C. et al., 2016. *MNRAS* 461, L102.

Sellwood, J. A. and J. J. Binney, 2002. *MNRAS* 336, 785.

Seyfert, C. K., 1943. *ApJ* 97, 28.

Shanks, T. et al., 2013. *The Messenger* 154, 38.

Shanks, T. et al., 2015. *MNRAS* 451, 4238.

Shapley, H., 1918. *ApJ* 48, 89.

Sharp, R. et al., 2015. *MNRAS* 446, 1551.

Sharp, R. et al., 2006. *SPIE* 6269, 62690G.

Shields, G. A., 1974. *ApJ* 193, 335.

Slipher, V. M., 1913. *Lowell Observatory Bulletin* 2, 56.

Smethurst, R. J. et al., 2015. *MNRAS* 450, 435.

Smith, G. A. et al., 2004. *SPIE* 5492, 410.

Smith, R. J., 2022. *MNRAS* 509, 5737.

Smith, R. J. et al., 2009. *MNRAS* 392, 1265.

Spolaor, M., C. Kobayashi, D. A. Forbes, W. J. Couch, and G. K. T. Hau, 2010. *MNRAS* 408, 272.

Springel, V., T. Di Matteo, and L. Hernquist, 2005. *ApJ* 620, L79.

Starobinskiĭ, A. A., 1979. *Soviet Journal of Experimental and Theoretical Physics Letters* 30, 682.

Starobinsky, A. A., 1982. *Physics Letters B* 117, 175.

Strom, S. E., K. M. Strom, J. W. Goad, F. J. Vrba, and W. Rice, 1976. *ApJ* 204, 684.

Sturm, E. et al., 2011. *ApJ* 733, L16.

Sybilska, A. et al., 2017. *MNRAS* 470, 815.

Szeto, K. et al., 2008. 7012, 70122G.

Tantalo, R., C. Chiosi, and A. Bressan, 1998. *A&A* 333, 419.

Taylor, E. N. et al., 2011. *MNRAS* 418, 1587.

Tempel, E., E. Tago, and L. J. Liivamägi, 2012. *A&A* 540, A106.

Terlevich, R., R. L. Davies, S. M. Faber, and D. Burstein, 1981. *MNRAS* 196, 381.

Thomas, D., C. Maraston, and R. Bender, 2003. *MNRAS* 339, 897.

Thomas, D., C. Maraston, and J. Johansson, 2011. *MNRAS* 412, 2183.

Thomas, D., C. Maraston, K. Schawinski, M. Sarzi, and J. Silk, 2010. *MNRAS* 404, 1775.

Tinsley, B. M., 1968. *ApJ* 151, 547.

— ,1972. *ApJ* 178, 319.

Tortora, C. and N. R. Napolitano, 2012. *MNRAS* 421, 2478.

Tortora, C. et al., 2011. *MNRAS* 411, 627.

Trager, S. C., S. M. Faber, G. Worthey, and J. J. González, 2000a. *AJ* 119, 1645.

— ,2000b. *AJ* 120, 165.

Trager, S. C., G. Worthey, S. M. Faber, D. Burstein, and J. J. González, 1998. *ApJS* 116, 1.

Tripicco, M. J. and R. A. Bell, 1995. *AJ* 110, 3035.

Tully, R. B. and J. R. Fisher, 1977. *A&A* 54, 661.

Van den Bergh, S., 1976. *ApJ* 206, 883.

Van de Sande, J. et al., 2017a. *MNRAS* 472, 1272.

Van de Sande, J. et al., 2017b. *ApJ* 835, 104.

Van de Sande, J. et al., 2018. *Nature Astronomy* 2, 483.

Van de Sande, J. et al., 2021a. *MNRAS* 505, 3078.

Van de Sande, J. et al., 2021b. *MNRAS* 508, 2307.

VanderPlas, J., 2014. *Frequentism and Bayesianism: A Python-driven Primer*. arXiv e-prints. URL: https://ui.adsabs.harvard.edu/abs/2014arXiv1411.5018V (visited on 06/26/2023). preprint.

Vanderriest, C., 1980. *PASP* 92, 858.

Vaughan, S. P., R. L. Davies, S. Zieleniewski, and R. C. W. Houghton, 2018. *MNRAS* 479, 2443.

Vaughan, S. P. et al., 2022. *MNRAS* 516, 2971.

Vazdekis, A. et al., 2015. *MNRAS* 449, 1177.

Veilleux, S., G. Cecil, and J. Bland-Hawthorn, 2005. *ARA&A* 43, 769.

Verro, K. et al., 2022. *A&A* 661, A50.

Von Spaeth, O., 2000. *Centaurus* 42.3, 159.

Walcher, C. J., P. Coelho, A. Gallazzi, and S. Charlot, 2009. *MNRAS* 398, L44.

Walcher, C. J. et al., 2016. *A&A* 594, A61.

Watson, F., 2004. *Stargazer : The Life and Times of the Telescope*.

Watson, P. J. et al., 2022a. *MNRAS* 510, 1541.

Watson, P. J. et al., 2022b. *MNRAS* 513, 5076.

Weedman, D. W., 1969. *ApJ* 155, L129.

Westmoquette, M. S., D. L. Clements, G. J. Bendo, and S. A. Khan, 2012. *MNRAS* 424, 416.

Whipple, F. L., 1935. *Harvard College Observatory Circular* 404, 1.

White, S. D. M. and M. J. Rees, 1978. *MNRAS* 183, 341.

Williams, T. B., 1976. *ApJ* 209, 716.

Wolf, C. et al., 2009. *MNRAS* 393, 1302.

Worthey, G., S. M. Faber, and J. J. Gonzalez, 1992. *ApJ* 398, 69.

Worthey, G., S. M. Faber, J. J. Gonzalez, and D. Burstein, 1994. *ApJS* 94, 687.

Worthey, G. and D. L. Ottaviani, 1997. *ApJS* 111, 377.

Wright, T., 1750. *An Original Theory or New Hypothesis of the Universe*.

York, D. G. et al., 2000. *AJ* 120, 1579.

Zheng, Z. et al., 2015. *ApJ* 800, 120.

Zheng, Z. et al., 2017. *MNRAS* 465, 4572.